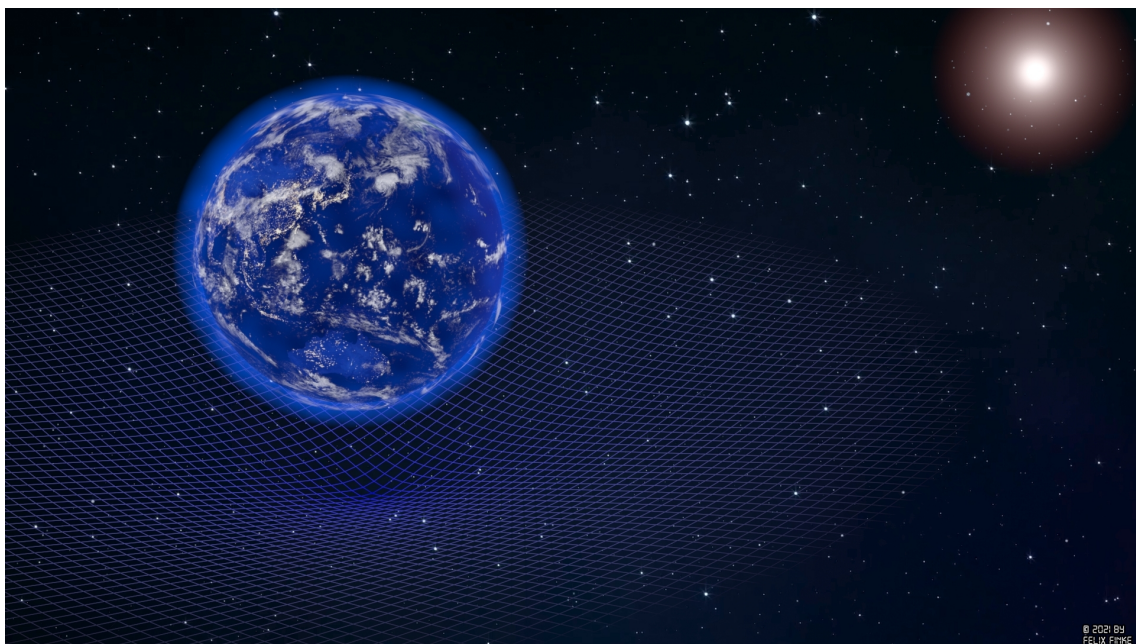# Test of General Relativity with GALILEO Satellites

Felix Finke

Universität Bremen 2022

Test of General Relativity with GALILEO Satellites

Vom Fachbereich für Physik und Elektrotechnik
der Universität Bremen

zur Erlangung des akademischen Grades eines
Doktor der Naturwissenschaften (Dr. rer. nat.)
vorgelegte Dissertation

von

M.Sc. Felix Finke

wohnhaft in Bremen

Contents

$\omega_\oplus$ Angular Velocity of Earth - $7.2921159 \times 10^{-5} \left[\frac{rad}{s}\right]$

ω Argument of Perigee

AU Astronomical Unit - $149597870700\,[m]$

E Eccentric Anomaly

e Eccentricity

m_e Effective Electron Mass - $9.10938356 \times 10^{-31}\,[kg]$

e Electric Charge - $1.602176565 \times 10^{-19}\,[C]$

$a_\oplus$ Equatorial Radius of the Earth - $6.3781366 \times 10^6\,[m]$

ϵ_0 Free Space Permittivity - $8.8541878128(13) \times 10^{-12} \left[\frac{A^2\,s^4}{kg\,m^3}\right]$

G Gravitational Constant - $6.67408 \times 10^{-11} \left[\frac{m^3}{kg\,s^2}\right]$

i Inclination

$M_\oplus$ Mass of the Earth - $5.9722 \times 10^{24}\,[kg]$

n Mean Angular Motion

M Mean Anomaly

P_{srp} Mean Solar Radiation pressure - $4.54 \times 10^{-6} \pm 3.35 \times 10^{-9} \left[\frac{kg}{m\,s^2}\right]$

h Planck constant - $6.62607015e \times 10^{-34} \left[\frac{J}{Hz}\right]$

$J_{2\oplus}$ Quadropole Moment of Earth - 1.082626×10^{-3}

Ω Right Ascension of the Ascending Node

a Semi Major Axis

$P_\odot$ Solar Constant - $1361 \pm 0.5 \left[\frac{W}{m^2}\right]$

σ_{sb} Stefan–Boltzmann constant - $5.670374419 \times 10^{-8} \left[\frac{W}{mK}\right]$

c Velocity of Light - $299792458 \left[\frac{m}{s}\right]$

List of abbreviations and acronyms

ACC	IGS Analysis Center Coordinator
ADEV	Allan Deviation
AltBOC	Alternative BOC modulation
APDL	ANSYS Parametric Design Language
AVAR	Allan Variance
BeiDou	BeiDou
BGD	Broadcast Group Delay
BKG	Bundesamt für Kartographie und Geodaesie
BOC	Binary Offset Carrier
BOL	Begin Of Life
BPSK	Binary Phase Shift Keying
BW	Bandwidth
CAD	Computer-Aided Design
CDMA	Code Division Multiple Access
CMCU	Clock Monitoring and Control Unit
C/NAV	Commercial Navigation
CODE	Center for Orbit Determination in Europe
CS	Commercial Service
DCB	Differential Code Bias
DLR	dlrDeutsches Zentrum für Luft- und Raumfahrt e.V.

DX   Distance Exchange

GSAT0202 FM02

GSAT0201 FM01

ECEF   Earth-Centered Earth-Fixed

ECI   Earth-Centered Intertial

ECMWF   European Centre for Medium-Range Weather Forecasts

ECOM   Empirical CODE Orbit Model

EC   European Commission

EEP   Einstein Equivalence Principle

EGM   Earth Gravitational Model

EOL   End Of Life

ESA   European Space Agency

EUSPA   European Union Agency for the Space Programme

EU   European Union

FEM   Finite Element Model

FE   Finite Element

F/NAV   Freely Accessible Navigation

FOC   Full Orbit Capability

GALILEO   European Global Navigation Satellite System

GCS   Ground Control Segment

GFZ   Geo Forschungs Zentrum

GLONASS Globalnaja nawigazionnaja sputnikowaja sistema

GLONASS Russian Global Navigation Satellite System

GLS   Generalized Least Squares

GMF   Global Mapping Function

GMM   Geometric-Mathematical Model

GMS   Ground Mission Segment

G/NAV   Governmental Navigation

GNSS   Global Navigation Satellite System

GPST	GPS System Time
GPS	Global Positioning System - NAVSTAR Global Positioning System
GSO	Geosynchronous Orbit
GST	GALILEO System Time
HF	High Frequency
HLV	Heavy-Lift Launch Vehicle
ICRF	International Celestial Reference Frame
IERS	International Earth Rotation Service
IGRF	International Geomagnetic Reference Field
IGS	International GNSS Service
ILRS	International Laser Ranging Service
I/NAV	Integrity Navigation
IOV	In-Orbit Validation
IRNSS	Indian Regional Navigation Satellite System
ITU	International Telecommunication Union
JPL	NASA Jet Propulsion Laboratory
LEO	Low Earth Orbit
LLI	Local Lorentz Invariance
LLR	Lunar Laser Ranging
LPI	Local Position Invariance
MBOC	Multiplexed Binary Offset Carrier modulation
MCMC	Markov Chain Monte Carlo
MCMH	Markov Chain Metropolis-Hastings
MEO	Medium Earth Orbit
MF	Medium Frequency
MGEX	Multi-GNSS Experiment
MICROSCOPE	Micro-Satellite à traînée Compensée pour l'Observation du Principe d'Equivalence
MLI	Multi-layer Insulation

MUF	Maximal Usable Frequency
NAVANT	Navigation Antenna (L-Band)
NGA	National Geospatial-Intelligence Agency
NGD	Non-Gravitational Disturbances
OLS	Ordinary Least Squares
ON	Orbit-Normal
OSPF	Orbit determination and time Synchronization Processing Facility
OS	Open Service
PHM	Passive Hydrogen Maser
POD	Precise Orbit Determination
POD	Precise Orbit Determination
PPP	Precise Point Positioning
PRN	Pseudo-Random Noise
PRS	Public Regulated Service
PSD	Power Spectral Density
PTF	Precise Timing Facility
QZSS	Quasi-Zenith Satellite System
RAFS	Rubidium Frequency Standard
RINEX	Receiver INdependent EXchange
RPR	Radiation Pressure
SARANT	Search and Rescue Service Antenna (L-Band)
SEP	Strong Equivalence Principle
SISA	Signal-In-Space-Accuracy
SLI	Single-layer Insulation
SLR	Satellite Laser Ranging
SORCE	Solar Radiation and Climate Experiment
SP3	Extended Standard Product
SRP	Solar Radiation Pressure
SS	Spread Spectrum

TAI	International Atomic Time
TCS	Thermal Control System
TDB	Barycentric Dynamical Time
TECU	Total Electron Content Unit
THEMIS	Time History of Events and Macroscale Interactions during Substorms
TMM	Thermal Mathematical Model
TRP	Thermal Radiation Pressure
TSI	Total Solar Irradiance
TT&C	Telemetry Tracking & Control
UFF	Universality of Free Fall
UHF	Ultra High Frequency
ULS	Uplink Station
UTC	Coordinated Universal Time
UV	Ultraviolet
VDA	Vacuum Deposited Aluminum
VHF	Very High Frequency
WEP	Weak Equivalence Principle
WSS	Wide-Sense Stationary
YS	Yaw-Steering
ZARM	Zentrum für angewandte Raumfahrttechnologie und Mikrogravitationsforschung

Introduction

In the history of applied physics, there are numerous discoveries and experiments that have been fundamental in shaping today's picture of physical world and serving as tools for the continuous verification of physical theories. One of the best verified (classical) theories is the General Theory of Relativity. It interprets the phenomenon of gravitation as a geometrical property of space and time. This theory has allowed us to gain a deeper understanding of the interaction between matter and space-time and, to that extent, explains many phenomena caused by the nature of gravity. As it will turn out in the following section, there have been many efforts in the last decades to carry out numerous tests of this theory, by which it always turned out that any predictions could be successfully proved by observations. Among the most impressive and vivid evidences are probably the detection of gravitational waves [1] in September 2015 and the first direct observation of the super-massive black hole in the galaxy M87 with the help of the Event Horizon Telescope in April 2017 [5], and the recently published (May 2022 [4]) results from direct observations of the shadow of the super-massive black hole Sagittarius A* at the center of our Milky Way galaxy in 2017.

Apart from the above-mentioned modern tests, there are three classical tests of General Relativity, which were already proposed by Albert Einstein [6]. Among these are (1) the perihelion precession of Mercury, (2) the deflection of light by the Sun, and (3) the gravitational redshift of light. As an additional test, the radar echo delay was added later (4), which was first predicted by *Irwin I. Shapiro* in 1964 [101] and successfully tested a few years later ([103], [102]). This effect is called after its discoverer and is therefore called *Shapiro time delay*. This work documents the results of a revisitation of one of these classical tests, specifically that of the gravitational redshift, which can be derived as a consequence of the equivalence principle, one of the fundamental principles of General Relativity. The opportunity has been given by the fortunate circumstance that the two GALILEO satellites FM01 and FM02 have been guided to elliptical orbits by a technical malfunction instead of being placed on circular orbits, as is usual for navigation satellites. Since then, the satellites rise and fall to their apogee and perigee positions in Earth's gravitational field twice a day. As a consequence of the Equivalence Principle, the frequencies of the high-precision atomic clocks that are part of the satellites' payload are thereby

subjected to a corresponding modulation. These two "satellite laboratories" thus provide an ideal experimental setting for a redshift test, the last precision measurement (Gravity Probe A) of which now dates back several decades.

In addition to the analysis and evaluation of the clock data of both satellites, the modeling of systematic effects plays a major role in the preliminary stage of the data analysis. As for systematic effects superimposed on satellite observation data used to estimate the clock data, these occur from various error sources, which can be divided into two categories: signal propagation effects and orbital perturbations. Of particular importance are those effects that have approximately the same signature or harmonic resonance as the redshift modulation. To investigate the latter in more detail, we present a novel finite element solar radiation pressure model for the Galileo satellites that accurately addresses the systematic orbit perturbations and discuss the model performance based on a parameter estimation framework using an obit determination procedure. We also discuss the modeling of measurement limitations potentially imposed upon the atomic clocks by magnetic and thermal perturbations. The focus is on estimating upper and lower bounds for a reasonable limitation of the measurement uncertainty given by these factors.

Basics of General Relativity

1.1 Equivalence Principle

The Equivalence Principle is an elementary prerequisite which substantially promoted the development of the theory of General Relativity. By the this principle, the effect of gravity should be represented as a curvature of space-time, and this idea led Einstein to the development and eventual publication of his field equations in 1915 [36]. We briefly review the implications of the Equivalence Principle, as well as the consequences that can be drawn from it, which have been verified over the years by numerous experimental tests. The Equivalence Principle encapsulates three different aspects:

- The Universality of Free Fall (UFF)

- The Local Position Invariance (LPI)

- The Local Lorentz Invariance (LLI)

The Weak Equivalence Principle (WEP) states that two test masses fall at the same rate regardless of their composition. This principle is also referred to as the UFF. Classical experiments to proof the UFF are Eötvös experiments: If one measures the relative acceleration of two different test masses A and B in a free-fall experiment, a possible difference in their drop rates can be interpreted as a violation of the WEP and is conventionally measured with the Eötvös parameter:

$$\eta_E = \frac{(m_i/m_g)_a - (m_i/m_g)_b}{(m_i/m_g)_a + (m_i/m_g)_b} \tag{1.1}$$

where m_g and m_i are the gravitational and inertial masses of the free-falling objects.

One of the most recent tests of the WEP have been performed by the Micro-Satellite à traînée Compensée pour l'Observation du Principe d'Equivalence (MI-CROSCOPE) satellite mission. This was to achieve an accuracy of 10^{-15}, and from an initial data analysis conducted by *Touboul et al.* [118] one obtained results of the order of the experiment's objective sensitivity. This outperforms the result of the most precise torsional balance experiment to date, carried out by *Wagner et al.* [124] in 2012, which achieved an accuracy of 10^{-13}. The future mission STEP (Satellite Test of the Equivalence Principle) ([66], [66], [110]) is planned to a have a very similar mission and payload design as the MICROSCOPE experiment and promises a precision level of 10^{-18}.

As a consequence of the WEP, which mainly articulates the observation that different test masses fall at the same rate in free-fall experiments, in 1907 Einstein came to the pioneering conclusion that it is generally impossible to distinguish whether the outcome of an experiment is affected by the presence of a homogeneous gravitational field or a homogeneous acceleration. Einstein thoroughly presents the Strong Equivalence Principle (SEP) in [35]. In his article, he first emphasizes the WEP, the equivalence of inertial and gravitational mass, and points out that the importance of this concept has far-reaching consequences: The physical equivalence with respect to *any* experiment of two different observer reference frames, one that rests in a homogeneous gravitational field and one that is homogeneously accelerated while unaffected by a gravitational field. In his publication, as a direct consequence of the SEP he used his findings to derive the redshift of light exchanged between two observers separated by a certain vertical distance, which is to be expected in a gravitational field. As a precious result, it shall be pointed out that with the help of the SEP alone, one is thus able to describe effects due to gravity, simply by using an accelerated reference frame. In literature terminologically the term Einstein Equivalence Principle (EEP) is used instead of SEP. Historically, this is owed to a variation of the SEP, in which experiments with non-gravitational interaction are considered. To remain compliant with the literature, we use the term EEP in this context.

A redshift test is a famous experiment to proof the LPI, which states that the outcome of any non-gravitational experiment is independent of space and time. Following Einstein's original considerations, the EEP implies that one measures a frequency shift between two different clocks, which are installed at fixed positions in a gravitational field (of the Earth) and have a fixed height distance to each other. In appeal to the LPI, if one compares the readings of these clocks in their respective local Lorentz frame, regardless of the position in space-time, one should come to the conclusion that their frequencies are equal. Thus, an important conclusion is that the measured redshift should not depend on the location of the experiment where the measurement takes place, just as the result of the measurement should not depend on the physical structure or the operation principle of the clock used. This is also known as the *Universality of Gravitational Red-*

TESTS OF LOCAL POSITION INVARIANCE

Figure 1.1: Overview of LPI experiments by *C. Will* [126], [12] to determine the violation factor α, which is the deviation from the predicted redshift to be measured between two different clocks in a gravitational field according to the given formula.

shift. A deviation from the predicted redshift is considered a violation of the LPI and thus the EEP. The article of *C. Will* [126], represents a concise compendium on "The Confrontation between General Relativity and Experiment" and we reproduce with figure 1.1 his representation of all the experiments performed until the year 2014 to verify the LPI.
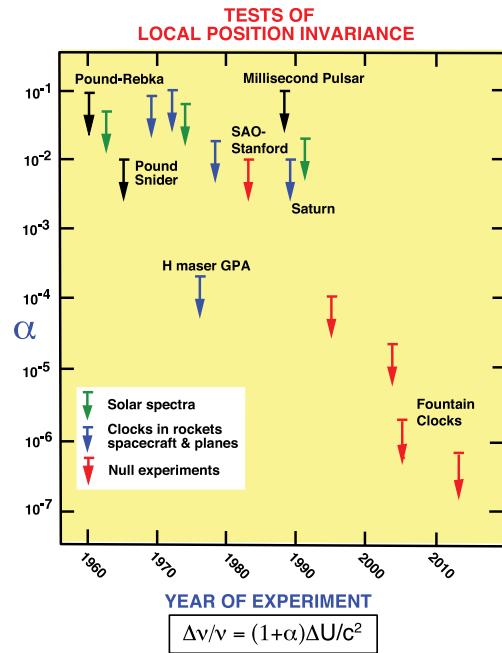
In 1959, *Pound and Rebka* [84] made use of the Mössbauer effect to demonstrate the frequency shift of sharp γ spectral lines due to the Earth's gravitational field over a vertical path of 22.5 meters in the tower of the Jefferson Physical Laboratory. The results of an improved version of this experiment was published in 1965 by *Pound and Snider* [85]. The most accurate experiment to date was Gravity Probe A (GP-A) conducted by *Vessot and Levine* ([122], [120], [121]) using a atomic Hydrogen Maser on a sounding rocket that was launched to an altitude of 10000km. During the nearly two-hour flight, the atomic clock's rate was continuously compared to an identical on-ground atomic clock. During the experiment, a two-way microwave link was established, both to eliminate the first-order Doppler effect by exploiting the signal echo, and to directly measure the frequency shift between the atomic clock on the rocket with that of the Hydrogen Maser on the ground. The confirmation of the LPI was at an accuracy level of 1.4×10^{-4}. The ACES (Atomic Clock Ensemble in Space) experiment is a planned experimental laboratory to be installed on the International Space Station (ISS). ACES is designed to test a new generation of atomic clocks (PHARAO (Projet d'horloge atomique par refroidissement d'atomes en orbite) Hydrogen Masers) under microgravity conditions. On the

one hand, researchers hope that the mission with its payload will contribute to the further development of a more precise, global time determination standard, and on the other hand the mission will be used to enable the evaluation of general relativity at an unprecedented level ([22], [67]). With this experiment it is expected to measure the redshift with an accuracy of 3×10^{-6}. Finally, the mission project STE-QUEST ([2], [7]) (Space-Time Explorer and Quantum Equivalence Principle Space Test) within the scientific space program *Cosmic Vision* of the European Space Agency (ESA) shall be mentioned, whose launch date was postponed to the year 2024. In contrast to other experimental proponents, it is intended to investigate two aspects of the General Theory of Relativity. On the one hand, it is planned to measure the relative acceleration of free-falling atoms by means of atom interferometry in order to confirm the WEP with an accuracy three orders of magnitude higher than MICROSCOPE. Second, the time dilation or gravitational redshift will be measured using the same atomic clock system used in the ACES experiment. To maximize this effect, an orbital eccentricity of ≈ 0.78 is targeted. Compared to ACES, an increase in accuracy by a factor of 45 to 400 is to be expected.

General Relativity has been unyieldingly tested, and no evidence of violations of its underlying principles have yet been found. On the way to a quantum mechanical description of gravity, in order to get closer to a possible unification of the fundamental forces governing physics, one is looking for alternative ways of description in order to overcome weaknesses of existing theories. One representative alternative theory is the Standard Model Extension (SME) ([24], [25]), which offers a framework for the evaluation and interpretation of potential EEP violations originating from Lorentz and CPT symmetry breaking. As far as a test of the EEP is concerned, certain coupling parameters can be derived from this theory for different particle species or bodies of different composition, respectively, that potentially indicate a violation of the LPI. *ChengGang et al.* [86] propose a combined WEP and LPI test to derive bounds to the violation coefficients predicted by the SME. The Earth E with a distributed ensemble of identical Strontium optical lattice clocks Sr in free-fall around the Sun was considered as the experimental environment. The analyzed violation signal $\beta_E - \xi_{Sr}$ refers to a non-vanishing redshift in the Earth's co-moving reference frame and was inferred from fractional frequency comparisons between these clocks, where β_E comes as a WEP and ξ_{Sr} as a LPI violation factor. In combination with the results from preceding precision tests[1], it was shown that SME parameter predictions can be indirectly constrained to $0.3 \pm 0.9 \times 10^{-4}$ in the best case.

By reference to this study, a series of tests ([50], [117], [77], [11]) could define lower bounds for LPI-specific violation parameters using experiments with non-gravitational interactions to assess the validity framework of the EEP and thus limit the scope for alternative theories. As a notable reference, a study by *N. Ashby et al.* in [11] shows that the LPI violation can be constrained at least by $|\alpha_{Cs} - \alpha_H| = 2.2 \pm 2.5 \times 10^{-7}$. This result was obtained from long-term measurements of the fractional frequency differences of Earth-bound Cesium fountains and Hydrogen Masers under the influence of the Sun's gravitational field.

---

[1]Such as this study on the redshift test with the GALILEO satellites.

1.1.1   General relativistic redshift modeling

Following [69] on p. 64, the frequency ω of a photon with four-momentum vector k_ν measured by an observer with four-velocity u^ν can be written as:

$$\omega = -k_\nu u^\nu \tag{1.2}$$

where we adopt the index notation from the literature. Comparing the frequencies perceived by two observers, the measured frequency ratio can be defined as:

$$1 + z = \frac{\omega}{\hat{\omega}} \tag{1.3}$$

which is a measure of redshift, whereby ω and $\hat{\omega}$ denote the different frequencies measured by each of the observers. A universal redshift formula for standard clocks[2] in General Relativity is described in [58] and states:

$$1 + z = \frac{g_{\mu\nu} \frac{d\lambda(s)^\mu}{ds} \frac{d\gamma^\nu}{d\tau}}{g_{\rho\sigma} \frac{d\lambda(s)^\rho}{ds} \frac{d\hat{\gamma}^\sigma}{d\hat{\tau}}} \tag{1.4}$$

where λ is a lightlike geodesic depending on an affine parameter s that connects the world-lines $\gamma(\tau)$ and $\hat{\gamma}(\hat{\tau})$ of the two observers each measuring proper time τ and $\hat{\tau}$, respectively. The integral curves of the observers give rise to a set of four-vector fields u and $\hat{u}$ describing their actual motion. Depending on the state of motion, the vector fields must be also evaluated with special consideration of the underlying space-time metric $g_{\mu\nu}$. Furthermore, the way of realization of signal exchange through $\lambda(s)$ must be known.

On account that the gravitational redshift phenomenon is central to this work, we would like to derive here the redshift for a typical special case of two observers at rest, inspired by the experiment of Pound and Rebka in no small part. We assume that there is a timelike Killing vector field ξ^ν proportional to the four-velocity u^ν of a *stationary* observer, which specifies the direction in which an underlying space-time metric is preserved. As such, u^ν can be identified by ξ^ν using a normalization condition as follows:

$$u^\nu = \frac{\xi^\nu}{\sqrt{-\xi_\nu \xi^\nu}} \tag{1.5}$$

Killing vectors give rise to a conserved quantity as long as geodesic motion is concerned. This implies a constant of motion p_0 along a photon's null geodesic, which can be derived from the projection of a Killing vector ξ^ν onto a tangent vector k_ν to the photon's null geodesic:

$$p_0 = -k_\nu \xi^\nu \tag{1.6}$$

Substituting 1.5 into 1.2 yields the frequency measured by the observer:

---

[2]A characterization of standard clock is presented by *V. Perlick* in [78]

$$\omega = \frac{k_\nu \xi^\nu}{\sqrt{-\xi_\nu \xi^\nu}} \tag{1.7}$$

Considering two stationary observers O and $\hat{O}$ at different locations with their four-velocities, applying equation 1.3 yields:

$$1 + z = \frac{\omega}{\hat{\omega}} = \sqrt{\frac{-\hat{\xi}_\nu \hat{\xi}^\nu|_{\hat{O}}}{-\xi_\nu \xi^\nu|_O}} \tag{1.8}$$

We would like to put the result in concrete terms by using an explicit form of a space-time metric. Following [18] page 85 ff, the Schwarzschild metric considers a static, spherically symmetric gravitational field and may be defined as:

$$ds^2 = g_{00}(r)dt^2 + g_{rr}dr^2 + r^2 d\Omega^2 \tag{1.9}$$

where we identify t as a time coordinate and r as a radial coordinate. In resemblance of the metric of a sphere, $r^2 d\Omega^2$ can be interpreted as the metric of surfaces with constant t and r. Performing a frequency comparison between the two stationary observers O and $\hat{O}$ resting at different positions r and $\hat{r}$, following 1.8, we obtain the expression:

$$1 + z = \frac{\omega}{\hat{\omega}} = \sqrt{\frac{g_{00}(\hat{r})}{g_{00}(r)}} = \sqrt{\frac{1 - r_s/\hat{r}}{1 - r_s/r}} \approx 1 - \frac{1}{2}r_s\left(\frac{1}{\hat{r}} - \frac{1}{r}\right) \tag{1.10}$$

where $r_s = 2GM$ represents the Schwarzschild radius, G denotes the gravitational constant, and M being the mass of the body constituting the source of the gravitational field. For a somewhat more detailed discussion of frequency comparisons in Schwarzschild space-time, considering various special cases of observer scenarios, we refer the reader to [81].

Let τ be the proper time of a clock on a satellite orbiting the Earth and t a fixed coordinate time, then according to *N. Ashby* [10] a certain time interval $\int dt$ can be calculated by integrating τ along the satellite's orbit:

$$\int dt = \int d\tau \left[1 - \frac{\Delta U_\oplus}{c^2} + \frac{v^2}{2c^2}\right] \tag{1.11}$$

In formula 1.11, $\Delta U_\oplus$ is the potential difference in Earth's gravitational field between two positions at different altitudes, v is the velocity of the orbiting satellite and τ represents the proper time as counted by the satellite's clock.

Coordinate time can be interpreted as the reading of a clock in a local inertial coordinate system. In the above formula, the coordinate time t is related to the proper time τ of the satellite clock, in the sense that this equation describes how to maintain time synchronization between two different observers. In order to bring the readings of the clocks of these observers into agreement, one requires additional information about their relative position and motion. Hence, one has to derive

the correct coordinate transformation, which relates the time measurements to each other. Under simplifying conditions, one obtains the integrand on the rhs defined above, which contains the mathematical traces of this transformation covering the relative position and motion. Term 1.11 contains two contributions with opposite signs. According to that formula, a clock at a higher potential, more distant from Earth would beat faster than a clock at a lower potential in the direct vicinity of the planet. That means that time has to be down-corrected for clocks on satellites flying at higher altitudes to be able to synchronize them with clocks at lower altitudes. The third term of the integral in the above formula features the 2nd order Doppler shift which is due to the velocity of the spacecraft. An example of a coordinate time is the GPS system time, serving as a synchronization reference between the GPS satellite clocks and the ground-based reference clocks. For the purpose of synchronization, the appropriate relativistic corrections from the equation 1.11 can be applied. Here, the reference clocks are regarded as ideal, standard clocks at rest, located on the Earth's geoid. The corresponding potential associated with the geoids level surface is proposed in [10].

$$\Phi_0 = -\frac{GM_\oplus}{a_\oplus} - \frac{GM_\oplus J_{2\oplus}}{2a_\oplus} - \frac{\omega_\oplus^2 a_\oplus^2}{2} \tag{1.12}$$

where the first term covers the contribution of the Earth's point-mass potential, the second term implies the quadrupole moment factor due to the Earth's oblateness and the third term accounts for the Earth's spin. For synchronization of a clock on a satellite in the Earth's potential U and a reference clock on the rotating geoid with the potential assumed in 1.12, one must replace ΔU by $V - \Phi_0$ in 1.11. Note that the time transformation 1.11 is presumed to hold in a space time domain which encompasses both the clock on the rotating geoid as well the satellite orbiting around Earth. For the value of the geoid's equipotential a value of $\Phi_0 = 6.969290134 \times 10^{-10}$ is taken from the numerical standards in [80].

We now look for an expression of the total relativistic time dilation based on equation 1.11. Substituting $\Delta U = V - \Phi_0$ into this equation, where U is sought to be the point-mass potential of the Earth one yields:

$$\int dt = \int d\tau \left[1 - \left(\frac{GM_\oplus}{rc^2} - \frac{\Phi_0}{c^2} \right) + \frac{v^2}{2c^2} \right] \tag{1.13}$$

Under the assumption of energy and angular momentum conservation, one finds the vis-viva equation for the specific energy of a body orbiting around a central mass:

$$-\frac{GM_\oplus}{r} + \frac{v^2}{2} = -\frac{GM_\oplus}{2a} \tag{1.14}$$

Equation 1.14 holds for orbiting objects whose mass is negligible in comparison the mass of their central body. Thereby, the Earth is assumed to generate the point-mass potential $U = \frac{GM_\oplus}{r}$. Inserting equation 1.14 into 1.13 by substituting the kinetic energy term, one obtains:

$$\int dt = \int d\tau \left[1 + \frac{\Phi_0}{c^2} + \frac{3GM_\oplus}{2ac^2} + \frac{2GM_\oplus}{c^2} \left(\frac{1}{r} - \frac{1}{a} \right) \right] \tag{1.15}$$

The first three terms of the integrand in formula 1.15 give a constant contribution to the redshift, whereas the last term varies with the distance to the Earth's center and can be understood as a redshift modulation depending on the elongation of the elliptic orbit. To compute the integral of the last term, one can first substitute the relation between the radius and the eccentric anomaly $r = a\left(1 - e\cos(E(\tau))\right)$ for r. Furthermore, making use of the differential dependency between the eccentric anomaly E and the time τ:

$$\frac{dE}{d\tau} = \frac{\sqrt{\frac{GM_{\oplus}}{a^3}}}{\left(1 - ecos(E(\tau))\right)} \tag{1.16}$$

one finally receives:

$$\frac{2GM_{\oplus}}{c^2} \int d\tau \left[\frac{1}{r} - \frac{1}{a}\right] = \frac{2GM_{\oplus}}{c^2} \int d\tau \left[\frac{ecos(E(\tau))}{a\left(1 - ecos(E(\tau))\right)}\right] \tag{1.17}$$

$$= \frac{2\sqrt{GM_{\oplus}a}\,e}{c^2} \int \left[\cos E(\tau)\right] d\tau \tag{1.18}$$

$$\Delta t_{rel} = 2\frac{\sqrt{GM_{\oplus}a}}{c^2} e\sin(E(\tau)) \tag{1.19}$$

An alternate expression is given by:

$$\Delta t_{rel} = 2\frac{\mathbf{rv}}{c^2} \tag{1.20}$$

where $\mathbf{r}$ and $\mathbf{v}$ stand for the position and velocity vectors of the satellite in an Earth-Centered Intertial (ECI) system. This last term 1.20 can be derived by equating the expressions for the mean anomaly $M = E(t) - e\sin E(t)$ and $M_0 + n\left(t - t_0\right)$ where M_0 declares the mean anomaly at some reference epoch $t_0 = 0$ and n is the mean angular motion $n = \sqrt{\frac{GM_{\oplus}}{a^3}}$ which directly follows from Keplers third law:

$$E(t) - e\sin(E(t)) = M_0 + \sqrt{\frac{GM_{\oplus}}{a^3}}\left(t - t_0\right) \tag{1.21}$$

$$\dot{E}(t)\left(1 - e\cos(E(t))\right) = \sqrt{\frac{GM_{\oplus}}{a^3}} \tag{1.22}$$

Equation 1.22 arises from differentiating formula 1.21 with respect to time which is exactly the same result as equation 1.16. Taking the first time derivative of the orbital radius that depends on the eccentric anomaly E results in

$$r = a\left(1 - e\cos(E(t))\right) \tag{1.23}$$

$$\dot{r} = ea\sin(E(t))\dot{E}(t) \tag{1.24}$$

Inserting (1.24) in (1.22) gives:

$$\dot{r}\left(1 - e\cos(E(t))\right) = \sqrt{\frac{GM_\oplus}{a^3}}\, ea\sin(E(t)) \tag{1.25}$$

Multiplying equation (1.25) by a and rewriting it with the help of formula (1.21) finally leads to the expression:

$$\dot{r}\, r = \sqrt{GM_\oplus a}\; e\sin(E(t)) \tag{1.26}$$

$$\Leftrightarrow 2\frac{\mathbf{r}\mathbf{v}}{c^2} = 2\frac{\sqrt{GM_\oplus a}}{c^2}e\sin(E(t)) \quad \square \tag{1.27}$$

which directly leads to equation 1.19 / 1.20. If the eccentricity or the radial orbital velocity vanishes, i.e. $\mathbf{r}$ is perpendicular to $\mathbf{v}$, both expression 1.19 and 1.20 become zero.

Chapter 1

Experimental setup

2.1 GALILEO-FOC satellite constellation

The European Global Navigation Satellite System (GALILEO) satellite system is an initiative launched by the European Union (EU) and its realization is under the operational leadership of the European Union Agency for the Space Programme (EUSPA)[1] together with the ESA as design authority and prime contractor. The GALILEO Full Orbit Capability (FOC) satellite constellation comprises twenty-seven plus three spare satellites arranged in a Walker Delta Pattern, which is parametrized by (27/3/1), where the spare satellites are not included. This means that the satellites occupy three different and equally spaced orbital planes, which are each inclined by $56°$ with respect to the Earth's equator. In addition, the nine satellites from each of the three groups are evenly distributed on their destination orbit, resulting in a phase constant of $40°$. An artificial representation of the complete constellation is shown in 2.2. The first two GALILEO satellites FM02 (GSAT0202) and FM01 (GSAT0201) of the FOC generation, which are the focus of this work, were mounted on a Fregat MT upper stage of a Soyuz ST-B rocket 2.1. These satellites are currently operational, but temporarily unusable. A new type of dispenser was then designed to be capable of carrying four satellites at once. Thereby, the Ariane 5 ES Heavy-Lift Launch Vehicle (HLV) was used to bring the satellites into their target orbits and the first launch of a quadruple of satellites was finally carried out on November, 17th 2016. As the life cycle of the first GALILEO satellites will end in the near future, the launch of the second generation of GALILEO satellites has recently been planned for 2024. The system concept and first batch of twelve second generation satellites will be manufactured in a collaboration between Thales Alenia Space and Airbus Defence & Space. According to announcements by ESA[2], the new satellite system will have an electric propulsion system, which could provide lifetime maneuverability. Furthermore it will be equipped with a more effective navigation antenna and an improved navigation timing system. To cope with the technical

---

[1]The EUSPA supports the European Union by taking care of the public interests related to the European Global Navigation Satellite System (GNSS) programs.

[2]https://www.esa.int/esearch?q=second+generation

requirements and the specific power budget needed for operations, the satellite bus system must be scaled accordingly. Therefore, the satellites will also be larger than their predecessors.

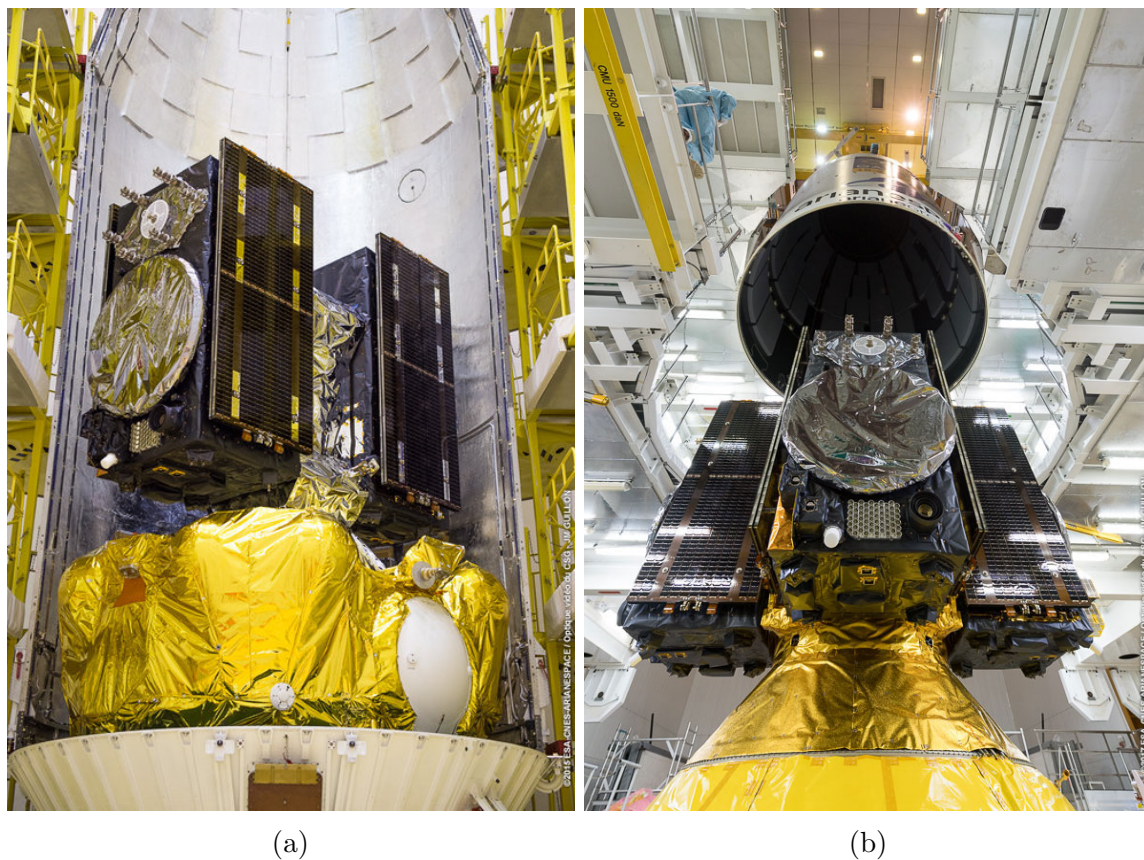(a)   (b)

Figure 2.1: Left, two GALILEO satellites attached to the dispenser unit mounted onto the Soyuz ST-B/Fregat-MT upper stage, which was destined to carry the satellites (E18 and E14) to their circular Medium Earth Orbit (MEO) orbit. The right picture shows the satellite arrangement (E21, E25, E27, E31) on the upper stage of the Ariane 5 ES. The first time, a quartet of GALILEO satellites was launched by the Ariane 5 ES rocket was on November, 17, 2016.
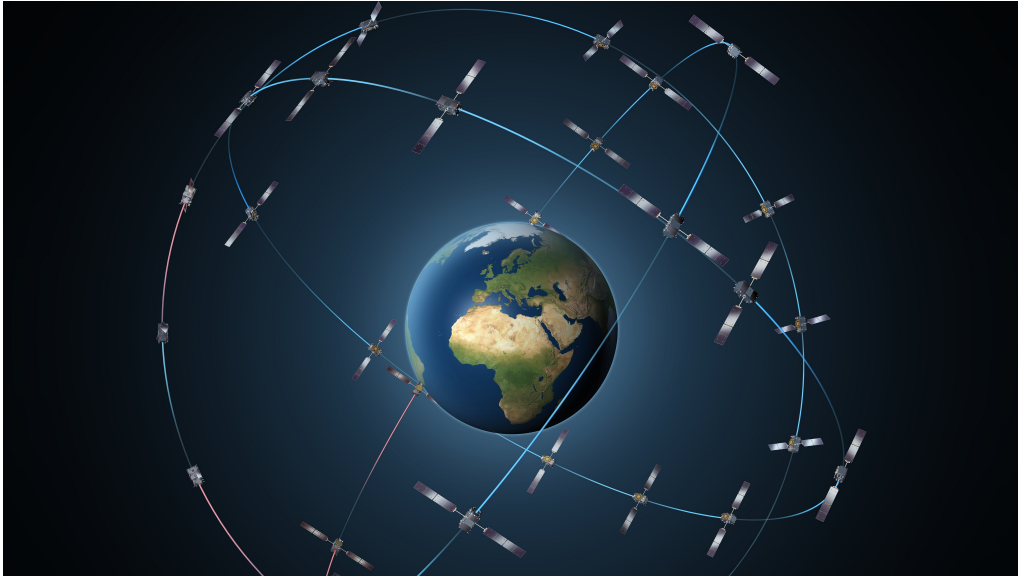
Figure 2.2: Complete GALILEO constellation along its three orbital planes. The picture was taken from the ESA homepage: `https://www.esa.int/ESA_Multimedia/Images/2014/07/Galileo_constellation`.

2.1.1 GALILEO FM01 and FM02 mission details

On August, 22nd 2014, the first two GALILEO satellites of the FOC generation were launched into their orbit. Instead of reaching their planned destination, an orbit injection failure lead to a significantly lower orbit characterized by a high eccentricity (0.23 instead of 0.0002 for a nearly circular orbit) and a lower inclination (49.7° instead of 55°). Table 4.2 shows the current orbital elements of the satellites GSAT0202 and GSAT0201. Preliminary investigations revealed that an anomaly in the Fregat upper stage[3] resulted in an incorrect thrust maneuver at the apogee injection point where the engines were ignited. Cause for the wrong thrust vector settings was a frozen hydrazine line, which was connected to a cryogenic helium feed line via the same support structure due to an assembly error[4]. However, this assembly error was not caused during hardware integration, but originated from deficiencies in the thermal design of the upper stage. In an attempt of mission recovery[5], ESA initiated eleven orbit correction maneuvers within seventeen days, which made it possible to raise the perigee of GSAT0201 by approximately 3500km to 17235km to reach a more circular orbit with an eccentricity of 0.162. This is equivalent to a revolution period of about thirteen hours. In this orbit configuration, GSAT0201 passes the same point on Earth once in twenty days, which is twice the time of the nominal configuration and still suffices to synchronize the satellite's flight pattern with that of the full constellation to conduct nominal navigation operations[6]. Finally, on November 29, 2014, the satellite's navigation payload was successfully activated

---

[3]`https://www.esa.int/ESA_Multimedia/Images/2003/04/Fregat_upper_stage_diagram`

[4]Arianespace press release: "Soyuz Flight VS09: Independent Inquiry Board announces definitive conclusions concerning the Fregat upper stage anomaly", October, 8th, 2014.

[5]Inside GNSS press release: "Galileo 5 and 6 Eccentric Satellites: Mission Recovery and Exploitation Part I", August, 15th, 2018.

[6]`https://www.esa.int/Applications/Navigation/Galileo_satellite_set_for_new_orbit`

and the first signals were received. A similar recovery campaign was launched for GSAT0202, followed by a first payload activation on March, 15th, 2015, after fourteen orbit correction maneuvers had been performed. These maneuvers used up almost all the fuel, rendering further thrust maneuvers impossible. The suborbital tracks of the satellite's trajectories recorded in late November 2015 are depicted in figure 2.3. On November, 30th, 2020, the use of the satellite signals from GSAT0202 and GSAT0201 was officially released for navigation purposes and correspondingly, the signal health status bit in the navigation data was changed from *Signal Component currently in Test* to *Signal OK* as explained in [119], so that all compatible receivers could automatically process the navigation signal. The European Commission published an official service notice[7] stating that the satellites can be used to experience a better navigation performance. However, after it became apparent during an user evaluation phase that some commercial receivers were having technical difficulties evaluating the signals from these satellites due to their different orbit dynamics. As a consequence, it was announced by the European Commission[8] on February, 16th, 2021 that the satellites had been temporarily removed again from the orbit constellation, while a solution is being investigated in the meantime. Since then, the signals from the satellites are no longer accessible to commercial receivers due to the health status bit removed again.

---

[7]`https://www.gsc-europa.eu/sites/default/files/sites/all/files/`
`Galileo-service-notice-04-v1.0.pdf`
[8]`https://www.gsc-europa.eu/sites/default/files/sites/all/files/`
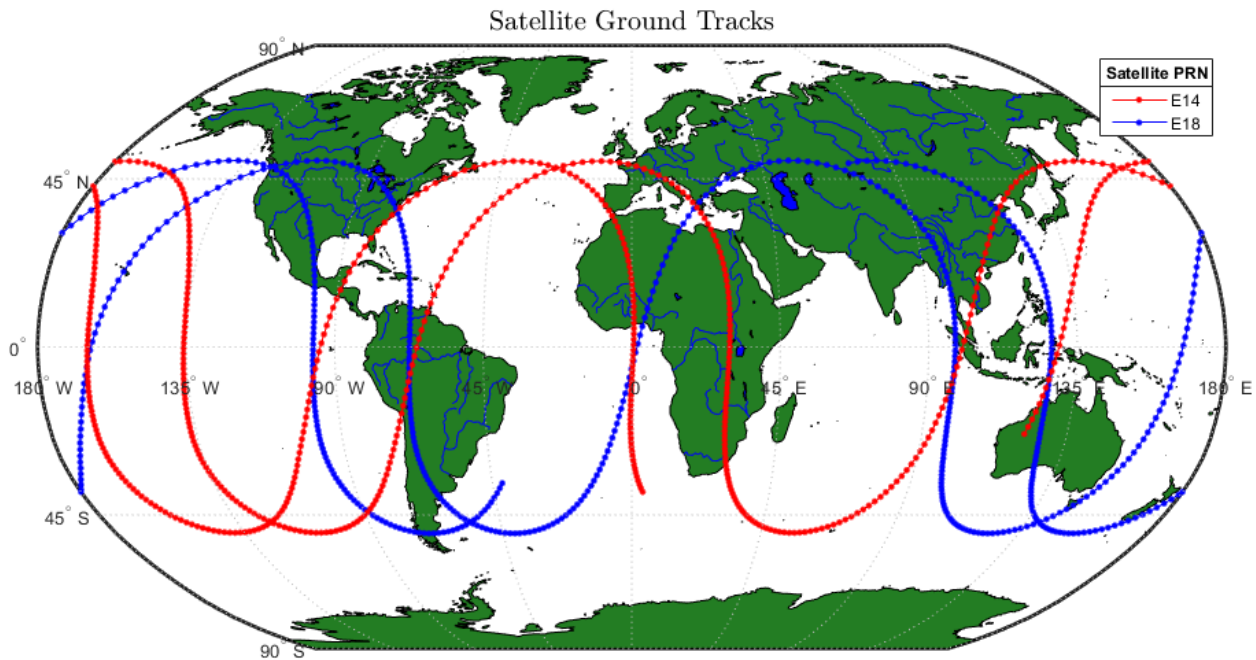`Galileo-service-notice-05-v1.0.pdf`

Figure 2.3: Comparison of ground tracks of GALILEO satellites E14 (blue) and E18 (red) recorded on November, 30th, 2015.

2.2 GALILEO services and signals

GNSS observables are provided in a special exchange format. The International GNSS Service (IGS) consortium established a working group, which manages maintaining, archiving and distributing GNSS raw data and and provides these to the GNSS community in the form of Receiver INdependent EXchange (RINEX) files. Among the fundamental observables are pseudo-range, phase and Doppler measurements, which are generated through acquisition and tracking of a variety of selected signals distributed among different navigation satellite systems as the Global Positioning System - NAVSTAR Global Positioning System (GPS), GALILEO, BeiDou (BeiDou), the Indian Regional Navigation Satellite System (IRNSS), the Russian Global Navigation Satellite System (GLONASS) or others including satellite based navigation augmentation systems. These observations are made available in the form of specific (mixed) RINEX observation data files by IGS data centers. According to the official interface control document [119], the GALILEO satellites continuously transmit three different signals on four different frequency bands. The signals are listed in table 2.1. Furthermore, the E5 signal is split into the E5a and E5b channels. These signals encode four different types of navigation message streams, which are partly publicly or commercially available on different signal channels. IGS data centers record and arrange these data into the RINEX GALILEO navigation message format. The four navigation messages comprise Freely Accessible Navigation (F/NAV) Integrity Navigation (I/NAV) and Commercial Navigation (C/NAV) data. F/NAV messages are provided via an Open Service (OS) data stream, the C/NAV message format is intended for the purpose of Commercial Services (CSs), and finally the I/NAV message format is shared among both mentioned user domains and should support open and commercial services. Unlike F/NAV, I/NAV provides a dual-frequency service enabling to receive double the information rate as compared to the F/NAV service. However, if received by a single frequency user, the data rate performance is the same as of the F/NAV service. Alongside these

message services, the GALILEO system also provides special encrypted Public Regulated Services (PRSs) in the form of Governmental Navigation (G/NAV) messages, and its use is restricted to governmental authorities only. The last column of table 2.1 indicates what services are distributed on which frequency channel.

The navigation data messages are maintained and regularly updated by the GALILEO Ground Mission Segment (GMS), which also comprises sensor and uplink stations. Payload and data management as timing service provision or satellite signal tracking and monitoring activities are among the basic tasks of the GMS. The resulting measurements are used by associated ground segment facilities to estimate ephemerides data or satellite clock parameters or to generate and evaluate the Signal-In-Space-Accuracy (SISA)[9] information to mention only a few fundamental GMS tasks associated with the service provider's scope of responsibility. To meet the data integrity and navigation performance level requirements, service parameters are continuously monitored, (re-)determined and frequently uplinked to the spacecrafts. These serve as validation and qualification hallmarks for the corresponding navigation data set or the satellite health status. A holistic view over the GALILEO specific ground infrastructure and related operations is presented in [54] page 378 ff.

For the purpose of completeness, we elucidate some fundamental aspects of the signal characteristics of the GALILEO satellites. However, an in depth discussion and analysis requires the development of the complex theoretical framework of signal design, which is well explained in [13] with special focus on the GALILEO system. From a GNSS user perspective, it is important that each satellite's signals and messages can be reliably and uniquely identified. This is a challenging requirement, since all satellites continuously broadcast simultaneously on a shared frequency band and additionally non-intentional interference by means of transmissions of other (navigation) satellite systems also crosstalk to the same spectrum. Moreover, the effect of signal dropping or intentional interference should also be minimized. Therefore, the signal must fulfill a certain level of robustness. Signals are thus modulated with particular Pseudo-Random Noise (PRN) spreading code sequences, which are unique to each satellite, to obtain a bandspread signal. To achieve this, the modulated information data/bit stream is multiplied with a specific spreading code sequence, which is generally of higher frequency than the original bit stream. In this way, the signal's power spectrum is distributed over a wider frequency domain, while after signal reception and de-spreading or de-modulation at the receiver, the original power spectrum can be recovered. As an example, the ratio between the original bit rate f_b and the resulting *chip* rate f_c of both the E5 signals amounts 1/10 after modulation. This equivalently states that the resulting spectrum is ten times larger. The techniques that manage spreading and de-spreading of the data stream are known as Spread Spectrum (SS) modulations. If signal disturbances through jamming are channeled through portions of the target frequency spectrum, they are spreaded after de-modulation and appear as noise for the user, which also makes information

---

[9]The SISA is an integrity indicator and indirectly characterizes space segment related error sources and evaluates their influence on the navigation performance. On the satellite system side, error sources can be satellite system failures, outages or degradation effects, but also satellite ephemerides and clock errors. There is a predefined index metric encoded in the GALILEO navigation message stream ([119] page 58) that indicates different levels of accuracy.

transmission more resistant against intentional interference. Spreading codes must be structured such that, after applying a matched filter or correlation filter at the receiver, ideally the autocorrelation envelopes of all other code sequences received at the same time instance are flat, which would correspond to uncorrelated noise. That's why these code sequences are also said to be orthogonal signal vectors: If the chip pattern of a particular transmitted code sequence is multiplied with that of a different code sequence, the product gives zero. The implementation of the special coding scheme is known as Code Division Multiple Access (CDMA) and all of the signals listed in 2.1 are SS CDMA encoded. This is convenient from a user's point of view, as it allows the differentiation of multiple spread spectrum messages on a shared frequency band where many users are transmitting signals simultaneously and further prevents unauthorized users from encoding dedicated messages. In [119], the GALILEO specific spreading (tiered) code characteristics and their generation technique as well as the concrete PRN code sequences of each GALILEO satellite are described.

In addition the SS modulation, the GALILEO signal processing pipeline further applies types of Binary Offset Carrier (BOC)-based subcarrier modulation procedures to all generated signal components. Negotiations between the European Union and the United States on the common use of frequencies of the GPS and GALILEO systems lead to the final decision to consider BOC[1, 1] as the baseline modulation technique for both constellations[10]. This was motivated mainly to ensure compatibility between GALILEO and GPS signal spectra. By using the BOC, a good spectral isolation is achieved, as well as suitable performance in terms of robustness against multi-path effects and phase noise. BOC is realized by multiplying each chip of the original signal component by a subcarrier composed of sequences of pairs consisting of +1 and -1. The ratio between the frequency f_s of the additional subcarrier and the chip rate f_c of the modulated signal is classified by two integer numbers n and m, which also inspires the notation BOC[n, m]. These numbers represent multiples of a reference frequency f_0, where $n/m = f_s/f_c$. The mixing process due to a BOC[$n, 1$] modulation thus leads to a symmetrical separation of the signal spectrum, with each of the spectral sidelobes shifted by the same amount $\pm n \cdot f_0$ away from the center. This outlines how the BOC subcarrier modulation can be used to distribute the spectral energy of the respective signal more efficiently and gives a methodology to design spectral compatibility between different satellite systems. As can be seen from the table below, there are several other methods based on the BOC modulation technique that also significantly improve the baseline method. For further detailed descriptions and analyses of all other types of modulations listed, the reader is referred to the literature cited above.

---

[10]See `https://eur-lex.europa.eu/LexUriServ/LexUriServ.do?uri=OJ:L:2011:348:0003:0016:EN:PDF` about the *Agreement on the promotion, provision and use of Galileo and GPS satellite-based navigation systems and related applications*

Signal	Frequency f MHz	Channel	BW Δf MHz	Nav. messages & service	Modulation type
E1	1575.420	E1A E1B E1C	24.552	PRS data I/NAV / OS / CS pilot	$\mathrm{BOC_{cos}}(15, 2.5)$ MBOC(6, 1, 1/11)
E5a	1176.450	E5a-I E5a-Q	20.460	F/NAV OS / CS	AltBOC(15, 10)
E5b	1207.140	E5b-I E5b-Q	20.460	I/NAV / OS / CS pilot	AltBOC(15, 10)
E5 (E5a + E5b)	1191.795		51.150		
E6	1278.750	E6A E6B E6C	40.920	PRS data C/NAV / CS pilot	$\mathrm{BOC_{cos}}(10, 5)$ BPSK(5)

Table 2.1: GALILEO satellite signal plan.

2.3 GNSS basic observables

2.3.1 Pseudo-ranges

A common way of determining the distance between a receiver and a satellite is to measure the satellite's signal time-of-flight. If one knows the time instant t^s at which the satellite transmits its signal as well as the time of signal reception t_r by the receiver, the apparent geometrical range $\tilde{\rho}_r^s$ can be derived from the signal time-of-flight:

$$\tilde{\rho}_r^s = c\,(t_r - t^s) \tag{2.1}$$

Technically, the time difference $t_r - t^s$ is usually determined by continuously searching for the specific ranging code[11] delay at which a maximum (auto-)correlation between the satellite's signal and the corresponding replica signal produced by the receiver occurs. In fact, given a signal from a particular channel, its correlation in the time domain is simultaneously performed with the search of the appropriate Doppler shift in the frequency domain. This is done to amplify the correlation function and hence helps increasing the detectability. If there are no further information about the orbital elements or position and velocity of the satellites in view, all potential pairs of code delays and Doppler shifts must be sequentially tested against a received signal during the acquisition phase[12]. Given that the receiver state is completely known, if satellite almanac and/or ephemerides data are known as well, the code delay and Doppler search turns out much less extensive. Since the pseudo-range measurements are not free from errors such as instrumental or signal propagation delays due to varying signal propagation conditions within the atmosphere, they do not indicate the real geometrical distance ρ_r^s between receiver r and satellite s. The time of transmission of the satellite's signal is defined by its atomic clock and the time of signal reception is tagged by the receiver's clock. Since the clocks of both the satellite and the receiver are independent and hence principally running asynchronously[13], one also has to account for any errors introduced among these timing systems. In that regard, for the pseudo-range $P_{r,f}^s(t)$ one can transcribe equation 2.1 as follows:

$$P_{r,f}^s(t) = \rho_r^s(t) + c\,(\Delta t_r(t) - \Delta t^s\,(t - \tau)) + \mathfrak{E}_P \tag{2.2}$$

Equation 2.2 now isolates the real geometrical distance $\rho_r^s(t)$ that corresponds to the signal time-of-flight τ from the remaining receiver and satellite clock error terms Δt. Additional corrections and likewise the pseudo-range measurement noise term are subsumed under $\mathfrak{E}_P$. The time argument t relates to a well-defined continuous

---

[11]The ranging codes are identical to the aforementioned PRN code sequences, which are distributed on several channels.

[12]Actually, the receiver must also compare against all locally stored satellite ranging code sequences, as long as no satellite almanac data is available.

[13]Due to the drift characteristics of the on-board atomic clocks, a time synchronization process with GALILEO System Time (GST) has to take place on an hourly basis to keep the difference of the ground and space segment time sufficiently small.

time scale as GPS System Time (GPST) or GST[14] for the individual measurement model terms. The level of pseudo-range measurement noise directly depends on the total signal Bandwidth (BW). We assume that the power spectrum is dominated by white noise. Therefore, its Power Spectral Density (PSD) evenly distributes the power intensity over all frequencies, i.e. it is constant over a certain frequency range. Consequently, if the BW is doubled, the overall noise level will also double.

According to table 2.1, the BW of both E5 signals is $20.460\,MHz$, i.e. the average correlation width corresponds to about $50ns$ or roughly $15m$. Assuming that nowadays receiver can determine the signal correlation peak with 1% accuracy, the measurement noise is at a level of $\approx 0.15m$.

2.3.2 Carrier phases

In contrast to pseudo-ranges, other than tracking the time difference of signal transmission t^s and signal reception t_r by continuously analyzing the ranging code delay, carrier phase observables directly measure the phase difference of space- and ground oscillators. Technically, *down-conversion* mixes the incoming signal of frequency f^s with a reference signal from a local oscillator in a superheterodyne receiver, which has a frequency f_r. During the frequency mixing process in the receiver, sums and differences of the input and local oscillator frequencies are produced[15]. One of the intermediate frequencies[16] of the emerging sidebands is then used as the *beat frequency* f_B, which is actually used to derive the carrier phase signal. The carrier phase definition has to be extended by an integer number $N_{r,f}^s$, since the phase measurement or rather phase difference measurement is ambiguous up to an integer multiple of whole cycles. This integer is known as the *carrier phase ambiguity*. It can be interpreted as the total number of full phase cycles of a signal with frequency f that fits within the time span since transmission of the satellite's signal and the time instant when the receiver locks up on the signal's phase. Each time the receiver loses track of the satellite's signal, the carrier phase ambiguity must be repeatedly estimated. As a result, an artifact called *cycle slip* occurs producing a jump in the measurement data. One arrives at the following mathematical description for the

---

[14]The GST is maintained by the Precise Timing Facility (PTF) of the GMS. The GST starting epoch is Sunday, 22 August 1999 and it is basically synchronized with International Atomic Time (TAI) and differs from Coordinated Universal Time (UTC) by a number of leap seconds as is also the case for GPST. The actual offset between GST and GPST is kept within limits of nanoseconds and the difference between GST and UTC, after application of scheduled leap seconds, is managed such that it does not exceed $50ns$.

[15]Mathematically this results from the product-to-sum identity, such that for the mixed (multiplied) signal s_{12} generated from two other signals s_1 and s_2 with frequencies f_1 and f_2 one can write:

$$s_{12}(t) = \sin\left(2\pi f_1 t\right)\sin\left(2\pi f_2 t\right) \tag{2.3}$$

$$= \frac{1}{2}\left(\cos\left(\boxed{2\pi\left(f_1 - f_2\right)t}\right) - \cos\left(2\pi\left(f_1 + f_2\right)t\right)\right) \tag{2.4}$$

$$\Phi_{r,f_1}(t) - \Phi_{f_2}^s(t)$$

[16]Filtering for lower intermediate frequencies has the advantage that one can achieve comparably good levels of selectivity with only small technical efforts. This is why the process is usually referred to as down conversion.

carrier phase observable:

$$\Phi_{r,f}^{s}(t) + N_{r,f}^{s} = \left(\Phi_{r,f_r}(t) - \Phi_{f^s}^{s}(t)\right) \tag{2.5}$$

In the above definition 2.5 t is related to a common receiver time scale as adopted in the previous section. The interpretation of pseudo-range measurements introduces the notion of apparent geometrical range, which is coupled to the signal time-of-flight. Apart from the ambiguity term, carrier phases can be considered to relate to the same concept. This motivates the notion of *phase pseudo-ranges*. It can be assumed that the phase of the wavefront emitted by the satellite at time t^s is the same than the phase arriving at the receiver at some later time t. As the signal is propagating from the satellite to the receiver, it generates a certain number of oscillations, where computing the time needed for one oscillation cycle just requires a reference frequency f as a conversion factor. The total propagation time of the signal is thus fixed by the total oscillation count over a certain period at some position where the signal is intercepted: $\tau = \frac{\Phi(t) - \Phi_0}{f}$, where τ again represents the signal time-of-flight related to the time instance of signal transmission and Φ_0 is an initial or fractional phase that has to be defined for each oscillator or clock. We assume that the satellite's and the receiver's clock both run at the same frequency f. Translating these findings to the terms on the rhs of equation 2.5 leaves us with:

$$\Phi_{r,f}(t) = ft + \Phi_{r,0} \tag{2.6}$$
$$\Phi_{f}^{s}(t^s) = ft^s + \Phi_{0}^{s} = f(t - \tau) + \Phi_{0}^{s} \tag{2.7}$$

Inserting both equations 2.6 and 2.7 into 2.5 gives us:

$$\Phi_{r,f}^{s}(t) = -f\tau + (\Phi_{r,0} - \Phi_{0}^{s}) - N_{r,f}^{s} \tag{2.8}$$

The first term in equation 2.8 can be finally rephrased in terms of the apparent geometrical range $\tilde{\rho}_r^s(t)$ between the receiver and the satellite, which leads to the interpretation of phase pseudo-ranges. After multiplication of 2.8 with the corresponding wavelength λ_f, we get:

$$\lambda_f \Phi_{r,f}^{s}(t) = \tilde{\rho}_r^s(t) + \lambda_f (\Phi_{r,0} - \Phi_{0}^{s}) - \lambda_f N_{r,f}^{s} \tag{2.9}$$

Similar as explained for the pseudo-range observable, the same error sources as previously presented also affect the carrier phase measurements. The difference of fractional phases $\Phi_{r,0} - \Phi_{0}^{s}$ are directly related to clock dithering effects. We adhere to the notation for clock errors in 2.2 and finally can write:

$$\lambda_f \Phi_{r,f}^{s}(t) = \rho_r^s(t) + c\left(\Delta t_r(t) - \Delta t^s(t - \tau)\right) - \lambda_f N_{r,f}^{s} + \mathfrak{E}_\Phi \tag{2.10}$$

ρ now captures the real geometrical distance and the last term $\mathfrak{E}_\Phi$ combines the remaining systematic errors relevant for the accurate description of carrier phase observations as well as the carrier-phase measurement noise. At present time it is

possible to resolve the phase measurement with an accuracy of 1%, which, depending on the signals used, converts into ranging noise levels of a few millimeters.

2.3.3 Doppler shift

The Doppler effect is a further independent observable that can be used to directly record the relative (radial) velocity between two objects. If an electromagnetic signal with an apparent frequency f^s is exchanged between two observers moving relative to each other, a change in frequency $\Delta f = f_r - f^s$ can be directly observed from the arriving signal, which is known as the *instantaneous Doppler shift*. As previously defined, we take f_r as the reference frequency generated by the local oscillator of the receiver. This frequency shift Δf is exactly the beat frequency f_B discussed in connection with carrier phase measurements and associated with the *beat phase* $\Phi^s_{r,f}(t)$ appearing in equation 2.5, which is henceforth denoted Φ_B. If the arriving signal's frequency f^s is larger than its actual value at the time of transmission, the beat frequency f_B increases. This is tantamount to a positive phase change $\frac{d\Phi_B}{dt} > 0$ and measures the signal of an approaching satellite. Inversely, if the incoming frequency becomes smaller, which is caused by a negative phase change $\frac{d\Phi_B}{dt} < 0$, this indicates that the objects move away from each other. The integral over subsequent frequency shifts thence must be related to the total change in distance between the moving objects:

$$\Phi_B = \int_{t_{r1}}^{t_{r2}} (f_r - f^s)\, dt \propto -c_\rho \Delta\rho \tag{2.11}$$

which is also known as the *integrated Doppler shift*. Note that the distance term in 2.11 has a negative sign, which is consistent with the previous explanation. The phase term Φ_B represents the number of integer phase cycles plus a fractional phase value. The integral boundaries t_{r1} and t_{r2} describe an arbitrary time interval, over which the beat phase is recorded and c_ρ is a unit conversion factor that is to be determined. If for the first term f_r of the integrand, these times are rewritten in terms of the sum of transmission times t^{s1}, t^{s2} and the corresponding signal times-of-flight τ_1, τ_2, one yields:

$$\Phi_B = \int_{t^{s1}+\tau_1}^{t^{s2}+\tau_2} f_r\, dt - \int_{t_{r1}}^{t_{r2}} f^s\, dt \tag{2.12}$$

Carrying out integration results in:

$$\Phi_B = f_r\left(\left(t^{s2} - t^{s1}\right) + (\tau_2 - \tau_1)\right) - \int_{t_{r1}}^{t_{r2}} f^s\, dt \tag{2.13}$$

Since the phase count must be conserved, we can assume that the integral over the received, apparent frequency f^s in expression 2.13 equals an integral over the actual transmitted frequency, whereas the boundary terms must be replaced by the associated transmission times t^{s1} and t^{s2}:

$$\Phi_B = f_r\left(\left(t^{s2} - t^{s1}\right) + (\tau_2 - \tau_1)\right) - \int_{t^{s1}}^{t^{s2}} f^s\, dt \tag{2.14}$$

This eventually leads to the following expression for the integrated Doppler shift:

$$\Phi_B = (f_r - f^s)\left(t^{s2} - t^{s1}\right) + f_r\left(\tau_2 - \tau_1\right) \tag{2.15}$$

$$\Leftrightarrow \Phi_B = (f_r - f^s)\left(t^{s2} - t^{s1}\right) + f_r\frac{\rho^s_{r,2} - \rho^s_{r,1}}{c} \tag{2.16}$$

If we now assume that the frequency of the receiver is calibrated to the transmit frequency of the satellite $f_r = f^s$, such that the first term in 2.16 cancels out, we get the desired rhs expression for equation 2.11.

Unlike the instantaneous Doppler measurements, its derivation from integrated frequency shifts (2.11) is more accurate. After satellite signal acquisition, the receiver starts providing accumulated carrier phase cycle counts. The continuously formed values can then be subjected to a moving average operation to obtain a smoother result for the carrier beat phase Φ_B and thence, after differentiation, a low-pass filtered beat frequency signal free of short-term fluctuations. Conversely, instantaneous Doppler data provide a more noisy snapshot of the beat frequency f_B and likewise for the line-of-sight velocity measurement $v_{\rho^s_r}$ related to some time interval dt. If one chooses the time interval sufficiently small, one can directly verify after differentiation of equation 2.16:

$$\frac{d\Phi_B}{dt} = f_B = -\frac{f_r}{c}v_{\rho^s_r} \tag{2.17}$$

Doppler shift observations are more precise than pseudo-range measurements and the current accuracy is in the mHz range. Taking the transmit frequency f^s_{E1} of the GALILEO E1 band, this results in a velocity error of $\approx 1.9 \times 10^{-4} ms^{-1}$.

The Doppler shift sign convention in RINEX (mixed) observation files are defined such that positive frequency shift recordings correspond to approaching satellites, wheres negative shifts indicate satellites moving away, which follows the logic above. The observation data collected in these files are given in values of Hz and the measurement precision also reaches levels of mHz. Depending on the satellite system and RINEX observation code, this corresponds to $\approx 1.0 - 3.0 \times 10^{-4} ms^{-1}$.

Doppler observations are subject to the bias rates of the aforementioned systematic clock errors, which were left out in the preceding derivation. After introduction of these errors, equation 2.17 can be rephrased as follows:

$$D^s_{r,f}(t) = -\frac{1}{\lambda}v_{\rho^s_r} - f\frac{(\Delta t_r(t) - \Delta t^s(t - \tau))}{dt} + \mathfrak{E}_D \tag{2.18}$$

$D^s_{r,f}$ refers to the Doppler shift measured on frequency channel f between a certain receiver and satellite. For completeness, as with the other measurements, the term $\mathfrak{E}_D$ is adopted to cover additional systematic errors including noise terms.

Chapter 2

CHAPTER 3

Orbit determination and SRP parameter estimation

The overall goal of this chapter is to investigate a new high resolution Solar Radiation Pressure (SRP) model and demonstrate its performance in comparison with current standard SRP models. However, it is not within the scope of this work to verify and validate this model under the hat of precise orbit determination, it should rather outline the general importance of detailed Non-Gravitational Disturbances (NGD) modeling for the purpose to improve orbit parameter estimation results especially with regards to the dependence on the SRP model used. We also show that the accuracy of clock data estimation is mainly limited by the accuracy of SRP modeling and raise its relevance for high-precision clock applications like the general relativistic redshift test, which is at the core of our analysis in chapter 4. Equation 1.19 describes that the speed of a satellite's clock varies with the periodicity of its orbit as also do SRP-related effects. This gives evidence that any perturbation mismodeling associated with effects of the same periodicity is thus detrimental for applications like a precision demanding redshift test.

3.1   Basic observation equations

Supplementary to the previously derived observation equations, we now consider in more detail, in addition to the clock error terms, the systematic measurement errors subsumed under $\mathfrak{E}$, which enter the equations 2.2, 2.10, and 2.18. To give a short preview, the most significant effects to be considered in accurate measurement modeling are orbital perturbations, receiver or satellite clock biases as well as other signal propagation delays due to interactions with the different atmospheric layers. Moreover, there are other types of systematic errors that must be considered in the observation equations depending on the positioning performance needs. Figure 3.1 represents the proportions among the main contributors of the aforementioned effects. For reasons of clarity, these are organized into two groups: signal propagation and orbit-related position errors and both are converted to meters. For the latter, we obtained the position errors $\Delta\rho$ from one-day arc simulations for the satellites GSAT0202 and GSAT0201, in which the respective effect responsible for $\Delta\rho$ is not taken into account. Other than third body perturbations arising from the Sun and the Moon, perturbations due to Earth's geopotential are even more pronounced (see also table 3.1 for a more comprehensive view on perturbation sources and effects). Since these disturbances by far outnumber the effects shown here in magnitude, they are not part of the charts. For the same reason, in the lhs pie chart we leave out the portions that quantify clock biases, which typically amount $300 - 500km$. Nevertheless, to conclude on the illustration, it becomes evident that the consideration of SRP on the orbit side is of paramount importance.
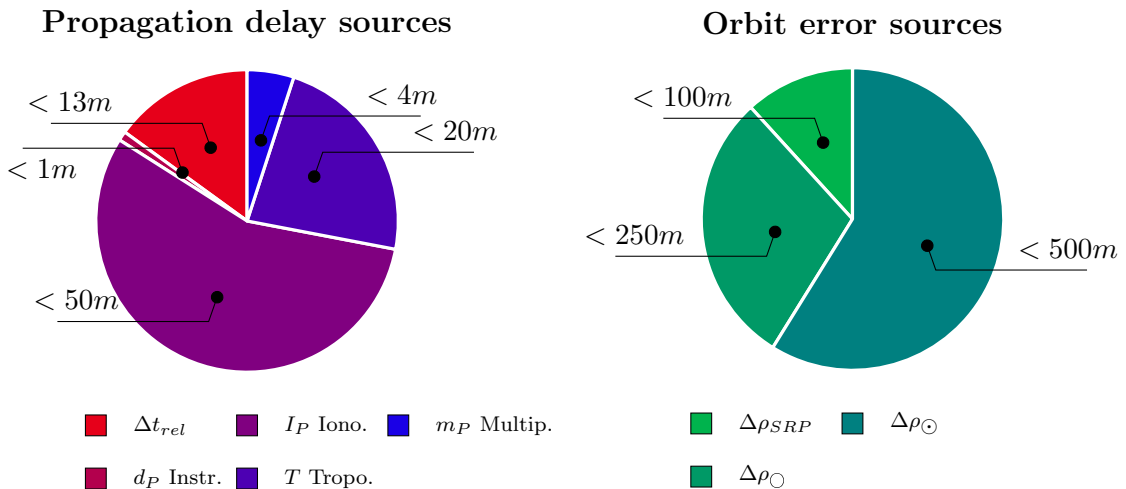
Figure 3.1: Sources of pseudo-range modeling errors.

The complete set of observation equations read:

$$P^s_{r,f}(t) = \rho^s_r(t) + c\left(\Delta t_r(t) - \Delta t^s(t-\tau)\right) + T^s_r$$
$$+ I^s_{P,r,f} + c\left(d_{P,r,f}(t) - d^s_{P,f}(t-\tau)\right) + m^s_{P,r,f}(t) + \epsilon_P \qquad (3.1)$$

$$\lambda_f \Phi^s_{r,f}(t) = \rho^s_r(t) + c\left(\Delta t_r(t) - \Delta t^s(t-\tau)\right) + T^s_r$$
$$- I^s_{\Phi,r,f} + c\left(d_{\Phi,r,f}(t) - d^s_{\Phi,f}(t-\tau)\right) + m^s_{\Phi,r,f}(t) - \lambda_f N^s_{r,f}$$
$$+ \lambda_f \Delta\Phi_{WU} + \epsilon_\Phi \qquad (3.2)$$

$$D^s_{r,f}(t) = -\frac{1}{\lambda_f} v_{\rho^s_r} - f\frac{d\mathfrak{d}^s_r(t)}{dt} + \epsilon_D \qquad (3.3)$$

$P^s_{r,f}$	=	Pseudo-range $[m]$	
$\Phi^s_{r,f}$	=	Carrier phase measurement in phase cylces	
$D^s_{r,f}$	=	Doppler shift measurement $[s^{-1}]$	
ρ^s_r	=	Distance between receiver r and satellite s $[m]$	$\|\mathbf{r}_r(t) - \mathbf{r}^s(t-\tau)\|$
$\Delta t_r, \Delta t^s$	=	Receiver and satellite clock biases for P and Φ $[s]$	
$d_{r,f}, d^s_f$	=	Receiver and satellite instrumental bias for P and Φ $[s]$	
$\pm I^s_{r,f}$	=	Ionospheric path delay $[m]$	
T^s_r	=	Tropospheric path delay $[m]$	
$m^s_{r,f}$	=	Multi-path error $[m]$	
λ_f	=	Wavelength corresponding to observation frequency f $[m]$	
$N^s_{r,f}$	=	Total number of phase cylces of carrier signal with frequency f	
$\Delta\Phi_{WU}$	=	Phase wind-up in fractions of the wavelength λ	
$\frac{d\mathfrak{d}^s_r}{dt}$	=	Clock rate	$\mathfrak{d}^s_r = (\Delta t_r(t) - \Delta t^s(t-\tau))$
ϵ	=	Measurement error	

Each of the first lines of equations 3.1 and 3.2 just contain frequency independent terms. Corrections that account for relativistic effects like the gravitational time dilation Δt_{rel} are already contained in the timing error terms Δt in equations 3.1 and 3.2, while for the Doppler measurements 3.3 this is absorbed analogously in the clock rate term. Satellite corrections as the clock bias $\Delta t^s(t-\tau)$ or the satellite's position $\mathbf{r}^s(t-\tau)$ are time shifted by the amount τ in order to relate them to the

correct time of transmission of the corresponding received signal.

GNSS satellites transmit signals on different frequency bands, see table 2.1 for the signal plan of the GALILEO satellite. This allows to combine different measurements to facilitate the analysis of certain effects from the spectrum of systematic error sources or get rid of particular terms. An example of a very useful combination is the *ionosphere-free combination* R_{IF}, which can be formed by a linear combination of two pseudo-range or carrier phase observations recorded by a dual-band receiver:

$$R_{r,IF}^s = R_{r,f_1,f_2}^s = aR_{r,f_1}^s - bR_{r,f_2}^s \qquad (3.4)$$

$$a = \frac{f_1^2}{f_1^2 - f_2^2}, \ b = \frac{f_2^2}{f_1^2 - f_2^2} \qquad (3.5)$$

where R_{IF} is a placeholder for either $P_{r,IF}^s$ or $\Phi_{r,IF}^s$ and IF is an identifier for a certain frequency combination. For GALILEO users, for example, typical combinations involve E1/E5a and E1/E5b signal pairs. Application of equation 3.4 removes the first order ionospheric effect (3.41) from pseudo-range or carrier phase observations that accounts for up to 99.9% of the total propagation delay. Subjecting a pair of pseudo-range observations 3.1 to equation 3.4 brings us:

$$P_{r,IF}^s = \rho_r^s + c\left(\Delta\hat{t}_r - \Delta\hat{t}^s\right) + T_r^s + m_{P,r,IF}^s + \epsilon_{P,IF} \qquad (3.6)$$

From this equation on, we omit the time dependence in this section to simplify the notation. To obtain expression 3.6, we recast definition 3.1 to construct P_{r,f_1}^s and P_{r,f_2}^s, respectively. As a first step, we redefine the clock error terms Δt by $\Delta\hat{t}$ in terms of mapping the instrumental biases to the clock offset. For $\Delta\hat{t}^s$ one receives:

$$\Delta\hat{t}^s = \Delta t^s + ad_{P,f_1}^s - bd_{P,f_2}^s \qquad (3.7)$$

Analogous to 3.7, one can form $\Delta\hat{t}_r$. Pairs of ionospheric and instrumental delay terms, which appear through a combination of observations P_{r,f_1}^s and P_{r,f_2}^s each linearly dependent on frequency[1]. This suggests to lump these contributions into a new term $\hat{I}_f$:

---

[1]In a linear combination of signals, the first order ionospheric delays are linked via the relationship:

$$I_{P,r,f_2}^s = \frac{f_1^2}{f_2^2} I_{P,r,f_1}^s \qquad (3.8)$$

As per GALILEO interface control document [119], the signal dependent group delay GD_{P,f_1} is a function of the difference of the instrumental delays: $GD_{P,f_1} = -b\left(d_{P,f_2}^s - d_{P,f_1}^s\right)$ and the relationship between the group delays associated with different signals is given by:

$$GD_{P,f_2}^s = \frac{f_1^2}{f_2^2} GD_{P,f_1}^s \qquad (3.9)$$

which is of the same form than the term for the ionospheric delay.

Chapter 3

$$\hat{I}_P = \frac{1}{b} I^s_{P,r,f} + \Delta d_P \tag{3.10}$$

where Δd_P corresponds to the difference $d^s_{P,f_2} - d^s_{P,f_1}$. One can now write:

$$P^s_{r,f_1} = \rho^s_r + c\left(\Delta\hat{t}_r - \Delta\hat{t}^s\right) + b\hat{I}_{P_1} + T^s_r + m^s_{P,r,f_1} + \epsilon_P \tag{3.11}$$

$$P^s_{r,f_2} = \rho^s_r + c\left(\Delta\hat{t}_r - \Delta\hat{t}^s\right) + a\hat{I}_{P_2} + T^s_r + m^s_{P,r,f_2} + \epsilon_P \tag{3.12}$$

We now resort to the definition 3.4 and substitute the placeholder by the pseudo-range components given by 3.11 and 3.12. This leads to equation 3.6. The ionosphere-free combination for carrier phases reads:

$$\lambda_N \Phi^s_{r,IF} = \rho^s_r + c\left(\Delta\hat{t}_r - \Delta\hat{t}^s\right) + \lambda_N \lambda_W \left(\frac{N^s_{r,f_1}}{\lambda_{f_1}} - \frac{N^s_{r,f_2}}{\lambda_{f_2}}\right)$$

$$+ \lambda_N \Delta\Phi_{WU} + m^s_{\Phi,r,IF} + \epsilon_{\Phi,IF} \tag{3.13}$$

$$\lambda_W = \frac{c}{f_1 - f_2}, \ \lambda_N = \frac{c}{f_1 + f_2} \tag{3.14}$$

$$N_{IF} = \lambda_W \left(\frac{N^s_{r,f_1}}{\lambda_{f_1}} - \frac{N^s_{r,f_2}}{\lambda_{f_2}}\right) \tag{3.15}$$

where λ_W and λ_N label virtual wavelengths called *wide-lane* and *narrow-lane*[2]. After building 3.13 from two carrier phase observations 3.2, the linear factor $(f_1^2 - f_2^2)$ in the denominator on the lhs cancels, so that just λ_N remains as a coefficient. That is the reason why the ionosphere-free combination is also called narrow-lane combination. One recognizes, that the integer nature of the carrier phase ambiguity of this new observation is lost after the use of equation 3.4. Due to the structure of the expression 3.13, it is not possible to disentangle the ambiguity terms and the corresponding coefficients. The third term 3.15 in parentheses on the rhs of formula 3.13 is therefore identified as the *float ambiguity N_{IF}*.

The overall measurement error, i.e. standard deviation of the ionosphere-free combination of pseudo-ranges P or carrier phases Φ is a function of the combination coefficients a and b. If one takes $\sigma_X = \sigma_P$ or $\sigma_X = \sigma_\Phi$ as the corresponding single-observation measurement errors, propagation of the combined measurement uncertainty results in: $\sigma_{IF} = \sqrt{a^2 + b^2}\sigma_X$. Projecting this to the E1/E5a combination of pseudo-range observations, one ends up with $\sigma_{E1,E5a} \approx 2.6\sigma_P$. For the sake of convenience, we assumed that single-observation measurements with σ_{E1} and σ_{E5a} signals produce the same amount of noise σ_P.

Depending on the use case, observation differences are conventionally used to eliminate clock error terms from the observations, which, for example, facilitates the isolation of orbit-related errors. If one forms *single differences* with respect to a

---

[2]The naming is due to the fact that the terms $\lambda_W = \frac{c}{f_1-f_2}$ and $\lambda_N = \frac{c}{f_1+f_2}$ describe signals with larger and smaller virtual wavelength, respectively.

station r_i that recorded signals from two different satellites simultaneously, the corresponding station clock error terms cancel out, while a difference of satellite clock biases remains. For the latter, the governing measurement equation is:

$$\Delta P_{r_i,f}^{s_i,s_j} = \left(P_{r_i}^{s_i} - P_{r_i}^{s_j}\right) \tag{3.16}$$

$$\Delta P_{r_i,f}^{s_i,s_j} = \Delta \rho_{r_i}^{s_i,s_j} + c\Delta t_{r_i}^{s_i,s_j} + \Delta T_{r_i}^{s_i,s_j} + \Delta I_{P,r_i,f}^{s_i,s_j} + \cdots \tag{3.17}$$

where $\delta t_{r_i}^{s_i,s_j}$ can be written as:

$$\Delta t_{r_i}^{s_i,s_j} = \left(\delta t_{r_i} - \delta t^{s_i}\right) - \left(\delta t_{r_i} - \delta t^{s_j}\right) \tag{3.18}$$

To comply with the conventional notation Δ for single differences, we have replaced the Δ in formulas 3.2 and 3.1 for receiver and clock errors by δ. Using the equation 3.17, one can form a second single difference with respect to another station r_j and compute *double differences* $\nabla\Delta$:

$$\nabla\Delta P_{r_i,r_j,f}^{s_i,s_j} = \left(P_{r_i}^{s_i} - P_{r_i}^{s_j}\right) - \left(P_{r_j}^{s_i} - P_{r_j}^{s_j}\right) \tag{3.19}$$

$$\nabla\Delta P_{r_i,r_j,f}^{s_i,s_j} = \nabla\Delta \rho_{r_i,r_j}^{s_i,s_j} + \nabla\Delta T_{r_i,r_j}^{s_i,s_j} + \nabla\Delta I_{P,r_i,r_j,f}^{s_i,s_j} + \cdots \tag{3.20}$$

Thus, if one takes the difference of two single differences, one obtains a double difference in which all clock error terms now cancel, as can be understood from equation 3.20. One quickly verifies that:

$$\nabla\Delta t_{r_i,r_j}^{s_i,s_j} = \left(\left(\delta t_{r_i} - \delta t^{s_i}\right) - \left(\delta t_{r_i} - \delta t^{s_j}\right)\right) - \left(\left(\delta t_{r_j} - \delta t^{s_i}\right) - \left(\delta t_{r_j} - \delta t^{s_j}\right)\right) = 0 \tag{3.21}$$

It is of major importance that all observations refer to one and the same epoch. If the observations are not synchronized, the advantages of difference formation cannot be exploited. From a practical point of view, it is usually difficult to find contiguous sets of common observations and this is usually linked to extensive data preparation in terms of selection and filtering. As a conclusion, forming differences enables to strip off the systematic clock errors from the observations, thus making it possible to decouple orbit errors from clock errors in parameter estimation procedures.

3.2 GNSS Measurement modeling

In the following section, we describe the systematic effects behind the individual terms of the observation equations 3.3, 3.2 and 3.1. Within the scope of this work, we will not discuss such corrections, which are commonly used for a centimeter resolution of the measurements. This includes satellite and ground antenna phase center offsets and corrections, site displacements due to Solid Earth Tides or polar tides as well as higher order ionospheric corrections. We also neglect multi-path effects from our considerations. Multi-path effects generally affect both code and phase observations and are usually caused by signal reflections within the environment. Therefore, the effects of multi-path can be influenced by the orientation and thus the adjustment of the tilt and height of the antenna. As explained in section 3.5, we try to minimize the effects by filtering measurement data associated with low elevation observations.

3.2.1 Satellite and receiver clock corrections

Time correction is conducted with a set of satellite specific clock bias and drift parameters $\{a_0,\ a_1,\ a_2\}$. These are estimated by the responsible Orbit determination and time Synchronization Processing Facility (OSPF) of the GMS, regularly uploaded via the Uplink Station (ULS) infrastructure and finally contained in the broadcast navigation messages F/NAV and I/NAV. These parameters are the coefficients of a time dependent polynomial of second order, which enables to predict the individual non-stochastic, long-term clock error $\Delta t^s(t)$ of the satellites' atomic clocks caused by various mechanisms. More precisely, it can be used to predict the clock correction with respect to an arbitrary time interval spanned by some time t, measured in a well-defined system time scale, and a reference time instant called *time of clock* t_{toc}, which is also part of the navigation message. If we take the time of message transmission $t = t^S$ as some arbitrary time instant, the associated error-corrected time $\tilde{t}^S$ given in the system time scale can be calculated as:

$$\tilde{t}^S = t^S - \Delta t^s\left(t^S\right) + \Delta t_{rel} + \epsilon_c \tag{3.22}$$

$$\tilde{t}^S = t^S - \left(a_0 + a_1\left(\tilde{t}^S - t_{toc}\right) + a_2\left(\tilde{t}^S - t_{toc}\right)\right) + \Delta t_{rel} + t_{BGD} + \epsilon_c \tag{3.23}$$

Both equations also contain a stochastic noise term ϵ_c that characterizes the specific clock noise. Complementary to the activities of the named GMS facilities, the PTF is the responsible GST timing service provider. It establishes a highly stable and accurate GALILEO system time scale constituting the reference for time synchronization of the space segment with its different on-board atomic clocks and the ground segment's master clock system. The satellite time correction parameters must be updated every few hours ensuring an accurate prediction of $\tilde{t}^S$, since its value must be within valid boundaries considering the individual clock behavior. The update frequency depends in particular on the respective clock stability.

Chapter 4 deals with the characterization of the specific atomic clocks of the GALILEO satellites GSAT0202 and GSAT0201 in preparation to the general relativistic redshift analysis at the core of that chapter. Of particular interest is the analysis of the

stochastic noise ϵ_c as well as the relativistic term Δt_{rel} affecting the behavior of the atomic clocks. The latter maps a periodical component due to the orbit eccentricity and is given by equation 1.20. For the two GALILEO satellites mentioned above the term is of special importance, because due to satellites' high eccentric orbits, the relativistic timing effect varies extraordinarily and so does the observed satellite range.

As per interface document, [119], the satellite time correction Δt^s is related to the ionosphere-free combination, by default, and thus contains an extra term, which takes into account the total group delay, also referred to as Broadcast Group Delay (BGD). Single frequency users must therefore compensate for this BGD to correctly describe the observation representation as stated by 3.1. The BGD depends on the difference of the satellite-related instrumental delay terms: $DCB_{f_1,f_2} = d^s_{P,f_1} - d^s_{P,f_2}$, which is typically known as Differential Code Bias (DCB) or *inter-frequency bias*[3] .

---

[3]The BGD depends on the frequency and the code combination used. The F/NAV and I/NAV messages encode the BGDs for the signal combinations E1/E5a and E1/E5b.

3.2.2 Tropospheric effects

The Earth's atmosphere consists of several layers that affect signal propagation time. For micro wave signals, such as GNSS L-Band signals, both the troposphere $(0 - 15\text{km})$ and the stratosphere $(15 - 45\text{km})$ are essentially neutral, non-dispersive media[4]. These signals travel with the same phase and group velocity, since their corresponding refractivity N_{Trop} stays rather unchanged for frequencies f up to 15GHz. The tropospheric path delay T_r^s between a satellite s and a receiver r can be written as:

$$T_r^s = 10^{-6} \int N_{Trop} ds \tag{3.24}$$

where the expression 3.24 is integrated over a certain path s. The path delay can amount up to 20m and therefore its prediction is of significant interest. The refractivity depends on the molecular makeup of both lower atmospheric layers, as well as on the present thermodynamic state profile describing the local weather conditions at the antenna site and over the slant range to the satellite. In that regard, one distinguishes between two different path delay contributions that originate from different refractivities: A *dry* component due to the hydrostatic conditions of the atmosphere as well as a *wet* component. The refractivity index can thus be decomposed into $N_{Trop} = N_{Trop,H} + N_{Trop,W}$, such that 3.24 can be expressed as:

$$T_r^s = 10^{-6} \int N_{Trop,H} ds + 10^{-6} \int N_{Trop,W} ds \tag{3.25}$$

The first part relates to the *zenith hydrostatic delay* (ZHD) and only depends on the total surface air pressure, whereas the other part relates to the *zenith wet delay* (ZWD), which further depends on both the local temperature as well as the partial water vapor pressure profile. Thereby, the hydrostatic component ZHD accounts for 90% of the signal propagation delay [61], additionally depends on the site's location and is also subject to seasonal variations of $\pm 10\%$ [80]. For the prediction of this component, the model of Saastamoinen [91] is often used. the ZHD is modeled as follows (as compared to [80]):

$$ZHD = \frac{0.0022767 \left[\frac{m}{hPa}\right] \cdot P_0}{1 - 0.00266 \cdot \cos 2\phi - 0.00000028 \left[\frac{1}{m}\right] \cdot H} \tag{3.26}$$

Where $P_0 \, [hPa]$ is the total air pressure as measured at the receiver's antenna reference point, ϕ is the geodetic latitude of the antenna's site with respect to the Earth's equator and $H \, [m]$ gives its geodetic height. The function in the denominator containing the both latter variables is an adaption term that takes into account the

---

[4]In fact, a negligible anomalous dispersion around the resonance frequencies of mainly water vapour and oxygen takes place. Unlike the behavior in a dispersive medium like the ionosphere the refractive index increases with increasing frequency.

latitude dependent mean gravitational acceleration[5]. The accurate determination of the ZWD is heavily involved, since it requires knowledge about all thermodynamic and meteorological subtleties as water vapor pressure or temperature distribution within the atmosphere and their corresponding seasonal, diurnal or hourly fluctuations. For practical reasons, the ZWD is therefore typically estimated jointly with other states and parameters in an estimation scheme. For the purposes of this study, for the determination of the total tropospheric delay, we start with a model of Saastamoinen that allows to predict the zenith total path delay ZTD including ZHD and ZWD. According to [94], the ZTD can be calculated from the following equation:

$$ZTD = \frac{0.0022767 \left[\frac{m}{hPa}\right](1+D)}{\cos z} \left(\mathfrak{p} + \left(\frac{1255\,[K]}{\mathfrak{T}} + 0.05 \right) \mathfrak{e} - B \tan^2 z \right) + \delta_R \tag{3.27}$$

$$D = 0.00266 \cdot \cos 2\phi + 0.00000028 \left[\frac{1}{m}\right] \cdot H \tag{3.28}$$

Under the simplifying assumption of a standard atmosphere, one can then assign empirical values to the input parameters pressure $\mathfrak{p}\,[hPa]$, temperature $\mathfrak{T}\,[K]$ and partial water vapor pressure $\mathfrak{e}\,[hPa]$ measured at the receiver's antenna reference point. Furthermore, B is a mapping correction depending on the height of the receiver station and δ_R is mapping correction bias depending on both the actual zenith angle z and the receiver station's height. These additional terms are tabulated and can be found e.g. in [106]. In order to relate the slant path delay associated with the apparent line-of-sight to the satellite to the actual zenith path delay, one conventionally uses mapping functions. From a brief inspection of formula 3.27, we see that it implicitly contains a mapping factor proportional to $\frac{1}{cosz}$. Another common approach is the usage of the mapping of Niell [74] with some Global Mapping Functions (GMFs) $M_H(\epsilon)$ and $M_W(\epsilon)$ for both path delay contributions:

$$T_r^s = M_H(\epsilon)\,ZHD + M_W(\epsilon)\,ZWD \tag{3.29}$$

These functions $M_H(\epsilon)$ and $M_H(\epsilon)$ are computed using the following expression 3.30:

---

[5]In the pertinent literature given, the model for the zenith hydrostatic delay is also based on an altitude dependent air density model. For the computation of the density distribution within an air column, a model for the local gravitational acceleration is needed, which is also a function of altitude. One could think of using a more complex model that considers a precise mapping of the Earth's surface at the corresponding site's location to determine the correct extent of the air column and the effect of the gravitational acceleration, accordingly. Instead of this, one introduces a weighted mean gravitational acceleration and computes a correction for this value with respect to the site's height on a well-defined geodetic reference surface.

$$M\left(\epsilon\right) = \frac{1 + \frac{a}{1 + \frac{b}{1+c}}}{sin\left(\epsilon\right) + \frac{a}{sin(\epsilon) + \frac{b}{sin(\epsilon)+c}}} \tag{3.30}$$

$$\mathfrak{a}\left(\phi, \ t_{doy}\right) = \mathfrak{a}_{av}\left(\phi\right) - \mathfrak{a}_{amp}\left(\phi\right)\cos\left(2\pi\frac{t_{doy} - t_0}{365.25\left[d\right]}\right) \tag{3.31}$$

With a set of coefficients $\mathfrak{a} \in \{a, \ b, \ c\}$ for each functions, which are tabulated in the respective literature for selected latitudes, such that one can interpolate their values for arbitrary locations[6]. Once these values have been determined, formula 3.31 can be applied for each of the parameters $\mathfrak{a} \in \{a, \ b, \ c\}$ to also take into account their temporal variations. The big advantage of this GMF is that it does not directly rely on any meteorological parameter measurements, but the parameters are derived from data products of global numerical weather simulations produced by the European Centre for Medium-Range Weather Forecasts (ECMWF). It also solely depends on the latitude ϕ of the site of interest, the actual day of the year t_{doy} relative to an initial day t_0 and the elevation ϵ of the satellite with respect to a topocentric coordinate system. Nevertheless, the model also implies some shortcomings, as discussed in [19]. The combination of the GMFs with the individual contributions in the expression for the ZTD as given in 3.29 now compensates its mapping deficiencies. Figure 3.2 demonstrates the performance of the model as written in 3.29 and its relevance for ground based station or satellite position estimation purposes.

---

[6]The mapping of Niell also considers a height correction term for the ZHD $\Delta M\left(\epsilon, \ H\right)$, similar to B appearing in formula 3.30
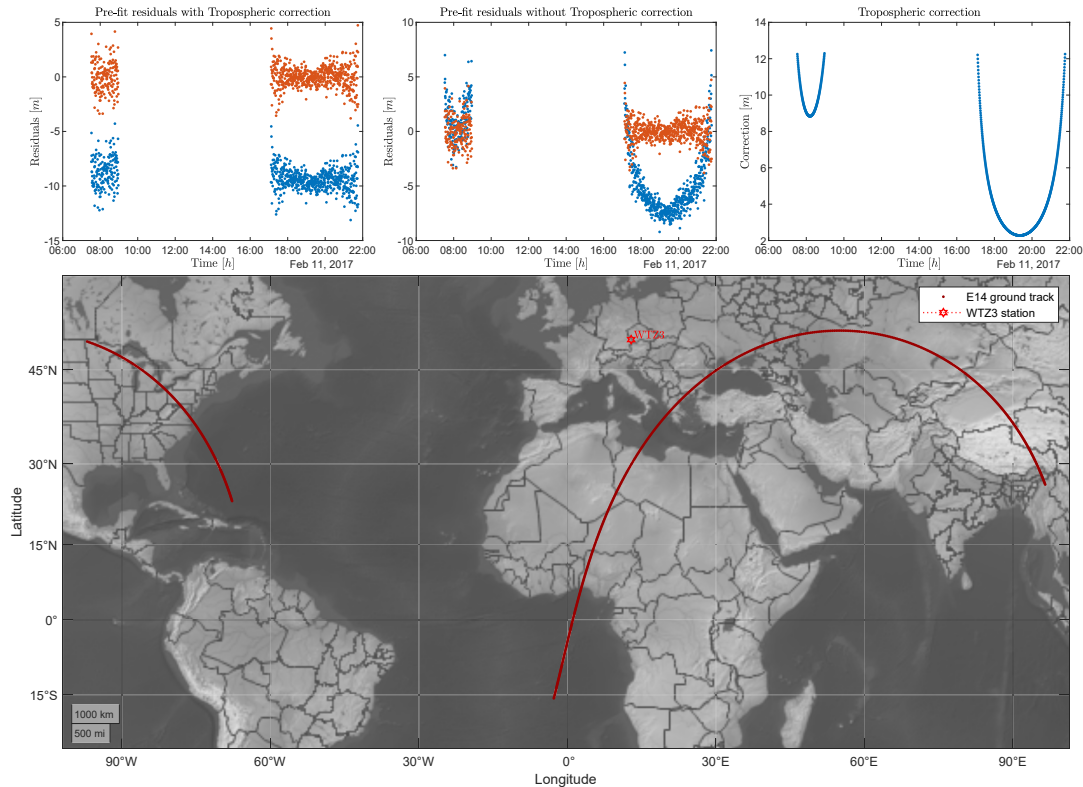
Figure 3.2: The map shows the ground track of the satellite GSAT0202 as recorded by the Geodetic Observatory Wettzell WTZ3 station in Bad Koetzting, Germany on February, 11, 2017. The blue scatter plot in the top-left shows the pre-fit pseudo-range residuals after subtraction of all known measurement corrections given in equation 3.1. After Least-Squares adjustment of station coordinates as well as station clock biases, the residuals change as given by the red scatter plots. The center plot compares the adjusted residuals with those that have not been corrected for tropospheric effects. The top-right figure reflects the output from the tropospheric correction model 3.29, i.e. the slant path delays for the two parts of the one-day arc shown on the map.

3.2.3 Ionospheric effects

The ionosphere extents from approximately 45km to 1000km above Earth's surface and a distinction is made between different layers called F-, E- and D layer[7]. Other than the troposphere, the ionosphere consists mainly of plasma, i.e. charged particles as ionized atoms, molecules and electrons, which are distributed less densely in lower altitude regimes and more densely at higher altitudes. The presence of the different layers and their degree of ionization mainly depends on the Sun's irradiation intensity, which is also coupled to the solar cycle (see also 3.3), and is therefore subject to seasonal and diurnal changes. During day, the particles in the ionosphere are ionized by Ultraviolet (UV) or X-ray radiation emanating from the Sun. Due to the higher ion production rate stimulated predominantly by extreme UV radiation at higher altitudes, the F-layer deforms and splits into 2 sub-layers $F2$ and $F1$. In addition also the E- and D-layer form at lower altitudes in which also oxygen

---

[7]Ordered by their occurrence over altitude from high to low.

and nitrogen atoms or molecules are excited by radiation in the far UV or Lyman-alpha spectrum. The degree of ionization is typically measured in Total Electron Content Units (TECUs) and is given in $[10^{16} e^-/m^2]$. In periods of low radiation intensity e.g. during night, the particles and molecules recombine and the individual ionospheric regions disappear. However, the top F layer still persists independently of the irradiation conditions. One of the characteristics of an ionized plasma is the ability of dispersive interaction with electromagnetic waves. In amateur radio applications for example, one takes advantage of this property and uses it to build up so-called Distance Exchange (DX) communication links, which rely on the reflection properties of the mentioned ionospheric layers. In particular, the F layer, which is permanently available, serves as a favorable medium for these large distance links making it possible to realize communication distances of 4000km or more with one *skip* via Medium Frequency (MF) to High Frequency (HF) transmissions. As a wieldy rule of thumb, the Maximal Usable Frequency (MUF) is often used as a first estimation that gives the highest radio frequency at which sky waves are still reflected at the ionosphere or equivalently the lowest frequency at which sky waves just leave the ionosphere given a certain angle of transmission α measured between antenna boresight direction and the local horizon. The MUF is defined as:

$$\omega_{MUF} \approx \frac{\omega_c}{\sin \alpha} \tag{3.32}$$

which includes the critical frequency $f_c \approx 8.98\sqrt{n_e}$ that depends on the electron density $n_e\,[e^-/m^3]$ as given in [29]. The former is referred to as the (electron) frequency of plasma oscillations as a response to time varying electromagnetic fields. In [95] the following expression 3.33 is derived, whereby several assumptions[8] are made, which approximate the conditions in the ionosphere:

$$f_c = \sqrt{\frac{n_e e^2}{m_e \epsilon_0}} \tag{3.33}$$

These plasma oscillations are also called *Langmuir waves* (see [60] and [95] for more details about *Langmuir probes*, which can be used for the determination of ionospheric parameters as electron density etc.). For frequencies f larger than f_c, radio or micro waves can pass the ionosphere and are affected by refraction mechanisms as is also the case for the troposphere. In contrast to the effects that occur within the troposphere, they are much more pronounced in the ionosphere due to large changes of the refractive index. In the frequency spectrum below the Very High Frequency (VHF) domain satisfying $f \leq f_c$, the waves are reflected. The propagation behavior of electromagnetic waves is described by a dispersion relation. Its derivation for transverse electromagnetic waves can be found in [95] or [73]. In addition to the previous assumptions about the state conditions of a ionospheric plasma, one thereby assumes that in the limiting case the Maxwellian RMS thermal velocity of the particles does not have a noticeable impact, so that in the limit the temperature tends to zero. This is also known as the *cold plasma* condition. The dispersion relation then states:

---

[8]One supposes a fully ionized, uniform and stationary plasma consisting of two particle species - electrons and heavy, positive ions -, which in addition is unmagnetized and electrically neutral, such that the number densities of the present charges are equal.

$$-k^2 + \frac{\omega^2}{c^2} - \frac{\omega_c^2}{c^2} = 0 \tag{3.34}$$

The phase and group refractive indices n_{ph} and n_{gr} can be derived from formula 3.34 by using the relations for the phase v_{ph} and group v_{gr} velocities:

$$n_{ph} = \frac{c}{v_{ph}}, \quad v_{ph} = \frac{\omega}{k} \tag{3.35}$$

$$n_{gr} = \frac{c}{v_{gr}}, \quad v_{gr} = \frac{d\omega}{dk} \tag{3.36}$$

Plugging these relations into the dispersion relation defined in 3.34 gives us:

$$n_{ph} = \sqrt{1 - \left(\frac{f_c}{f}\right)^2} \tag{3.37}$$

$$n_{gr} = \frac{1}{\sqrt{1 - \left(\frac{f_c}{f}\right)^2}} \tag{3.38}$$

Using the expression for the plasma frequency f_c and plugging it into the first order Taylor-expanded expressions of the functions 3.37 and 3.38 lets us rewrite n_{ph} and n_{gr}:

$$n_{ph} \approx 1 - \frac{40.31}{f^2} n_e \tag{3.39}$$

$$n_{gr} \approx 1 + \frac{40.31}{f^2} n_e \tag{3.40}$$

Similarly as stated in formula 3.24, we can now adopt a definition for the ionospheric path delay affecting a signal along the path between a receiver and a satellite:

$$I_{r,f}^s \Big|_{ph,gr} = \int \left(n_{ph,gr} - 1\right) ds = \mp \frac{40.31}{f^2} \int n_e ds \tag{3.41}$$

where we have to integrate over the path-depending phase or group refractive indices. As a conclusion, for carrier phase measurements the correction considers a propagation path advancement, while for wideband signals as pseudo-range/code measurements one has to correct for a propagation path lag, because the integral in expression 3.41 depends on the sign.

A more general expression for the refractive index is given by the Appleton formula discussed in [29]. In contrast to the hypotheses made above, one drops the assumption of an unmagnetized plasma and additionally considers the magnetization through the Earth's magnetic field. As a basis for reflection, we follow the considerations in [80] and give a recap on the results:

$$n_{ph}^2 = 1 - \frac{2X(1-X)}{2(1-X) - Y_T^2 \pm \sqrt{\left[Y_T^4 + 4(1-X)^2 Y_L^2\right]}} \tag{3.42}$$

$$X = \frac{\omega_c^2}{\omega^2}, \ Y_T = -\frac{\omega_g}{\omega^2}\sin\theta, \ Y_L = -\frac{\omega_g}{\omega}\cos\theta, \ \omega_g = \frac{eB}{m_e} \tag{3.43}$$

where ω_g measures the electron gyrofrequency. B specifies the Euclidian vector norm value of the magnetic field strength and θ describes the angle between the wave vector of the electromagnetic signal and the magnetic field vector. According to the calculations in [80], a second order Taylor approximation of the Appleton relation is proposed and inserted into the definition of the path delay 3.43. The result is a third order series in the frequency f:

$$\left. I_{r,f}^s \right|_{ph} = -\frac{I_1}{f^2} - \frac{I_2}{f^3} - \frac{I_3}{f^4} \tag{3.44}$$

The constants I are integral expressions that must be evaluated depending on the required level of accuracy. For the purpose of demonstration, we reproduce I_2:

$$I_2 = 1.128 \cdot 10^{12} \int n_e B \cos\theta ds \tag{3.45}$$

The first order term I_1 was is already given by 3.41. Calculating the ratio of the first two terms of the above series 3.44 using adequate values for n_e and $B\cos\theta$ as well as appropriate boundaries for evaluating the integral results in a propagation delay error of about 0.1% for E1 band signals (corresponding to a frequency of $f = 1575.42 MHz$), which translates to a few centimeters of range error. This confirms the importance of higher order ionospheric effects for high-precision geodesic applications like Precise Point Positioning (PPP). If one rejects the assumption about the magnetic influence, the Appleton relation 3.43, after subjecting it to a first order Taylor expansion, reduces to 3.39.

For single frequency users, it is important to correct the ionospheric path delay by a proper model, since it amounts up to $\approx 50m$ depending on the frequency band used. As stated earlier, dual-frequency observations can be exploited to almost completely neutralize the first order ionospheric path delay 3.41 by forming linear combinations of measurements 3.6 and 3.13, whereas the remaining error also depend on the frequency combinations used. Especially for GALILEO satellite system users, the official open service document [100] recommends the fairly new NeQuick ionospheric model[9] ([55]) to take into account the path delay. This model allows to compute the delay on the basis of a set of regularly updated empirical parameters. With these parameters, the electron concentration can be determined point-wise along the path between receiver and satellite in dependence of the actual receiver's

---

[9] Actually, the NeQuick 2 model is currently an International Telecommunication Union (ITU) recommendation for the evaluation of wave propagation effects in the ionosphere (`https://www.itu.int/rec/R-REC-P.531/en`). The latest information about the model and details about its implementation can be found in [99].

geographic position. Subsequently, the TECU result is then used to obtain the trans-ionospheric path delay by evaluation of the integral 3.41. The Nequick model allows to characterize the dynamics of the ionospheric profile, i.e. it covers time dependent variations in thickness of the individual layers mentioned before and hence enables to describe electron density variations, which e.g. depend on solar activity and, not least, seasonal or monthly changes in solar radiation. Another commonly used model for the prediction of the electron concentration and thus ionospheric path delay is the Klobuchar model ([59]). For a comprehensive representation of ionospheric physics and processes affecting the interaction with electromagnetic radiation, the reader is referred to [57].

3.2.4 Ambiguity Resolution

In section 2.3.2, the carrier phase ambiguity was introduced and for the accurate orbit positioning purposes, it is necessary to solve for this term. After the receiver's phase-locked loop tracks the signal, it continuously counts the number of (fractional) phase cycles. Aside from this recorded portion, the integer value $N_{r,f}^s$ appearing in equation 3.2 is unknown, but stays constant over the time of a satellite pass[10]. We outlined that with the loss-of-lock and re-initialization of the phase tracking, the ambiguity inevitably changes its value. This typically results in cycle slips, which are detectable as jumps in the phase observations. Thus, to properly resolve the ambiguity, one must identify periods of time over which N does not change. At first glance, equations 3.1 and 3.2 differ essentially in the phase wind-up and ambiguity terms. This instructs to form their difference in order to isolate the ambiguity term and analyze its temporal behavior:

$$P_f - \lambda_f \Phi_f = -2I_{\Phi,f} + \lambda_f N_f + \epsilon \tag{3.46}$$

where phase wind-up effect is neglected. It is evident that by using equation 3.46, all the common terms that appear in the underlying equations are eliminated, except for the ionospheric and noise terms. To get rid of the ionospheric term as well, one typically follows a similar strategy and forms the *Melbourne-Wübbena* combination arranged from differences of wide- and narrow-lane combinations:

$$\Phi_W - P_N = \lambda_W N_W + \epsilon \tag{3.47}$$
$$\Phi_W = (a_W \Phi_{f_1} + b_W \Phi_{f_2}) \tag{3.48}$$
$$P_N = (c_N P_{f_1} + d_N P_{f_2}) \tag{3.49}$$
$$a_W = \frac{f_1}{f_1 - f_2}, \ b_W = -\frac{f_2}{f_1 - f_2} \tag{3.50}$$
$$c_N = \frac{f_1}{f_1 + f_2}, \ d_N = \frac{f_2}{f_1 + f_2} \tag{3.51}$$
$$N_W = N_{r,f_1}^s - N_{r,f_2}^s \tag{3.52}$$

where the subscripts W and N denote wide-lane and narrow-lane related terms. Constructing this equation reduces the problem to the determination of the wide-lane ambiguity N_W generated by Φ_W, which corresponds to the wide-lane wavelength λ_W previously introduced in equation 3.13. To see the direct relationship with N_W, one can rewrite the expression for the ionosphere-free combination 3.13 as follows:

$$\lambda_N \Phi_{r,IF}^s = \rho_r^s + c\left(\Delta \hat{t}_r - \Delta \hat{t}^s\right) + \lambda_N \left(N_{r,f_1}^s - \frac{\lambda_W}{\lambda_{f_2}} N_W\right) \tag{3.53}$$
$$+ \lambda_N \Delta \Phi_{WU} + m_{\Phi,r,IF}^s + \epsilon_{\Phi,IF}$$

---

[10]This is only the case if the receiver keeps track of the phase for as long as the satellite transit lasts.

The application of equation 3.47 offers the great advantage that jumps in the evolution of N_W are much more pronounced and therefore easier to find due to the enlargement of the wavelength λ_W. The actual detection can be done by intervalwise determination of statistical properties of N_W like the empirical mean or the associated RMS value. Intervals in which these properties change significantly potentially contain a cycle slip candidate. Once the cycle slip location is detected and at least one continuous time span can be isolated with the help of the statistical wide-lane ambiguity analysis, one can start time-averaging N_W over the identified period and fixing it to the nearest integer. Therefore, the double-differenced version of formula 3.47 is commonly used:

$$\nabla\Delta\Phi_W - \nabla\Delta P_N = \lambda_W \nabla\Delta N_W + \epsilon \tag{3.54}$$

Together with the estimation result of the (double differenced) float ambiguity term N_{IF} occuring in the expressions for the ionosphere-free combination 3.13 and 3.53, it is now possible to solve for $\nabla\Delta N^s_{r,f_1}$, which follows from 3.15:

$$\nabla\Delta N^s_{r,f_1} = \nabla\Delta N_{IF} + \frac{\lambda_W}{\lambda_2}\nabla\Delta N_W \tag{3.55}$$

There are different ambiguity resolution algorithms. Probably the most famous one is the Least-Squares Ambiguity Decorrelation Adjustment (LAMBDA) method, which was first introduced by *Teunissen, P.* ([113], [114], [76]) and is based on an integer Least-Squares approach. The reader will find a practical introduction to the subject in [109] on page 495 ff.

3.2.5 Phase wind-up

Another important effect, which is of electromagnetic nature and plays a role in Precise Orbit Determination (POD) is the carrier phase wind-up effect, which applies for circular-polarized electromagnetic signals. While the satellite coasts on its orbit around Earth, it permanently rotates according to the special Yaw-Steering (YS) attitude mode described in section 3.3.3.1. The satellite is thus kept slewed properly ensuring that its solar panels are always in an optimal position to receive maximum Sun illumination such that maximum power can be provided to the spacecraft, while its main navigation antenna dish remains oriented in Earth direction. As a consequence, the satellite antennas boresight direction permanently changes with respect to the principal direction of the receiver antenna. Depending on the relative attitude between both the satellite and the receiver antenna, the signal is shifted in phase. From a receiver's perspective, this phase shift is observed as a range shift and can amount several centimeters. The carrier phase wind-up correction $\Delta\Phi_{WU}$ can be calculated with the following expression derived in [128]

$$\Delta\Phi_{WU} = \text{sign}\left(\zeta\right)\arccos\left(\frac{\mathbf{D_s}\mathbf{D_r}}{\|\mathbf{D_s}\|\,\|\mathbf{D_r}\|}\right) \tag{3.56}$$

where $\mathbf{D_s}$ and $\mathbf{D_r}$ define the effective dipole directions of the satellite's transmitting antenna and the receiving antenna. Formula 3.56 is valid for a crossed dipole element, which can be also used as a simplified equivalent antenna model for the Navigation Antenna (L-Band) (NAVANT) of the GALILEO satellites. ζ is defined as

$$\zeta = \mathbf{p}\left(\mathbf{D_s} \times \mathbf{D_r}\right) \tag{3.57}$$

In this expression, $\mathbf{p}$ labels the direction between transmitter and receiver. The effective dipole directions can be computed from

$$\mathbf{D_s} = \mathbf{e}'_a - \mathbf{p}\left(\mathbf{p} \cdot \mathbf{e}'_a\right) - \left(\mathbf{p} \times \mathbf{e}'_b\right) \tag{3.58}$$

$$\mathbf{D_r} = \mathbf{e}_a - \mathbf{p}\left(\mathbf{p} \cdot \mathbf{e}_a\right) - \left(\mathbf{p} \times \mathbf{e}_b\right) \tag{3.59}$$

In equation 3.58 $\mathbf{e}'_a$ and $\mathbf{e}'_b$ specify the unit vectors of the dipole elements residing on the satellite, where as 3.59 applies vice versa for the receiver antenna. It is assumed that the antenna phase center coincides with the cross point of the two dipoles. A generalization of the above mentioned phenomenon also addressing the change in carrier phase wind-up due to reflected electromagnetic waves is discussed in [16].

3.3 Orbit and perturbation force modeling

Orbit modeling is a vital task that supports mission planning and concurrent orbit design activities in the context of space mission preparation and development objectives. In this section, we focus on orbital perturbation modeling and in particular the modeling of NGD, which are of special interest for the evaluation of GNSS satellite orbits. For a discussion of the major causes for radiation generated perturbations, we refer to the respective literature, e.g. [68]. Satellites that orbit Earth on the MEO are predominantly affected by SRP. The only perturbation effects that exceed those caused by SRP are of gravitational nature like third body attractions from the Sun and the Moon as well as the effects of lower and higher order harmonics of the Earth's gravity field. In order to compare different perturbations, we have calculated the accelerations and potential radial errors for a selected collection of perturbation sources. The reader can find the corresponding values sorted by their contributions in the table 3.1. The respective profiles are plotted in 3.4.

Perturbation source	Acceleration $|\vec{a}|_{max}\,[m/s^2]$	Position error $|\vec{r}|_{max}\,[m]$
Harmonic gravity field	0.72	∞
Lunar $\bigcirc$	$4.50 \cdot 10^{-6}$	$5.11 \cdot 10^2$
Solar $\odot$	$2.24 \cdot 10^{-6}$	$2.54 \cdot 10^2$
Solar radiation pressure	$1.38 \cdot 10^{-7}$	$0.90 \cdot 10^2$
Thermal radiation pressure	$8.50 \cdot 10^{-9}$	$5.00 \cdot 10^{-1}$
Post-Newtonian correction[1]	$3.89 \cdot 10^{-10}$	$5.00 \cdot 10^{-2}$
Venus $\female$	$4.65 \cdot 10^{-11}$	$5.00 \cdot 10^{-3}$
Jupiter $\jupiter$	$1.75 \cdot 10^{-11}$	$2.00 \cdot 10^{-3}$
Mars[2] $\mars$	$9.05 \cdot 10^{-14}$	$1.00 \cdot 10^{-5}$

[1] See [105] for further information on the Post-Newtonian framework and its use in the application of celestial mechanics. In the Appendix A.2 one finds the formula describing the relative motion in a PPN two-body setting, which is used here to evaluate the influence of the relativistic correction.
[2] Saturn $\saturn$ is the second most massive planet in the solar system. Despite its greater distance, it causes nearly the same gravitational perturbation as Mars with respect to Earth $\earth$.

Table 3.1: Perturbations as measured for GALILEO satellite GSAT0202. Orbit errors reflect results after a simulation duration that corresponds to one orbital revolution.

SRP depends primarily on spacecraft specific characteristics, such as the form factor, i.e. the respective geometry and surface area as well as the surface material composition and condition. SRP perturbations periodically vary all orbital

elements and satellites with a poor area to mass ratio feature the highest sensitivity to those disturbances. In particular, the attitude of the satellite and its trajectory also play a crucial role. Satellites which are permanently Sun lit throughout the orbit receive a larger amount of direct solar radiation as compared to satellites, which undergo eclipse periods. In this regard, the most notable quantity that determines the amount of time a satellite faces direct sunlight is the Sun's elevation above the orbital plane, β. This angle defines the angular distance between a ray drawn from Earth to the Sun and its corresponding projection onto the orbital plane of a satellite (see 3.8). Finally, even the level of activity of the Sun has a small, but rather negligible effect on the change in SRP, i.e. it undergoes small fluctuations resulting from the eleven-year solar cycle, which amounts up to $\approx 0.08\%$ over one period according to [30]. In a quite recent study by *de Witt et al.* [33], a composite Total Solar Irradiance (TSI) from various data sets has been estimated. Although the process of data analysis is still not finalized, preliminary results reveal that the TSI closely approaches the result of *Frölich* [42], which amounts $1361 \pm 0.5 W/m^2$. Moreover, the seasonal change of the amount of TSI experienced by the satellite due to the varying distance to the Sun amounts up to $\approx 7\%$ and largely outranges the aforementioned effect.
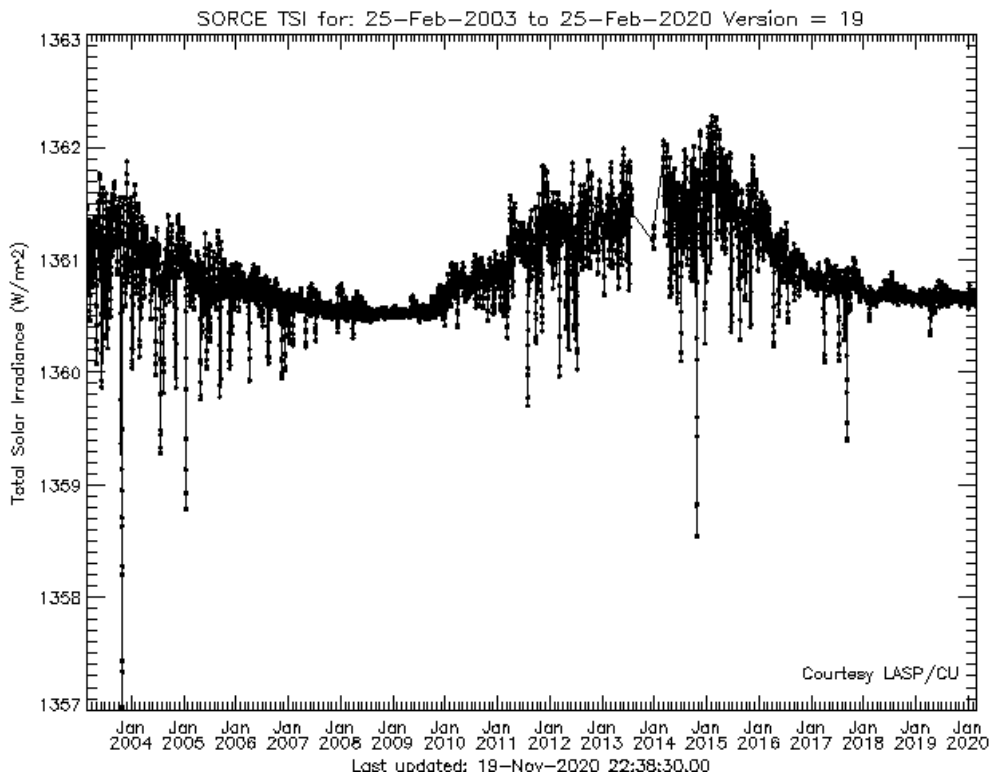
Figure 3.3: Data plot of the total solar irradiance covering the entire mission duration of the Solar Radiation and Climate Experiment (SORCE) satellite[a]. Among other investigations, the mission aimes at taking high-precision measurement data of the total solar irradiance. One well recognizes the approximate 11-year change of the solar activity.

---

[a]https://lasp.colorado.edu/home/sorce/data/tsi-data/

3.3.1 Perturbation modeling strategy

The main forces that govern the perturbed dynamics of an Earth-bound satellite are of gravitational nature. In 3.3, table 3.1 reveals that by far the largest contribution is due to the Earth's harmonic gravity field. The equation that describes the motion of GNSS satellites sufficiently well reads:

$$\frac{d^2 \mathbf{r}}{dt^2} = \mathbf{a}_{Geo} + \mathbf{a}_{Tide} + \mathbf{a}_{PM} + \mathbf{a}_{PN} + \mathbf{a}_{srp} + \mathbf{a}_{a,IR} \qquad (3.60)$$

$\mathbf{a}_{Geo}$	Acceleration due to the Earth's harmonic gravity field	$[m/s^2]$
$\mathbf{a}_{Tide}$	Acceleration due to lunisolar Solid Earth Tides and Ocean Tides	$[m/s^2]$
$\mathbf{a}_{PM}$	Third body perturbations due to other celestial bodies	$[m/s^2]$
$\mathbf{a}_{PN}$	Acceleration related to post-Newtonian perturbations	$[m/s^2]$
$\mathbf{a}_{srp}$	Solar Radiation Pressure (SRP) generated acceleration	$[m/s^2]$
$\mathbf{a}_{a,IR}$	Earth albedo and IR acceleration	$[m/s^2]$

Geopotential perturbations: The Earth's geopotential is driven by its irregular mass density distribution and can be expanded into a series of spherical harmonics:

$$u = \frac{GM_\oplus}{r} \sum_{n=0}^{\infty} \sum_{m=0}^{n} \frac{a_\oplus{}^n}{r^n} \left(P_n^m \left(\sin\theta \right) \left(C_{nm} \cos m\phi + S_{nm} \sin m\phi \right) \right) \qquad (3.61)$$

$$u = \frac{GM_\oplus}{r} + \left(\sum_{n=2}^{N_z} \frac{J_n P_n^0 \left(\sin\theta \right)}{r^{n+1}} \right) + \left(\sum_{n=2}^{N_t} \sum_{m=1}^{n} \frac{P_n^m \left(\sin\theta \right) \left(C_{nm} \cos m\phi + S_{nm} \sin m\phi \right)}{r^{n+1}} \right)$$

$$(3.62)$$

u	Gravitational potential	$[J/kg]$
r	Distance between center of Earth and point of interest	$[m]$
θ	Polar angle in spherical coordinates	$[deg]$
ϕ	Azimuth angle in spherical coordinates	$[deg]$
N_z	Total number of zonal components in the expansion	
N_t	Total number of tesseral components in the expansion	

with the coefficients of degree n and order m:

$$C_{nm} = \frac{2 - \delta_{0m}}{M_\oplus} \frac{(n-m)!}{(n+m)!} \int \frac{s^n}{a_\oplus{}^n} P_n^m \left(\sin\theta\right) \left(\cos m\phi\right) \rho(\mathbf{s}) d^3s \qquad (3.63)$$

$$S_{nm} = \frac{2 - \delta_{0m}}{M_\oplus} \frac{(n-m)!}{(n+m)!} \int \frac{s^n}{a_\oplus{}^n} P_n^m \left(\sin\theta\right) \left(\sin m\phi\right) \rho(\mathbf{s}) d^3s \qquad (3.64)$$

where one has to integrate over the Earth's volume d^3s, which at every point $\mathbf{s}$ has a density $\rho(\mathbf{s})$. The coefficients C_{nm}, S_{nm} and J_n are provided as data products, for example, by the Geo Forschungs Zentrum (GFZ)[11]. The terms P_n^0 and P_n^m are the Legendre polynomials and associated Legendre functions, respectively. Equation 3.62 makes it easier to discern between different components of the gravity field model. Apart from the Earth monopole value represented by the first therm, the geopotential coefficient J_2 makes the largest contribution. This shape factor resembles the effect of the Earth's oblateness. According to the Numerical Standards of the International Earth Rotation Service (IERS), a value of $J_2 = 1.0826359 \times 10^{-3} \pm 1 \times 10^{-10}$ is recommended. The J_3 term is already three orders of magnitude smaller. The most recent 2020 version of the Earth Gravitational Model (EGM) improving the EGM2008 predecessor was planned to be published[12] by the National Geospatial-Intelligence Agency (NGA) in 2020, see [14]. The release is announced to comprise a harmonic gravity field model up to degree (n) and order (m) 2159. Its precursor model, the experimental global gravity field model, was published by [129], which extends to degree (n) and order (m) 5400. The perturbing accelerations follow from constructing the gradient of the potential 3.61. For the benefit of the reader, we provide the results for the single vector components of $\mathbf{a}_{Geo} = \sum_{n,m} [\ddot{x}_{nm}, \ddot{y}_{nm}, \ddot{z}_{nm}]$ given in [70] in an Earth-Centered Earth-Fixed (ECEF) coordinate system:

$$\ddot{x}_{nm} \overset{m=0}{=} \frac{GM_\oplus}{a_\oplus{}^2} \left(-C_{n0} V_{n+1,1}\right) \qquad (3.65)$$

$$\ddot{x}_{nm} \overset{m>0}{=} \frac{GM_\oplus}{2a_\oplus{}^2} \left(-C_{nm} V_{n+1,m+1} - S_{nm} W_{n+1,m+1}\right) \qquad (3.66)$$

$$+ \frac{(n-m+2)!}{(n-m)!} \left(C_{nm} V_{n+1,m-1} + S_{nm} W_{n+1,m-1}\right) \qquad (3.67)$$

$$\ddot{y}_{nm} \overset{m=0}{=} \frac{GM_\oplus}{a_\oplus{}^2} \left(-C_{n0} W_{n+1,1}\right) \qquad (3.68)$$

$$\ddot{y}_{nm} \overset{m>0}{=} \frac{GM_\oplus}{2a_\oplus{}^2} \left(-C_{nm} W_{n+1,m+1} - S_{nm} V_{n+1,m+1}\right) \qquad (3.69)$$

$$+ \frac{(n-m+2)!}{(n-m)!} \left(C_{nm} W_{n+1,m-1} + S_{nm} V_{n+1,m-1}\right) \qquad (3.70)$$

$$\ddot{z}_{nm} \overset{m>0}{=} \frac{GM_\oplus}{a_\oplus{}^2} \left((n-m+1)\left(-C_{nm} V_{n+1,m} - S_{nm} W_{n+1,m}\right)\right) \qquad (3.71)$$

V_{nm} and W_{nm} define the following recurrence relations:

---

[11] http://isdc.gfz-potsdam.de/grace-isdc/
[12] https://ui.adsabs.harvard.edu/abs/2020EGUGA..22.9884B/abstract

$$V_{mm} = (2m-1)\left(\frac{xa_\oplus}{r^2}V_{m-1,m-1} - \frac{ya_\oplus}{r^2}W_{m-1,m-1}\right) \tag{3.72}$$

$$W_{mm} = (2m-1)\left(\frac{xa_\oplus}{r^2}W_{m-1,m-1} - \frac{ya_\oplus}{r^2}V_{m-1,m-1}\right) \tag{3.73}$$

$$V_{nm} = \frac{2n-1}{n-m}\frac{za_\oplus}{r^2}V_{n-1,m} - \frac{n+m-1}{n-m}\frac{a_\oplus^2}{r^2}V_{n-2,m} \tag{3.74}$$

$$W_{nm} = \frac{2n-1}{n-m}\frac{za_\oplus}{r^2}W_{n-1,m} - \frac{n+m-1}{n-m}\frac{a_\oplus^2}{r^2}W_{n-2,m} \tag{3.75}$$

Solid Earth Tides: The shape of the Earth is persistently subjected to tidal forces caused by the gravitational fields of other celestial bodies, especially that of the Sun and the Moon. These tidal forces produce permanent and periodic shape deformations, where displacements of the Earth's crust are called *Solid Earth Tides*. The deformations are in turn responsible for corresponding variations of the Earth's geopotential, which is actually observed in the vicinity of the Earth. Among time-varying deformations, tidal effects are also responsible for slight changes in orbital precession and nutation. Another form of tide-induced perturbations are *Ocean Tides*, which also generate variations in the Earth's geopotential. Both effects are conventionally modeled as corrections ΔC_{nm} and ΔS_{nm} to the standard coefficients 3.63 and 3.64 that describe the geopotential model. According to [70], the lunisolar Solid Earth Tides can be written as:

$$\Delta C_{nm} = 4k_n\left(\frac{GM}{GM_\oplus}\right)\left(\frac{a_\oplus}{s}\right)^{n+1}\sqrt{\frac{(n+2)(n-m)!3}{(n+m)!3}}P_n^m(\sin\phi)\cos m\phi \tag{3.76}$$

$$\Delta S_{nm} = 4k_n\left(\frac{GM}{GM_\oplus}\right)\left(\frac{a_\oplus}{s}\right)^{n+1}\sqrt{\frac{(n+2)(n-m)!3}{(n+m)!3}}P_n^m(\sin\phi)\cos m\phi \tag{3.77}$$

M	Mass of celestial body	$[kg]$
s	Distance between Earth and celestial body	$[m]$
k_n	Love number of degree n	
ϕ	Earth-fixed latitude	$[deg]$
λ	Earth-fixed longitude	$[deg]$

The contribution of the tides to the geopotential depend on the *Love numbers*. These numbers are dimensionless parameters describing the susceptibility of the Earth's shape to external and Earth-related tidal effects. They thus indicate by how much the effect of the tidal potential on the elastic Earth is greater than on a rigid Earth body.

Ocean Tides: The same tidal forces that cause Solid Earth Tides also lead to a periodic redistribution of the global seawater and thus to fluctuations of seawater levels. Depending on the phase and amplitude of the rise and fall of the seawater level, the Earth's gravity field reacts with a corresponding time-varying change. Ocean Tides can be modeled as ([34], [70], [112] gives in particular expressions for temporal deviations of the second degree coefficients, which have the biggest impact):

$$\Delta C_{nm} = \frac{4\pi G a_\oplus{}^2 \rho_w (1 + k'_n)}{GM_\oplus (2n + 1)} \sum_{f(n,m)} (C^+_{fnm} + C^-_{fnm}) cos\,(\theta_f) + (S^+_{fnm} + S^-_{fnm}) sin\,(\theta_f)$$

(3.78)

$$\Delta S_{nm} = \frac{4\pi G a_\oplus{}^2 \rho_w (1 + k'_n)}{GM_\oplus (2n + 1)} \sum_{f(n,m)} (C^+_{fnm} - C^-_{fnm}) cos\,(\theta_f) - (S^+_{fnm} - S^-_{fnm}) sin\,(\theta_f)$$

(3.79)

ρ_w	Seawater density	$[kg/m^3]$
k'_n	Ocean load deformation factors	
$C^\pm_{fnm}, S^\pm_{fnm}$	Ocean Tide coefficients/amplitudes of tide constituent frequency f	$[m]$
θ_f	Weighted sum of six Doodson variables/Tide constant of tide constituent frequency f	

The signs in the superscripts of $C^\pm_{fnm}$ and $S^\pm_{fnm}$ represent prograde and retrograde wave amplitudes associated with frequency f and degree and order n and m. The six *Doodson numbers* encode the tidal harmonic components (e.g. short-term and long-term) and are associated with the six fundamental *Doodson arguments* specified in [65]. They enable to develop the tide-generating potential in dependence of the Sun's and Moon's orbits. The methodology goes back to Arthur Thomas Doodson, see [32]. Finally, the tide-induced acceleration $\mathbf{a}_{Tide}$ can be computed by using the formulas 3.65 to 3.71.

Point-mass perturbations: The prediction of satellite orbital perturbations $\mathbf{a}_{PM}$ due to other celestial bodies regarded as point-masses can be achieved with:

$$\mathbf{a}_{PM} = -GM_\oplus \left(\frac{\mathbf{r} - \mathbf{s}}{|\mathbf{r} - \mathbf{s}|^3} + \frac{\mathbf{s}}{|\mathbf{s}|^3} \right)$$

(3.80)

where $\mathbf{r}$ and $\mathbf{s}$ are the geocentric position vectors of the satellite and the point-mass of another celestial body with respect to the J2000[13] ECI reference frame realisation.

---

[13]This is an inertial reference frame in which the equations of motion for the solar system may be integrated. This reference frame is specified by the orientation of the Earth's mean equator and equinox at a particular epoch - the J2000 epoch. This epoch is Greenwich noon on January 1, 2000 Barycentric Dynamical Time (TDB) (source: `https://naif.jpl.nasa.gov/pub/naif/toolkit_docs/FORTRAN/req/time.html`)

As a basis for the computation of the celestial body positions involved in perturbation modeling, the *JPL Planetary and Lunar Ephemerides*[14] database is used. It contains coefficients of Chebyshev polynomial fits to the Cartesian planetary positions in the International Celestial Reference Frame (ICRF), which slightly deviates from the J2000 reference frame. The Chebyshev polynomials are related to the TDB scale.

Relativistic orbital perturbations: The magnitude of the relativistic post-Newtonian correction $\mathbf{a}_{PN}$ that play a role in the satellite's equations of motion is referenced in table 3.1. The equations of motion for a satellite on its trajectory is given by the geodesic equation:

$$\frac{dx^\mu}{d\tau} = \Gamma^\mu_{\nu\sigma} \frac{dx_\nu}{d\tau} \frac{dx^\sigma}{d\tau} \tag{3.81}$$

where τ in equation 3.81 is to be interpreted as the reading of a clock. For a point mass describing e.g. a satellite, the parameter represents proper time. The *Christoffel symbols* Γ are given in [83] on page 375 and are based on a space-time metric expansion of 1PN order, which can be used to describe a post-Newtonian system under the conditions of slow motion and weakly curved space-time:

$$g_{00} = -1 + \frac{2}{c^2}U + \frac{2}{c^4}\left(\Psi - U^2\right) + O(c^{-6}) \tag{3.82}$$

$$g_{0j} = -\frac{4}{c^3}U_j + O(c^{-5}) \tag{3.83}$$

$$g_{jk} = \delta_{jk}\left(1 + \frac{2}{c^2}U\right) + O(c^{-4}) \tag{3.84}$$

where U and Ψ are the near zone potentials, which are listed in [83] on page 358 and give rise to the metric components $g_{\mu\nu}$. The subscript for the potential U in 3.83 denotes its partial derivative with respect to the jth coordinate. The general notation follows the conventions established by the author. Through the use of the above mentioned Christoffel symbols, an equation for the desired description of post-Newtonian motion $\mathbf{a}_{PN}$ can be found (see [105]):

$$\frac{d\mathbf{v}}{dt} = -\frac{GM_\oplus}{r^3}\mathbf{r} + \frac{GM_\oplus}{c^2}\left(2(\beta + \gamma)\frac{GM_\oplus}{r^4}\mathbf{r} - \frac{v^2}{r^3}\mathbf{r} + 2(\gamma + 1)\frac{\mathbf{r} \cdot \mathbf{v}}{r^3}\mathbf{v}\right) \tag{3.85}$$

v	Euclidian vector norm of the velocity	$[m/s]$
β	Curvature parameter (equal to 1 in General Relativity)	
γ	Non-linearity parameter (equal to 1 in General Relativity)	

---

[14] https://ssd.jpl.nasa.gov/ftp/eph/planets/bsp/

The second term in brackets in formula 3.85 can be finally identified as the perturbing acceleration $\mathbf{a}_{PN}$ in equation 3.60.

Earth albedo and Earth infrared radiation: In addition to SRP, we would like to mention other NGD sources for completeness, although they play a rather minor role for a perturbation analysis for satellites located on a MEO: Earth albedo and earth infrared radiation, which act in the same way as SRP. The former considers essentially the fraction of sunlight reflected from the Earth's surface described by the albedo factor α. In principle, albedo covers the same optical spectrum as the radiation responsible for SRP, but its intensity generally depends on the wavelength of the sunlight reflected from the Earth and can be specified for ranges of wavelengths. The average albedo value is approximately 0.34, which is equivalent to an average surface flux of $\alpha P_{\odot} \approx 463 W/m^2$. In contrast, the Earth's infrared radiation depends on the Earth's specific thermal re-emission pattern and encompasses a longer wavelength spectrum than albedo, averaging about $\approx 230 W/m^2$. According to [71], the total effect caused by both phenomena is two orders of magnitude smaller than the perturbations caused by SRP. Both effects can be modelled as:

$$\mathbf{a}_{a,IR} = \sum_{j} \left(c_a \alpha I_a \cos \theta_{j,E} + c_{IR} I_{IR} \right) \left(\frac{A_s}{c \, m} \frac{A_j}{\pi r_j^2} \cos \theta_{j,s} \, \mathbf{r}_j \right) \tag{3.86}$$

c_a, c_{IR}	Earth albedo and infrared coefficients	
I_a, I_{IR}	Radiation flux radiated from Earth	$[W/m^2]$
α	Albedo factor	
A_j	Earth's jth surface element with unit surface normal vector $\mathbf{n}_j$	$[m^2]$
$\theta_{j,E}$	Angle between $\mathbf{n}_j$ and surface-Sun vector	$[deg]$
$\theta_{j,s}$	Angle between $\mathbf{n}_j$ and surface-satellite vector	$[deg]$
$\mathbf{r}_j$	Unit vector from A_j to satellite and according distance r_j	$[m]$
m	Satellite's mass	$[kg]$

Equation 3.86 assumes that the Earth's surface is divided into a number of area elements A_j. The considerations become more complicated if one also makes a geometric differentiation for the satellite: For any relative orientation of surface elements A_j and surfaces A_i describing the distinct shape of the satellite, we would obtain additional visibility factors describing the intensity of radiative exchange due to the geometry of any conceivable configuration. By analogy, in section 4.2.1.2, we calculate such visibility factors describing the radiative coupling between individual surfaces within a satellite in the context of a thermal analysis, see also equation 4.47. For simplicity, we have introduced a surface measure A_s for the satellite, which remains constant for all times. For consistency, we also neglect these additional NGD sources in section 4.2.1.2.
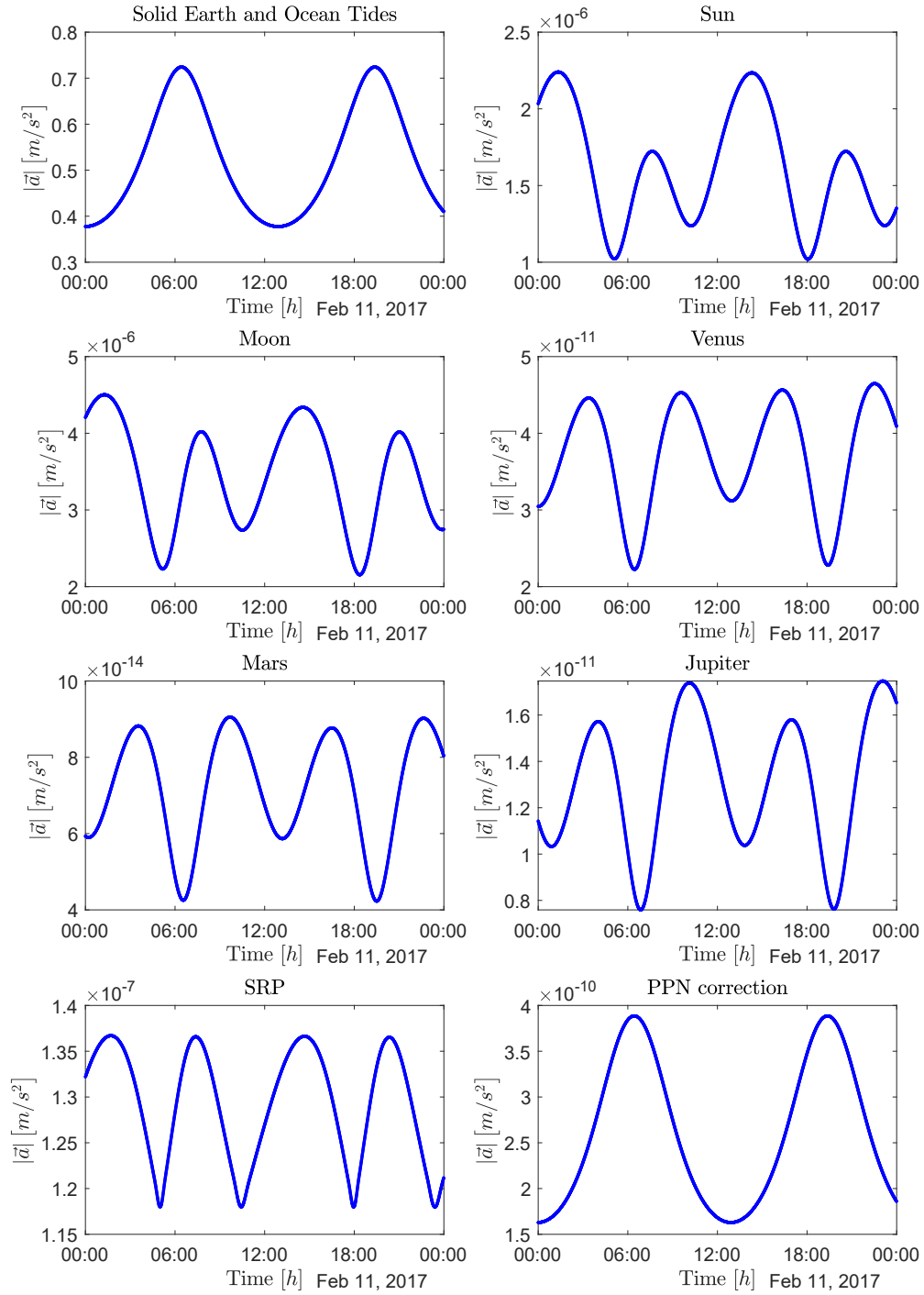
Figure 3.4: Comparison of various selected perturbation series computed through the use of an orbit simulation for GSAT0202. The figures show the 2-norm values of the underlying acceleration vectors. The maximum values of the time series are listed in table 3.1.

3.3.2   Advances in SRP modeling

There have been major advances in the modeling of radiation pressure effects in the last decades targeting at a better understanding of the impact on GNSS orbits. For the GPS system, the so-called ROCK models were introduced in the first half of the 1990s by *Fliegel et al.* [41] [40] to cover perturbations as solar and thermal radiation pressure effects. Before that time, no steps were taken to investigate these effects analytically, instead sticking to the strategy of deriving statistical parameters directly from orbit estimation. For the Block I, Block II and Block IIa satellites, various a-priori model candidates were first formulated by *Fliegel et el.* [41] and the model predictions were tested against pseudo-range tracking data. At a later time, already before the Block IIR GPS satellite generation became operational a model redesign was proposed in [40]. The ROCK models basically represent the GPS satellites as a collection of geometrical primitives like flat surfaces or cylindrical bodies with sets of optical material properties assigned. With these a-priori features, they can rather adequately reflect their geometrical composition. The computation of the perturbation forces are carried out in a satellite-fixed coordinate system, in which the positive Z-direction points nadir, the positive Y-axis is directed along the solar panel pivot axis and the X-direction completes the right-handed coordinate system, such that radiation pressure effects are confined to the X, Z -faces. In order to increase the accuracy, it has been recommended to augment the ROCK models by further estimation of two parameters. One for the absorption of the Y-bias, acting in the directions of the solar panel axes, and another additional scale term. With these additional parameters, the ROCK models represented a suitable choice for pseudo-range-based orbit estimation procedures. However, model results have demonstrated that it is insufficient for high-precision geodetic applications requiring centimeter accuracy.

At a later time, a new empirical SRP model, the Empirical CODE Orbit Model (ECOM) was proposed by *Beutler et al.* in [15] and it essentially decomposes the radiation induced accelerations in a body-fixed system (DYB-system) that is both Sun- and solar panel axis-aligned. This approach was based on the assumption that the effects of SRP can be better isolated in this axis system, thus simplifying the physical interpretation of the empirical parameters. This in turn was inspired by the model employed by *Colombo et al.* [26], which was designed to mainly capture resonant effects from orbital perturbations caused by the Earth's gravity field. Unlike the Sun-aligned ECOM frame, the Colombo model instead expediently refers to an axis system aligned in radial direction. The ECOM coordinate system is defined such that the D-axis points from the satellite towards the Sun, the Y-axis is aligned with one of the satellite's solar panel axes, following the convention of the ROCK models, and the B-axis completes the right-handed coordinate system. Following that definition, the specific DYB-system can be constructed as follows:

$$
\begin{aligned}
\mathbf{e}_D &= \mathbf{e}_\odot \\
\mathbf{e}_Y &= \mathbf{e}_y \\
\mathbf{e}_B &= \mathbf{e}_\odot \times \mathbf{e}_y
\end{aligned}
\tag{3.87}
$$

For a better view on the orbit configuration, the typical spacecraft's attitude and its

corresponding axis orientation, see 3.8. Within this Sun-aligned coordinate system, the empirical accelerations for each of the directions given in 3.87 are modeled by first order Fourier series with a set of three coefficients $\{D_0, \ D_c, \ D_s, \ Y_0, \ Y_c, \ Y_s, \ B_0, \ B_c, \ B_s\}$. Thereby, the periodic terms are functions of the orbit angle with respect to the spacecraft's latitude, u, which describes the angular distance of the satellite with respect to its ascending node:

$$
\begin{aligned}
a_D &= D_0 + D_c cos(u) + D_s \sin(u) \\
a_Y &= Y_0 + Y_c cos(u) + Y_s \sin(u) \\
a_B &= B_0 + B_c cos(u) + B_s \sin(u)
\end{aligned}
\tag{3.88}
$$

The use of this purely empirical model is still common practice and especially its reduced form with five parameters including all constant terms and the once-per-revolution B_c and B_s -terms to treat SRP induced perturbed satellite motion for the purpose of orbit determination. Originally, this model was used as an extension to the a-priori ROCK models, and it was shown by *Beutler et al.* [15] that by using this semi-empirical approach the predictions of SRP effects for the GPS satellites could be significantly improved.

Springer et al. [108] started a dedicated research to determine an optimal parameterization for the ECOM for accurate orbit estimation of the GPS satellites. The key reason for the study involved model shortcomings encountered in orbit estimation tests with different parameter configurations. Parameter tests were then performed based on multiple-day orbit estimates in which the respective coefficients of the three ECOM parameter sets were varied for the constant and periodic terms. A comprehensive study of various SRP parameterizations based on two different orbit estimation approaches[15] ultimately revealed an optimal set of six acceleration parameters $\{D, \ Y, \ B, \ Z_1, \ X_1, \ X_3\}$ for the description of SRP induced perturbations $(\mathbf{a}_{srp})$:

$$
\begin{aligned}
\mathbf{a}_{srp} = D \cdot \mathbf{e}_D &+ Y \cdot \mathbf{e}_Y + B \cdot \mathbf{e}_B \\
&+ Z_1 \sin(u - u_0) \cdot \mathbf{e}_Z + (X_1 \sin(u - u_0) + X_3 \sin(u - u_0)) \cdot \mathbf{e}_X
\end{aligned}
\tag{3.89}
$$

Equation 3.89 includes three constant ECOM terms for the DYB-accelerations and two additional terms accounting for first and third order harmonics in the $\mathbf{e}_X$ and $\mathbf{e}_Z$-axis defining the spacecraft body-fixed system[16], where the harmonic functions depend on the spacecraft's latitude u[17] with respect to the Sun's latitude in the orbital plane u_0.

---

[15]On the one hand, a rather conventional orbit estimation procedure based on GPS observations was used and the results were compared to estimations based on fits to precise SP3 orbital data. The details of the procedure are documented by *Springer et al.* in [107]

[16]The Z -axis points in radial direction and the X -axis is perpendicular to the plane spanned by the Y and the Z -axes.

[17]The spacecraft's argument of latitude is the sum of the argument of perigee and the true anomaly.

The successful search for an optimal parameterization was followed by a five-day orbit fit study based on precise SP3 orbital data of the Center for Orbit Determination in Europe (CODE) covering a time span of 5.5 years in an attempt to find a universal a-priori model that would meet the requirements of long-time orbital perturbation analyses. As a result, the following sets of expressions were obtained for the Block II and Block IIa GPS satellites:

$$D(\beta_0) = D_0 + D_{C2}\cos(2\beta_0) + D_{C4}\cos(4\beta_0)$$
$$Y(\beta_0) = Y_0 + Y_C\cos(2\beta_0)$$
$$B(\beta_0) = B_0 + B_C\cos(2\beta_0) \qquad\qquad (3.90)$$
$$Z_1(\beta_0) = Z_0 + Z_{C2}\cos(2\beta_0) + Z_{S2}\sin(2\beta_0) + Z_{C4}\cos(4\beta_0) + Z_{S4}\cos(4\beta_0)$$
$$X_1(\beta_0) = X_{10} + X_{1C}\cos(2\beta_0) + X_{1S}\cos(2\beta_0)$$
$$X_3(\beta_0) = X_{30} + X_{3C}\cos(2\beta_0) + X_{3S}\sin(2\beta_0)$$

which redefines the six harmonic coefficients appearing in equation 3.89 as a function of harmonic series of the Sun's elevation above the orbital plane β, which is shown in 3.8. The insertion 3.90 into 3.89 then brings the final new CODE SRP model. The accompanying eighteen series coefficients in equation 3.90 can be found in [108].

In the end of 2014, *Montenbruck et al.* [71] published a new SRP model for the GALILEO In-Orbit Validation (IOV) satellites. This work was motivated by the appearance of deficiencies in the respective orbit solutions as became evident from long-term Satellite Laser Ranging (SLR) residual analysis. To overcome this problem, a semi-empirical SRP model was developed. This combines satellite-taylored a-priori box model information with the a five-parameter ECOM model $\{D_0,\ Y_0,\ B_0,\ B_c,\ B_s\}$. For the a-priori box model, six additional parameters were introduced $\left\{a_C^{\alpha\delta},\ a_S^{\alpha\delta},\ a_A^{\alpha\delta},\ a_C^{\rho},\ a_S^{\rho},\ a_A^{\rho}\right\}$ that account for the particular shape of the satellite and its deviation from an ideal box model. These parameters are composed of combinations of characteristic SRP accelerations that isolate the effect of the satellite's individual $\{+Z,\ -Z,\ +X\}$ surfaces. The subscripts C, S and A denote the single contributions of the satellite's cubic, stretched and anti-symmetric geometrical shape, the superscripts indicate the type of radiation exchange with the satellite's surfaces (α and δ declare absorption and diffuse reflection and ρ denotes specular reflection. The orbit solutions show that the additional a-priori model helps to notably reduce radial orbit errors, as is confirmed by the SLR residuals as well as the satellite clock residuals in comparison to the results computed with a pure ECOM model. The study demonstrates that some empirical parameters are highly sensitive to changes in a-priori parameters that quantify the cubic shape and cuboidness of the satellite (a_C and a_S), which underpins the relevance of proper geometrical modeling, whereby it was found that there is no pronounced dependence on parameters that determine the asymmetry of the spacecraft (a_A). The shape of the GALILEO IOV satellites is strongly related to that of the FOC satellites, see figure 3.5. However, it has to be noted that in contrast to the IOV satellites, the surfaces of the FOC satellites have different material characteristics. This could especially affect the outcome of the ECOM parameter estimation results related to changes in the a_A parameters absorbing the $+Z,\ -Z$ -face asymmetry. Moreover, the missing

correlation of harmonics of the B parameter and the new a-priori parameters could reflect further modeling deficiencies not captured by the adopted approach.

In 2015, *Arnold et al.* [9] reissued the ECOM to fill the performance gaps that resulted primarily from the increasing deployment of the Globalnaja nawigazionnaja sputnikowaja sistema (GLONASS) constellation. In an extensive long-term study, GPS and GLONASS observations were used, to also determine geodetic performance indicators such as the quality of the geocenter z-coordinates or Earth rotation parameter solutions. The orbit model for each satellites was equipped with a five-parameter ECOM. In particular, the GLONASS solutions gave poor results compared to GPS as well as combined solutions. The study suggests the following, more universal model for the absorption of radiation-induced perturbations, also referred to as the extended ECOM or ECOM2 model:

$$D\left(u\right) = D_0 + \sum_{n=1}^{n_D} D_{c,2n}\cos\left(2n\Delta u\right) + D_{s,2n}\sin\left(2n\Delta u\right) \tag{3.91}$$

$$Y\left(u\right) = Y_0 \tag{3.92}$$

$$B\left(u\right) = B_0 + \sum_{n=1}^{n_B} B_{c,2n-1}\cos\left((2n-1)\Delta u\right) + B_{s,2n-1}\sin\left((2n-1)\Delta u\right) \tag{3.93}$$

where Δu was already defined in equation 3.89. The upper bounds n_D and n_B of the sums are user-defined and must be carefully chosen depending on the application. The five-parameter ECOM is basically a reduced realization of the above formulation with $n_D = 0$ and $n_B = 1$, which we henceforth refer to as ECOM1. For small changes in β_0, [9] suggests also that the coefficients of the series 3.93 can be written
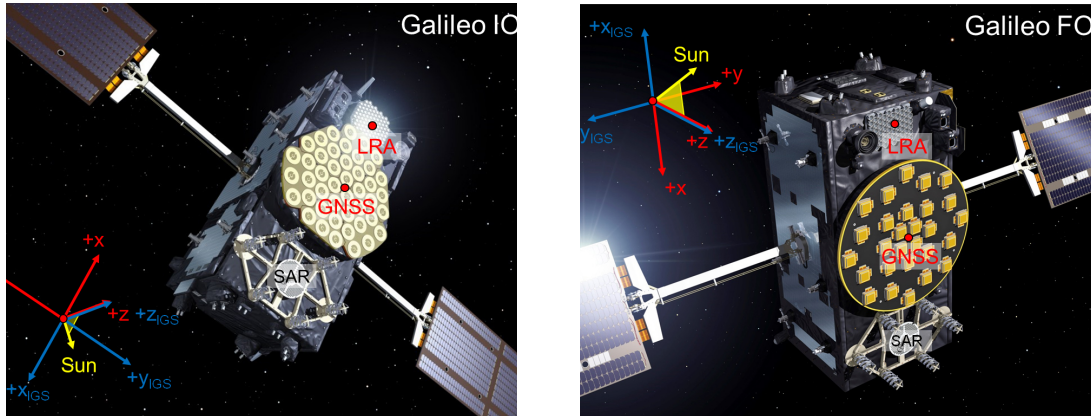
Figure 3.5: Artificial representation of the GALILEO satellites[a]. There are different reference coordinate systems shown in these pictures. The red one specifies the manufacturer-specific axis system, whereas the blue-labeled one indicates the coordinate system as adopted by the IGS. In this thesis, the description of any satellite body-fixed related effects are described in the last-mentioned coordinate system, if not otherwise stated.

---

[a]https://www.igs.org/mgex/constellations/

in dependence of the Sun's latitude and the B_c and B_s coefficients of the ECOM1. The study implies that although the ECOM1 is still sufficient for high-precision applications such as geodetic surveys, the ECOM2 is especially a good substitute to also establish compatibility with the GLONASS system. *Prange et al.* later also showed that the ECOM2 can be even a beneficial candidate model for the improvement of GALILEO and Quasi-Zenith Satellite System (QZSS) orbit solutions.

A ray-tracing approach based on a medium-fidelity Computer-Aided Design (CAD) model was developed out by *Darugna et al.* [28] to improve the orbit determination results for the QZSS based on observation data covering a two-year period from 2015 to 2016. Four solutions were compared, calculated using different models: Two purely empirical models with two different ECOM parametrizations and two a-priori models, one box-wing realization and the ray-tracing model. It was shown that the employment of an a-priori model significantly reduces the parameter estimation effort. Thus, in this respect, all ECOM parameters could be reduced using the a priori models. As an independent test, SLR residuals were used as a measure for the accuracy of the orbit solutions. The according analysis gave evidence that the ray-tracing model performed best, showing the smallest SLR residuals, when the satellite is in YS mode. However, the box-wing a-priori model showed better results, when the satellite is in Orbit-Normal (ON) mode. The ray-tracing model implications gave reason that this effect emerged owing to thermal radiation mismodeling such that improvements are expected to be achieved with more detailed knowledge about the thermal control system as well as more information about small scale structures and optical material properties of the satellite.

The European GNSS Service Centre first published the GALILEO metadata during 2016 and updated it in the first half of 2019. These contain physical and technical information on the GALILEO IOV and FOC generations that are of particular interest for PPP and POD applications. These include the special spacecrafts' attitude control laws, geometrical and physical properties such as the dimensions and mass as well as center of mass of the satellites. There are also lists of optical material properties among the information describing the average absorption and reflection behavior of the outer surfaces of a simplified box-wing satellite substitute model, which especially serves the purpose of more advanced radiation pressure studies.

Bury et al. [20] used the official GALILEO metadata for a comparative study, focusing primarily on testing the performance of the specified box-wing model under consideration of different ECOM1 and ECOM2 parameter configurations. 200 days of tracking data from 2017 from over 100 GNSS ground stations were used as a data basis. Using the different parameter configurations, orbit solutions were calculated and compared based on their SLR residuals. Semi-empirical models endowed with a box-wing model with generally fewer ECOM parameters were found to produce better results than purely empirical models or even the stand-alone box-wing model. The best performance was obtained by a three-parameter semi-empirical model using only the constant terms from the five-parameter set also analyzed in [71].

Sidirov et al. [104] introduced an a-priori model that accounts for Thermal Ra-

diation Pressure (TRP) effects emanating from the thermal radiators mounted on the $-X$ -face by also using the official GALILEO metadata. In addition, the orbit model was equipped with an extended ECOM2 parameter model to more effectively describe the TRP-related effects, especially during eclipse phases. Besides once-per-revolution harmonic terms acting in D -direction needed for low Sun elevations β, the ECOM2 should also absorb the thermally induced effects generated by the radiators installed at the $\pm Y$ surfaces. Using this model, it was shown that improved orbit and clock solutions could be obtained, and after an independent evaluation via SLR measurements, a 14% reduction in SLR residuals was also observed.

The advances that have been made in the field of NGD modeling in recent years have shown that the performance of GNSS systems has been tremendously enhanced for the benefit of a wide range of applications. These include improvements in geodetic datums, accurate studies of geodynamic processes, and other Earth science contributions, as well as support for fundamental physics studies. A distinction is made between different types of SRP models that have been retrospectively proven to perform well. Empirical models such as the ECOM1 or ECOM2, semi-empirical models that are additionally equipped with an analytical model, such as a geometrical box-wing model. Finally, the trend is towards finer resolutions of geometrical structures to account for the most real mapping of the satellite.

3.3.3 Solar radiation pressure

Solar Radiation Pressure (SRP) is caused by the interaction of photons from the Sun with a satellite's surface. During the process of interaction, photons exchange momentum with the target surface resulting in a phenomenon we call SRP. From the definition of proper time and the definition of the four-momentum p^μ, see [79], one can deduce the following relativistic momentum normalization condition:

$$\eta_{\mu\nu}p^\mu p^\nu = m^2\eta_{\mu\nu}u^\mu u^\nu = -m^2c^2 \tag{3.94}$$

$$\Leftrightarrow \quad E = \sqrt{m^2c^4 + |\mathbf{p}|^2 c^2} \tag{3.95}$$

where we adopted the index notation from equation 1.2. Since photons have zero rest mass ($m = 0$), the above expression 3.95 reduces to:

$$E = |\mathbf{p}|c \tag{3.96}$$

Computing the time derivative of 3.96, we get an expression for the SRP :

$$\frac{dE}{c\,dt} = \frac{d|\mathbf{p}|}{dt} \tag{3.97}$$

$$\Leftrightarrow \quad \frac{P_\odot}{c} = P_{srp} \tag{3.98}$$

where $P_\odot$ is the solar constant at a distance of AU from the Sun and P_{srp} is the corresponding solar radiation pressure. The equation for the associated acceleration $\mathbf{a}_{srp}$ appearing in 3.60, perturbing the satellite's motion is stated as follows:

$$\mathbf{a}_{srp} = -\eta\left(C_{srp}\frac{P_\odot}{c}\frac{A_S}{m_S}\frac{1AU^2}{|\mathbf{s}|^2}\frac{\mathbf{s}}{|\mathbf{s}|}\right) \tag{3.99}$$

The solar flux amount, $P_\odot$, follows a nearly 11 year activity cycle that depends on the number of solar spots, see figure 3.3. It also depends on the distance from the satellite to the Sun $|\mathbf{s}| = |\mathbf{r}_\odot - \mathbf{r}|$ (measured in scales of $1AU$), and for Earth-bound satellites it varies between approximately $\approx 1418W/m^2$ at perhelion and $\approx 1326W/m^2$ at aphelion. Among the solar flux, the SRP-related force acting on a satellite heavily depends on the actual surface area to mass ratio A_S/m_S, which is sensitive to the orientation of the spacecraft at a certain epoch. Moreover one has to consider eclipse conditions throughout periods in which the satellite is either totally or just partially obscured by the Earth or the Moon. This is also reflected by the scale factor η which takes values between 0 and 1. Finally, a conventional form factor C_{SRP} enteres the equation, which usually has to be determined statistically as an empirical form factor for a particular satellite.

The combination of both an analytical treatment as given per 3.99 and additional empirical information absorbed via 3.88 finally gives us:

$$\mathbf{a}_{srp,DYB} = -\eta \left(C_{srp} \frac{P_{\odot}}{c} \frac{A_S}{m_S} \frac{1 AU^2}{|\mathbf{s}|^2} \frac{\mathbf{s}}{|\mathbf{s}|} \right) \Bigg|_{DYB} + \begin{pmatrix} D_0 & D_c & D_s \\ Y_0 & Y_c & Y_s \\ B_0 & B_c & B_s \end{pmatrix} \begin{pmatrix} 1 \\ \cos(\mu) \\ \sin(\mu) \end{pmatrix} \quad (3.100)$$

Depending on the choice of the reference coordinate system in which the acceleration $\mathbf{a}_{srp}$ is actually to be expressed, the terms in the formula 3.100 must be transformed accordingly. The subscript DYB indicates that the description refers to the DYB-coordinate system defined in 3.87.

As discussed above, instead of estimating only one scaling parameter C_{srp}, one conventionally determines additional sets of empirical acceleration parameters for each of the directions in the DYB-coordinate system to increase the SRP model accuracy. Note that we introduced the orbit angle μ in the above equation 3.100 as also proposed in [71] instead of u as in written in equation 3.89. The figure in 3.8 illustrates the μ angle. In general, one can adjust the complexity of the describing Fourier expansion in a user-defined coordinate system as needed:

$$a_X(\mu) = X_0 + \sum_{n=1}^{n_X} X_{c,n} \cos(n\mu) + X_{s,n} \sin(n\mu) \quad (3.101)$$

which has a similar form as the ECOM2 model presented in equations 3.91 to 3.93, if one refers to the DYB-coordinate frame. In this way, depending on the number of parameters $\{X_0, X_{c,n}, X_{s,n}\}$ for each direction X, one can progressively enhance the level of detail concerning the mapping of the satellite's real geometry. Thus, it is possible to determine customized SRP models for specific types of GNSS-satellites. Depending on the choice of the specific coordinate system, SRP effects can be investigated for their directional properties. Once a coordinate system has been chosen, the parameterization can be used to study a variety of causes that may account for SRP perturbations. However, for pure modeling of SRP, the empirical modeling strategy 3.101 might prove to be insufficient because no distinction by cause is possible. Effects as the Y-bias[18] which originate mainly from TRP effects, are inevitably absorbed by the decomposition 3.101, rendering it difficult to distinguish between different types of radiation pressure (or other) effects. Accurate radiation pressure analyses can therefore only be performed a-posteriori. If $a_X(\mu)$ describes the ECOM2 in the DYB-coordinate system and the satellite is perfectly symmetric, it is expected that due to the symmetry of the description all asymmetric functions can be omitted. Of course, this is only valid under the condition that the attitude is perfect (see also [9]), which will be discussed in more detail for the GALILEO satellites in the next section.

---

[18]The GALILEO satellites have space radiators of different size at the bus panels perpendicular to the Y-axis (see pictures 3.5). This leads to a heat power imbalance between both sides and thus different thermal radiation pressure induced forces.

3.3.3.1 Satellite attitude

In preparation to orbit simulations, it is important to clarify the attitude settings of the GALILEO satellites, since the satellite's orientation predefines the illumination and thus shadowing pattern, which has a profound influence on the amount of SRP generated forces. The effect of attitude on self-shadowing behavior is particularly more pronounced for SRP models with some level of surface complexity and is rather unimportant for simplified satellite models (like a box-wing model). However, in any case, the satellite's attitude at any given time also determines the instantaneous Solar incidence angle and therefore the cross sectional area relative to the Sun. A typical control mode under which GNSS satellites operate is the YS control mode and for further considerations we assume that the GALILEO satellites do not deviate from this nominal attitude mode at any time. The nominal YS attitude control law satisfies two constraints. It ensures that the satellite's main antenna dishes always point nadir while the solar panel axis keeps perpendicular to the satellite-Sun direction during flight, so that the solar generator always faces the Sun and gains maximum power output during flight. These two attitude constraints lead to a continuous rotation of the spacecraft about its pointing axis.

In accordance with the definition from 3.5, the construction of the body-fixed system of the spacecraft is done as follows (see also figure 3.6 for illustration of the axis system):

$$
\begin{aligned}
\mathbf{e}_z &= \frac{\mathbf{r}_S}{|\mathbf{r}_S|} \\
\mathbf{e}_y &= \frac{\mathbf{e}_z \times \mathbf{e}_\odot}{|\mathbf{e}_z \times \mathbf{e}_\odot|} \\
\mathbf{e}_x &= \mathbf{e}_y \times \mathbf{e}_z
\end{aligned}
\tag{3.102}
$$

For the following considerations, it is assumed that the rotation of the solar panels equals 0° when the surface normals face in the direction of the $\boldsymbol{e}_z$ axis of the spacecraft. At local midnight, when the satellite is farthest from the Sun, the $\boldsymbol{e}_y$-axis is aligned in flight direction, while the panels are turned by an angle of β about this axis, which is identical to the Sun's elevation. At the same time, the spacecraft body is oriented such that the $\boldsymbol{e}_z$-direction points nadir. After a quarter revolution about the Earth, the solar panels have continuously rotated by another $90° - \beta$, so as to compensate for the advance in orbital revolution. Thereby, the spacecraft body has yawed by a rotation angle of β around the $\boldsymbol{e}_z$-axis. This ensures that the Sun direction stays perpendicular with respect to the solar panels. At local noon, the solar panels have undergone a rotation of $180° - \beta$ around the $\boldsymbol{e}_y$-axis in total since local midnight, while the spacecraft body finds itself in the same attitude as half an orbital revolution before. The following table 3.2 clarifies the different attitude phases over one orbital revolution. Note, that the initial configuration of the satellite is supposed to characterize the situation at local midnight:

Orbit angle μ	Body e_z-axis rotation	Solar Panel e_y-axis rotation
0°	0°	β
90°	$90° - \beta$	90°
180°	0°	$180° - \beta$
270°	$-90° + \beta$	90°

Table 3.2: Satellite attitude phases throughout an orbital revolution.
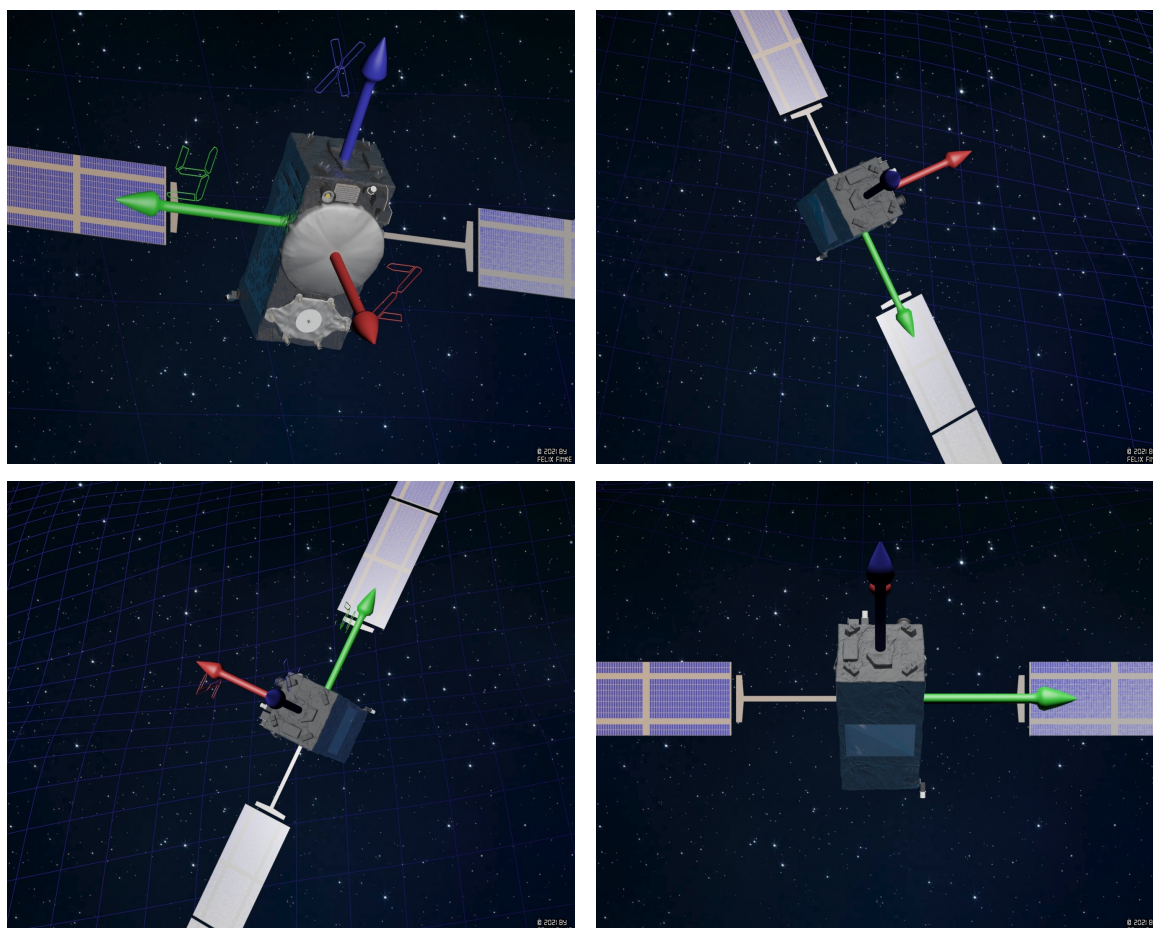
Figure 3.6: Attitude of the GALILEO satellites at different phases throughout the orbit as viewed from the Sun. Beginning from the upper left picture and following in clockwise direction, the pictures show the satellite's orientation with respect to the Sun for $\mu \in \{0°, 90°, 180°, 270°\}$. The definition of the coordinate system is in alignment with the IGS convention (see 3.5)
.

where $\mathbf{e}_z$ is the nadir axis which can be directly computed from the satellite's position vector $\mathbf{r}_S$, $\mathbf{e}_y$ describes the solar panel axis and $\mathbf{e}_x$ completes the right-handed axis system. The spacecraft is thus yawing continuously (compare table 3.2 and figure 3.6) about the $\mathbf{e}_z$ axis, while the surface areas of the satellite which are perpendicular to the $\mathbf{e}_Y$ direction are never illuminated. The β angle mentioned above is the angle between the vector from Earth towards the Sun and the corresponding projection of that vector onto the satellite's orbital plane. It can be computed by the following formula:

$$\beta = \arcsin\left(\cos\Omega_\odot \sin\Omega_{sat} \sin i_{sat} - \sin\Omega_\odot \cos\epsilon_\odot \cos\Omega_{sat} \sin i_{sat} + \sin\Omega_\odot \sin\epsilon_\odot \cos i_{sat}\right)$$

(3.103)

Equation 3.103 results from using the dot product of both the vector pointing from the satellite to the Sun and the satellite's orbit normal unit vector. For further considerations, we express these vectors with respect to the ECI coordinate system. In a first step, the Sun vector $\mathbf{s}_{ECI}$ can be found by a rotation $\mathbf{R_z}(\Omega_\odot)$ of the celestial x-axis about the corresponding z-axis by the Suns right ascension $\Omega_\odot$ and a subsequent rotation $\mathbf{R_x}(\epsilon_\odot)$ about the new x-axis by the Sun's declincation $\epsilon_\odot$. In a similar way, the orbit normal vector $\mathbf{n}_{ECI}$ can be constructed. Therefore, we first perform a rotation $\mathbf{R_z}(\Omega_{sat})$ of the z-axis by the right ascension Ω_{sat} and finally a rotation $\mathbf{R_x}(i_{sat})$ about the celestial x-axis by the inclination i_{sat} is performed to adjust for the latitudinal alignment of the normal vector with respect to the ECI system:

$$\mathbf{s} = \begin{pmatrix} \cos\Omega_\odot & -\sin\Omega_\odot & 0 \\ \sin\Omega_\odot & \cos\Omega_\odot & 0 \\ 0 & 0 & 1 \end{pmatrix} \begin{pmatrix} 1 & 0 & 0 \\ 0 & \cos\epsilon_\odot & -\sin\epsilon_\odot \\ 0 & \sin\epsilon_\odot & \cos\epsilon_\odot \end{pmatrix} \mathbf{e}_{x,ECI}$$

(3.104)

$$\mathbf{n} = \begin{pmatrix} \cos\Omega_{sat} & -\sin\Omega_{sat} & 0 \\ \sin\Omega_{sat} & \cos\Omega_{sat} & 0 \\ 0 & 0 & 1 \end{pmatrix} \begin{pmatrix} 1 & 0 & 0 \\ 0 & \cos i_{sat} & -\sin i_{sat} \\ 0 & \sin i_{sat} & \cos i_{sat} \end{pmatrix} \mathbf{e}_{z,ECI}$$

(3.105)

Since β is defined with respect to the orbital plane, we have to compute $\mathbf{s} \cdot \mathbf{n} = \cos\left(\frac{\pi}{2} - \beta\right)$, leaving us with the expression $\mathbf{s} \cdot \mathbf{n} = \sin(\beta)$ from which equation 3.103 follows.
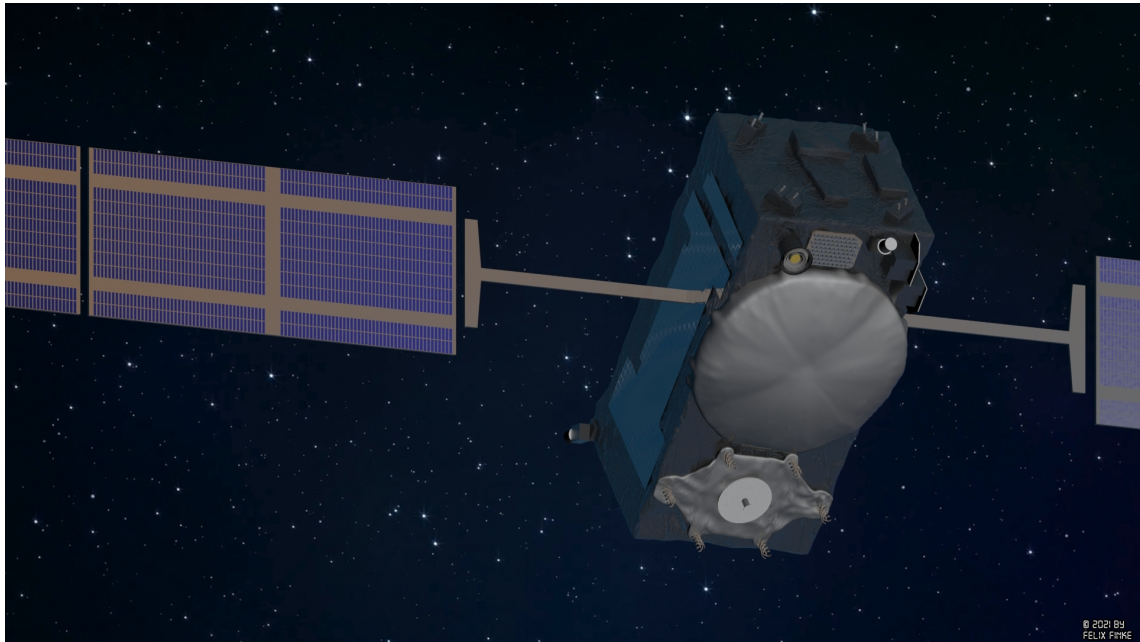
Figure 3.7: Illustration of the exterior structure of a GALILEO satellite unit.
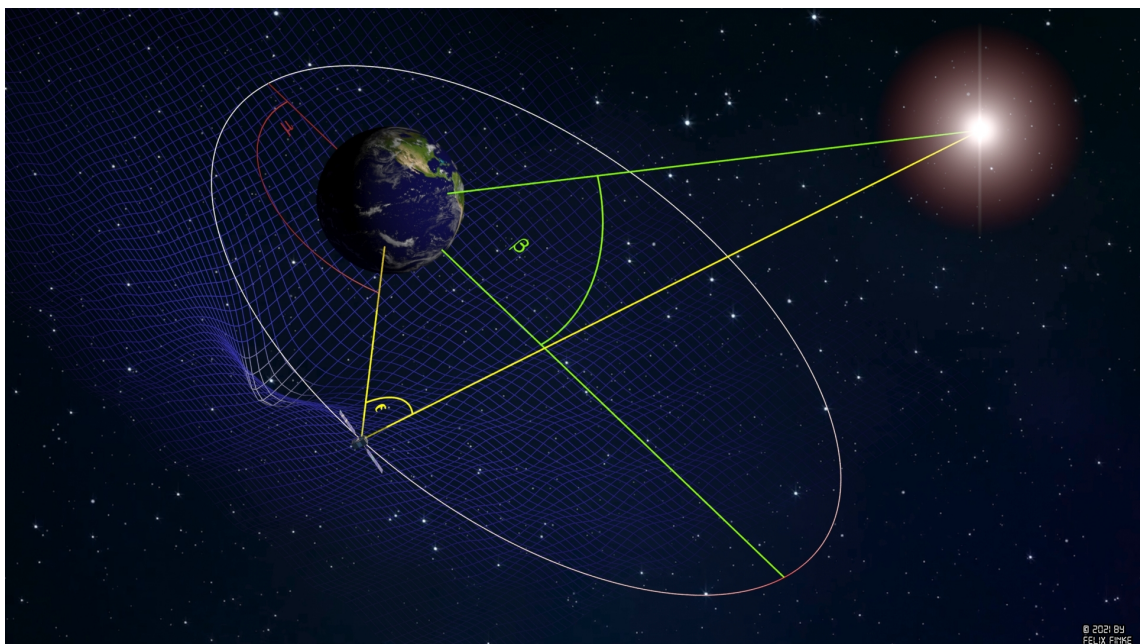
Figure 3.8: Scene of a GALILEO satellite orbiting the Earth in the YS control mode. The orbit has an eccentricity of 0.162^a, therefore its ellipticity is overdrawn in the scene for the sake of clarity. The three angles β, ϵ and μ in this order represent the angle between a line drawn from Earth to the Sun and its corresponding projection onto the orbital plane (β), the angle between a line connecting the satellite and the Earth and a line directed from the satellite to the Sun (ϵ) and finally a measurement μ, which amounts the angular distance between the orbital midnight point with respect to Earth and the satellite's radius beam. Note that β keeps actually constant throughout an orbital revolution. The bigger it is, the more the satellite is to exposed the Sun. If the β angle is small enough, the satellite experience eclipse periods.

---

^{a}https://www.gsc-europa.eu/system-service-status/orbital-and-technical-parameters

3.3.3.2 FE model design

The GALILEO satellites are equipped with large bus system components as solar panels as shown by the illustration 3.7, responsible for the largest proportion of SRP-related perturbations. Payload components and various subsystem modules attached to the satellite body (see image 3.9) contribute to a significant portion of the satellite's total surface area, and depending on their location on the satellite, they generate considerable self-shadowing effects. In particular, these components are also mainly responsible for the specific geometrical asymmetry of the satellite, which is primarily related to the $\pm Z$ surfaces. As a result, solar illumination leads to a more complex perturbation profile as a function of the satellite's orientation and thus attitude, which is discussed in 3.3.3.1. In anticipation of this, we refer to figure 3.22b, which shows a typical acceleration profile under given illumination conditions 3.22a. The possible self-shadowing pattern can be thought of as cross sectional projections of those satellite components installed on the respective satellite face, whereby the projection direction corresponds to the solar irradiance direction. Due to the asymmetric shape of the satellite, the total set of possible projection patterns is highly dependent on the satellite face under consideration and is relatively large for the $+Z$-face. Therefore, the satellite's response to SRP-related perturbations is also expected to vary accordingly over the period of an orbit. In light of the study [71], this motivates to carefully model the asymmetry of the satellite in view of its possible influence on SRP. Since correct modeling of SRP effects obviously requires detailed knowledge of the satellite's shape, it is favorable to choose a modeling approach that enables to incorporate high fidelity design and structural information, which is consistent with the current SRP modeling paradigm, especially for the GALILEO satellites. To cope with that requirement we introduce a Finite Element Model (FEM) consisting of surface elements.
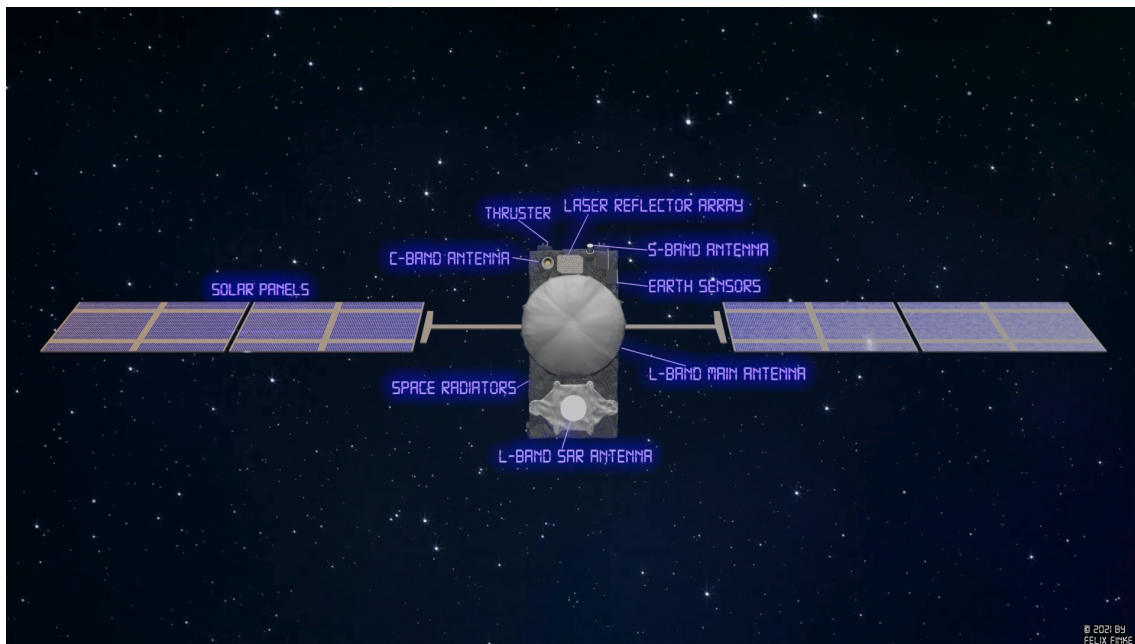
Figure 3.9: Artificial representation of the GALILEO satellite with all its payload and subsystem components attached.

This section is structured such that it guides step-wise through the Finite Element (FE) modeling approach used to obtain a high-fidelity SRP model. The FE model is created in ANSYS Parametric Design Language (APDL).

At a first stage, a full parametric Geometric-Mathematical Model (GMM) is built. The dimensions of the satellite's cubage as well as its outer dimensions in a deployed state with the solar panels unfolded could be directly taken from official sources[19]. The dimensions of other exterior components as antenna payloads could then be derived from dimensionless engineering drawings using a scaling approach. However, for some components as the laser retro-reflector array, official data in the form of geometrical specifications are also available[20]. After the surface geometry is built, single exterior assemblies as payload components are *pre-meshed* to ensure that the mesh fulfills particular requirements in preparation for the final surface meshing procedure. In contrast to automated mesh generation techniques, the APDL mapped meshing approach is used that allows to take over full control of the mesh topology generation process to receive a customized mesh. However, the use of this approach is tied to the requirement that each area must be either triangular or quadrilateral, which generally involves high modeling efforts. After the pre-mesh is generated, material properties are assigned to each satellite component, and finally the model is meshed with 4-node *SURF152* elements and exported in preparation for orbit simulations. For the export we use the interface methods defined by the software HPS (Hybrid Simulation Platform for Space Systems). The HPS is a MATLAB/Simulink-based library of simulation models and tools for the simulation of space GNC systems and consists of more than 90 interconnected modules, which are steadily used and improved throughout the dlr (DLR) and Zentrum für angewandte Raumfahrttechnologie und Mikrogravitationsforschung (ZARM) projects ([97], [63]).

---

[19]A description of the system parameters and key features can be found on:`https://www.ohb-system.de/files/images/mediathek/downloads/190603_OHB-System_Galileo_FOC-Satellites_2019-05.pdf`

[20]An official inquiry for the pre-launch parameters that define the characteristics and position of the laser retro-reflector array on the GALILEO was made: `https://ilrs.gsfc.nasa.gov/docs/2014/GAL201-GAL202_ILRS_SLR_MissionSupportRequestForm_RRAInfo.pdf`. The knowledge of the three-dimensional position of the reflector helped to support laser ranging activities and the resulting measurements allowed to increase the orbit analysis accuracy.
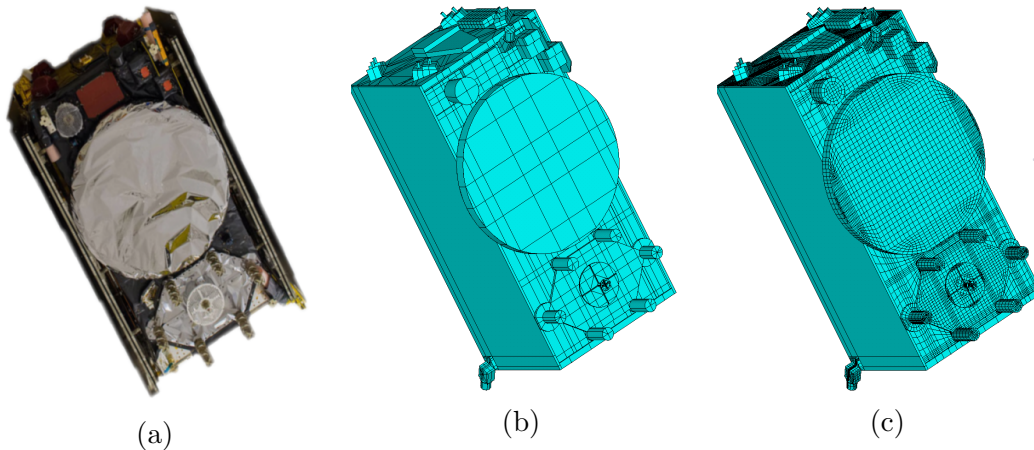
Figure 3.10: Different modeling stages. Based on the real satellites geometry (3.10a), a parametric GMM of the satellite's body is created (3.10b). Subsequently, this surface model is meshed (3.10c). Note that figure 3.10a shows the real satellite with the solar panels folded.

As can be observed from figure 3.9 and 3.10 most of the subsystem components are located on the $+Z$ -face of the satellite. Although most of the exterior surfaces of the satellite are covered with Black Kapton, exceptional shielding in form of Germanium coated Kapton Single-layer Insulations (SLIs) can be found on both the NAVANT and the Search and Rescue Service Antenna (L-Band) (SARANT) antennas, whereas the latter consists of an array of six resonant quadrifilar helices and a short backfire L-Band antenna located at the center of the array which is characterized by a white painted ground plate.

(1: 3.19) The bus panels coated with Black Kapton are each modeled as simple, independent plates, and to account for the full SLI coverage,

(2: 3.14) the NAVANT is represented by a cylindrical surface.

(3: 3.15) The geometrical mapping of the SARANT is somewhat more complex. The grounding plane with the feed system of the SARANT is completely covered with SLI and is therefore represented as a flat, polygonal surface whose outer sides are each extended by a circular plate. The array of the six antennas are modeled as simple cylinders placed on the corners of the polygonal surface. Finally, the short backfire L-Band antenna is implemented as a simple circular plate with a cylinder mounted on top.

(4, 5, 6: 3.14) The majority of the remaining instruments are located above the NAVANT within the +X-hemisphere of the satellite. The systems installed on the +Z-bus panel cast considerable shadowing on the spacecraft bus and main antenna during periods of high Sun elevation θ (see shadow simulation series 3.12 and formula 3.106 in connection with θ): The C-Band horn antenna is thereby represented as a cone-shaped geometry and next to it are the laser retro-reflector array and also the Earth IR sensors, both modeled as cubical shapes.

(7: 3.14) The satellites are each equipped with two S-band antennas, which serve to transmit telemetry and telecommand signals. One is also located on the +Z-bus face, the other is mounted to the clock panel at the edge of the +Y-face and is oriented in the -X-direction (see figure 3.10 and 3.17).

(8: 3.16) At the top of the satellite, there is a pair of thrusters positioned along each corner of the +X-panel. (9: 3.16) In addition, solar sensors are also mounted onto the spacecraft bus. The entire panel is covered with Multi-layer Insulation (MLI). Unlike the instruments on the +Z-bus panel, these components generate shadowing mainly when the Sun elevation angle is rather low.

(10: 3.17) Depending on the satellite's attitude phase, the -Z-surface is increasingly illuminated, most notably if $\mu = 180°$ (see attitude phases visualized by 3.6). This leads to an increased irradiation of the space radiator installed in that area.

The solar panels were not included in the FEM because their surface area contributions to SRP are constant over all orbit phases due to the special YS attitude mode (see table 3.2 and figure 3.19). The space radiators at the long sides, perpendicular to the spacecrafts solar panel axis, were also not covered by the FEM, because they do not contribute to SRP for the same reason.

(a)   (b)
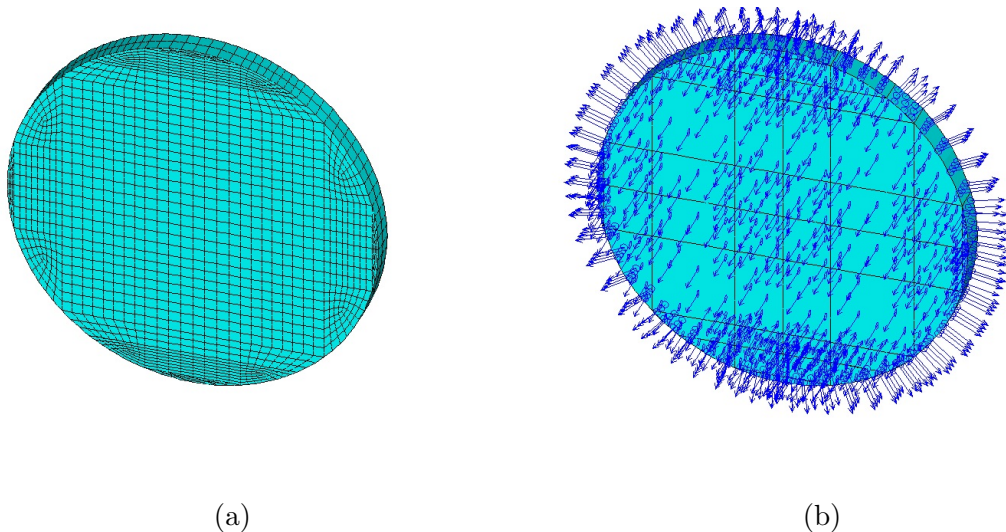
Figure 3.11: Before the meshing process, it must be ensured that the surface normals face outwards. This serves as a criterion for the determination of the correct lighting conditions.
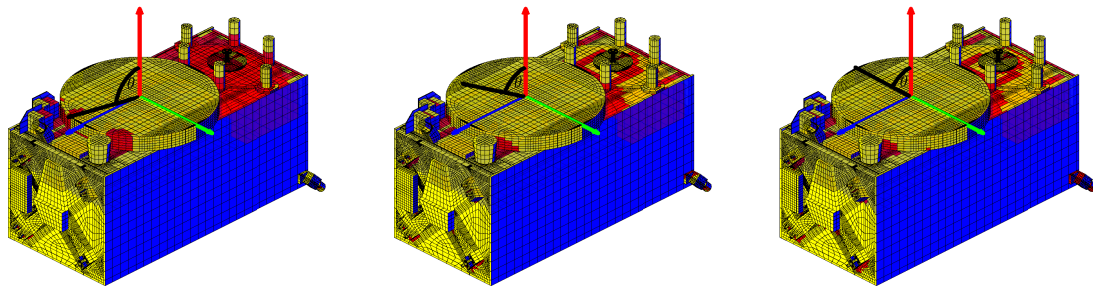
(a) $\theta = 80°$ (b) $\theta = 60°$ (c) $\theta = 50°$
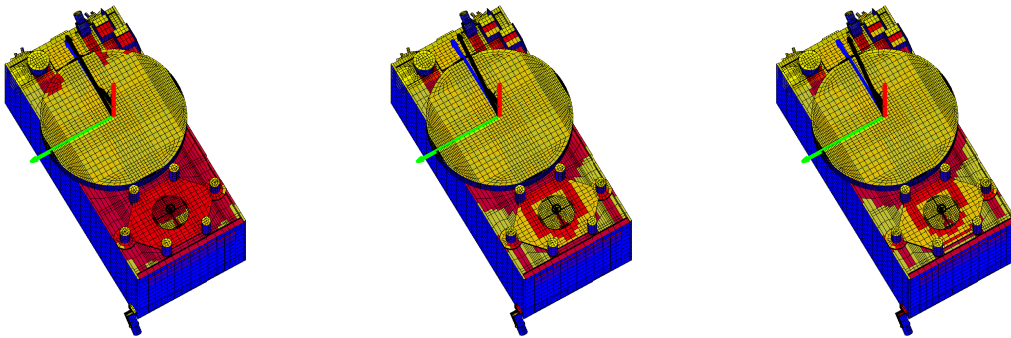
(d) $\theta = 80°$ (e) $\theta = 60°$ (f) $\theta = 50°$

Figure 3.12: GALILEO satellite FE model with self-shadowing profiles generated for different illumination conditions. θ is the Sun elevation angle.

When creating a surface model, it occasionally happens that individual areas are oriented incorrectly, so that they have to be revised in a preprocessing step before meshing. An algorithm was written that automatically keeps track of surface areas of the GMM that needs to be reoriented. After the final meshing operation, the surface elements automatically inherit the normal directions of the underlying areas. ANSYS provides the option to graphically check the normal vectors for each surface element individually, which of course becomes cumbersome, if the number of elements is large. The reason for this effort is to ensure the correct orientation of the surface elements as an important prerequisite for the accurate determination of the self-shadowing profile under given illumination conditions. In this context, correct means that all normal vectors have to point outwards.
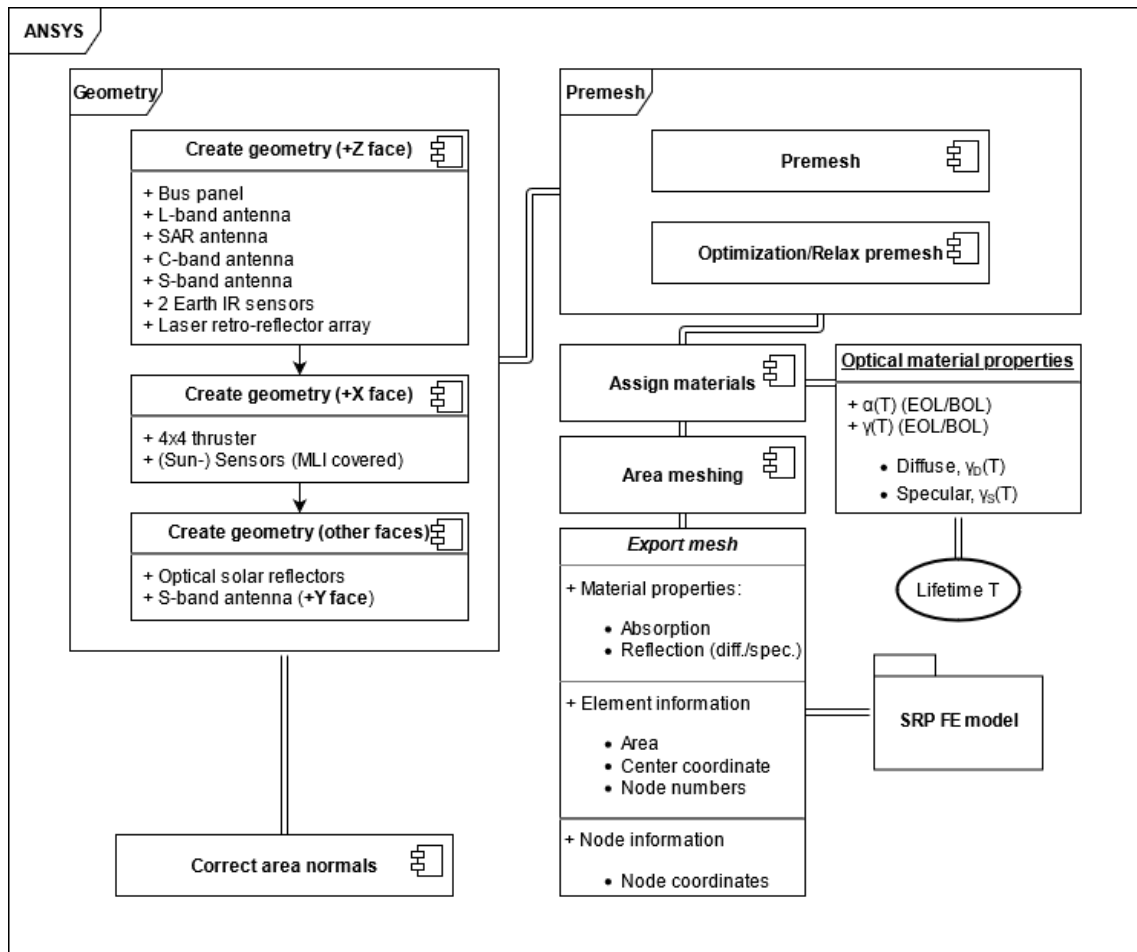
Figure 3.13: SRP modeling approach.

Figure 3.14: NAVANT and other +Z-face components.

Figure 3.15: SARANT placed on +Z-face.
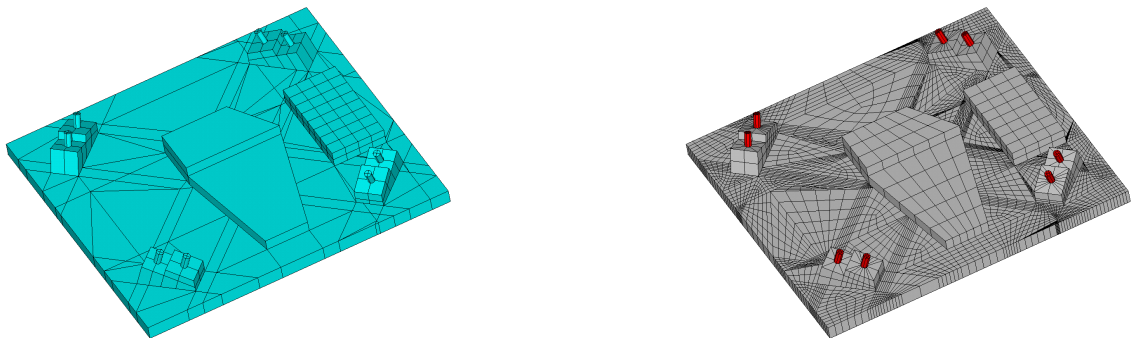
Figure 3.16: MLI-covered +X-face with thrusters and Sun sensors.
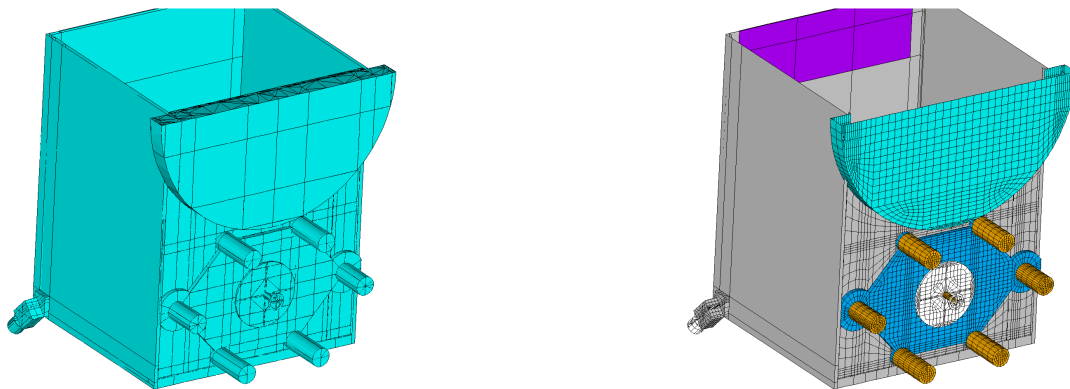
Figure 3.17: View on the -X hemisphere of the GALILEO satellite.

Throughout the modeling process, satellite system components are attached and added to the GMM. Depending on the shape of the modeled geometry, the resulting pre-mesh usually becomes more and more complex. If a new component is added to the model, it has to be integrated into the existing overall geometry, such that the involved components share common boundaries. Since the integration is realized with boolean operations, the addition of further model parts potentially introduce new geometrical entities and in particular new areas and associated lines and vertices to the existing GMM. The example shown in figure 3.18 illustrates a detailed view onto the modeled +X-face of the GALILEO satellite, which is extended by a new component (3.18a). The overlap of both the existing and new components produce intersections and hence a more complicated geometry in the underlying solid model. An algorithm was written in APDL that automatically detects new triangular areas in the vicinity of the new boundary line produced by intersection operations (3.18b). If any of the side lengths of such a new triangular area undershoots a certain limit, it is removed from the geometrical model. The corresponding vertex of that area, which is lying either inside our outside the projection area of the new component, is thereby moved and merged into the nearest vertex located on the boundary line (3.18c). Figure 3.18d focuses a particular area of interest demonstrating the outcome of this optimization process. The resulting optimized pre-mesh is then ready for the actual meshing operation (3.18d). The aforementioned procedure is requisite to remove unnecessary areas, whose absolute size is unfavorable for the subsequent meshing step. The general meshing procedure of a single surface area depends on the element division number, which is an edge size control parameter. It predefines and controls the number divisions applied to a specific line element as part of the boundary of an area element. If the underlying surface area is already very small, the edge division operation produces even smaller elements and this directly affects the mesh of adjacent area elements. It is therefore appropriate to choose a certain lower limit for the minimum edge length of an element. As we will see later, the element's edge size is also an important control parameter to tune the quality of the simulated cast shadows by creating a mesh that is as homogeneous as possible.

(a) (b) (c) (d)
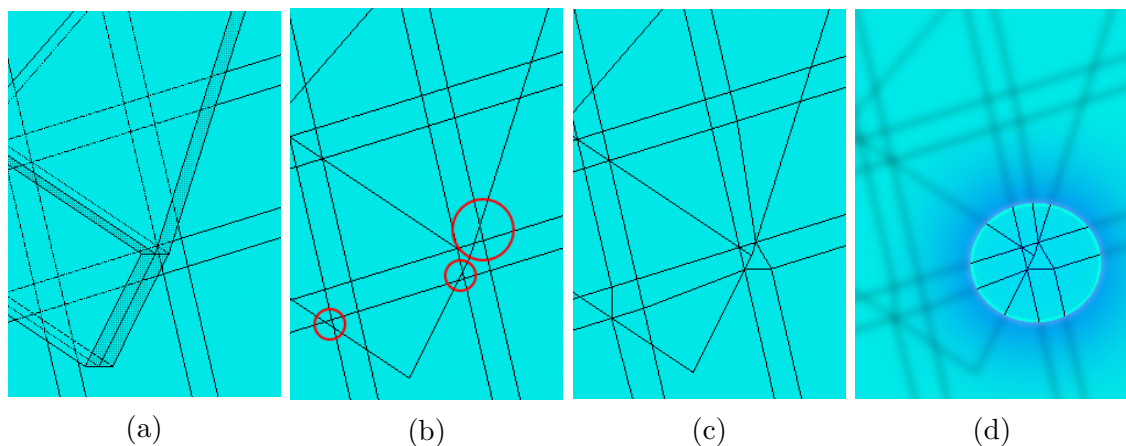
Figure 3.18: FEM pre-mesh optimization process using the example of the propulsion/X -panel modeling.
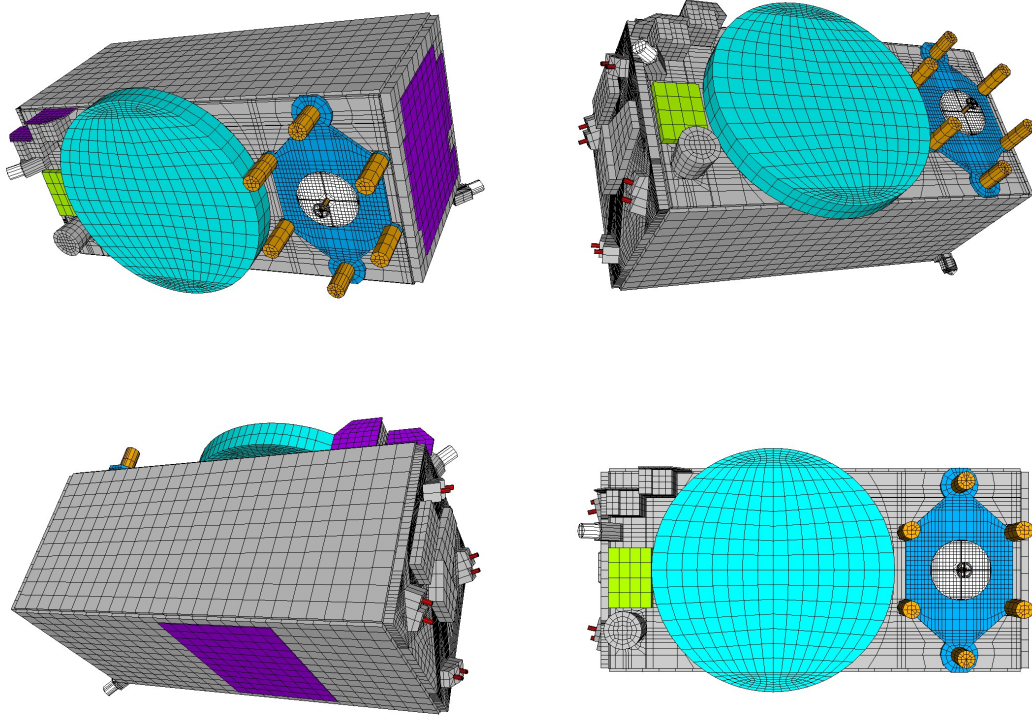
Figure 3.19: GALILEO satellite FE surface model of the body from several perspectives. Different optical material properties assigned to individual parts of the satellite are illustrated by different colors (see table 3.3 for material property information).

We now consider the element-wise calculation of the SRP acceleration. Therefore we extend the formula 3.99 for the finite element case as follows:

$$\mathbf{a}_{srp,n} = -\eta \left(C_{srp} \frac{P_\odot}{c} \frac{1}{m_S} \frac{1AU^2}{|\mathbf{s}|^2} \frac{\mathbf{s}}{|\mathbf{s}|} \right)$$
$$\sum_{n=1}^{N} \chi_n \left[(1 - \gamma_{s,n}) \mathbf{s} + 2 \left(\gamma_{s,n} \cos \theta_n + \frac{1}{3} \gamma_{d,n} \right) \mathbf{n} \right] \cos \theta_n A_n \quad (3.106)$$

Each surface element A_n has an individual orientation with respect to the Sun. This is defined by θ_n, which characterizes the angle between the element's surface normal and the irradiation direction $\mathbf{s}$. In addition, A_n is associated with certain material parameters that determine the radiation exchange behavior: γ_s and γ_d constitute the specular and diffuse reflection parameters. Table 3.3 comprises all optical material properties, which are assigned to component-specific surface collections throughout the FE modeling process. In addition, χ_n accounts for (1) Sun visibility and (2) self-shadowing due to occlusion by other surface elements and is either 1 or 0. (1) For each given satellite-Sun orientation and corresponding Sun incidence angle θ_n it has to be checked whether the respective element A_n is potentially illuminated by the Sun or not. (2) If this is true, it is necessary to check whether the direct line-of-sight

to the Sun from the element's perspective is free or obstructed by other elements. Therefore, depending on the complexity of the FE model, conservatively speaking the computational complexity increases with N^2, so it is reasonable to predetermine self-shadowing for each satellite-Sun configuration and store the information in a lookup table χ to minimize the total computational time during an orbit simulation. A shadowing pattern produced by the FE model is shown in the figures 3.20 and 3.13. For the same reason, lookup tables for the normalized resultant SRP forces and corresponding torques[21] are also created in dependence of χ after exporting the FE model following the procedure presented in 3.13. Subsequently, at any time during orbit simulation, the correct resultant SRP acceleration $\mathbf{a}_{srp}$ for any satellite-Sun orientation can then be derived from the respective normalized force table and scaled in dependence of the current satellite-Sun distance.

---

[21]Actually, torques are rather irrelevant, since we assume a perfect YS attitude control mode.
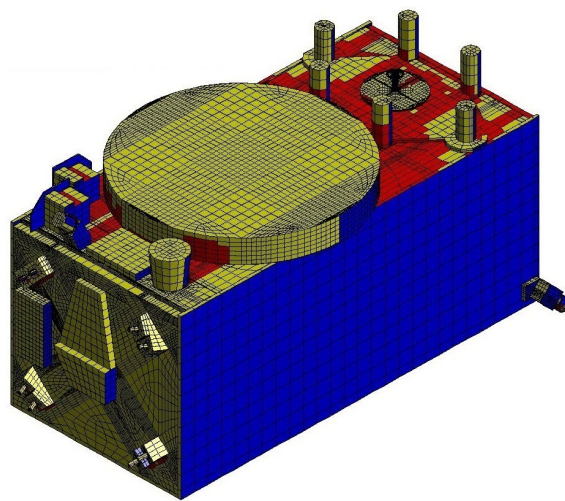
Figure 3.20: GALILEO satellite FE model with self-shadowing profile. The Sun incidence angle is chosen as 70°. The surface elements shown in yellow are directly illuminated, blue are the elements that are not sunlit, while red represents shaded areas.

We briefly outline the algorithm used to find the correct self-shadowing profile for arbitrary illumination directions. This requires all geometrical information such as element and associated node coordinates (see also figure 3.13), which are exported as a result from the modeling process. On this basis, we first discriminate which elements face the Sun and which have their backsides facing towards it. In this way, the total number of element candidates can be reduced to a minimum, for which it is still necessary to check in the following whether they are hidden by other elements or not. Here, the benefit of the surface normal correction procedure becomes apparent. Since it was ensured that all surface normals correctly refer to the outer surfaces of the FE model, it is now possible to properly determine the visibility of an element's *outer face* relative to the Sun. To evaluate the self-shadowing, a ray cast procedure is performed for each pair of elements. Hereinafter, we would like to stick to the concept as presented in the thesis [88] on page 40 ff. The initial spawn point of a ray is identified as the center of one element and its direction is given by its inverse surface normal vector. To check if the ray intersects another surface element, it must be determined whether the intersection point lies within its surface or not. To this end, we divide the quadrilateral element into two triangles and check the intersection condition using barycentric coordinates in dependence of the triangle's element nodes[22]. The set of all points $\mathbf{p}$ that lie inside a triangle forming its convex hull is given by:

$$\mathbf{p} = \mathbf{p}_0 + s\mathbf{p}_1 + t\mathbf{p}_2 \qquad (3.107)$$

under the condition that $s, t > 0 \ \wedge \ s + t < 1$. The vector $\mathbf{p}_0$ defines the origin node of a triangle and $\mathbf{p}_1$ and $\mathbf{p}_2$ point from $\mathbf{p}_0$ to the other element nodes. The parameters s and t can be computed from:

$$s = \frac{\mathbf{p} \times \mathbf{p}_2 - \mathbf{p}_0 \times \mathbf{p}_2}{\mathbf{p}_1 \times \mathbf{p}_2} \qquad (3.108)$$

$$t = \frac{\mathbf{p} \times \mathbf{p}_1 - \mathbf{p}_0 \times \mathbf{p}_1}{\mathbf{p}_1 \times \mathbf{p}_2} \qquad (3.109)$$

To achieve an appropriate shading resolution, several conditions must be met. (1) The element size (element's edge size) must be chosen appropriately[23], and (2) the aspect ratio must be as uniform as possible, otherwise the shading errors will be larger. Suppose we consider the shadow cast by a square surface element of size A_n on a uniform and flat arrangement of other square elements, then the maximum projection error that arises from the presented algorithm is $A_n/2$. If the element casting the shadow is larger than the element onto which the shadow is projected, the area size of the projection will be too small and vice versa. In order to find the optimal mesh settings and thus the appropriate element size, we perform an area convergence study. For this reason, an illumination scenario is set up in which the sun is very low, which should be reflected by an elevation angle of $\theta = 70°$ (this

---

[22]It should be noted that all geometric entities, such as surface element node coordinates, of the FE model are interpreted in a global reference frame aligned with the Cartesian system represented in 3.5 or 3.12.

[23]The element size must be chosen so that the shadow projection or contours of the FE model's small scale structures can still be mapped by the surface elements that receive the shadow.

corresponds to the scenario depicted in 3.20) with respect to the satellite's Z-axis and we choose this larger angle to evoke a relatively large shadow. The objective is now to evaluate changes in the total illuminated area as a function of the applied element size. This size is gradually reduced by increasing the number of element divisions, resulting in a finer mesh resolution. It is expected that the accuracy of shadow mapping cannot be further improved once a certain element division number N is reached. Eventually, this is demonstrated by figure 3.21 and confirms that the shadow does not become more 'crisp' beyond $N = 3$. For $N > 3$, the curve fluctuates by a negligible amount within a convergence radius that describes surface area deviations strictly smaller than 20cm^2.
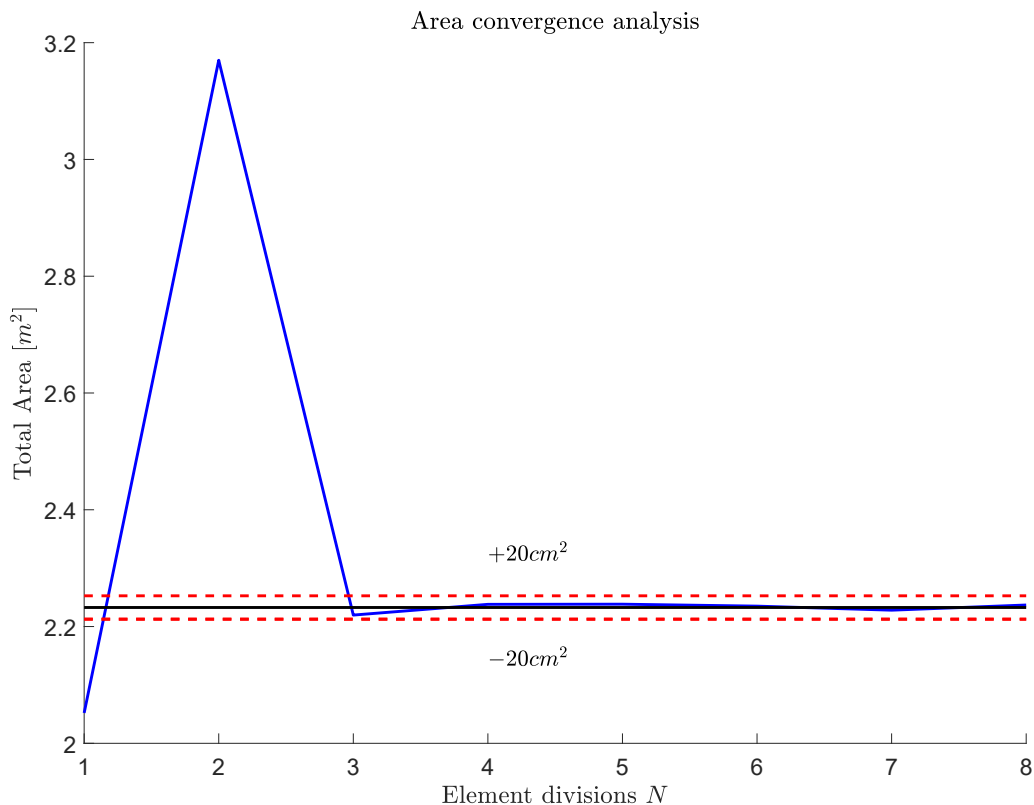
Figure 3.21: Surface area convergence diagram. If the element division number exceeds $N > 3$, the value describing the total illuminated area converges, which is equivalent to saying that no better resolution of self-shadowing is possible. The red lines limit the convergence radius and the black line describes the average value of all determined values without the two outliers and also represents the center for the convergence environment.

In [125], the reader finds a derivation of the single terms in the expression given in squared brackets under the sum defined in equation 3.106. To describe SRP, one basically differentiates between three momentum exchange mechanisms between electromagnetic radiation and surfaces: Absorption, specular and diffuse reflection, while transmission effects are regarded negligible and not taken into account in this study. Incoming energy thus distributed according to the relation:

$$\alpha + \gamma_S + \gamma_D = 1 \tag{3.110}$$

For a surface element A_n, which absorbs energy from incoming solar radiation, the net force $F_{\alpha,n}$ due to the corresponding momentum transfer can be written as:

$$F_{\alpha,n} = -\alpha_n \frac{P_\odot}{c} \cos\theta_n \mathbf{s} A_n \tag{3.111}$$

where α denotes the absorption coefficient of the material attributed to the surface element and the term $\cos\theta_n = \mathbf{n} \cdot \mathbf{s}$ features the view factor of the surface element. For specular reflected radiation, one finds:

$$F_{\gamma_s,n} = -2\gamma_{s,n} \frac{P_\odot}{c} \cos^2\theta_n \mathbf{n} A_n \tag{3.112}$$

The above expression 3.112 accounts for two separate force contributions experienced by the surface element. One is caused by the normal force component of the incident radiation related to the $\mathbf{s}$ direction and the second one is the normal force component emerging from the radiation reflected in $-\mathbf{s} + 2\mathbf{n}\cos\theta_n$ direction. For the effect of diffusely reflected radiation, we decompose the resulting force into two components. One component accounts for a force which acts in the negative $\mathbf{s}$ direction, such as defined by equation 3.111. The other force component results from an average momentum transfer due to immediate diffuse re-emission of that absorbed radiation in all directions. The latter, pure diffuse component is computed by evaluating the integral of the governing radiation distribution function over an entire hemisphere. The according integral is parameterized by $\phi \in [0, \ 2\pi]$ and $\beta \in \left[0, \ \frac{\pi}{2}\right]$ and gives us:

$$F_{\gamma_d,n} = - \gamma_{d,n} \frac{P_\odot}{c} \left(\frac{1}{2\pi} \int_{\phi=0}^{2\pi} \int_{\beta=0}^{\frac{\pi}{2}} 2 f_{diff}(\beta, \ \phi) \cos\beta \sin\beta d\beta d\phi \right) \cos\theta_n \mathbf{n} A_n \tag{3.113}$$

$$F_{\gamma_d,n} = - \gamma_{d,n} \frac{P_\odot}{c} \left(\frac{1}{2\pi} \int_{\phi=0}^{2\pi} \int_{\beta=0}^{\frac{\pi}{2}} \cos\beta \sin 2\beta d\beta d\phi \right) \cos\theta_n \mathbf{n} A_n \tag{3.114}$$

In the above equation 3.113, the distribution function $f_{diff}(\beta, \ \phi)$ initially describes a generic type of re-emission pattern, which depends on the emission direction via β and ϕ and is substituted by Lambert's cosine law $f_{diff}(\beta, \ \phi) = \cos\beta$ in the subsequent step 3.114. It states that an ideal diffuse reflector emits radiation in an axially symmetric fashion, whereas the radiant intensity is proportional to $\cos\beta$. This can be also interpreted as a reduction of the solid angle as viewed from the perspective of an observer from a specific angle β onto the radiating surface. The expression $2\cos\beta \sin\beta d\phi$ under the integral in equation 3.113 gives the base length

of a differential surface area element in azimuth direction at the elevation angle β, whereas $d\beta$ is the side length of the other edge. The bracket in equation 3.114 results in a contribution of 2/3 such that the sum of both force components can be finally written as:

$$F_{\gamma_{d,n}} = -\gamma_{d,n} \frac{P_\odot}{c} \left(\cos\theta_n \mathbf{s} + \frac{2}{3} \cos\theta_n \mathbf{n} \right) A_n \tag{3.115}$$

Summing up the terms 3.111, 3.112 and 3.115 and making use of the relation 3.110 gives us the requested relation in equation 3.106.

(a)   (b)
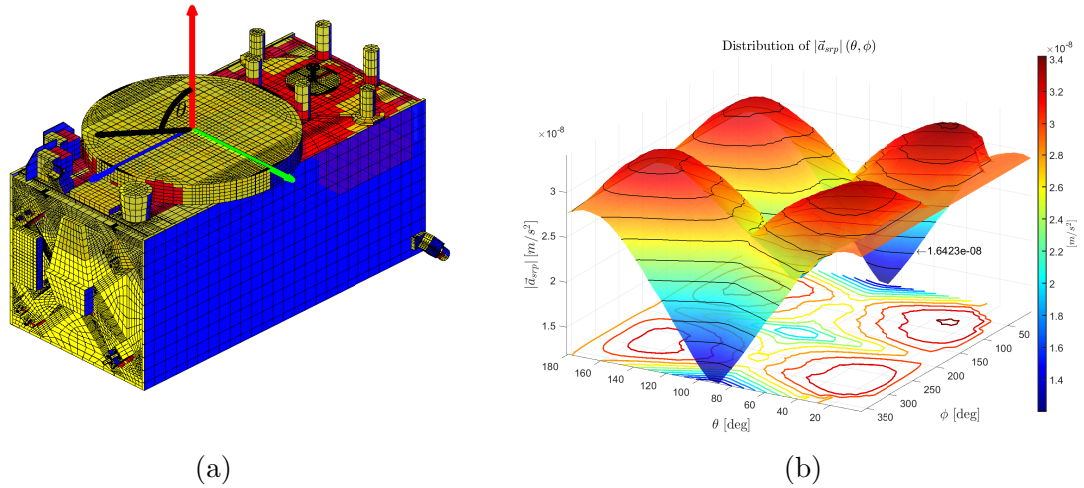
Figure 3.22: The right graph 3.22b shows the SRP acceleration as the vector 2-norm $|\vec{a}_{srp}|$ with respect to spherical coordinates in the range $0 \leq \theta \leq 180\,[deg]$ and $0 \leq \phi \leq 360\,[deg]$. Picture 3.22a illustrates a simulated scenario where the Sun direction (black arrow) forms an incidence angle of $\theta = 70°$ with the Z-axis (red arrow). The coordinate system is in alignment with the IGS frame as compared to 3.5. In the surface plot 3.22b the float number indicates the value calculated as a result of the illumination scenario.

In a next step, material degradation modeling will be discussed and subsequently, the effect on the SRP perturbation force profile will be studied. The goal is to create a modeling tool to determine the time-varying behavior of optical material parameters that must be assigned to the respective surface elements A_n during the FE modeling process prior to mesh generation according to 3.13. There are various causes of degradation. The reader will find a more detailed treatment of this topic in the respective literature [111], [82], [44]. The latter also reports on degradation rates of common thermal finishes. Since the satellites are destined to resist space exposure for at least twelve years in a MEO, a significant change in surface material properties is to be expected. As introduced earlier, incident radiation can interact with surfaces via different mechanisms and the relation between their different contributions is decribed by equation 3.110. As a consequence, assuming constant or increasing absorption properties, the reflectivity values of the surfaces are expected to diverge over time in that the ability of specular reflection decreases. An elaborate material degradation study has been carried out for the spacecraft MICROSCOPE, see [63]. The study shows that changing material parameters, and in particular the degradation of solar panel surfaces and the associated changes in optical material properties, has a noticeable impact on the dynamics of SRP-related effects. This demonstrates the prominence of degradation phenomena in SRP modeling and motivates a further investigation of these effects as they pertain the GALILEO satellites. Especially for the GALILEO satellites, technical discussions with [75] revealed that the degradation of the solar panel surfaces is expected to be responsible for a significant loss in power generation during the End Of Life (EOL) phase. Consequently, as the absorptivity of the panels increase, the SRP induced force also gets higher according to equation 3.111.

From the perspective of thermal control, the inevitable degradation of spacecraft coatings over a satellite's life time turns out to be strongly unfavorable. Depending on the life cycle stage, overheating becomes increasingly problematic due to changes in absorptivity, so that the thermal control system must be designed to handle excessive heat generation during the EOL phase. To overcome these issues one typically uses radiators, which are appropriately sized. Since the radiators are thus over-dimensioned for the performance needs during the satellite's Begin Of Life (BOL) phase, additional heat must be produced to maintain a desired temperature level. One can thus deduce from the point of view of thermal control design that changes in surface material properties definitely produce issues that also impact the course of SRP induced perturbations.

The exterior surfaces of a satellite are continuously affected by (UV) radiation, free particles or contaminants that cause optical surface material degradation, which is typically accompanied with an increase in absorptivity and a decrease in specular reflectivity. For empirical reasons, we expect a logarithmic time evolution of the absorptivity, which only depends on the EOL and BOL values. These are enlisted in the table 3.3. For the description of the time dependent behavior of the absorptivity α, we define:

$$\frac{d\alpha}{dt} = \frac{p}{1+t} \tag{3.116}$$

where p is a specific degradation rate factor that is to be determined for each material. With the initial value for $\alpha = \alpha_{BOL}$, 3.116 can be solved as follows:

$$\alpha(t) = \alpha_{BOL} + p \cdot \ln(1 + t) \tag{3.117}$$

Finally, we can solve for the factor p by setting $\alpha = \alpha_{EOL}$ and t to the specific total life time t_{EOL}:

$$p = \frac{\alpha_{EOL} - \alpha_{BOL}}{\ln(1 + t)} \tag{3.118}$$

With this, the absorptivity for any epoch can now be estimated with the help of relation 3.117.

For the estimation of both the specular and diffuse reflectivity, we follow an analog scheme. We assume that for any material, the effect of diffuse reflection becomes more pronounced over time relative to the effect of specular reflection. An exponential degradation law is adopted to describe this relationship:

$$\beta(t) = \frac{\gamma_S(t)}{\gamma_D(t)} \exp^{-\lambda(t)} \tag{3.119}$$

Here the specular and diffuse reflection coefficients are denoted as γ_S and γ_D, the λ factor is used to adjust the rate of change of $\beta(t)$ and could reflect the characteristic resistance against relative changes of the respective material. Applying the relation 3.110 to the aforementioned equation, one yields:

$$\gamma_S(t) = \frac{\beta(t)(1 - \alpha)}{1 + \beta(t)} \tag{3.120}$$

$$\gamma_D(t) = \frac{(1 - \alpha)}{1 + \beta(t)} \tag{3.121}$$

As mentioned above, there are various effects that lead to material degradation and thus to an increase in absorption properties. In the following, we give a brief overview of the prevailing mechanisms. Regarding the consequences of UV irradiation, one distinguishes between two different phenomena. As UV photons interact with the spacecraft's surface, they can cause charge separation in crystal lattices, which in turn produces color defects. The electrons of the so-called *F-centers*, which consist of vacancies in the crystal lattice, absorb electromagnetic radiation in the visible spectrum, which leads to discoloration of the material at the respective location. Another sort of process induced by UV light absorption involves chemical reactions through which bonds of polymer chains dissociate, which can be observed at thermal control surfaces such as (coated) polyimide films, often constituting a spacecraft's outer protective cover (e.g. Kapton-based materials). This produces reactive species, which can redeposit on neighboring surfaces by recombination with other molecules to generate new stable chemical compounds. In addition to UV light exposure, the GALILEO satellites are affected by high-energetic particles and radiation. The particle populations and radiation levels present in higher orbits as

the MEO or Geosynchronous Orbit (GSO) are known to be more severe than it is the case on altitude levels of Low Earth Orbit (LEO) orbits. This is owed to the radiation belts that extend to orbits where spacecrafts like GNSS satellites typically reside, and consequently they are more affected by high-energetic particles and radiation. As for the effects on surfaces, this can cause micro-damages by initiating chemical reactions through ionization. New formations of polymer molecules are potentially created as a result, similar to the effect of UV radiation.

According to the BOL and EOL values in table 3.3, the top layer of the Black Kapton blanket exhibit a slow degradation rate and associated change in reflective material properties. This material is hence exptected to outlast the lifecycle of most of the other surface coatings covering a spacecraft. As the surfaces of outer thermal control coatings as MLI are typically wrinkled, this also suggests to reason that the amount of diffusely reflected radiation is at least as high as the amount of specular reflected radiation, but also rather unaffected over time. This would translate to a value of β of nearly 1 and a λ-factor of almost 0.

In fact, as can be viewed from picture 3.23d in the figure 3.23 below, the absorption parameter for the MLI behave relatively constant, whereas for white paint, an increasing trend can be observed over time. The SARANT and NAVANT blankets also exhibit a similar behavior regarding the absorption properties. It should be noted that for most of the time in orbit, only three of the bus panels ($+Z - Z$ and $+X$-faces) of the GALILEO satellites are illuminated due to the special attitude mode (see also 3.6). This leads to higher loads of UV light exposure and thus an increased surface degradation impact, especially on larger surface structures, which are visualized in 3.8 and 3.9. As a consequence, under ideal conditions, the illumination intensity tends to zero on the other satellite faces. Especially, the surface properties of three different materials play a crucial role. The MLI and two slightly different Kapton-Germanium single layer insulation blankets, which protect the spacecraft's antennas from direct radiation exposure by significantly reducing its solar absorptance and infrared emittance. The antenna modules' blankets approximately take up $\approx 70\%$ of the total satellite's $+Z$-face. The upper side of the grounding plane of the SARANT is completely covered by a Kapton-Germanium SLI, with the reflective Germanium film facing space. The NAVANT is the satellite's navigation antenna and its Sun shield also consists of a Kapton-Germanium SLI. Its according BOL absorption parameter is just 70% of that of the SARANT and the corresponding reflection parameters γ_S and γ_D are larger by 50% and 30%, respectively. Unlike the behavior of MLI, we expect a faster change in surface conditions and chose a λ-factor around 0.5 due to the special illumination conditions.
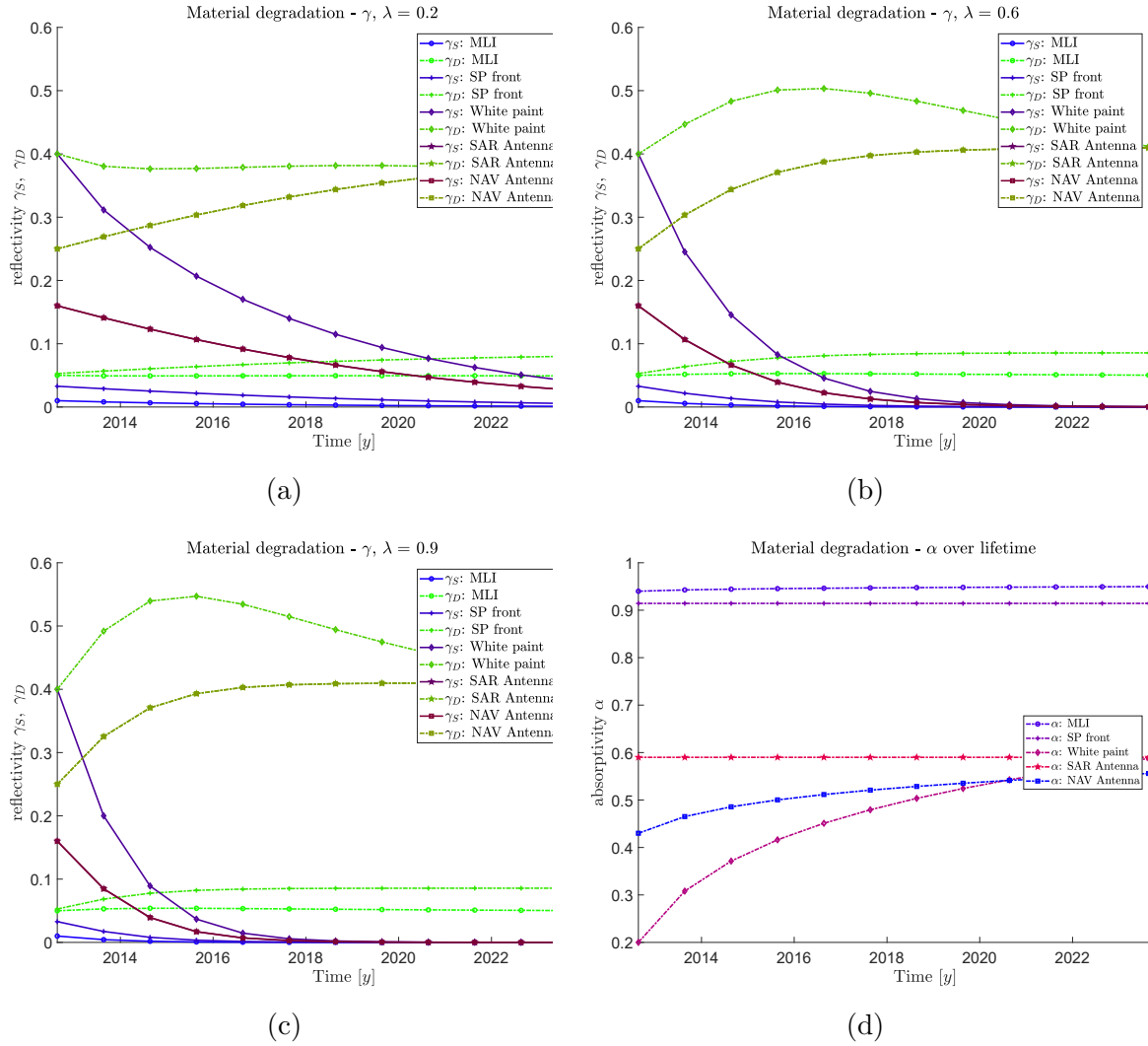
Figure 3.23: Parameter time series analysis for selected surface material parameters in dependence of λ.

The pictures in 3.23a to 3.23c show the evolution of selected material parameters in dependence of the scaling factor λ. One can see that with small values of λ, slow degradation can be modeled and this applies vice versa to large values. Finally the pictures in 3.24 describe the SRP generated acceleration profile and its temporal variations. The initial BOL distribution is shown on the right and the contour diagrams on the left show the effect of progressive surface material degradation due to space environment exposure. The changes after three and ten years, respectively, are shown relative to the BOL distribution.
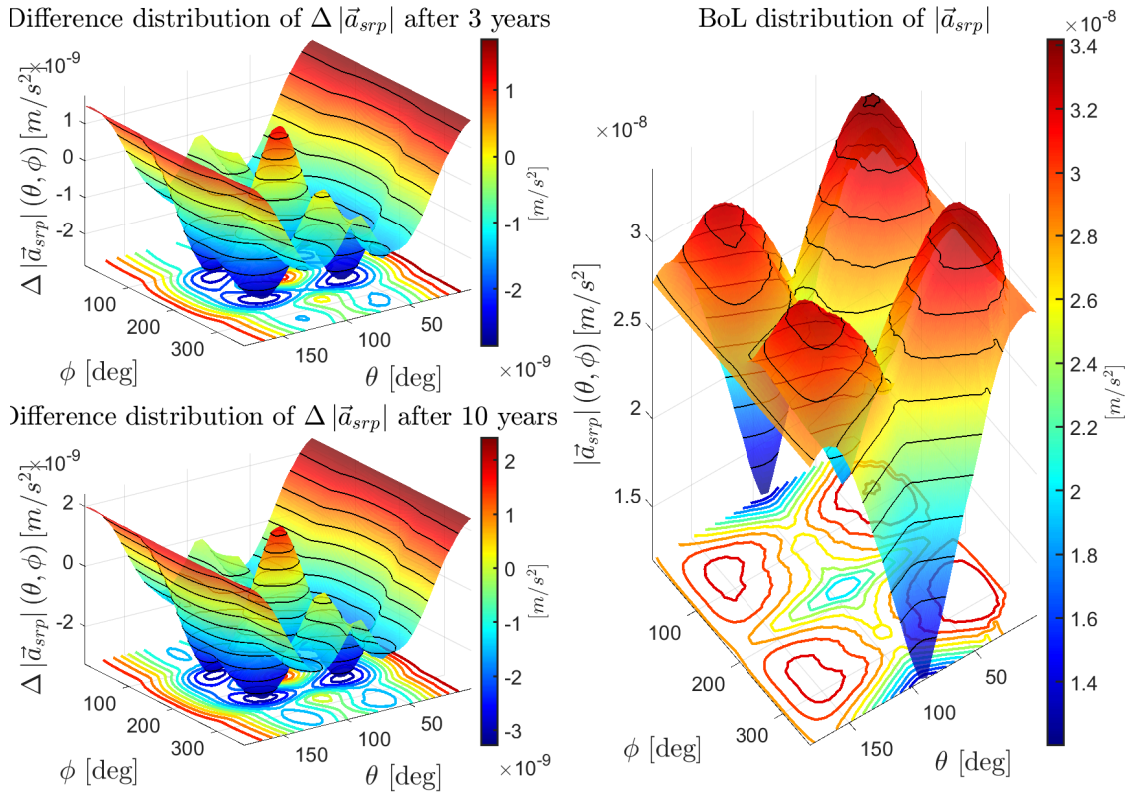
Figure 3.24: The right graph shows the initial SRP acceleration profile of the spacecraft's body at BOL (compare figure 3.22b). The left side represents the profile changes $\Delta \vec{a}_{srp}$ after three and ten years relative to the initial BOL distribution.

Material parameter	α_{BOL}	α_{EOL}	$\gamma_{s,BOL}$	$\gamma_{s,EOL}$	$\gamma_{d,BOL}$	$\gamma_{d,BOL}$	ϵ	Color (FE-model)
Black Kapton (MLI BP Z306)	0.94	0.95	0.01	0.01	0.05	0.04	0.89	grey
GE-Kapton (SLI NA-VANT)	0.43	0.56	0.24	0.15	0.33	0.29	0.69	light-blue
GE-Kapton (SLI SARANT)	0.59	0.59	0.16	0.11	0.25	0.30	0.80	blue
Solar panel (front)	0.92	0.92	0.03	0.03	0.05	0.05	0.80	n.A.
Radiator	0.08	0.23	0.72	0.62	0.20	0.15	0.80	n.A.
Alodine (1200S)	0.43	0.43	0.47	0.47	0.10	0.10	0.12	orange
White Paint (SG 121 FD)	0.20	0.60	0.40	0.10	0.40	0.30	0.88	white
Fused silica	0.12	0.17	0.85	0.8	0.03	0.03	0.24	green

Table 3.3: Table of optical material parameters including the emission coefficients ϵ of any materials assigned to the FEM. For better identification purposes, the different material domains of the FEM in figure 3.19 have color indications which can be cross-referenced with the information in this table

3.4   SRP parameter estimation strategy

We pursue the goal to provide a performance study that compares empirical SRP parameters with respect to SRP models of different fidelity levels. These force parameters appear in the satellite equations of motion 3.60 as n_p independent coefficients $\mathbf{p} = \{p_1, \ldots, p_n\}$ in the acceleration term, $\mathbf{a}_{srp}$. In the special case of a nine-parameter ECOM, the expression $\mathbf{a}_{srp}$ is extended by the second term on the rhs in formula 3.100. 3.60 can be rewritten as a system of six first order differential equations for the satellite states $\mathbf{y}(t) = (\mathbf{r}(t), \mathbf{v}(t))^T$, where the sum of accelerations is mapped by a function $\mathbf{a}$:

$$\frac{d\mathbf{y}(t)}{dt} = \mathbf{F}\left(t, \mathbf{y}(t)\right) = \begin{pmatrix} \mathbf{v}(t) \\ \mathbf{a}\left(t, \mathbf{r}(t), \mathbf{v}(t), p_1, \ldots, p_n\right) \end{pmatrix} \qquad (3.122)$$

In the context of this description, we are primarily interested in the *cause* of the satellite motion and not foremost in the description of the actual state of motion $\mathbf{y}(t)$ of the satellite, being composed of position and velocity, which can be directly derived from formula 3.122. This type of problem formulation is a classic example of an inverse problem typically encountered in statistical orbit determination. A comprehensive overview of the technical framework necessary for statistical orbit determination is provided by e.g. [96] or [70] and in this section we will mainly follow the instructive concepts outlined in the literature.

The force parameter estimates are computed with the help of a batch weighted linear Least-Squares adjustment method. For each epoch and corresponding set of measurements, a system of observation equations can be composed that implicitly includes the unknown quantities as satellite states and parameters originating from the orbit model. Since the functional relationships between the measurements and these parameters are generally non-linear and solving the unknowns directly is typically a difficult problem, approximate solutions based on linearized observation equations including the orbit model must be constructed. The determination of the unknowns is done by inversion of a system of linear normal equations resulting from the condition that the weighted sum of squared residuals must reach a minimum. These residuals represent the difference between the observed and computed values, where the latter can be derived from a combination of (linearized) measurement and orbit models. The result consists of estimated state and parameter corrections that are used as adjustments by applying them to a set of initial values. The steps of linearization, solution of the normal equations and parametric adjustments of input values are repeated until the increments are small enough in relation to the sought accuracy of the parameters and hence the orbit fit suffices a well-defined convergence criterion.

3.4.1 Variational equations

This section outlines the derivation of the variational equations that serve as the basis for the orbit model. For an arbitrary time instant for which observation data are available, a relationship between measurements and satellite states $\mathbf{y}(t)$ as well as force parameters $\mathbf{p}$ must be established. This is achieved by constructing the so-called *state transition matrix* $\boldsymbol{\Phi}(t, t_0)$, which can be interpreted as a Jacobian matrix describing the approximate state change of the satellite under the influence of all orbital perturbations. To obtain $\boldsymbol{\Phi}$, one takes the partial derivative of the function $\mathbf{F}(t, \mathbf{y}(t))$ in 3.122 with respect to an initial state $\mathbf{y}_0 = \mathbf{y}(t_0)$, followed by integration of the equations of motion:

$$\frac{\partial}{\partial \mathbf{y}_0} \frac{d\mathbf{y}(t)}{dt} = \frac{\partial \mathbf{F}(t, \mathbf{y}(t))}{\partial \mathbf{y}(t)} \frac{\mathbf{y}(t)}{\mathbf{y}_0} \tag{3.123}$$

$$\frac{d\boldsymbol{\Phi}(t, t_0)}{dt} = \frac{\partial \mathbf{F}(t, \mathbf{y}(t))}{\partial \mathbf{y}(t)} \boldsymbol{\Phi}(t, t_0) \tag{3.124}$$

Similar to the calculation of the state transition matrix, the same linearization approach can be performed to find the so-called *sensitivity matrix* $\mathbf{S}(t, t_0)$.

$$\frac{\partial}{\partial \mathbf{p}} \frac{d\mathbf{y}(t)}{dt} = \frac{\partial \mathbf{F}(t, \mathbf{y}(t))}{\partial \mathbf{y}(t)} \frac{\partial \mathbf{y}(t)}{\partial \mathbf{p}} + \frac{\partial \mathbf{F}(t, \mathbf{y}(t))}{\partial \mathbf{p}} \tag{3.125}$$

$$\frac{d\mathbf{S}(t)}{dt} = \frac{\partial \mathbf{F}(t, \mathbf{y}(t))}{\partial \mathbf{y}(t)} \mathbf{S}(t) + \frac{\partial \mathbf{F}(t, \mathbf{y}(t))}{\partial \mathbf{p}} \tag{3.126}$$

The combination of 3.124 and 3.126 finally gives us the variational equations:

$$\frac{d}{dt} [\boldsymbol{\Phi}, \mathbf{S}] = \left[\begin{array}{c|c} \mathbf{0}_{3\times3} & \mathbb{1}_{3\times3} \\ \hline \frac{\partial \mathbf{a}(t, \mathbf{r}(t), \ldots)}{\partial \mathbf{r}(t)} & \frac{\partial \mathbf{a}(t, \mathbf{r}(t), \ldots)}{\partial \mathbf{v}(t)} \end{array} \right] [\boldsymbol{\Phi}, \mathbf{S}] + \left[\begin{array}{c|c} \mathbf{0}_{3\times6} & \mathbf{0}_{3\times n_p} \\ \hline \mathbf{0}_{3\times6} & \frac{\partial \mathbf{a}(t, \mathbf{r}(t), \ldots)}{\partial \mathbf{p}} \end{array} \right] \tag{3.127}$$

To resolve $\boldsymbol{\Phi}$ and $\mathbf{S}$, the equations 3.127 must be numerically integrated together with the state vectors $\mathbf{r}(t)$ and $\mathbf{v}(t)$, since the evaluation of the partial derivatives requires the knowledge of the position and velocity of the satellite. As initial values, $\boldsymbol{\Phi}_0 = \mathbb{1}_{6\times6}$ and $\mathbf{S} = \mathbf{0}_{6\times n_p}$ are used for the matrices. Care must be taken throughout the integration process. Depending on the complexity of the dynamics $\mathbf{F}(t, \mathbf{y}(t))$, the time intervals must be chosen small enough to avoid rapid growth of integration errors.

3.4.2   Linearization

As noted earlier, linearization of the governing observation equations including the orbit model is a prerequisite for the practical implementation of statistical orbit determination and must be supplied in preparation to the parameter estimation process. The measurements $z(t)$ can be modeled by the observation equations (3.1, 3.2, and 3.3), so that at a particular epoch t_k, $z(t_k) = z_k$ may be expressed as follows:

$$z_k = h\left(\mathbf{y}(t_k), t_k\right) + \epsilon_k \tag{3.128}$$

where ϵ is the measurement error associated with the discrete measurement z_k. Equation 3.128 is generally non-linear and also depends on the solution of 3.122 describing the orbit. It is our objective to find the best estimates for the satellite states and force model parameters through an iterative weighted linear Least-Squares fitting procedure. Consequently, the equations 3.122 and 3.128 must be converted into their respective linear forms. A Taylor expansion of 3.128 around $z(t_0) = z_0$ helps to explicitly link the measurements to the satellite states $\mathbf{y}(t)$:

$$z\left(t\right) \approx z_0 + \frac{\partial h\left(\mathbf{y}(t), t\right)}{\mathbf{y}(t)} \Delta \mathbf{y}(t) \tag{3.129}$$

$$\Delta z(t) \approx \frac{\partial h\left(\mathbf{y}(t), t\right)}{\mathbf{y}(t)} \Delta \mathbf{y}(t) \tag{3.130}$$

where $\Delta \mathbf{y}(t) = (\mathbf{y}(t) - \mathbf{y}_0)$ summarizes the difference of the actual satellite state with respect to a reference state $\mathbf{y}_0$.

Solving the variational equations 3.127 already provides us with the state transition matrix $\mathbf{\Phi}$, which represents the first order approximation of the function $\mathbf{F}\left(t, \mathbf{y}(t)\right)$ around a given state $\mathbf{y}_0$. For sufficiently small deviations from $\mathbf{y}_0$, this matrix describes the satellite's state evolution via the *orbit state partials*. Similar to the state transition matrix, the $\mathbf{S}$ matrix contains the *force model partials* describing the sensitivity of position and velocity, and hence the shape of the orbit, to force model parameters. However, in the context of our investigations, we aim at an increased understanding of the effects related to SRP and hence restrict the $\mathbf{S}$ matrix to the description of the SRP model partials. The relationship between the measurement partials and the orbit-related partials can be expressed as follows:

$$\left[\frac{\partial z(t)}{\partial \mathbf{y}(t_0)}, \quad \frac{\partial z(t)}{\partial \mathbf{p}}\right] = \left(\frac{\partial z(t)}{\partial \mathbf{y}(t)}\right)^T \left[\mathbf{\Phi}(t, t_0), \quad \mathbf{S}(t, t_0)\right] \tag{3.131}$$

The *measurement partials* $\frac{\partial z(t)}{\partial \mathbf{y}(t_0)}$ with respect to the satellite's state must be calculated from a measurement model. For this purpose, the observation equations, which have already been described and established in section 3.1, are linearized. In the special case of the dual-frequency ionosphere-free combination, one usually refers to the equations 3.6 and 3.13, respectively. The measurement partials with respect to satellite position and velocity become:

$$\frac{\partial z(t)}{\partial \mathbf{y}(t_0)} = \frac{\partial \rho_r^s}{\partial \mathbf{y}(t_0)} = -\frac{(\mathbf{r}_r(t) - \mathbf{r}^s(t - \tau))}{\rho} \tag{3.132}$$

where the function $z(t)$ must be replaced with the corresponding observation model $P_{r,IF}^s$ or $\Phi_{r,IF}^s$. Expression 3.132 shows that the ρ-term only produces satellite position partials and it is the only one in the mentioned observation models, which directly relates to the satellite's states. We write out the comma-separated contributions in 3.131 in their full form. For the first part, we have:

$$\frac{\partial z(t)}{\partial \mathbf{y}(t_0)} = \begin{bmatrix} \frac{\partial z}{\partial x} & \frac{\partial z}{\partial y} & \frac{\partial z}{\partial z} & 0_{1\times3} \end{bmatrix} \begin{bmatrix} \frac{\partial x}{\partial x_0} & \frac{\partial x}{\partial y_0} & \frac{\partial x}{\partial z_0} & \frac{\partial x}{\partial \dot{x}_0} & \frac{\partial x}{\partial \dot{y}_0} & \frac{\partial x}{\partial \dot{z}_0} \\ \frac{\partial y}{\partial x_0} & \frac{\partial y}{\partial y_0} & \frac{\partial y}{\partial z_0} & \frac{\partial y}{\partial \dot{x}_0} & \frac{\partial y}{\partial \dot{y}_0} & \frac{\partial y}{\partial \dot{z}_0} \\ \frac{\partial z}{\partial x_0} & \frac{\partial z}{\partial y_0} & \frac{\partial z}{\partial z_0} & \frac{\partial z}{\partial \dot{x}_0} & \frac{\partial z}{\partial \dot{y}_0} & \frac{\partial z}{\partial \dot{z}_0} \\ \frac{\partial \dot{x}}{\partial x_0} & \frac{\partial \dot{x}}{\partial y_0} & \frac{\partial \dot{x}}{\partial z_0} & \frac{\partial \dot{x}}{\partial \dot{x}_0} & \frac{\partial \dot{x}}{\partial \dot{y}_0} & \frac{\partial \dot{x}}{\partial \dot{z}_0} \\ \frac{\partial \dot{y}}{\partial x_0} & \frac{\partial \dot{y}}{\partial y_0} & \frac{\partial \dot{y}}{\partial z_0} & \frac{\partial \dot{y}}{\partial \dot{x}_0} & \frac{\partial \dot{y}}{\partial \dot{y}_0} & \frac{\partial \dot{y}}{\partial \dot{z}_0} \\ \frac{\partial \dot{z}}{\partial x_0} & \frac{\partial \dot{z}}{\partial y_0} & \frac{\partial \dot{z}}{\partial z_0} & \frac{\partial \dot{z}}{\partial \dot{x}_0} & \frac{\partial \dot{z}}{\partial \dot{y}_0} & \frac{\partial \dot{z}}{\partial \dot{z}_0} \end{bmatrix} \tag{3.133}$$

The partials of the measurements with respect to the SRP parameters are:

$$\frac{\partial z(t)}{\partial \mathbf{p}} = \begin{bmatrix} \frac{\partial z}{\partial x} & \frac{\partial z}{\partial y} & \frac{\partial z}{\partial z} & 0_{1\times3} \end{bmatrix} \begin{bmatrix} \frac{\partial x}{\partial p_1} & \cdots & \frac{\partial x}{\partial p_n} \\ \frac{\partial y}{\partial p_1} & \cdots & \frac{\partial y}{\partial p_n} \\ \frac{\partial z}{\partial p_1} & \cdots & \frac{\partial z}{\partial p_n} \\ \frac{\partial \dot{x}}{\partial p_1} & \cdots & \frac{\partial \dot{x}}{\partial p_n} \\ \frac{\partial \dot{y}}{\partial p_1} & \cdots & \frac{\partial \dot{y}}{\partial p_n} \\ \frac{\partial \dot{z}}{\partial p_1} & \cdots & \frac{\partial \dot{z}}{\partial p_n} \end{bmatrix} \tag{3.134}$$

For clarity, we dropped the superscript satellite index s in the coordinate notation of the partial derivatives. As can be seen from the equation 3.127, one must evaluate the partial derivatives of the accelerations with respect to the satellite states and force parameters as input values for the matrices to obtain $\mathbf{\Phi}$ and $\mathbf{S}$ after integration. Since we do not have any velocity dependent terms in our orbit model 3.60, no velocity dependent partials must be calculated. In section 3.3.1, the individual acceleration contributions due to geopotential perturbations are discussed and subsequently 3.3.3 focuses on SRP-related perturbations. The gradient of geopotential and point-mass perturbations in an ECEF coordinate system is given in [70] on page 245 and 247, respectively. Since the relativistic orbital perturbations are in fact very small, we neglect their contribution to the gradient. In order to find the gradient of the SRP parameters, it is necessary to first choose a suitable coordinate system in which the position partials are calculated based on equation 3.101. We compute the partial derivatives of the accelerations in the special body-fixed DYB-system defined in 3.87. Starting from the nine-parameter ECOM implied by equation 3.100, we then obtain the following terms for the corresponding directions:

$$\frac{\partial \mathbf{a}_{srp,D}}{D_0} = 1, \; \frac{\partial \mathbf{a}_{srp,D}}{D_c} = \cos(\mu), \; \frac{\partial \mathbf{a}_{srp,D}}{D_s} = \sin(\mu)$$

$$\frac{\partial \mathbf{a}_{srp,Y}}{Y_0} = 1, \; \frac{\partial \mathbf{a}_{srp,Y}}{Y_c} = \cos(\mu), \; \frac{\partial \mathbf{a}_{srp,Y}}{Y_s} = \sin(\mu) \quad (3.135)$$

$$\frac{\partial \mathbf{a}_{srp,B}}{B_0} = 1, \; \frac{\partial \mathbf{a}_{srp,B}}{B_c} = \cos(\mu), \; \frac{\partial \mathbf{a}_{srp,B}}{B_s} = \sin(\mu)$$

The gradient from equation 3.135 is then transformed into a suitable, common coordinate system so that it can finally be combined with the vector of partials formed from $\mathbf{a}_{srp}$ with respect to the SRP scaling parameter C_{srp}.

The observation equations depend on additional n_m parameters of the measurement model that we have not previously considered and which are decoupled from the orbit model. Depending on the required accuracy, the linear observation model is extended to include the estimation of the clock parameters, however, we restrict ourselves to the use of precise clock solutions provided by the IGS as explained in the next section 3.5. Furthermore, especially for applications as POD, corrections for the zenith wet delay are also typically added to the unknowns, and a corresponding mapping function as presented in 3.29 must be prepared as part of the measurement model.

3.5 Parameter Estimation

In the previous subsection, we established the variational equations 3.127 and specified the components of their solution, the state transition matrix $\boldsymbol{\Phi}$ and the sensitivity matrix $\mathbf{S}$ (3.133 and 3.134). We have seen that the variational equations must be integrated jointly with the differential equation system of the orbit model 3.122, since the former depend on its solutions. More precisely, derivatives appear in the governing system of equations 3.127, which must be evaluated for particular times for the respective integration steps. Following this orbit propagation process, we need to evaluate the residuals for each measurement record with respect to the associated computed values in preparation to the estimation scheme. Here, the computed values are derived from the linear model 3.130, formed from the solutions of the underlying variational equations for specific times, which of course must coincide with the time tags of the available measurement records. In this section, we focus on the actual measurement data processing and outline the structure and solution of the objective normal equation system.
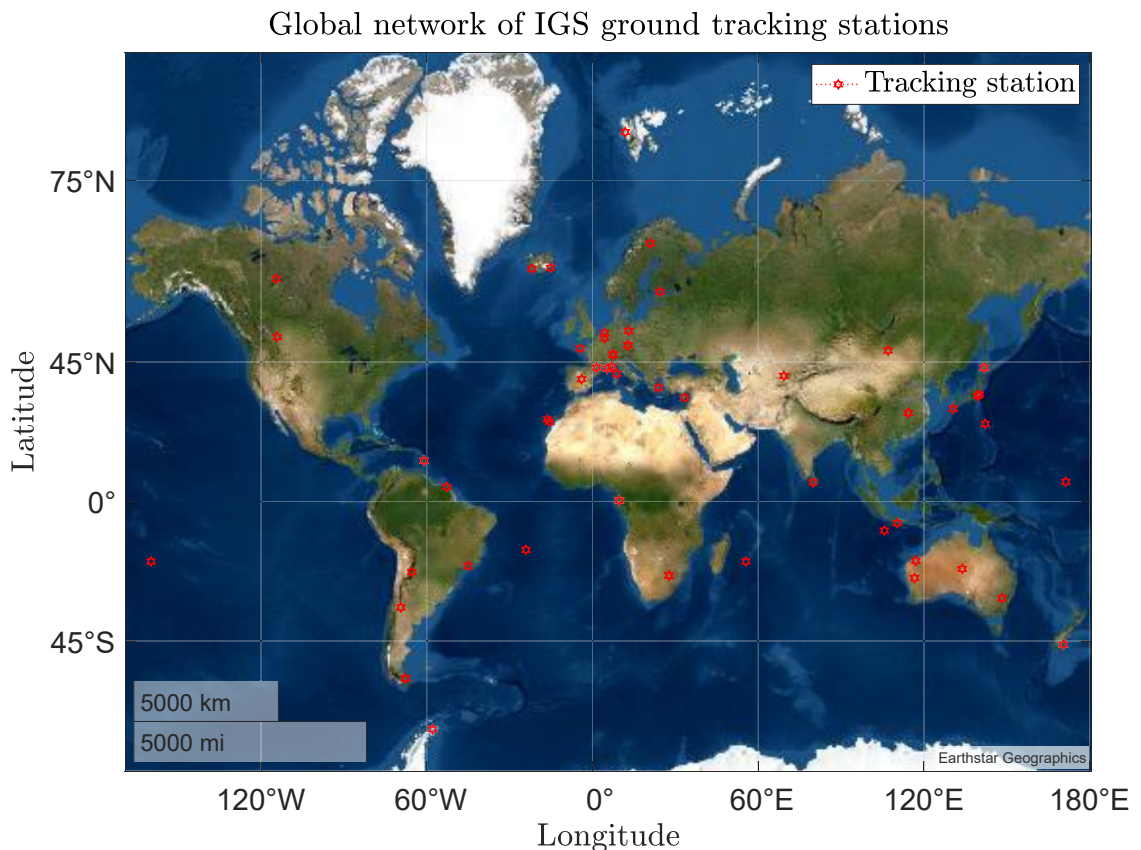
Figure 3.25: Distribution of IGS Multi-GNSS Experiment (MGEX)-related GNSS tracking stations whose measurement data are included in the analysis.

Data preparation and processing As station and satellite clock data we use the IGS MGEX solutions generated by the CODE analysis center and finally provided to the IGS[24] [27]. The satellite raw data data used for the study are sourced from the IGS data center of the Bundesamt für Kartographie und Geodaesie (BKG)[25]. It also provides GNSS observation data and derived products from a global network of ground stations cooperating with the IGS, which are organized in the standardized RINEX exchange format.

For the SRP parameter study, a monolithic set of measurement data of all available tracking stations (see map 3.25) covering a one-month period (February 11, 2017 to March 12, 2017) is used for the purpose of long-arc force parameter adjustments. The variations of the Sun's elevation β over this time are very small and reach approximately 3°. This is due to the fact that β floats around its maximum within this period such that no eclipses occur. The RINEX data are preprocessed sequentially before each iteration. A RINEX file is always related to observations of a specific tracking station. It contains observation data of multiple GNSS constellations and covers a time period of one day. The preprocessing is done in a day-wise fashion and includes filtering the data for observations of the specific satellites GSAT0202 and GSAT0201 per station. In addition we select the signals of interest for which code or carrier phase observations are available. We intend to use dual-frequency pseudo-range observations and focus on the signal types E1, E5a and E5b providing us C1C, C5Q and C7Q observation codes. Consequently, if for any day, a RINEX file associated with a certain tracking station does not contain at least two concurrent series of different observation code data, the complete data set is discarded for that day. Depending on the actual satellite's operational or health status, which is part of the GNSS observation data records in the RINEX file, several flags are (un-)set epoch-wise and must be checked:

1. OK

2. Power failure between previous and current epoch

3. Start moving antenna

4. Header information follows

5. External event (epoch is significant, same time frame as observation time tags)

6. Cycle slip records (as information about carrier phase condition)

This helps to decide whether a data record of a certain epoch should be removed or not.

Pre-fit residuals For each station r and epoch n for which measurement data of satellite s exist, we determine the pre-fit residuals identified with the lhs of the linear observations model 3.130. In order to do so, all the systematic error terms appearing in equation 3.136 must be evaluated to obtain Δz_n related to a time instant t_n.

---

[24]`http://ftp.aiub.unibe.ch/CODE_MGEX/CODE/`
[25]`ftp://igs.bkg.bund.de/IGS/obs/`

$$\Delta z_n = P_{r,IF}^s - \rho_{r,0}^s - c\left(\Delta\hat{t}_r - \Delta\hat{t}^s\right) - T_r^s - \epsilon_{P,IF} \tag{3.136}$$

As a reminder, we would like to remark that multi-path effects are neglected. As explained in 3.1, the signal transmission time is necessary for the correct determination of the satellite's state at the time of observation and hence the distance $\rho_{r,0}^s$. Starting with a satellite's ephemeris at a given time, the correct signal propagation time for the observation epoch t_n is determined iteratively: The initial state is used to derive an initial estimate of the distance between the receiver and the satellite. Between the time of transmission and reception, the Earth rotates by a small amount. One must therefore perform a transformation of the current position and velocity of the satellite. As a result, one obtains a new state from which an updated signal path range and thus signal propagation time is calculated. Usually, one has to repeat this procedure three to four times to get proper results. The orbit propagation algorithm returns values for position and velocity every 30 seconds to cope with the RINEX data sampling rate. To relate the predicted satellites states to the iterated transmission times, we need to interpolate them. For this purpose, we use the approach found in [93], which proposes a harmonic series expansion for the interpolation of precise satellite ephemerides. The underlying algorithm ensures that the accuracy of the precise orbit data remains within the centimeter range. Finally, the state transition matrix $\mathbf{\Phi}$ as well as the sensitivity matrix $\mathbf{S}$ are also evaluated at the respective time of signal transmission by interpolation. One must be careful with the observation time scale because it must match the time scale, which refers to the propagated satellite states.

Weighted Least-Squares adjustment To solve for the vector of state and parameter adjustments $\Delta\hat{x}$ we have to find the solution to the following optimization problem, i.e. the minimization of the sum over the weighted mean-squared error with respect to all N data records remaining after preprocessing:

$$\underset{\Delta\hat{x}}{argmin} \sum_{n=0}^{N} q_n \left(\Delta z_n - \mathbf{H}_n^T \mathbf{\Psi}_n \Delta\hat{x}\right)^2 \tag{3.137}$$

where q_n are considered the weights associated with the nth observation. To determine the weights q_n, we refer to our empirical background knowledge of instrument precision, which determines the measurement dispersion of each z_n. The corresponding uncertainties associated with the different observation types have already been discussed in 2.3 and 3.1. In expression 3.137, the matrix $\mathbf{\Psi}$ was introduced. It combines the two matrices $\mathbf{\Phi}$ and $\mathbf{S}$:

$$\mathbf{\Psi} = \begin{bmatrix} \mathbf{\Phi} & \mathbf{S} & 0_{6 \times n_m} \\ 0_{n_p \times 6} & \mathbb{1}_{n_p \times n_p} & 0_{n_p \times n_m} \\ 0_{n_m \times 6} & 0_{n_m \times n_p} & \mathbb{1}_{n_m \times n_m} \end{bmatrix} \tag{3.138}$$

As a consequence, the measurement matrix $\mathbf{H}$ must take the following shape:

$$\mathbf{H}^T = \begin{bmatrix} -\dfrac{\left(\mathbf{r}_r(t) - \mathbf{r}^s(t-\tau)^T\right)}{\rho} & 0_{1 \times 3} & 0_{1 \times n_p} & 0_{1 \times n_m} \end{bmatrix} \tag{3.139}$$

In addition to the number of force model parameters n_p, the number of measurement parameters n_m predetermine the dimensions of both the matrices $\mathbf{\Psi}$ and $\mathbf{H}$. The solution to the problem 3.137 reads:

$$\Delta \hat{x} = \left(\mathbf{X}^T \mathbf{Q} \mathbf{X}\right)^{-1} \mathbf{X}^T \mathbf{Q} \Delta \mathbf{z} \tag{3.140}$$

Equation 3.140 represents the normal equations and its solution gives the best linear unbiased estimate $\Delta \hat{x}$. In 3.140, we introduced $\mathbf{X}$ as a substitute for the product $\mathbf{H}\mathbf{\Psi}$ and the matrix $\mathbf{Q}$ characterizes the measurement dispersion. An optimal solution to the weighted Least-Squares problem 3.137 requires that the matrix $\mathbf{Q}$ produces the least variance among all possible linear unbiased estimates $\Delta \hat{x}$. We assume that the measurements errors are uncorrelated. Consequently, we set q_n equal to the inverse variances $q_n = \sigma_n^{-2}$, which serve as weights, and identify them with the diagonal elements of the matrix $\mathbf{Q}$ to satisfy the optimality criterion[26]. The updated state and parameter vector $\hat{\mathbf{x}}$ is then obtained from adding 3.140 to the reference vector $\mathbf{x}_0$, which served as an initial state for orbit propagation:

$$\hat{\mathbf{x}} = \mathbf{x}_0 + \Delta \hat{x} = \mathbf{x}_0 + \left(\mathbf{X}^T \mathbf{Q} \mathbf{X}\right)^{-1} \mathbf{X}^T \mathbf{Q} \Delta \mathbf{z} \tag{3.141}$$

We write the mean-squared error of the measurements as $\mathbb{E}\left[\epsilon \epsilon^T\right]$ and it contributes to the respective covariance matrix of the estimation results, which can generally be described as follows:

$$Cov\left(\Delta \hat{x}, \Delta \hat{x}\right) = \left(\mathbf{X}^T \mathbf{Q} \mathbf{X}\right)^{-1} \left(\mathbf{X}^T \mathbf{Q}\right) \mathbb{E}\left[\epsilon \epsilon^T\right] \left(\mathbf{Q} \mathbf{X}\right) \left(\mathbf{X}^T \mathbf{Q} \mathbf{X}\right)^{-1} \tag{3.142}$$

Since the errors are uncorrelated and assumed to be entirely described by the empirical measurement uncertainties characterized by the matrix $\mathbf{Q}$ adopted above, one immediately verifies that the description of the corresponding covariance matrix reduces to:

$$Cov\left(\Delta \hat{x}, \Delta \hat{x}\right) = \left(\mathbf{X}^T \mathbf{Q} \mathbf{X}\right)^{-1} \tag{3.143}$$

With the help of 3.143 the estimation precision, i.e. standard deviation of the nth element of the vector $\Delta \hat{x}$ can be derived from the following expression:

$$\sigma_{\Delta \hat{x}_n} = \sqrt{Cov\left(\Delta \hat{x}_n, \Delta \hat{x}_n\right)} \tag{3.144}$$

---

[26]If the measurements are correlated, the covariance matrix is generally fully populated. In this case the matrix $\mathbf{Q}$ in 3.140 must be the inverse of the measurement covariance matrix to still solve 3.137 under the imposed conditions. In chapter 4, equation 4.23 gives an example of a covariance matrix that maps the measurement dispersion produced by a first order autoregressive process.

Observation weighting It is common to complement the above weighted Least-Squares scheme with some limiting assumptions about the weights. It is assumed that with decreasing elevation of the satellite the received signal quality becomes worse. Therefore, an elevation dependent model is applied to down-weight the observations when the satellite is at low elevations (see [37]):

$$\sigma_{Q,n}^2 = \sigma_{X,n}^2 \left(1 + 10 e^{-\frac{\epsilon(t_n)}{\epsilon_{cut}}} \right) \tag{3.145}$$

where the subscript X is a placeholder for the observation identifier P (pseudo-range) or Φ (carrier phase). The fraction in the exponent is the ratio of the time dependent elevation $\epsilon(t_n)$ of the satellite with respect to a topocentric coordinate system and a cutoff value ϵ_{cut}, which is chosen to amount 10°. If the elevation reaches the threshold ϵ_{cut}, the corresponding data record is rejected.

Normal equation stacking Depending on the purpose of the orbit determination application, a distinction is made between arc-related parameters and global parameters whose values are to be estimated over multi-arcs. In our case, for the determination of satellite states and SRP parameters, this means that the adjustments relate to different time intervals. The satellite state estimates are corrected arc- or day-wise, while SRP parameter updates reflect the best estimates based on multi-arc periods encompassing the entire data set. After each Least-Squares adjustment iteration, changes of SRP parameters thus affect the entire multi-arc orbit simulation process predicting the new satellite positions and velocities, while updates to the latter affect each one-day arc propagation independently. Since the matrix $\mathbf{Q}$ is diagonal, the structure of the multi-arc-related normal equation system 3.140 is essentially determined by the shape of $\mathbf{X}$:

$$\mathbf{X} = \begin{bmatrix} \mathbf{X}_1 & & \cdots & & \mathbf{X}_{1g} \\ & \mathbf{X}_2 & & & \mathbf{X}_{2g} \\ \vdots & & \ddots & & \vdots \\ & & & \mathbf{X}_n & \vdots \\ 0 & & \cdots & & \mathbf{X}_{ng} \end{bmatrix} \tag{3.146}$$

From $\mathbf{X}$, it becomes obvious that most of the matrix elements are zero, because the arc-related parameters associated with the state transition partials in the $\mathbf{X}_k$ matrices are independent from each other. Therefore, they are arranged on the diagonal of the block matrix. However, there are common arc-interrelated SRP parameters upon which all trajectories depend, that is why the last column is fully populated with the sensitivity matrices $\mathbf{X}_{kg}$ containing the SRP parameter partials. The subscript g indicates that the matrices $\mathbf{X}_{kg}$ are tied to the global SRP parameters. In short form, the normal equation system is conveniently written as:

$$\Delta \hat{x} = \mathbf{N}^{-1}\mathbf{b} \tag{3.147}$$

$$\mathbf{N} = \left(\mathbf{X}^T \mathbf{Q} \mathbf{X}\right) \tag{3.148}$$

$$\mathbf{b} = \mathbf{X}^T \mathbf{Q} \Delta \mathbf{z} \tag{3.149}$$

where we have identified the individual terms of equation 3.140 with the components $\mathbf{N}$ and $\mathbf{b}$ of the normal equation system. Accordingly, the combined multi-arc normal equation system is assembled as follows:

$$
\begin{bmatrix}
\Delta \hat{x}_{6\times 1} \\
\Delta \hat{x}_{6\times 1} \\
\vdots \\
\vdots \\
\Delta \hat{x}_{n_p \times 1}
\end{bmatrix}
=
\begin{bmatrix}
\mathbf{N}_1 & & \cdots & & \mathbf{N}_{1g} \\
& \mathbf{N}_2 & & & \mathbf{N}_{2g} \\
\vdots & & \ddots & & \vdots \\
& & & \mathbf{N}_n & \mathbf{N}^T_{(n-1)g} \\
\mathbf{N}^T_{1g} & \mathbf{N}^T_{2g} & \cdots & \mathbf{N}^T_{(n-1)g} & \mathbf{N}_{ng}
\end{bmatrix}^{-1}
\begin{bmatrix}
\mathbf{b}_1 \\
\mathbf{b}_2 \\
\vdots \\
\vdots \\
\mathbf{b}_n
\end{bmatrix}
\tag{3.150}
$$

Each normal matrix $\mathbf{N}_k$ in 3.150 comprises information related to the kth arc. The row dimension of each $\mathbf{N}_k$ is equal to $n_r \times n_t(r)$. n_r corresponds to the total number of tracking stations, each providing a certain number of data epochs $n_t(r)$.

Solution The iterative solution of 3.141 quickly converges to an optimal estimate $\Delta \hat{x}$, which can be concluded from the two figures 3.26 and 3.28. The former represents the residuals $\Delta z(t)$ before the first Least-Squares adjustments are used to adapt the parameters of the orbit model. In addition to the plots for the residuals associated with satellite GSAT0202, for completeness the residuals for GSAT0201 are also shown in figures 3.27 and 3.29. As input to the orbit model we make use of the new FE SRP model for both satellites (see 3.19) introduced in section 3.3.3.2. Each subplot shows a collection of residuals related to the arcs named in the titles and the associated data points represent the values calculated based on all available station-specific observation data, where the coloring serves as a mapping between these values and particular stations. The harmonics describe the remaining systematic effects that are presumed to originate exclusively from SRP or TRP effects. The second plot 3.28 shows the residuals with respect to an updated orbit model, where the satellite states and SRP parameter corrections $\Delta \hat{x}$ have been added to the reference values $\mathbf{x}_0$. The SRP parameter updates in numbers can be found in the table 3.4, where the estimation results with respect to a box-wing FE model and the proposed high-fidelity FE model are compared. We also note that the estimation results based on the observation data of the satellite GSAT0201 agree very well with those from GSAT0202. The box dimensions and the optical properties are thereby configured according to the official GALILEO satellite metadata[27]. The estimation parameters in the table compose the parameters of an ECOM1 model following the SRP parameter specifications in [71]. The choice of this model is justified by (1) the high β angle during the analysis period, which is not expected to

---

[27]https://www.gsc-europa.eu/support-to-developers/galileo-satellite-metadata

require coverage by the once-per-revolution terms D_c and D_s, and (2) the residual effects due to the asymmetry of the spacecraft should be adequately covered by the once-per-revolution terms B_c and B_s. The benchmark discovers that among the estimated values, mostly the D_0 components differ from each other. The D_0 coefficient measures the acceleration against the direction to the sun and the difference that emerges from the two estimates for the different a-priori models measures $\Delta D_0 \approx 1 \times 10^{-9} m/s^2$. This shows that the high-fidelity FE model improves the prediction of SRP perturbations over the simpler a-priori box-wing model. The Y_0 component is negligible small, which is reasoned by the perfect YS attitude mode assumed throughout the orbit simulations.

The orbit simulation performance of the high-fidelity FE Model versus a purely empirical ECOM1 model is further demonstrated by plot 3.30. The convergence speed of the estimation procedure given the purely empirical model appears to be rather slow as compared to the FE model. It is also evident that the plots representing the performance of the empirical model cover a wider range of values, while the orbit predictions using the FE model are closer to the comparative precise orbit solution. We also compared the orbit prediction performance between the high-fidelity FE and the FE box-wing model. The RMS values were found to produce similar results over the simulated orbit arcs in each case. However, the more complex model apparently proves to be more physically meaningful, as confirmed by the parameter estimation results.
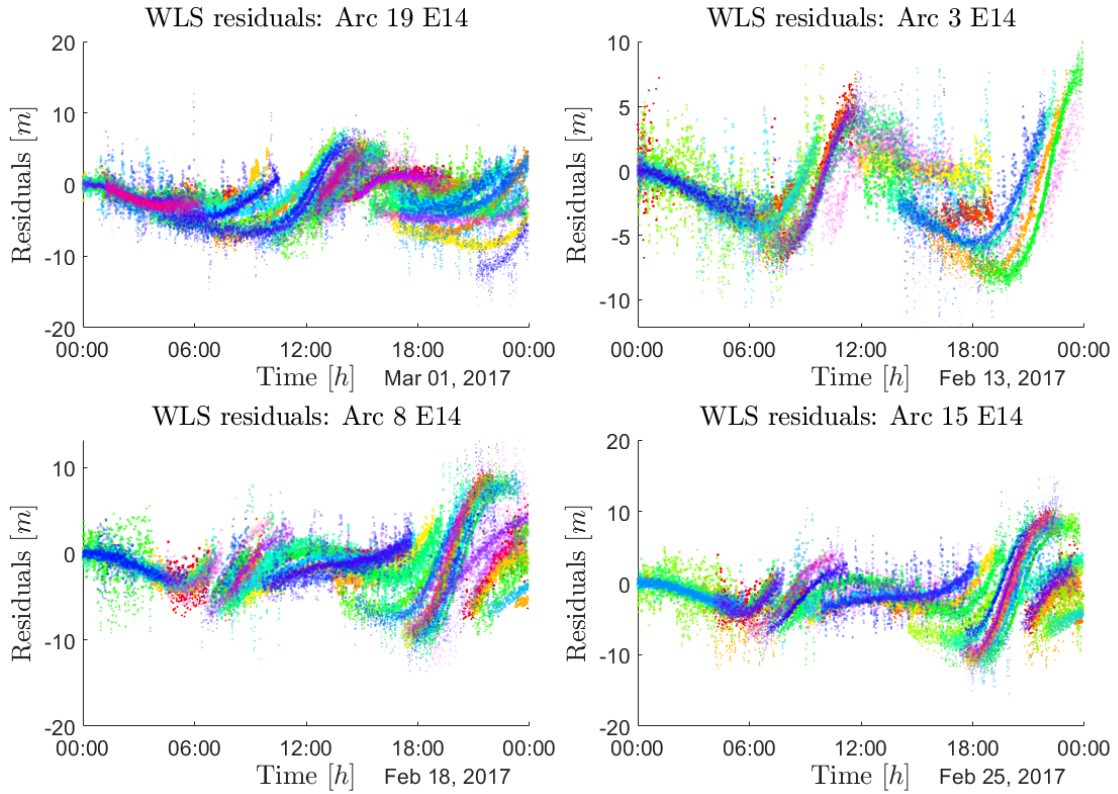
Figure 3.26: Orbit residuals before the first adjustment step. As input to the orbit model, we combined a five-parameter ECOM1 model with an a-priori FE model introduced in section 3.3.3.
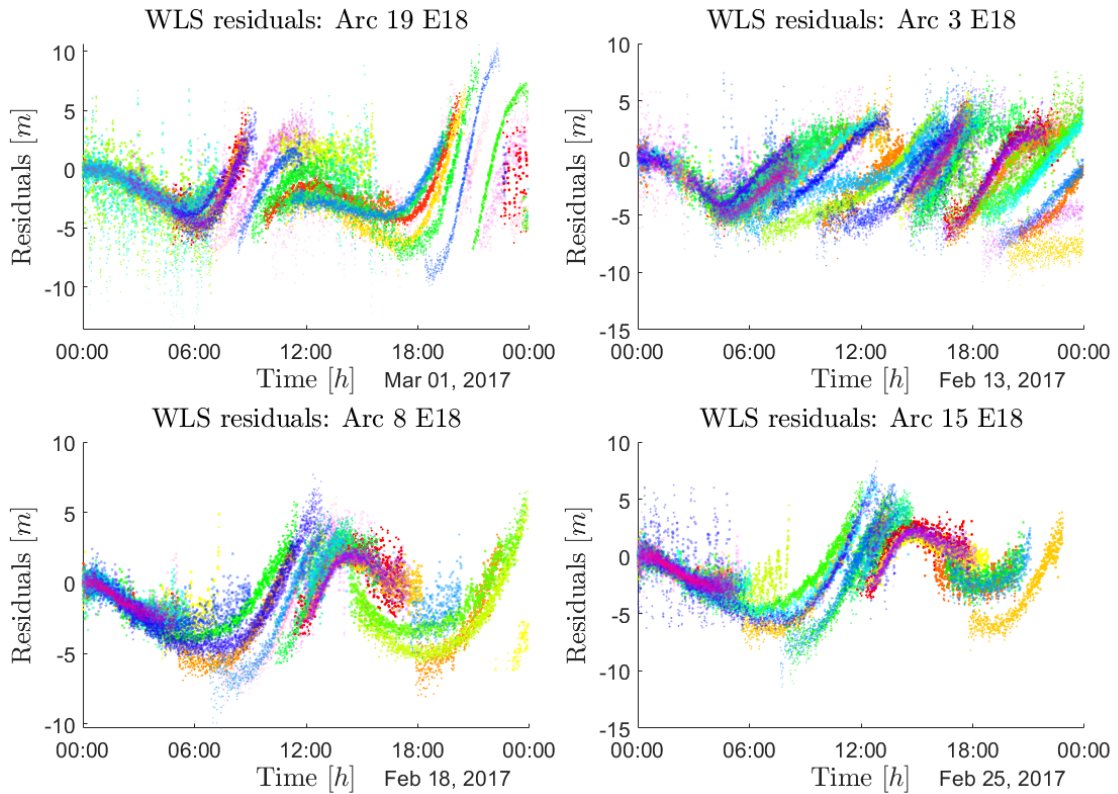
Figure 3.27
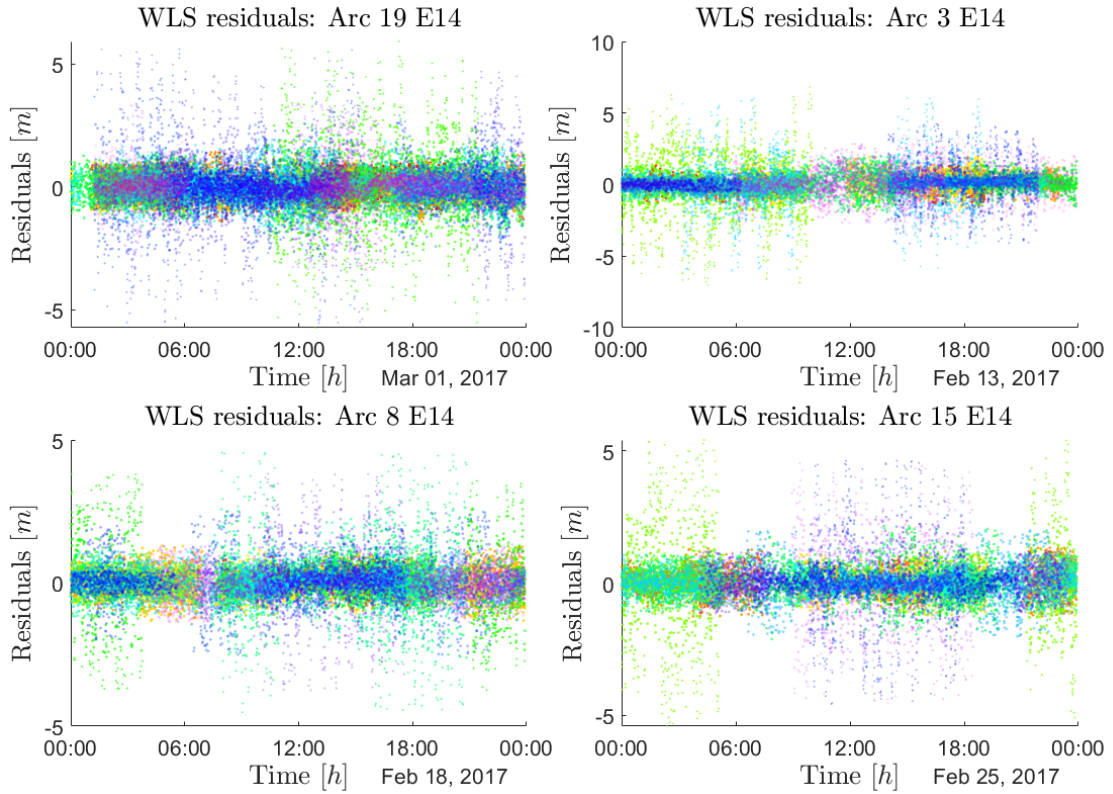
Figure 3.28: After one iteration, the Least-Squares adjustment could significantly reduce the residuals pictured in 3.26. The resulting SRP parameter estimates are presented in table 3.4.
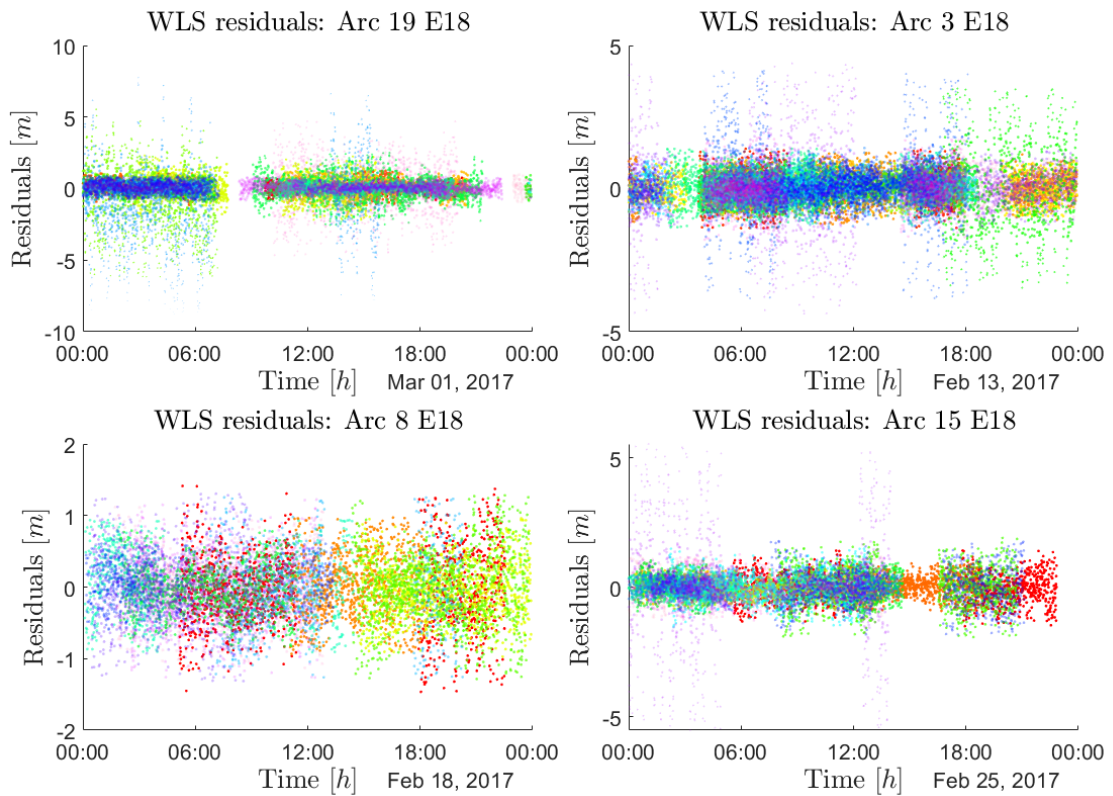
Figure 3.29
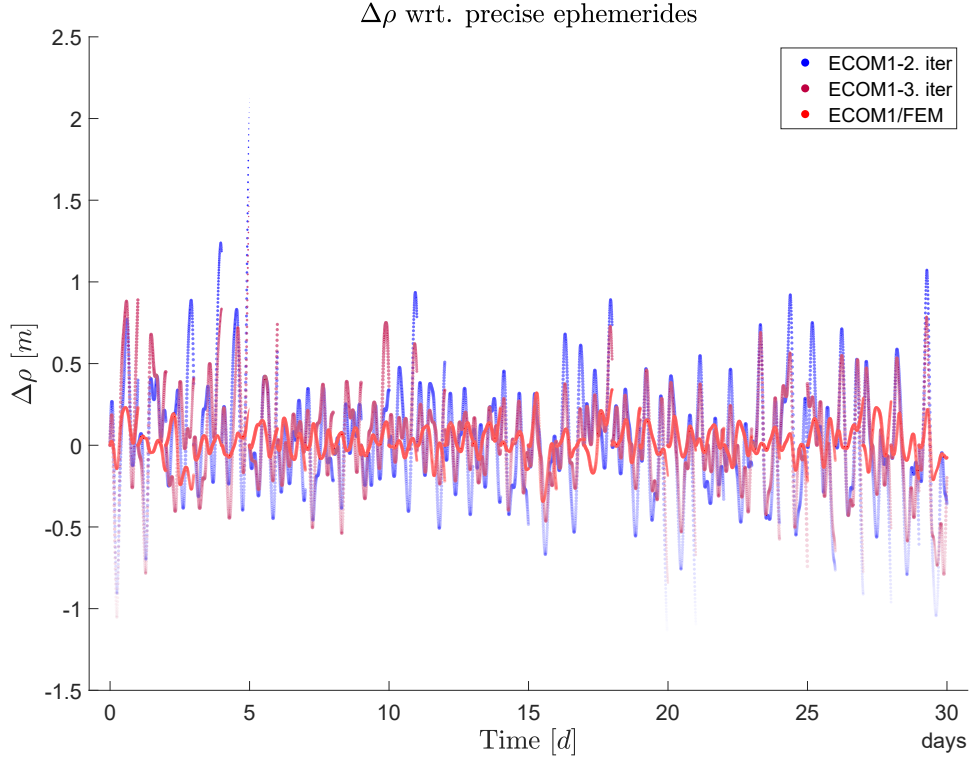
Figure 3.30: Comparison of relative orbit prediction performance based on different SRP models with respect to precise orbit solutions for satellite GSAT0202. The orbit propagation results visualized by the blue and dark red lines are each calculated on the basis of purely empirical SRP models, while the red curve reflects the performance of a semi-empirical model based on a high-fidelity FE model.

SRP Parameter	Box-Wing + ECOM1	FEM + ECOM1
C_{srp}	$1.20 \pm 4.47 \times 10^{-3}$	$1.19 \pm 4.36 \times 10^{-3}$
D_0	$-3.80 \times 10^{-9} \pm 3.17 \times 10^{-10}$	$-2.87 \times 10^{-9} \pm 3.14 \times 10^{-10}$
Y_0	$-6.62 \times 10^{-10} \pm 2.46 \times 10^{-11}$	$-6.84 \times 10^{-10} \pm 2.42 \times 10^{-11}$
B_0	$2.38 \times 10^{-9} \pm 3.75 \times 10^{-10}$	$2.89 \times 10^{-9} \pm 3.69 \times 10^{-10}$
B_c	$1.10 \times 10^{-9} \pm 1.43 \times 10^{-10}$	$1.32 \times 10^{-9} \pm 1.41 \times 10^{-10}$
B_s	$-1.77 \times 10^{-11} \pm 4.00 \times 10^{-11}$	$-2.41 \times 10^{-11} \pm 3.91 \times 10^{-11}$

Table 3.4: Parameter estimation results comparing the model performance two different a-priori SRP models.

3.6   Satellite clock estimation

Satellite clock biases are typically estimated at every measurement epoch[28] and can thus only affect those quantities, which are estimated simultaneously. If in addition to the clock biases, the satellite states and dynamic model parameters are also unknown, one strategy for their determination is to take a detour via the application of the double-differenced ionosphere-free combination. This makes it possible to eliminate the systematic clock errors from the underlying observation equations as demonstrated in 3.20 and focus on the accurate resolution of the remaining orbit-related states and parameters to derive an orbit solution. However, double-differencing has the disadvantage that observation data from two satellites and two stations must be available for sufficiently long time periods. Furthermore, the corresponding data recordings must have been obtained from different observation data streams via different frequency channels, which is necessary to form ionosphere-free combinations. Apart from the fact that double differences generate higher noise levels, the data requirements also make it less likely to find a sufficient number of appropriate joint observations for each time period. Once the orbit is accurately known, the clock biases can then be determined in a zero-differenced fashion from the observation model. Zero-differencing was our method of choice in the preceding section, where the plain ionosphere-free combination was used to yield the pre-fit residuals 3.136. In a parallel study from 2016, *Giorgi et al.* [45] provided preliminary results on the gravitational redshift derived directly from observation data of the Geodetic Observatory Wettzell, WTZ3. Here, a similar approach was taken to estimate the differential clock biases on an epoch-by-epoch basis using a particular observation model, and finally determine the redshift from the estimated results. The database used to calculate the pre-fit residuals included orbit solutions, daily station coordinates, and station clock corrections and the tropospheric zenith delays from CODE, among others.

Figure 3.31 shows different sets of clock offsets derived from precise clock solutions produced in collaboration with ESA. The characteristic non-stochastic clock drift has already been detrended for each individual data set. In each subplot of 3.31, large data sets of clock errors from two different clock solutions are compared. These were determined using two independent estimation strategies. The blue data series reflects the estimation results using an orbit model configured with a purely empirical ECOM2 model[29], while the red plotted data points outline the behavior of the results under the influence of a semi-empirical ECOM1 that was augmented with an a-priori box-wing model. It was our objective to evaluate the performance of different standard SRP models in terms of clock estimate accuracy improvements: It can be seen from the RMS values that the use of a semi-empirical model renders smaller residuals and outperforms the purely empirical model on average. From the description of the procedure for estimating clock offets, it becomes clear that any shortcomings on the orbit modeling side are inevitably absorbed by the clock estimates, which is equivalent to the statement that the accuracy of the clock es-

---

[28]As can be seen from the RINEX data files, a thirty second sampling interval is common.

[29]The ECOM2 was parametrized with constant accelerations in all directions D_0, Y_0 and B_0, second order harmonics in D -direction $D_{c,2}$ and $D_{s,2}$ and first order harmonics in B -direction $B_{c,1}$ and $B_{s,1}$.

timation is limited by the SRP model chosen. Similar insights into the clock data performance of GALILEO satellites are discussed, for example, by *Sidorov et al.* [104].
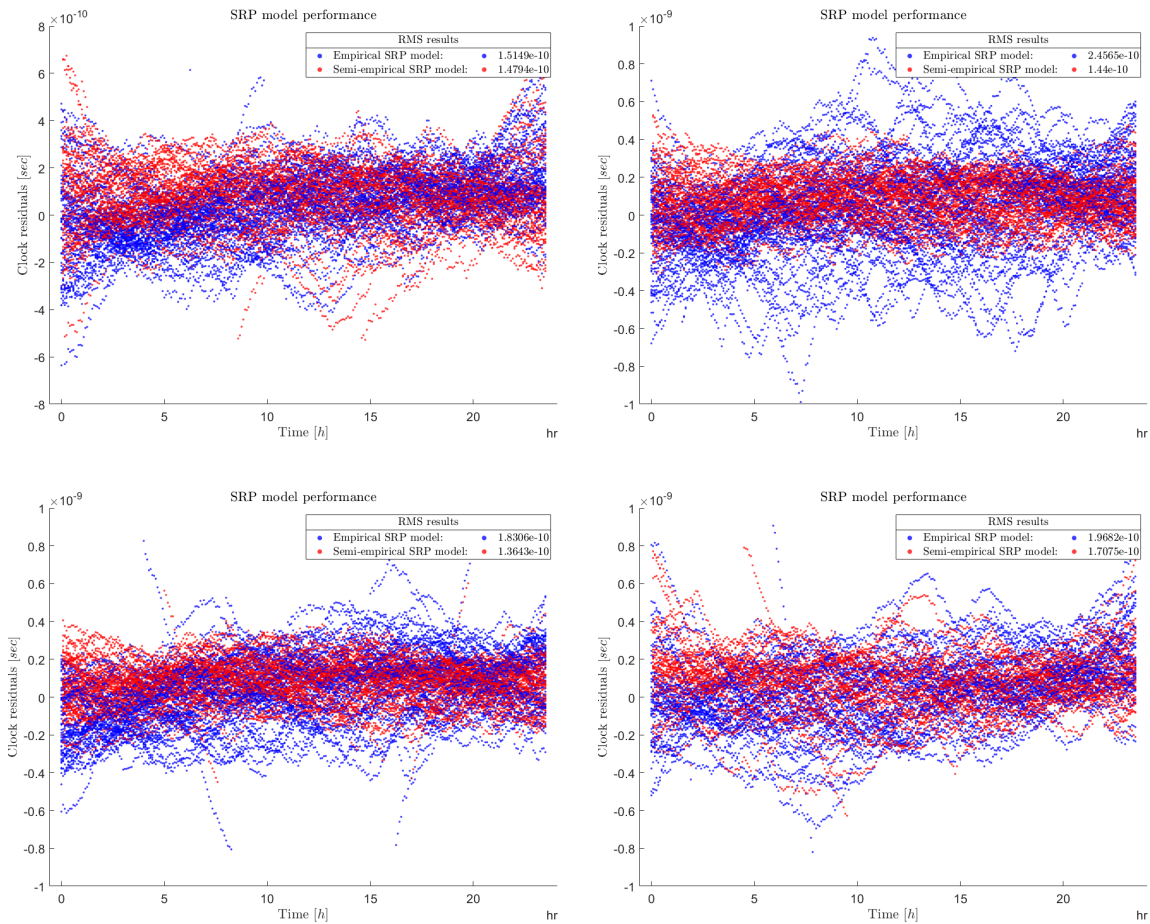
Figure 3.31: Day-wise clock residuals. The plots show the distribution of clock residuals over a one-day period. Each plot combines two different data sets, each comprising fifty contiguous days of clock data estimation results. Each data set is computed on the basis of different SRP models.

Chapter 3

Clock data analysis

4.1 Clock data processing

Various resources are suitable for processing and analyzing clock data. The IGS is a data service of the *International Association of Geodesy*. It consists of a worldwide consortium of associated institutions as tracking stations that provide GNSS data from which a variety of products and solutions are derived and which are also useful for scientific purposes. The IGS initiated the MGEX to increase the ability of the associated station network to track and analyze the observation data of all GNSS constellations including the GALILEO system. The resulting products of the IGS also comprise combined satellite ephemerides, global tracking station coordinates and velocities, station and satellite clock solutions, Earth rotation parameters, as well as global atmospheric maps and data. These products are released on a weekly basis and are reprocessed regularly to address changes in modeling approaches and strategies. Data products derived from the MGEX are provided by a number of analysis centers and include, for example, precise orbit and clock products that are also suitable for our analysis. A table of all products distributed by the IGS can be found on the corresponding IGS website[1][2]. The ESA Navigation Support Office is a standalone facility, which also produces and administrates GNSS products especially for satellite constellations as GPS, GALILEO and GLONASS. Satellite precise orbit and clock solutions are made available in the form of Extended Standard Product (SP3)[3] files from which clock timing data are used throughout our analysis. In detail, the SP3 files contain position, timing information/time offsets of the specific satellite clocks, velocity and the clock's rate-of-change results derived from day-wise POD best fit solutions to GNSS observations, which are sampled in five minute intervals. One must be careful with the usage of the data, since the data at hand is related to the GPS time scale.

The clock database content encompasses a total duration of nearly three years.

---

[1]`https://www.igs.org/products`
[2]`https://igs.org/mgex/data-products/`
[3]`ftp://igs.org/pub/data/format/sp3_docu.txt`

The starting date of the epoch under consideration is November, 11, 2015 and the last day is December, 17, 2017. Over the data collection period, five of the eight atomic clocks on the satellites were active. Table 4.1 shows the operational periods of these clocks. The Passive Hydrogen Maser (PHM) is chosen to be the primary and master clock on each of the GALILEO satellites and the Rubidium Frequency Standard (RAFS) is the secondary unit serving as a backup. For the purpose of redundancy, there are always both clock units of one type (PHM or RAFS) active at a time. With a minimum Allan Variance (AVAR) of $\sigma_y(\tau) \approx 5 \times 10^{-15}$, the former is proven to exhibit the best long-term stability over durations of approximately one day, whereas the latter renders a better short- and mid-term stability, while the long-term stability is around $\sigma_y(\tau) \approx 5 \times 10^{-14}$ - one magnitude below the performance of the PHM. Thereupon, the clock performance of the PHM gives reason to carry out clock data analyses based on time durations of about one day. The SP3 files including the clock data feature day-boundary discontinuities. Data analyses based on these files, which require the inclusion of data intervals beyond one day are thence deemed unreliable for a relativistic precision test. In consequence of the last two arguments, we adopt a day-wise data analysis approach described in this section. Results of on-ground life cycle and performance tests as well as details about the quality of operational performance can be found in [90]. Figure 4.1 shows the in-orbit frequency stability performance of the PHMs of different GALILEO satellites. After time periods longer that one day, the Allan Deviation (ADEV) typically increases again due to effects like temperature drifts or other environmental disturbances. The technical specifications of the GALILEO are summed up in [98].

Clock	Satellite	Start Date	End Date	Number of days	Set
PHM-B	GSAT0201	11-Jan-2015	15-Jun-2016	522	1
PHM-A	GSAT0201	02-Jul-2016	16-Dec-2017	533	2
PHM-B	GSAT0202	19-Mar-2015	04-Nov-2015	231	3
RAFS	GSAT0202	05-Nov-2015	02-Jul-2016	241	4
PHM-A	GSAT0202	03-Jul-2016	17-Dec-2017	533	5

Table 4.1: Satellite clock operation periods.
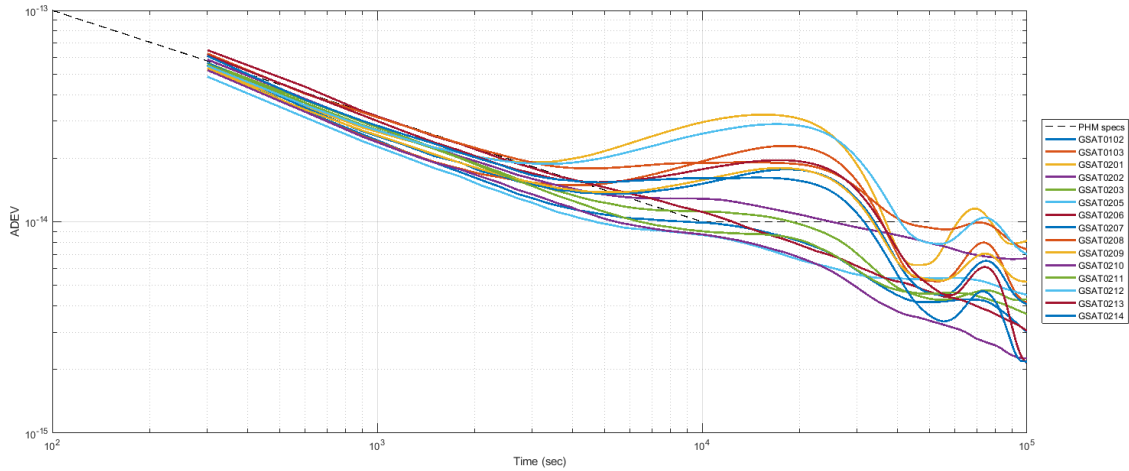
Figure 4.1: Frequency stability of the PHMs used for the GALILEO satellites in terms of the ADEV. The picture was taken from a presentation of *P. Rochat* [89]
.

There are different kinds of effects which absorb into the clock solutions. Among orbital perturbations and those that affect the signal propagation between satellite and receiver station, there are relativistic timing effects. One of these is the general relativistic redshift which is responsible for a difference in the elapsed proper time of the clocks of two observers as discussed in 1.1.1. The integration of the redshift components over a time interval covering one orbital revolution yields a handy expression for the relativistic time dilation, equation 1.19. This term explicitly relates this timing effect to the eccentricity of the orbit of a satellite in a Keplerian setting. For the GALILEO satellites, the different modeled relativistic redshift corrections as well as the associated time dilation effect are subsumed in equation 4.2. One well recognizes the inverse relationships between each of the different redshift corrections and their independent variables - position and velocity - according to formula 1.11. As a result of the varying orbital eccentricity, a maximum peak modulation of $\approx 370\ ns$ over one orbital period can be read off the curve representing the time dilation (see figure 4.2c). The Keplerian orbital elements describing the geometry of the orbits of GSAT0202 and GSAT0201 are given in table 4.2. Since only their orbit phasing is different by approximately 180°, as indicated by the value of the mean anomaly M, we also expect a constant phase shift in the redshift as well as in the amount of other perturbations subjecting the satellites. The phasing difference corresponds to an orbital period of $\approx 6.5h$.

Satellite	e	$a\ [km]$	$i\ [deg]$	$\Omega\ [deg]$	$\omega\ [deg]$	$M\ [deg]$
GSAT0202	0.162	27977.6	49.7	52.521	56.198	136.069
GSAT0201	0.162	27977.6	49.7	52.521	56.198	316.069

Table 4.2: Keplerian elements of GSAT0202 and GSAT0201.
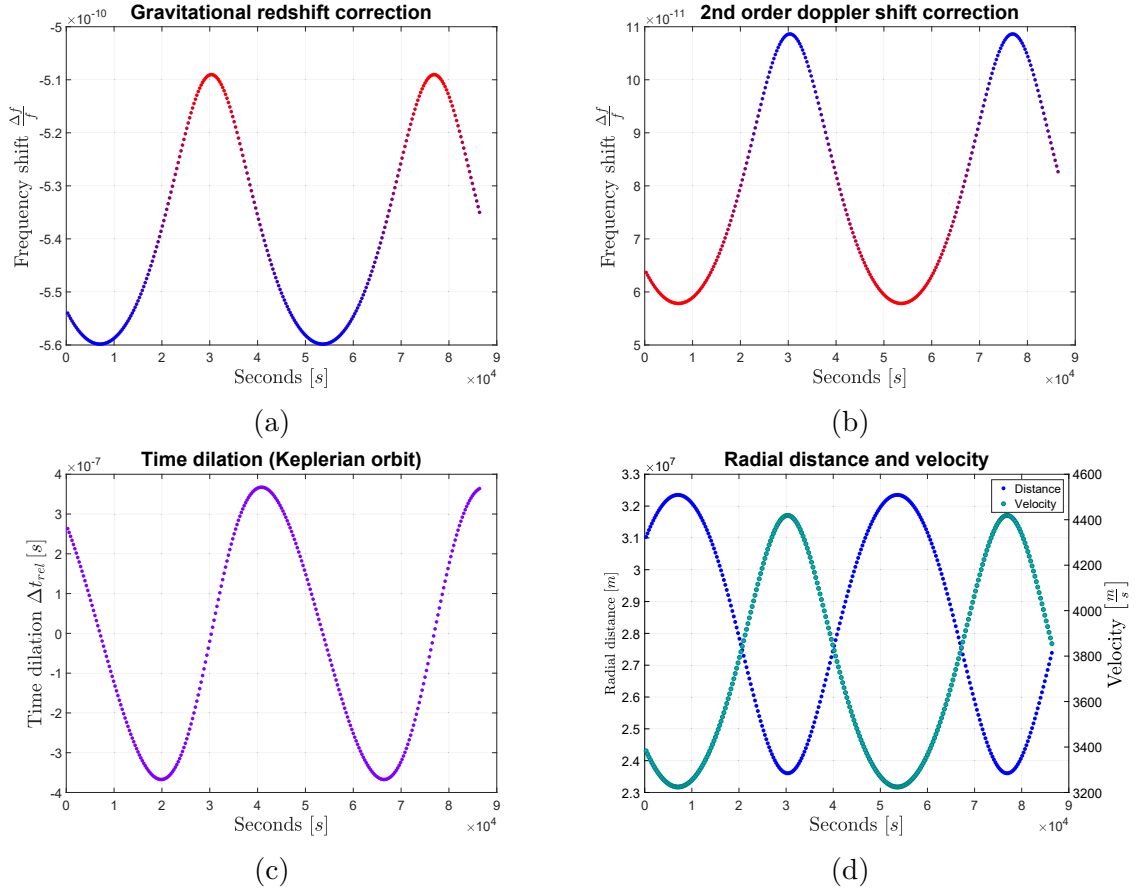
Figure 4.2: Different relativistic redshifts over one orbital revolution. Picture 4.2d shows the radial distance of the satellite with respect to Earth's center over one day as well as its velocity. The function plots in the first row show the gravitational (4.2a) as well as the 2nd order Doppler shift (4.2b) corrections computed with the real SP3 orbit solutions for satellite GSAT0202. Plot 4.2c demonstrates the total relativistic time dilation according to 1.20. The colormap applied for the plots 4.2a and 4.2b indicates the amount of redshift to be corrected for. Red labels higher redshift, blue labels lower redshift.

The plots in figure 4.2 also indicate that the expected frequency shifts owing to the single redshift components (4.2a and 4.2b) affecting the rate of the satellites' clocks are larger than the frequency stability on orbital time scale as specified in figure 4.1 above. Thus, the requirements for a precision test of the redshift under the experimental settings realized with the help of the clock equipment of the GALILEO satellites are met under the prerequisite that one uses clock data over a period which matches the favored stability regime of approximately one day. The specific relativistic redshift model to be tested is the integrand of equation 1.11. For the potential U, we insert the following expression:

$$U = -\frac{GM_\oplus}{r}\left(1 - \frac{J_{2\oplus}a_\oplus{}^2}{r^2}\left(\frac{3z^2}{2r^2} - \frac{1}{2}\right)\right) \tag{4.1}$$

An assessment of the influence of higher order gravitational potentials of the Earth reveals that the amount of expected relativistic redshift contributions are rather

negligible, because their impact is beyond the sensitivity limit of the clocks. To test the LPI, one conventionally introduces a test parameter α which quantifies a possible violation of the modeled redshift:

$$\frac{\Delta f}{f} = (1 + \alpha)\left(-\frac{GM_\oplus}{c^2 r}\left(1 - \frac{J_{2\oplus}a_\oplus{}^2}{r^2}\left(\frac{3z^2}{2r^2} - \frac{1}{2}\right)\right) + \frac{v^2}{2c^2}\right) \qquad (4.2)$$

Before we continue with the fitting procedure based on that model 4.2, some preprocessing has to be applied to the clock data beforehand. At first, we identify outliers in the data sets based on the Grubbs criterion [49]. This criterion requires that the data to be tested for outliers is approximately normal distributed. Therefore, a Chi-squared test is carried out previously, in order to check whether the test is reasonable or not. For the case that the Grubbs criterion is not fulfilled, we identify a data element as an outlier, if it is more than three standard deviations away from the mean.

Atomic clocks typically exhibit frequency drifts and their noise characteristics can be described by specific stochastic noise processes. Motivated by the considerations in section 3.2.1, we choose a time-dependent linear polynomial with real-valued coefficients as a suitable model to describe the non-stochastic long-term behavior of the clocks. It implies a bias value a_0 and a linear drift parameter a_1. For RAFSs another quadratic drift parameter a_2 is usually added. All these parameter values are also typically contained in the GNSS navigation messages as broadcast ephemerides so that each user can correct the clock bias and drift with respect to some reference time (compare 3.22 and 3.23) which is conventionally given in some GNSS specific time system. Thereby the quadratic factor is often omitted for PHMs or set to zero, because it is negligibly small. In the following, these parameters are fitted in parallel to the violation parameter for each day.

Before the satellites are launched into space, a frequency bias is applied to the atomic clocks, in order to synchronize them with ground based reference clocks. This constant rate component corresponds to the 2nd and 3rd terms in equation 1.15 and just depends on the altitude of the destination orbit and Φ_0. Additionally, the second-order Doppler effect and the eccentricity effect are considered. The latter is typically very small for GNSS satellites that nominally fly on a nearly circular trajectory. For geodetic or positioning purposes, though, this relativistic frequency modulation component is applied to the clock data by default. Conventionally, formula 1.20 is used for this purpose [4]. However, this model is not appropriate for a precision test of the relativistic redshift, because it is based on a Keplerian assumption implying unperturbed satellite motion around Earth. We engage this issue by introducing and applying two model corrections to the clock data. The first correction can be determined from the difference between the numerically integrated expression 1.13 and the corresponding result from equation 1.20. For the evaluation of the individual terms the orbit data of the respective satellite are needed. For this we use the current precise orbit solutions from the SP3 files. The second correction fixes the error which arises due to the omission of the quadrupole potential term which is now included in the relativistic redshift model 4.1. The amounts of both corrections are displayed in figure 4.3. The Fourier transformations of the prepro-

---

[4]https://gssc.esa.int/navipedia/index.php/Relativistic_Clock_Correction

cessed clock data, before and after the corrections have been applied, demonstrate that the harmonics of twice the orbital frequency f_{orb} significantly reduce (see figure 4.4) which is very close to the 4th harmonic of the Earth's rotation rate f_{day}. In addition to the higher order potential term mentioned above, the question arises whether other contributions due to third body perturbations must also enter the relativistic redshift model. We shortly outline the redshift contributions of the Lunar and Solar tidal potentials. According to [127], each of these potentials U_B can be computed by:

$$U_B = \mu_B \left(\frac{1}{|\mathbf{r} - \mathbf{r}_B|} - \frac{1}{|\mathbf{r}_B|} - \frac{\mathbf{r} \cdot \mathbf{r}_B}{|\mathbf{r}_B|^3} \right) \tag{4.3}$$

Where $\mathbf{r}$ and $\mathbf{r}_B$ are vectors with respect to the satellite and the third body in the ECI frame. Table 4.3 indicates that the influence of the perturbing third body potentials is rather small and hardly change the value of the relativistic redshift in contrast to the other two redshift model corrections already mentioned. Therefore, we disregard these effects with respect to our analysis.

Effect	Peak-to-peak amplitude
Deviation from Keplerian orbit	80 ps
Gravitational redshift due to J_2	30 ps
Gravitational redshift due to Moon	4 ps
Gravitational redshift due to Sun	2 ps

Table 4.3: Relativistic redshift due to other third body potentials.
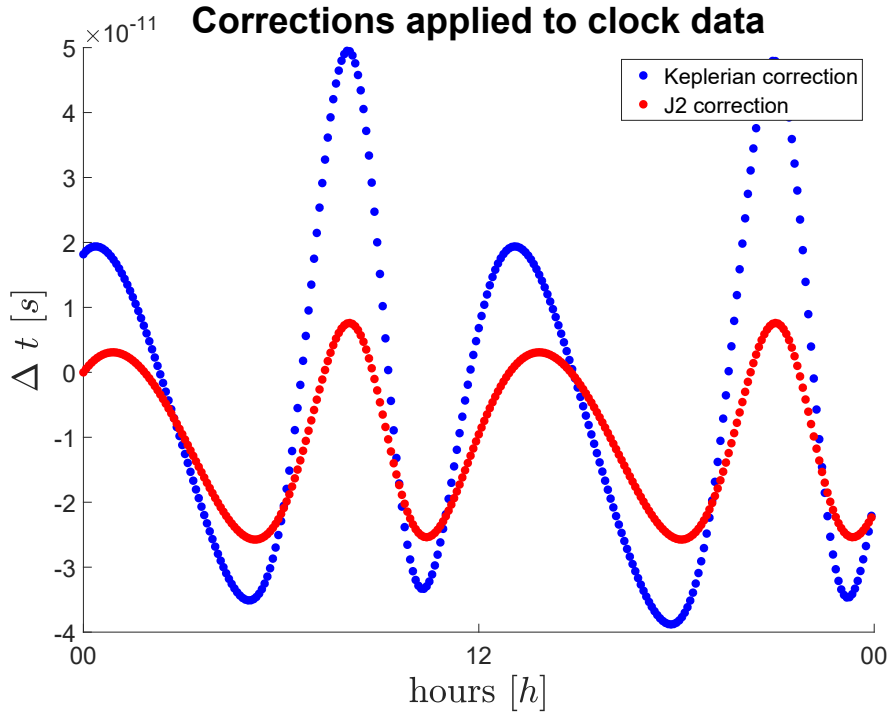
Figure 4.3: Both Keplerian and J2 corrections for GPS week 1979 applied to the clock solution of satellite GSAT0202.
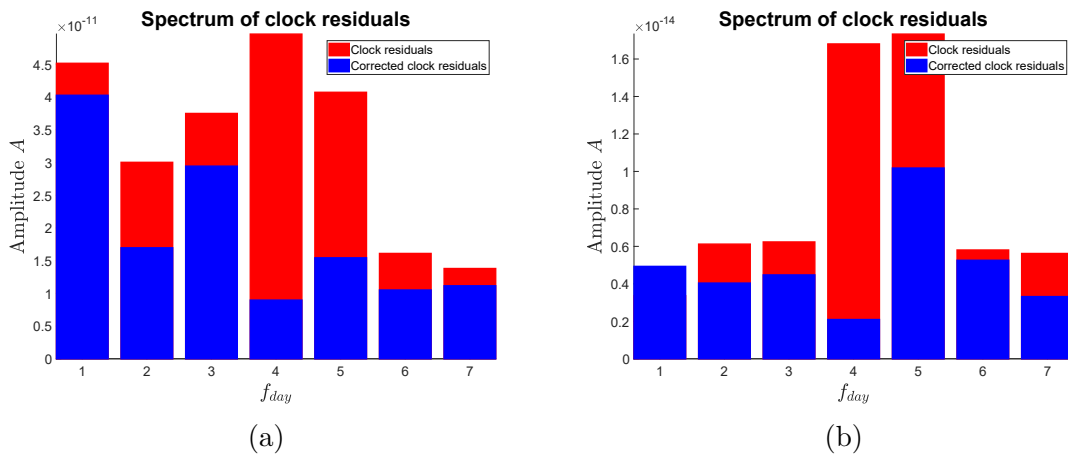
Figure 4.4: Fast Fourier transformations of raw and differentiated clock data (4.4a and 4.4b) after detrending and correction of systematic model errors. It is evident that the 4th harmonic could be reduced significantly in both clock data sets after the application of both Keplerian and J2 corrections. The fundamental frequency here is the Earth's rotation rate f_{day}.

The spectral analysis above (4.4) shows that both corrections constitute crucial model enhancements that must be considered for a careful redshift analysis. Therefore we take the integral of 4.2 as a fit function for α:

$$\Delta t_{rel} = \int d\tau \left[-\frac{GM_\oplus}{c^2 r} \left(1 - \frac{J_{2\oplus} a_\oplus{}^2}{r^2} \left(\frac{3z^2}{2r^2} - \frac{1}{2} \right) \right) + \frac{v^2}{2c^2} \right] \tag{4.4}$$

which rephrases the expression for the elpased time of the clock we already encountered in 1.11. Note that unlike the definition of α in Figure 1.1 in Chapter 1.1, the equation 4.4 includes both relativistic effects. The complete fit function now reads:

$$f_n \left(t, \alpha, a_1, a_0 \right) = \left(\alpha_n \Delta t_{rel} \left(t \right) + a_{1,n} t + a_{0,n} \right) \tag{4.5}$$

where the index n runs over a number of points in time t_i comprised by a linearly spaced time vector $\mathbf{x}$. We now adopt an ordinary Least-Squares method used for estimation. The basic assumptions for an Ordinary Least Squares (OLS) fit imply a linear function of the model predictors and a white noise model ϵ_G with expectation value $\mathbb{E}\left[\epsilon_G\right] = 0$ as well as variance $\mathbb{V}\left[\epsilon_G\right] = \sigma^2$ which represents the noise process inherent to the clock data. An OLS estimate minimizes the mean-squared error:

$$\underset{\beta}{argmin} \sum_{n=0}^{N} \left(y_n - f_n \left(t, \beta \right) \right)^2 \tag{4.6}$$

where $\beta = (\beta_1, \ldots, \beta_p)$ contains all p parameters to be estimated, y_n represents the sampled clock data and $f_n \left(t, \beta \right)$ is the linear function depending on these parameters and the regressor values t. The data are re-sampled such that the index n runs over the number of seconds of a day. In matrix representation the clock data model reads:

$$\mathbf{y} = \mathbf{x}\beta + \epsilon_G \tag{4.7}$$

Taking the gradient of the mean-squared error with respect to the parameters and making use of the necessary optimality criterion we get:

$$\nabla_\beta \frac{1}{n} \left(\mathbf{y} - \mathbf{x}\beta \right)^T \left(\mathbf{y} - \mathbf{x}\beta \right) \overset{!}{=} 0 \tag{4.8}$$

$$\frac{2}{n} \left(\mathbf{x}^T \mathbf{y} + \mathbf{x}^T \mathbf{x}\beta \right) = 0 \tag{4.9}$$

$$\frac{2}{n} \mathbf{x}^T \left(\mathbf{y} - \mathbf{x}\beta \right) = 0 \tag{4.10}$$

$$\frac{2}{n} \mathbf{x}^T \mathbf{e} = 0 \tag{4.11}$$

in equation 4.11, the error $\mathbf{e} = \mathbf{y} - \mathbf{x}\beta$ is introduced which is to be minimized[5]. Solving for the parameter vector β we obtain the Gaussian normal equations:

---

[5]In order to fullfill the equation, the error vector must be orthogonal to the regressor and its expectation value must cancel out, i.e. that our problem formulation includes a number of constraints, which equals the number of parameters to be estimated plus one $(dim(\beta) + 1)$.

$$\beta = \left(\mathbf{x}^T \mathbf{x}\right)^{-1} \mathbf{x}^T \mathbf{y} \tag{4.12}$$

However there is an issue with the applicability of the OLS method to the clock data fit. Atomic clocks exhibit predominantly random noise ϵ_{RW}, or $\frac{1}{f^2}$ noise, which does not comply with our assumption that the data is subjected to white noise. That implies that the optimal Least-Squares estimate would not be unbiased, because $\mathbb{E}\left[\epsilon_{RW}\right] \neq 0$:

$$\mathbb{E}\left[\beta\right] = \mathbb{E}\left[\left(\mathbf{x}^T \mathbf{x}\right)^{-1} \mathbf{x}^T \left(\mathbf{x}\beta + \epsilon_{RW}\right)\right] \tag{4.13}$$

$$\Leftrightarrow \mathbb{E}\left[\beta\right] = \beta + \left(\mathbf{x}^T \mathbf{x}\right)^{-1} \mathbf{x}^T \mathbb{E}\left[\epsilon_{RW}\right] \neq \beta \tag{4.14}$$

An acceptable solution to this problem is the application of a noise transformation prior to fitting the data. Random walk noise maps a Wiener process $\mathfrak{W}$ which is continuous over time and has uncorrelated and stochastically independent increments[6]. Its representation can be given in integral form:

$$\epsilon_{RW} = \int_0^t d\epsilon_G \tag{4.15}$$

In other words, differentiation of the clock data with underlying random walk noise transforms into a data series, which is characterized by Gaussian or white noise ϵ_G. The plots in 4.5 show the clock data before and after noise transformation. As a consequence, the fitting model also changes to the integrand of 4.4, which is named f_{rel} hereinafter, such that the fit function 4.5 and the corresponding mean-squared estimator now translates to:

$$f_n\left(t, \alpha, a_0\right) = \left(\alpha_n f_{rel}\left(t\right) + a_{0,n}\right) \tag{4.16}$$

$$\Rightarrow \underset{\beta}{argmin} \sum_{n=0}^{N} \left(y_n - \alpha_n f_{rel}\left(t\right) - a_{0,n}\right)^2 \tag{4.17}$$

where we are left with a constant offset and the model for the frequency shift.

---

[6]White noise is independent of time, thus its power spectral density does not change and keeps stationary $PSD(\epsilon_G) = const$. On the contrary, a Wiener process is time dependent in a sense that its variance drifts over time, i.e. it has Gaussian increments $\mathfrak{W}_{t+\Delta t} - \mathfrak{W}_t \sim \mathcal{N}(0, \Delta t)$. Therefore, its power spectral density is not flat. The associated frequency spectrum can be computed as $PSD(\epsilon_{RW}(t)) = \frac{PSD(\epsilon_G)}{f^2}$, which can be proven by a Fourier transform of expression 4.15 $\epsilon_{RW} = \int_0^t \frac{d\epsilon_{RW}(t)}{dt}$.

(a)   (b)
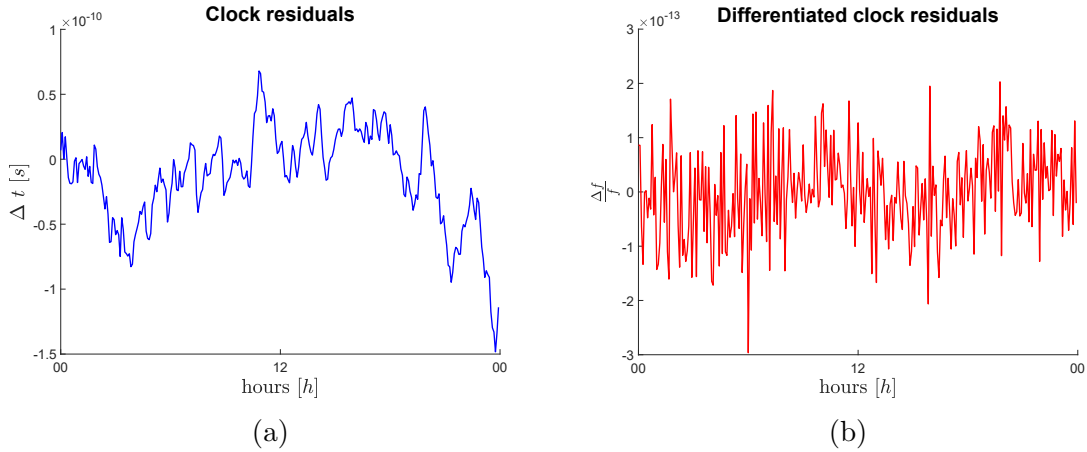
Figure 4.5: Comparison of detrended and corrected clock data before and after application of differentiation. In 4.5a one observes random walk noise predominating the clock residuals in the time domain whereas 4.5b shows the same example data set subjected to white noise in the frequency regime.

The inspection of the correlogram 4.6 of a sample time series suggests that the differentiated clock data still contains significant first order serial correlation, which we assume to be stationary. This is observed in all data sets that have been analyzed. A parameter estimation in an OLS fashion as in 4.12, carried out with autocorrelated data sets would thus turn out inefficient. The application of the Durbin-Watson-Test
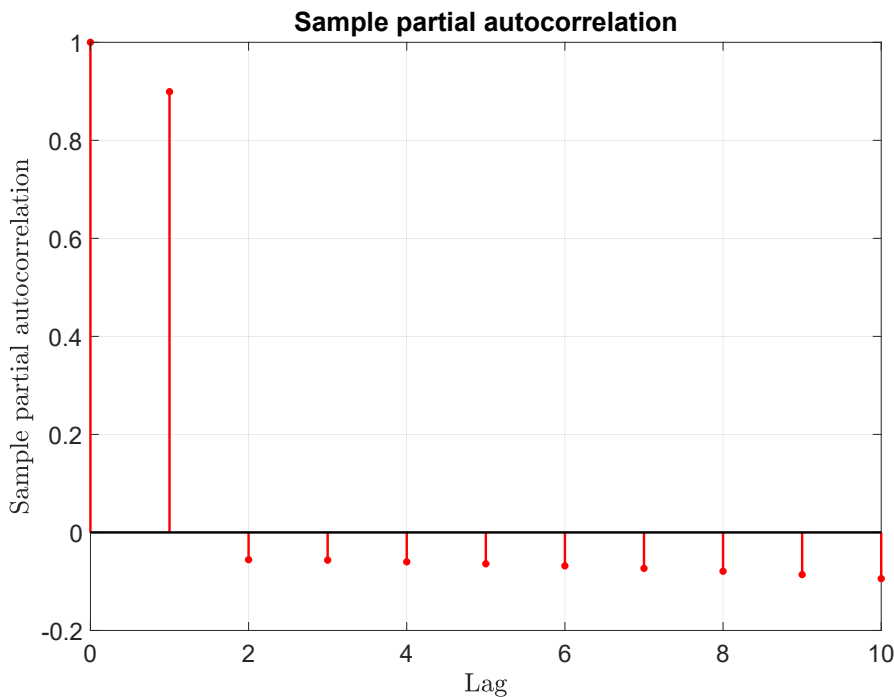
Figure 4.6: Autocorrelation computed from a sample clock data set. The horizontal axis scales the lag space. Since there is obviously significant autocorrelation at lag 1, a first order autoregressive model (AR(1)) is chosen to correct the data series, i.e. we presume each sample of the time series to linearly depend on its previous value.

[17] additionally helps to confirm that the null hypothesis assuming no autocorrelation must be rather rejected. The Durbin-Watson test is used to identify whether the sum of the differences of subsequent residuals have a significant amount or not:

$$d = \frac{\sum_{n=0}^{n} (e_t - e_{t-1})^2}{\sum_{n=0}^{n} e_t^2} \tag{4.18}$$

According to this test, the values obtained from the sample sets are substantially located in an interval between 0 and 2. Therefore, the assumption of positive auto-correlation among the error terms is strongly supported. For OLS, it was assumed that the residuals are perfectly white $N(0, \sigma^2)$ implying a constant variance for all times, but this assumption is no longer valid when the model errors are not uncorrelated. In order to overcome the model deficiencies, a Generalized Least Squares (GLS) scheme is introduced. This helps us to reformulate the Least-Squares approach such that the correlation is considered in the time series modeling. First, we re-specify the error term appearing in formula 4.7, which should now capture the underlying correlation. For this purpose we chose an AR(1) process[7] denoted as

$$e_t = \rho e_{t-1} + \epsilon_G \tag{4.19}$$

where $|\rho| < 1$ is the correlation parameter of the subsequent delayed argument e_{t-1} which measures the strength of linear coupling to the present left-hand-side value and ϵ_G models white noise characterized by $\epsilon_G \sim \mathcal{N}(0, \sigma_{\epsilon_G}^2)$. Without loss of generality we also set $\mathbb{E}[e_t] = 0$, hence there is no other parameter to be estimated than ρ. By regression of the vector $\mathbf{e}_t$ on $\mathbf{e}_{t-1}$, which represents the time-shifted values of the vector $\mathbf{e}$ (see 4.11) of the remaining residuals resulting from the OLS method, the new correlation parameter ρ can be estimated. The according relation for the Least-Squares estimate of this parameter reads:

$$\nabla_\rho \frac{1}{n} (\mathbf{e}_t - \mathbf{e}_{t-1}\rho)^T (\mathbf{e}_t - \mathbf{e}_{t-1}\rho) \overset{!}{=} 0 \tag{4.20}$$

$$\frac{2}{n} \mathbf{e}_{t-1}^T (\mathbf{e}_t - \mathbf{e}_{t-1}\rho) = 0 \tag{4.21}$$

$$\rho = (\mathbf{e}_{t-1}^T \mathbf{e}_{t-1})^{-1} \mathbf{e}_{t-1}^T \mathbf{e}_t = \frac{\sum_{i=2}^{n} e_{t-1} e_t}{\sum_{i=2}^{n} e_{t-1}^2} \tag{4.22}$$

Next, the covariance matrix of the AR(1) process 4.19 can be expressed from pairs of lagged residuals:

---

[7]The differentiated clock data exhibit a noisy, but stable behavior and therefore one can assume that the underlying process is Wide-Sense Stationary (WSS) requiring that its expectation $\mathbb{E}[e_t]$ value and variance $\mathbb{V}[e_t]$ both do not vary with respect to time.

$$Cov\left(e_t, e_{t-k}\right) = \mathbf{V} = \frac{\sigma_{\epsilon_G}^2}{1-\rho^2} \begin{bmatrix} 1 & \rho & \dots & \rho^{t-1} \\ \rho & 1 & \dots & \rho^{t-2} \\ \vdots & \vdots & \ddots & \vdots \\ \rho^{t-1} & \rho^{t-2} & \dots & 1 \end{bmatrix} \tag{4.23}$$

For further reading about the treatment of disturbance processes and especially serial correlation within time series, we refer the reader to [48]. The fraction in the above formula 4.23 on the rhs is the variance of the AR(1) process denoted as $\mathbb{V}\left[e_t\right] = \frac{\sigma_{\epsilon_G}^2}{1-\rho^2}$. This can be shown by a short calculation. In a first step, recursive back-substitution into formula 4.19 is performed and consequently we take the variance of the back-substitution result:

$$e_t = \sum_{i=0}^{\infty} \rho^i \epsilon_{G_{t-i}} \tag{4.24}$$

$$\mathbb{V}\left[e_t\right] = \mathbb{E}\left[\left(\sum_{i=0}^{\infty} \rho^i \epsilon_{G_{t-i}}\right)\left(\sum_{i=0}^{\infty} \rho^i \epsilon_{G_{t-i}}\right)\right] = \sum_{i=0}^{\infty} \rho^{2i} \mathbb{E}\left[\epsilon_{G_{t-i}}^2\right] \tag{4.25}$$

$$\mathbb{V}\left[e_t\right] = \frac{\sigma_{\epsilon_G}^2}{1-\rho^2} \tag{4.26}$$

For the step from 4.25 to 4.26 we make use of the identity of geometric series under the above condition that $|\rho| < 1$. Note that the mixed terms in 4.25 vanish, since the error terms $\epsilon_{G_{t-i}}$ are independent of each other. The single entries of the covariance matrix can be induced systematically from the following relations:

$$Cov\left(e_t, e_{t-1}\right) = \mathbb{E}\left[e_t e_{t-1}\right] \tag{4.27}$$

$$Cov\left(e_t, e_{t-1}\right) = \mathbb{E}\left[\left(\rho e_{t-1} + \epsilon_{G_{t-1}}\right) e_{t-1}\right] = \quad \mathbb{E}\left[\rho e_{t-1} e_{t-1}\right] + \mathbb{E}\left[\rho e_{t-1} \epsilon_{G_{t-1}}\right] \tag{4.28}$$

$$Cov\left(e_t, e_{t-1}\right) = \rho \mathbb{E}\left[e_t^2\right] = \rho \mathbb{V}\left[e_t\right] \tag{4.29}$$

$$\vdots \tag{4.30}$$

$$Cov\left(e_t, e_{t-k}\right) = \mathbb{E}\left[\left(\rho e_{t-1} + \epsilon_{G_{t-1}}\right) e_{t-k}\right] = \quad \mathbb{E}\left[\rho e_{t-1} e_{t-k}\right] + \mathbb{E}\left[\rho e_{t-k} \epsilon_{G_{t-1}}\right] \tag{4.31}$$

$$Cov\left(e_t, e_{t-k}\right) = \rho \mathbb{E}\left[e_t e_{t-k}\right] = \rho^k \mathbb{V}\left[e_t\right] \tag{4.32}$$

Where the WSS property was used in the last step 4.32 ($Cov\left(e_t, e_{t-k}\right) = \mathbb{V}\left[e_t\right]$) saying that the covariance between samples with different time tags just depend on the time-lag between these samples. As an aside, the time-lag governs the decay of the covariance between different samples of the AR(1) process. For any pairs of samples with covariance $Cov\left(e_t, e_{t-k}\right) = \rho^k \mathbb{V}\left[e_t\right]$, one finds from equating 4.32 with $\mathbb{V}\left[e_t\right] e^{-\frac{1}{\tau}}$ a characteristic time constant of $\tau = -\frac{k}{\ln(\rho)}$ by comparison of the exponents. Finally, we arrive at the new covariance matrix 4.23 and use it to transform the OLS model, which then produces new values for our estimation parameters. After reformulation of the underlying model equation 4.7, the Least-Squares model now reads:

$$\mathbf{Ty} = \mathbf{Tx}\beta + \mathbf{T}e \tag{4.33}$$

with some transformation matrix $\mathbf{T}$ that can be obtained from the decomposition $\mathbf{T}^{-1}\mathbf{T} = \mathbf{V}$. Replacing $\mathbf{x}$ by $\mathbf{Tx}$ in 4.12, we yield a new expression for our estimator:

$$\beta_{AR} = \left(\mathbf{x}^T\mathbf{V}^{-1}\mathbf{x}\right)^{-1}\mathbf{x}^T\mathbf{V}^{-1}\mathbf{y} \tag{4.34}$$

whereas equation 4.34 represents the new estimator β_{AR}, which contains our desired violation parameter estimates and the bias for each day according to 4.5. In this model, due to the noise transformation, the optimal Least-Squares estimate β_{AR} is now unbiased and the remaining noise reduces to white noise as was assumed in 4.7. The day-wise results of the Least-Square fits of model 4.2 to each of the clock data sets covering the time intervals given in table 4.1 are subsumed in figure 4.7.
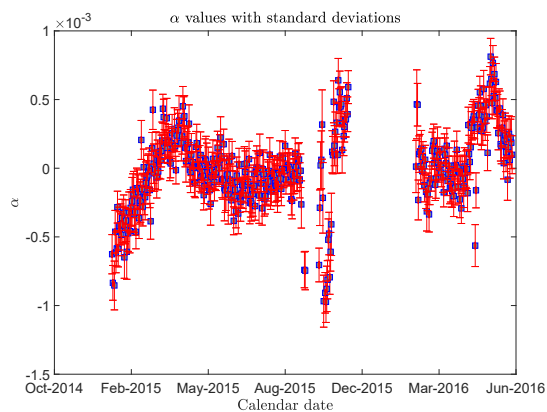
(a) Clock data set 1 results
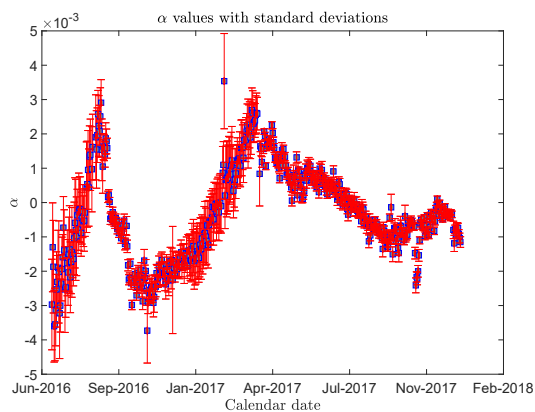
(b) Clock data set 2 results
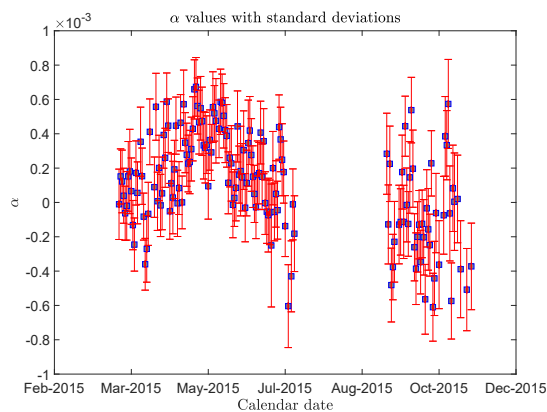
(c) Clock data set 3 results
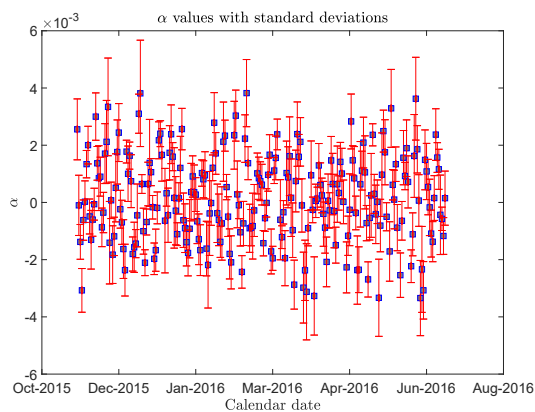
(d) Clock data set 4 results
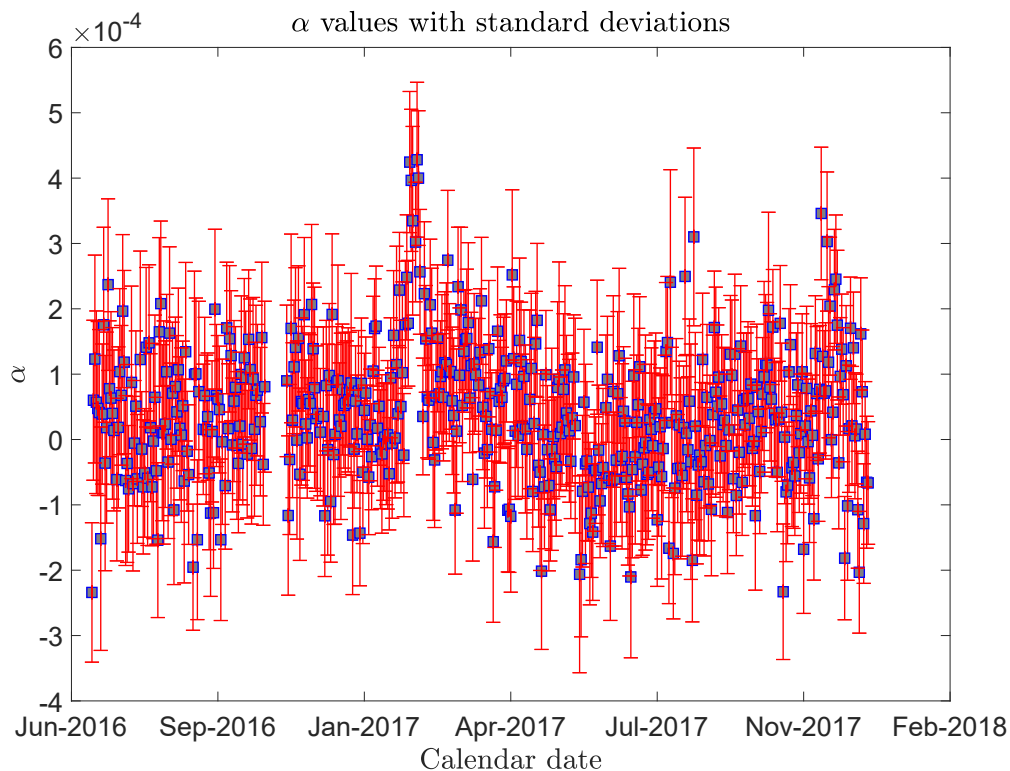
(e) Clock data set 5 results

Figure 4.7: Results of daily violation parameter estimations for each clock data set listed in table 4.1.

Data anomalies and data fusion

As the results show, clock 5 reveals the most stable behavior, although some anomalous observations can be identified around February 2017, which are the most prominent among others in the data set. Figure 4.7d presents the fit results of the RAFS data of satellite GSAT0202, which is of inferior frequency stability over the specific time regime of one orbital revolution in comparison to the other PHMs. For that reason, we discard these results from our analysis. The results of clock 2 (see figure 4.7b) exhibit strong drift behavior over the whole analysis epoch. From internal conversations with the subject matter experts from ESA, it was confirmed that there have been persisting non-nominal operations flagged by the specific clock unit throughout that period. We therefore also exclude that data from our analysis. Among persisting anomalies, as experienced by PHM-B of satellite GSAT0201, also sporadic events were reported by the redundant PHM-A unit of GSAT0201. Table 4.4 sums up the events especially associated with the redundant clock, that are responsible for any frequency anomalies during the corresponding time period. Other than those events caused by operational changes, there was one radiation event detected by both clocks PHM-B on GSAT0202 and PHM-A on GSAT0201, which caused a frequency jump.

Event	Occurance
Increase of clock cavity temperature	17-Sep-2015
SARANT antenna activation (current/temperature changes)	24-Oct-2015
Gyro activation (current/temperature changes)	07-Nov-2015
Radiation flare	11-Oct-2015

Table 4.4: Reported anomalies concurrent to the operations of PHM-A unit of GSAT0201.

We finalize the data analysis by combining the independent α results per set. Thereby, we apply inverse-variance weighting to calculate the optimal weighted average and the associated variance for each of the selected sets of estimated α parameters (see [52] for details regarding this approach). The optimal estimator for the average α value can be computed as:

$$\hat{\alpha} = \frac{\sum_{i=1}^{n} \frac{\alpha_i}{\sigma_i^2}}{\mathbb{V}(\hat{\alpha})} \tag{4.35}$$

where $\mathbb{V}(\hat{\alpha})$ is the variance:

$$\mathbb{V}(\hat{\alpha}) = \frac{1}{\sum_{i=1}^{n} \frac{1}{\sigma_i^2}} \tag{4.36}$$

The final statistical results are summed up in table 4.5.

4.2   Bayesian clock data post-processing

In this section, we employ a Bayesian post-processing scheme that is applied to the α data sets produced, as described in the preceding section 4.1, to infer a combined statistical result. From the data sets generated, we thereby focus on the data sets 1, 3 and 5 based on PHM data, since they exhibit the most reliable behavior throughout the corresponding epoch as pointed out above.

A Bayesian framework helps to consistently estimate a combined statistical distribution from the data at hand to obtain the desired posterior from which we can derive the final sample mean and the corresponding sample variance for the assessment of the violation parameter α. Bayesian inference requires an initial hypothesis that reflects accumulated knowledge about the data generating environment. We thus need to identify prior information that might narrow down the statistical parameter space. In particular, we will have a look at certain systematic effects potentially influencing the satellites' clocks performance and constrain their maximum contribution to a change in the estimated α value due to their effect on the clock's frequency.

Bayesian inference is a handy tool when it comes to the interpretation of data B in the case that some additional proposition or several hypotheses A can be thrown about the data generating environment. Bayes theorem states the following:

$$P(A|B) = \frac{P(B|A)P(A)}{P(B)} \tag{4.37}$$

The lhs describes the conditional probability that some statement A about the environment is true given B, it is also called the *posterior probability*. The rhs states just the inverse and is proportional to the probability function $P(B|A)$ and the function $P(A)$ (*prior probability*) which is also called *initial belief*. We think of the rhs as an update of the prior probability $P(A)$, which can be computed with the help of our measurement statistics produced by the environment $P(B|A)$. If $P(\cdot|\cdot)$ could be modeled by a Gaussian distribution, A would describe the mean value, whereas B would represent the current measurement distribution. The update then leads to augmented knowledge about our initial hypothesis in that it describes the location of the Gaussian mean somewhat more precise. Generally $P(B|A)$ is not a probability distribution, it is often called *likelihood*. In most cases, there is only limited knowledge about A, or it even cannot be observed directly, so that one starts with only little information allowing a rough estimation about A. $P(B)$ is the so-called *marginal likelihood* and takes the same value for all possible propositions A. It is the integral over all hypotheses $P(B|A)P(A) = \int_0^1 dA\,(P(B|A)P(A))$.

$\alpha \pm \Delta\alpha\,(\times 10^{-5})$	Clock 1	Clock 3	Clock 5
Statistics	-0.33 ± 0.6	8.13 ± 1.5	3.53 ± 0.5

Table 4.5: Final statistical results for the estimated α parameters of all considered clock data sets.

Lets demonstrate with a simple example the application of Bayes theorem. We do a dice experiment and would like to find out whether the dice is fair or not. When rolled, an ideal dice would give an equally likely chance that its upper face shows any number of pips counting an integer between one and six. The experiment should take a sequence of $n = 120$ dice rolls, where we expect that during the experiment all faces show up approximately an equal number of times. The probability that a particular integer number is realized after a couple of rolls is given by the Binomial Distribution, which reads:

$$f_{bin}(k|n,p) = \binom{n}{k} p^k (1-p)^{n-k} (k) \tag{4.38}$$

This is now our *likelihood* function producing our measurements. For $p = \frac{1}{6}$, the Binomial Distribution gives the maximum probability for 20 realizations of any particular integer after the experiment has been done. Given that the dice is not ideal, what would the result look like, if we cannot expect that $p = \frac{1}{6}$? Let us assume we have a collection of random outcomes after a sequence of 120 dice rolls and take this as our statistics for further investigations. For our hypothesis that should explain the *initial belief* on how the probability parameter is distributed, we take a Beta Distribution which is the conjugate prior of the Binomial Distribution:

$$f_{beta}(p|a,b) = \frac{1}{B(a,b)} p^{a-1} (1-p)^{b-1} \tag{4.39}$$

where $B(a,b)$ is the normalization coefficient $\int_0^1 dp \left(p^{a-1} (1-p)^{b-1} \right)$. The Beta Distribution depends on two hyper parameters a and b which determine the shape of the distribution. As starting parameters we choose $a = 1$ and $b = 1$. For these parameters, the Beta distribution represents a linear polynomial revealing poor information about the location of the real probability value. In dependence of the outcome of each dice roll, the Beta Distribution parameters are then updated such that the shape of the resulting curve converges gradually to the function, which correctly describes the distribution of the current measurement statistics and the location of the plausible probability value. In case of success, a is increased by one and b is incremented accordingly for each failure. The product of the Binomial Distribution 4.38 and the Beta Distribution 4.39 gives us the desired posterior distribution:

$$f_{bin}(k|n,p) \, f_{beta}(p|a,b) = \binom{n}{k} \frac{\left(p^{k+a-1} (1-p)^{n-k+b-1} \right)}{B(a,b)} \tag{4.40}$$

$$f_{bin}(k|n,p) \, f_{beta}(p|a,b) = B(a+k, b+n-k) \tag{4.41}$$

$$f_{beta}(p|\bar{a}, \bar{b}) = B(a+k, b+n-k) \tag{4.42}$$

The product is thus again a Beta Distribution with a new set of hyperparameters. Note that after normalization of equation 4.40 which results in 4.41 the constant factors of both the Beta and Binomial Distribution cancel out.
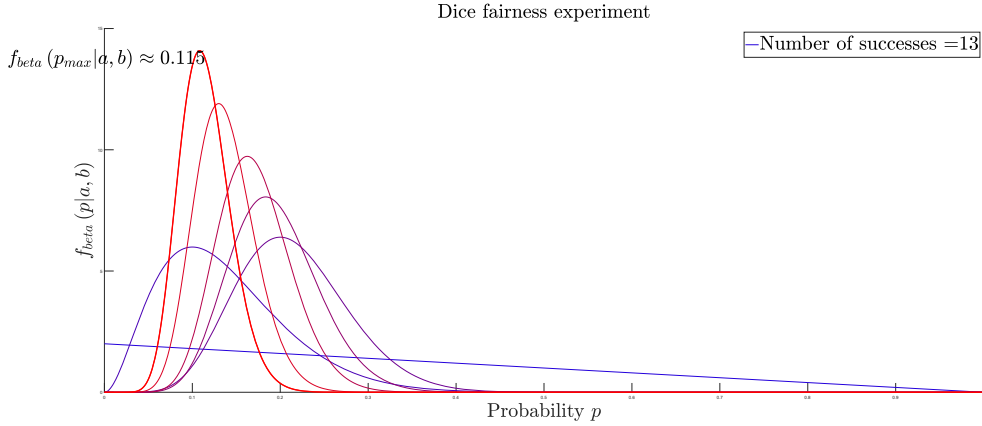
Figure 4.8: Evolution of the posterior probability distribution over 120 dice rolls. The more often the experiment is done, the more precise becomes the localization of the real probability parameter p. The blue curve shows the posterior after the first trial with parameters $a = 1$ and $b = 1$, the other curves give the distributions after $\{20, 40, 60, 80, 100, 120\}$ trials. A gradually increasing red color saturation level corresponds to later trials.

The Bayesian approach presented above is now applied to the problem of numerically determining the combined sample mean and corresponding sample variance of our α data sets (see Figure 4.7). For each data set, we build a Markov chain using a Markov Chain Metropolis-Hastings (MCMH) algorithm to generate independent draws from the desired posterior probability distribution $f_{post}(\mu_\alpha | x_1, x_2, \ldots, x_n)$ of the α sample mean μ_α. This is proportional to the joint probability of a likelihood function f_{like} and prior distributions π:

$$f_{i,post}(\mu_\alpha | x_1, x_2, \ldots, x_n) \propto f_{i,like}(x_1, x_2, \ldots, x_n | \tau_1, \ldots, \tau_n)\, \pi_{i,\tau_1} \cdots \pi_{i,\tau_n} \qquad (4.43)$$

where $x_1, x_2, \ldots, x_n \in X_i$ are α data samples associated with one of the α data sets $\{X_1,\ X_3,\ X_5\}$. π_{i,τ_k} denotes the candidate prior distributions used to determine the shape parameters τ_k of $f_{i,like}$. For example, common informative priors are normal distributions $\pi \sim \mathcal{N}(\mu, \sigma)$, while in contrast, typical uninformative priors are flat or uniform distributions $\pi \sim \mathcal{U}(-\sigma, \sigma)$ with boundaries $\pm\sigma$. Once the posterior is found, we can then in turn use each of the resulting posterior distributions $f_{i,post}$ to derive the combined sample mean and corresponding sample variance from a combined posterior distribution. Before starting to draw data samples, we must first define reasonable prior distributions, which should reflect information about any systematics associated with the clock experiment. In conjunction with the likelihood function $f_{i,like}$, we can then generate an update of the distribution for the parameters being sought.

The algorithm 1 in section A.1 of the appendix A shows an MCMH algorithm in detail. In anticipation of the output, a brief note on the Bayesian inference results and the resulting marginalized posterior distributions for all α data sets in A.2 should be highlighted here.

4.2.1 Prior analysis

The atomic clocks of the Galileo satellites reside in a protected and controlled environment that stabilizes the frequency generation process. However, this process is affected by environmental disturbances like temperature drifts and magnetic field variations, which have an impact on the clock data from which we infer the statistics of the violation parameter. In the following, the impact of both magnetic and temperature perturbations is addressed. For a more comprehensive description of systematic effects such that magnetic field perturbations affecting atomic clock transition frequencies, the reader is referred to [64].

As a basis for the quantitative evaluation of clock frequency changes due to temperature or magnetic field strength variations, we refer to the pertinent technical documentation [90]. In this article, the on-ground performance of both RAFS and PHMs is described, whereby for our considerations we focus on the performance specifications of the PHMs. The PHM specifications define, that the clock sensitivity due to temperature variations amounts:

$$\frac{\Delta f}{f} = 2 \times 10^{-14} \Delta T \tag{4.44}$$

and the respective drift due to magnetic field strength disturbances reaches a sensitivity of:

$$\frac{\Delta f}{f} = 3 \times 10^{-13} \Delta B \tag{4.45}$$

4.2.1.1 Prior analysis: Magnetic perturbations

The atomic clocks feature a magnetic shielding that protects against magnetic field perturbations. Satellites are magnetically noisy and can cause electromagnetic interferences due to satellite mission operations. Table 4.4 shows a list of events associated with operational activities like reaction wheel loading/offloading responsible for abrupt changes in current flow on the spacecraft bus. This in turn generates electromagnetic disturbances at the location of the atomic clock depending on the magnetic field attenuation due to the permeability of structural elements including satellite assemblies and finally the protective shielding around the atomic clock. Another source of magnetic perturbations is the Earth's magnetic field. We limit the investigation of possible magnetic field perturbations to the modeling of the Earth's magnetic field due to the absence of supplementary measurement data. The magnetic field strength is predicted by using the 12th generation of the International Geomagnetic Reference Field (IGRF) model [116] [115]. From consultation of mission data from the Time History of Events and Macroscale Interactions during Substorms (THEMIS) [8] satellite constellation, especially the THEMIS-A[8] mission data, it can be validated that the model values produced by the IGRF deviates up to a maximum value

---

[8]The THEMIS-A satellite is one of 5 satellites continuously recording magnetic field data, in order to explore the causes and properties of magnetic storms occurring in the magnetosphere.

of 10% from the corresponding measurements, see figure 4.9.
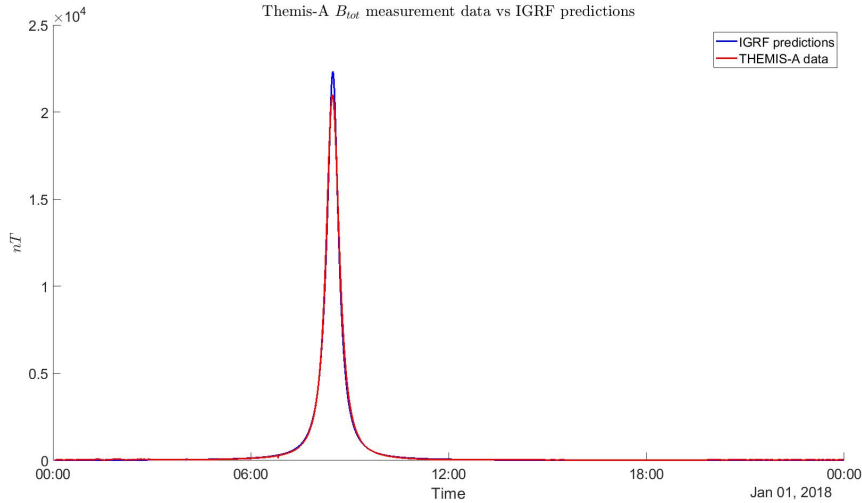
Figure 4.9: Comparison of results from the 12th generation IGRF model and the THEMIS-A mission data.

Note that this maximum deviation occurs for satellite altitudes that are beyond the MEO regime, occupied by the GALILEO satellites, where the magnetosphere is increasingly affected by interactions of the solar wind with the Earth's magnetic field. For a conservative estimation of the effect of the magnetic field acting on the satellites' clocks, their magnetic sensitivity is taken as uniform in all spacial directions, since no further details on the technical shielding specification are known[9]. The frequency shift is now computed using 4.45, where we use the total magnetic field strength in place of B, computed at the position of the spacecraft as given as per SP3 file. This frequency shift is then added as a correction term to the $f_{rel,n}$ term in equation 4.17. Subsequently, the exact same fitting approach as above is carried out to generate new α parameters for a certain data set. From these daily fit parameters, we determine the overall weighted average and the associated standard deviation for each clock data set. By taking the difference of the resulting and the uncorrected α parameter values, one can now compute a correction $|\Delta\alpha_B|$. Since we do not know whether the magnetic field correction is to be added or subtracted from the according α value, we assume a uniform distribution $\pi \sim \mathcal{U}(-\Delta\alpha_B, +\Delta\alpha_B)$ with the parameter boundaries of $-\Delta\alpha_B$ and $+\Delta\alpha_B$, whereas the correction amounts to $\pm\Delta\alpha_B = \pm 1.5 \times 10^{-5}$.

---

[9]The PHMs have a cylindrical magnetic shield assembly that protects the atomic clocks predominantly against magnetic field perturbations in radial direction, the symmetry axis is thereby deemed most sensitive. A more accurate approach would require the correct values for the magnetic permeability to compute the proper magnitude of the magnetic field strength component projected onto the symmetry axis.

4.2.1.2 Prior analysis: Temperature perturbations

We further investigate temperature systematics of the PHM that also lead to frequency shifts of the atomic clock according to relation 4.44. Thereby, we follow the same approach as we did above for the identification of an α correction term due to magnetic field systematics. In particular, we examine the transient thermal behavior of the satellite's PHM unit over one orbit, provided that the satellite is not eclipsed during the orbital period. With the analysis, we not only aim at quantifying the clock's change in temperature, but also seek for a better understanding of the phase relation between temperature systematic effects and the predicted redshift. However this task is particularly challenging, since no temperature housekeeping telemetry data are available for the satellite. For that reason, it is also not possible to determine effective material parameters, which otherwise could greatly facilitate a thermal analysis. Temperatures of the inside as well as the outside of the satellite are typically used to derive intensive material properties as the effective conductivity or emissivity of the spacecrafts bus structure. With these performance parameters, one can characterize the process of heat transfer specific to that structure. Despite that these essential information are not accessible, as far as the GALILEO FOC satellites are concerned, we construct a conservative grey-box Thermal Mathematical Model (TMM) describing the heat transfer through the antenna bus panel into the satellite's clock compartment. For that purpose, we use official data from documents for the GALILEO IOV satellites [47], since their structural build up is very similar to that of the GALILEO FOC satellites. Furthermore, the satellite layout as found from the pictures and general thermal engineering guidelines for spacecraft units (see [44]) are taken into account to get a reasonable picture on thermal design aspects. In addition, we complement these information with basic assumptions about the satellite's thermal environment. In this regard, we limit the factors of influence to the total solar irradiation, the satellite experiences throughout its orbit. The fraction of Earth albedo or Earth infrared radiation is thereby neglected for the reason of its marginal contribution in proportion to the direct solar radiation.

(a)   (b)
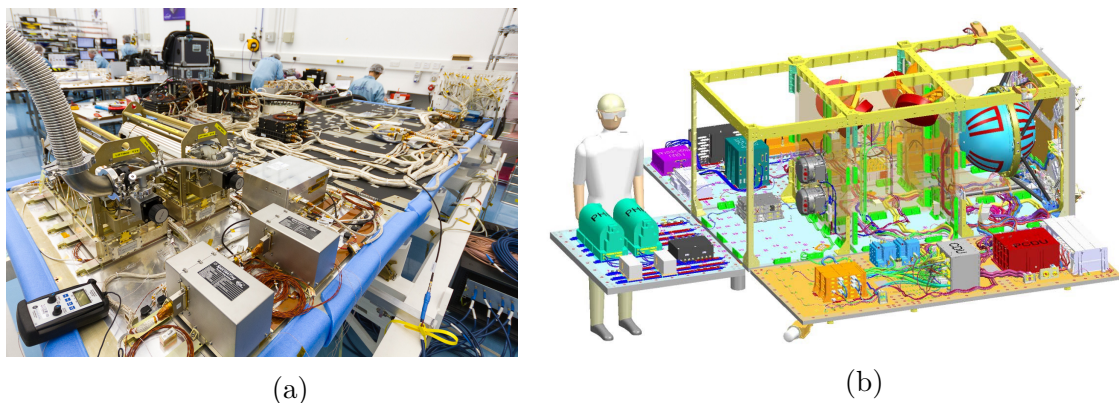
Figure 4.10: The left picture shows the timing subsystem of the GALILEO satellites [10]. The payload includes the RAFSs, which can be seen as grey boxes center bottom on picture 4.10a, as well as the PHMs, which are placed next to them, center left. The picture on the right is taken from [72] and helps to identify the location of the clocks.

The GALILEO satellites interior is split into 3 compartments as can be seen from figure 4.10b, which we assume to be thermally isolated from each other. Each platform component typically requires that its temperature control unit maintains the operating temperature within acceptable limits. Both PHMs as well as the RAFS and the Clock Monitoring and Control Unit (CMCU)[11] belong to the timing subsystem and are accommodated in one and the same compartment. We further restrict any considerations regarding the thermal analysis to this control volume. According to the Thermal Control System (TCS) design specifications, the lower T_{lb} and upper T_{up} bounds of the nominal operating temperature range of the PHMs read approximately $T_{lb} = 268K$ and $T_{up} = 283K$. Moreover, the acceptable temperature ranges of any neighboring electronic units are comparable to that of the clocks. For the analysis, we choose an arbitrary set-point temperature of $T_c = 278K$ as a reference. From internal discussions with the ESA, it was revealed that the temperature control unit, responsible for the PHMs, keeps this payload within a temperature range of $\pm 0.5K$ relative to the set-point value. Whenever this limit is over- or undershot, the controller starts regulating the temperature. Thereby, the time it takes for the TCS to bring the temperature down to the desired reference value is $600s$.

The clocks are assembled on aluminum shelves, also called doubler plates, which are mounted on the clock panel. These provide typically high conductivity values such that the heat received from that component is spread out by conduction and mainly transmitted through the mounting panel as well as distributed throughout the compartment by thermal radiation. Thereby, the effective surface area from which the heat is then re-emitted, is designed depending on the heat generated by the mounted unit. The more heat is produced by that unit, the larger the size has to be choosen to obtain a better heat distribution performance. The application of doubler plates thus avoids direct power dissipation via the components structural footprint into the mounting panel. In order to make the temperature profile among the electronic components in the compartment approximately uniform, a surface finishing with high emissivity properties is conventionally used for the compartments interior. From picture 4.10a one can deduce that the GALILEO satellites have a black paint (BP Z306, $\epsilon = 0.89$) control coating applied to the internal face sheets, representing the seperating layer between the panels honeycomb structure and the interior of the clock compartment. Only the clock mounting panel is left as bare aluminum. This layer is a typical sandwich element that covers the honeycomb structure from both sides (see 4.11a).

For the thermal analysis, we conservatively model the PHM payload as one thermal mass, distributed among the clock panel. Since no further information is available, based on our reasoning above, we assume that this panel also acts as the main heat

---

[11]The CMCU belongs to the navigation timing subsystem and acts as the 10.23Mhz master clock generator for the navigation payload/clocks, which is used for both the GALILEO satellites and the IOV satellites. It is an interface that manages the selection and processing of all clock signals (PHM and RAFS) and handles the distribution of its reference output signal. In case that the input signal phase drift of a certain atomic clock exceeds predefined limits, the CMCU switches seamlessly between the hot redundant clock stage, which is operating in parallel to the active main clock unit. Technical details about the CMCU can be found in the technical data sheet [3] from the manufacturer as well as in [39]

sink in contrast to other compartment walls. The other panels, as the compartment separation panel, are consequently expected to show a nearly adiabatic behavior, such that the control volume effectively involves a configuration of three separate components exchanging energy by radiative heat transfer: The compartment panel with the antenna module attached, the clock panel and the adiabatic environment consisting of the remaining panels of the enclosure.

The satellite bus structure is composed of honeycomb, overlayed by a MLI blanket, where the latter forms the outermost thermal protection and boundary layer to space. Honeycomb panels are constructed by an array of closely spaced hexagonal cells made from an aluminum alloy (Al5056) with a characteristic thickness. This core material is of low density and therefore strongly limits heat transport by conduction. In addition, the contribution of heat transfer by conduction perpendicular through the honeycomb panel significantly exceeds heat transfer in lateral direction. The core panel is also covered by face sheets also made from aluminum alloy (Al2024 T81), which are connected through adhesives with the core panel. We stick to the assumption that both layers of face sheets are black-painted, except for the sheet covering the clock panel, which was identified to consist of bare aluminum. Picture 4.11a shows a 3D model of a honeycomb slab with black-painted face sheets.

MLI blankets consist of multiple different layers that fulfill several thermal design requirements. On the one hand, MLI should prevent the spacecraft from excessive heating during periods of Sun exposure, on the other hand, it should minimize heat loss through the satellite's boundaries to the deep space environment. Picture 4.11b shows the systematic lay-up of the external MLI as used for the GALILEO satellites. The outside of the first layer, facing deep space, is made of black-painted Kapton. For the interior of the spacecraft, we argued that black-painted surfaces enhance radiation exchange and maintain a uniform temperature, for the outer-cover the main design driver is electrostatic discharge compatibility, i.e. the surface must pro-

(a)

1 x 1,6 mil black Kapton XC160/VDA

10 x 0.25 mil VDA/Mylar/VDA, perf.

10 x Dacron Spacer

1 x 1 mil VDA/ Mylar /VDA, perf.

■ VDA-coating

(b)
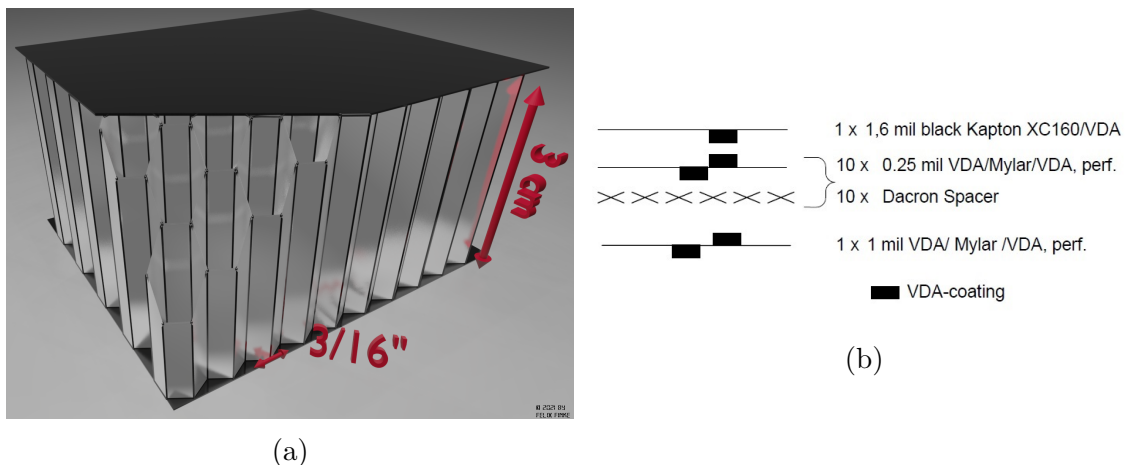
Figure 4.11: Artificial representation of an aluminum based honeycomb structure with one side being black-painted and the other side featuring a bare aluminum face sheet (4.11a). The thickness of the honeycomb structures used for the GALILEO satellites range from 3cm to 5cm. The cell size amounts $L_{cell} = 3/16$" $(4, 8mm)$. 4.11b shows the lay-up of the external MLI sections.

vide charge balance and prevent from surface potential buildup. Despite that the absorption properties of black finishes typically lead to significant heating during Sun exposure, the characteristic $\frac{\alpha}{\epsilon}$ ratio of Black Kapton still ensures a balanced thermal behavior. To fit the thermal requirements, Mylar polyester film layers are laminated with low emissivity Vacuum Deposited Aluminum (VDA)-films in order to minimize heat exchange by radiation between the inner MLI layers. In addition, Dacron spacer are placed between the Mylar layers to minimize the effective contact area for heat exchange by conduction.

Since no further effective material properties are given for the honeycomb material, we employ a fully coupled TMM to describe the radiative heat transport within the single cells of the honeycomb structure. For the purpose of ease, we approximate the geometry of the hexagonal cells as cylinders with a radius r_c derived from the cell size $r_c = L_c/\sqrt{3}$. This facilitates the computation of view factors describing the geometrical radiative coupling between the surfaces involved as we will see below. In order to properly model also the radiative exchange between individual surfaces within the cells, the honeycomb core structure is further subdivided into a number of additional layers. For reasons of computational efficiency, we define a total of 5 layers ($1\times$ face sheet, $3\times$ bulk material layer and $1\times$ face sheet) to map these effects.

For diffuse-grey surfaces, radiation exchange between a surface element i in a closed environment of N individual, isothermal area elements is governed by the following equation:

$$Q_{ij} = \sum_{j=1}^{N} F_{ij} A_i \epsilon_{ij} \sigma_{sb} \left(T_i^4 - T_j^4 \right) \tag{4.46}$$

where $F_{ij} A_i$ in 4.46 is often described as a geometrical radiation resistance. It is a measure of how much radiation flux can pass from one surface A_i to another surface A_j and is driven by the view factor F_{ij}. The matrix ϵ_{ij} is the effective emittance (see [56], [87] for a detailed view on the derivation). Note that in contrast to black bodies absorbing any incoming radiation, grey-diffuse surfaces emit and reflect incoming radiation. Thereby, optical material parameters of grey bodies do not change with the wavelength of the radiation and the emission pattern is direction independent.

The view factor evaluation is computational intensive and heavily depends on the shapes and the geometrical arrangement of the surfaces involved. Mostly, view factors are computed numerically and several implementations have been adopted for that purpose (see [46] and [23] for details on the Hemicube method as integrated in the FEM framework ANSYS or [123] and [51] for details on Monte Carlo method based view factor evaluation approaches). The definition of the view factor integral is given by:

$$F_{12} = \frac{1}{\pi A_1} \int_{A_1} \int_{A_2} \left(\frac{\cos \alpha_1 \cos \alpha_2}{r^2} \right) dA_1 dA_2 \tag{4.47}$$

where A_1 and A_2 correspond to the area elements viewing each other under the angles α_1 and α_2 relative to their surface normals and placed at a distance of r apart
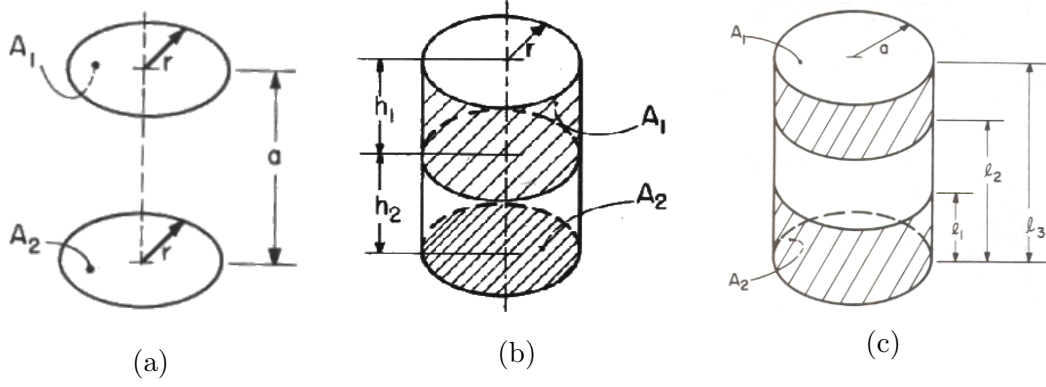
Figure 4.12: Visualization of the different geometrical arrangements relevant for the view factor computation.

from each other. In the following we present several kinds of view factors.

Analytic forms of several specific configuration factors are well tabulated and can be found in the literature (see [38] [21] and [62]). The configuration factors between two parallel discs, F_{dd}, can be computed by:

$$F_{dd} = \frac{1}{2} \left(\frac{2R^2 + 1}{R^2} - \sqrt{\left(\frac{2R^2 + 1}{R^2} \right)^2 - 4} \right) \tag{4.48}$$

where $R = \frac{r}{a}$ is the ratio of the discs radius to the distance a of the two discs. As next, the configuration factor between the interior surface of a cylindrical section and a coaxial disc, F_{cd}, with equal radius placed at a certain distance from that geometry is considered:

$$F_{cd} = \frac{1}{4} \left(\left(1 + \frac{H_2}{H_1} \right) \sqrt{4 + (H_1 + H_2)^2} - (H_1 + 2H_2) - \frac{H_2}{H_1} \sqrt{4 + H_2^2} \right)$$
$$H_1 = \frac{h_1}{r} \tag{4.49}$$
$$H_2 = \frac{h_2}{r}$$

In the above equation 4.49, h_1 is the height of the cylindrical section and h_2 corresponds to the distance from the base of that element to the bottom disc of a neighboring cylindrical section (see picture 4.12b). r denotes the radius of both the section and the disc.

Finally, the view factor between two neighboring sections of coaxial, cylindrical shells, F_{cc}, can be obtained by:

$$F_{cc} = \frac{1}{4\left(L_3 - L_2\right)} \left(2L_1\left(L_3 - L_2\right) + \left(L_3 - L_1\right) X\left(L_3 - L_1\right)\right.$$
$$\left. - \left(L_2 - L_1\right) X\left(L_2 - L_1\right) - L_3 X\left(L_3\right) + L_2 X\left(L_2\right)\right) \tag{4.50}$$
$$L = \frac{l}{r}$$
$$X\left(L\right) = \sqrt{L^2 + 4}$$

where L in equation 4.50 is associated with the different distances that determine the geometrical size and spacing of the arrangement, see figure 4.12c, and r denotes the common radius of the coaxial, cylindrical sections. Note that in the three analytic solutions above for the configuration factor integrals, the radius r is actually the cell radius r_c, as defined before.

As next, we compute the configuration factors that present the fractions of diffuse radiation exchanged between the different surface elements within the timing system compartment. Picture 4.13 gives a schematic view on the enclosure. Following the reasoning above, we model the enclosure as an effective three-element enclosure. The according view factors needed are summed up in table 4.6.

	Antenna panel(ap)	Clock panel(cp)	Adiabatic walls(aw)[3]
Antenna panel	$F_{ap \to ap} = 0$	$F_{ap \to cp} = 0.268$	$F_{ap \to aw} = 0.732$
Clock panel	$F_{cp \to ap} = 0.170$	$F_{cp \to cp} = 0$	$F_{cp \to aw} = 0.830$
Adiabatic walls	$F_{aw \to ap} = 0.166$	$F_{aw \to cp} = 0.296$	$F_{aw \to aw} = 0$

[3] $A_{ap} = 0.84m^2$, $A_{cp} = 1.32m^2$, $A_{aw} = 3.70m^2$

Table 4.6: Configuration factors computed for the simplified three-element enclosure.

In table 4.6, we make use of the following relations for view factors considered in enclosures, which reduces the total number of integral evaluations to only one:

$$F_{ij} = F_{ji} \frac{A_j}{A_i} \tag{4.51}$$

$$1 = \sum_{j=1}^{N} F_{ij} \tag{4.52}$$

The net energy transfer as described in 4.46 from the antenna panel to the clock panel can be written as:
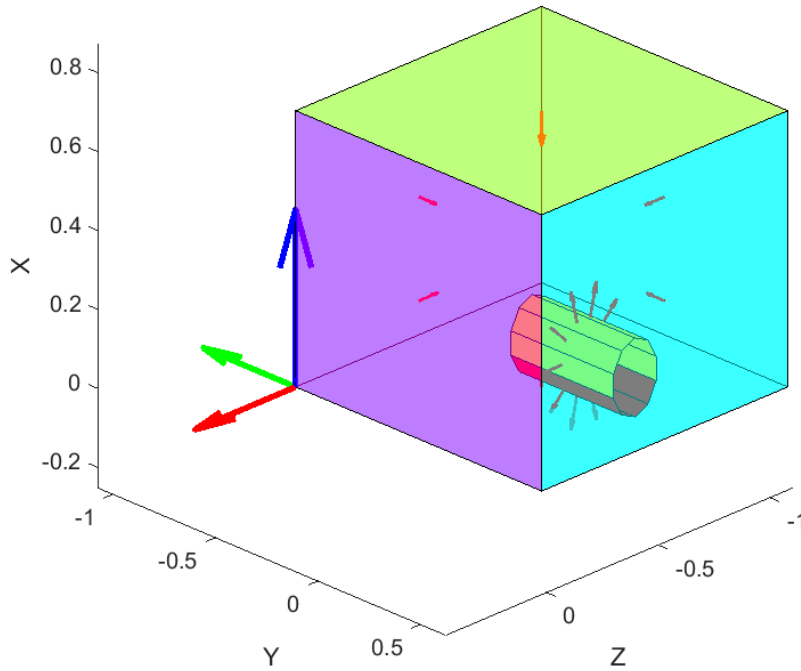
Figure 4.13: Schematic view on the spacecrafts timing system compartment. The dimensions of the box are $0.7 \times 1.2 \times 1.1 \, [m^3]$ $(X \times Y \times Z)$. The magenta colored surface is considered the antenna mounting panel through which incoming radiation is exchanged with the enclosure. Note that due to the special attitude of the spacecraft, the other cyan colored surfaces do not receive heat from the outside. The green area element features the separation panel to the neighboring spacecraft compartment. The cylindrical shape within the box demonstrates the location of the clock. Below this element, the clock's mounting panel is located, which is treated as the main heat sink of the enclosure.

$$Q_{ap} = \frac{\sigma_{sb}\left(T_{ap}^4 - T_{cp}^4\right)}{\frac{1-\epsilon_{ap}}{\epsilon_{ap}A_{ap}} + \frac{1}{R} + \frac{1-\epsilon_{cp}}{\epsilon_{cp}A_{cp}}} \tag{4.53}$$

$$R = \frac{1}{\frac{1}{A_{ap}F_{ap\to aw}} + \frac{1}{A_{cp}F_{cp\to aw}}} + A_{ap}F_{ap\to cp} \tag{4.54}$$

We can now set up the TMM to compute the transient behavior of the thermal mass located in the interior of the enclosure. Thereby, every uniform surface, e.g. a face sheet or the MLI, is modeled as a separate node, which exchanges radiation with its direct environment and consequently has one temperature degree of freedom. This directly implies that each surface involved in radiative heat exchange is considered isothermal. A surface node can receive or emit heat only from and to its neighboring nodes. The material properties implied by the TMM are summed up in table 4.7. For the sake of simplification, the model reflects that heat exchange by radiation dominates any other heat transport mechanisms such as conduction. From energy conservation, the enthalpy rate of change of the node representing the outermost spacecraft layer is given by:

$$\rho_1 A_{ap} d_1 c_1 \frac{dT_1}{dt} = (\alpha P_\odot A_{ap}) \cos\theta(t) - \sigma_{sb}\epsilon_{MLI}A_{ap}\left(T_1^4 - T_{DS}^4\right) - \sigma_{sb}\epsilon_{MLI}^* A_{ap}\left(T_1^4 - T_2^4\right)$$

$$(4.55)$$

In the heat balance equation 4.55 for the first node, the subscript HC stands for honeycomb, as we assume that this node is directly coupled with the MLI-node via radiative heat exchange. The first term on the rhs denotes the portion of incoming solar irradiance, which varies with the Sun elevation θ with respect to the satellite body-fixed system and is evaluated prior to the start of the solution process for the thermal model. In addition, an absorptivity of $\alpha = 0.94$ is used for the BP Z306 coating. The second term governs the radiation power exchange with the space environment, where $T_{DS} = 3K$ labels the deep space temperature. Note that all structural dimensions and material parameters influencing the change of internal energy are MLI related. The ϵ_{MLI}^* parameter defines the effective emissivity[12] that was measured for the exterior MLI blankets for the IOV satellites in a vacuum test, whereas ϵ_{MLI} specifies the emissivity of the outer surface. For the five nodal equations governing the thermal energy exchange within the honeycomb structure, we write:

$$\rho_i A_{ap} d_i c_i \frac{dT_i}{dt} = \sigma_{sb}\epsilon_{MLI}^* A_{ap}\left(T_1^4 - T_i^4\right) + N_{cell} \sum_{j=2}^{N+2-1} F_{ij} A_i \epsilon_{ij} \sigma_{sb}\left(T_i^4 - T_j^4\right)$$

$$(4.56)$$

$$\rho_{i+1} A_{ap} d_{i+1} c_{i+1} \frac{dT_{i+1}}{dt} = N_{cell} \sum_{j=2}^{N+2-1} F_{i+1j} A_{i+1} \epsilon_{i+1j} \sigma_{sb}\left(T_{i+1}^4 - T_j^4\right) \qquad (4.57)$$

$$\vdots$$

The first term in 4.56 on the rhs is just the contribution from the first node and the sum explains the heat energy interchange within the honeycomb structure, which is interdependent on all participating layers ($N = 5$). The A_i under the sum quantifies the size of an individual area element of a cell - the area of a disc, or the area of a cylindrical section - and the corresponding configuration factor F_{ij} accounts for the geometrical arrangement of that area element with respect to the set of all other surrounding, visible surface elements that form an enclosure (see pictures 4.12a, 4.12b and 4.12c). The multiplication of the sum by the total number of cells N_{cell} then gives the total net energy transfer between all involved cell areas establishing the subdivision layers j and a layer i. The view factors F_{ij} have been computed with the help of the view factor integral solutions 4.48 to 4.50. For $i = 1$ and $i = 5$, net heat transfer between the top and bottom cell sides and cylindrical sections is addressed - where their sum[13] actually constitutes the total area of a face sheet side -, where

---

[12]The effective emissivity generally depends on the total number of sheets/films of a MLI and is a technical measure for the quality of heat flux going through the layers by means of a certain temperature difference.

[13]As described in table 4.6, the antenna panel side of the timing system compartment amounts $A_{ap} = 0.84m^2$.

the other indices indicate the contribution of net heat transfer among individual cylindrical sections.

Starting with the energy balance of the last node given by equation 4.57, the nodal equations defining the heat transfer within the compartment and beyond its boundaries through the clock mounting panel read:

$$\rho_6 A_{ap} d_6 c_6 \frac{dT_6}{dt} = N_{cell} \sum_{j=2}^{N+2-1} F_{6j} A_6 \epsilon_{6j} \sigma_{sb} \left(T_6^4 - T_j^4\right) - \frac{\sigma_{sb}\left(T_6^4 - T_7^4\right)}{\frac{1-\epsilon_{ap}}{\epsilon_{ap} A_{ap}} + \frac{1}{R} + \frac{1-\epsilon_{cp}}{\epsilon_{cp} A_{cp}}} \tag{4.58}$$

$$\rho_7 A_{cp} d_7 c_7 \frac{dT_7}{dt} = \frac{\sigma_{sb}\left(T_6^4 - T_7^4\right)}{\frac{1-\epsilon_{ap}}{\epsilon_{ap} A_{cp}} + \frac{1}{R} + \frac{1-\epsilon_{cp}}{\epsilon_{cp} A_{cp}}} - \sigma_{sb} \epsilon_{cp} A_{cp} \left(T_7^4 - T_{i+7}^4\right) \tag{4.59}$$

$$\rho_i A_{cp} d_i c_i \frac{dT_i}{dt} = \sigma_{sb} \epsilon_{cp} A_{cp} \left(T_7^4 - T_i^4\right) + N_{cell} \sum_{j=8}^{N+8-1} F_{ij} A_i \epsilon_{ij} \sigma_{sb} \left(T_i^4 - T_j^4\right) \tag{4.60}$$

$$\rho_{i+1} A_{ap} d_{i+1} c_{i+1} \frac{dT_{i+1}}{dt} = N_{cell} \sum_{j=8}^{N+8-1} F_{i+1j} A_{i+1} \epsilon_{i+1j} \sigma_{sb} \left(T_{i+1}^4 - T_j^4\right) \tag{4.61}$$

$$\vdots \tag{4.62}$$

$$\rho_{12} A_{cp} d_{12} c_{12} \frac{dT_{12}}{dt} = \sum_{j=8}^{N+8-1} F_{12,j} A_{12} \epsilon_{12,j} \sigma_{sb} \left(T_{12}^4 - T_j^4\right) - \sigma_{sb} \epsilon_{MLI}^* A_{cp} \left(T_{12}^4 - T_{13}^4\right) \tag{4.63}$$

$$\rho_{13} A_{cp} d_{13} c_{13} \frac{dT_{13}}{dt} = \sigma_{sb} \epsilon_{MLI}^* A_{cp} \left(T_{12}^4 - T_{13}^4\right) - \sigma_{sb} \epsilon_{MLI} A_{cp} \left(T_{13}^4 - T_{ext}^4\right) \tag{4.64}$$

$$\frac{dT_7(t)}{dt} = \begin{cases} \dfrac{Q(t)_{ap} - \sigma_{sb} \epsilon_{cp} A_{cp} \left(T_7(t)^4 - T_8(t)^4\right)}{\rho_7 A_{cp} d_7 c_7} & \text{if } T_7 \geq T_c \pm 0.5K \tag{4.65} \\[2ex] -\dfrac{T_7(t) - T_c}{t_p - t_c} & \text{else} \tag{4.66} \end{cases}$$

Material	MLI	Honeycomb (Al5056)	Face sheet (BP Z306)[4] /(Al2024 T81)[5]	PHM
Density $\rho \left[\frac{kg}{m^3}\right]$	38.67	32.04	2780	642.86[6]
Specific heat $c \left[\frac{J}{kgK}\right]$	1290	904	875	494
Emissivity ϵ/ϵ^*	0.89[7]/0.011[8]	0.09	0.89/0.09	0.15
Thickness $d \, [m]$	0.02	0.03	0.0005	0.01

[4] BP Z306 used as a functional coating facing the inside of the clock module compartment   [5] Bare material   [6] The clock's volume is approximately $18l$ [7] Surface emissivity   [8] Effective emissivity

Table 4.7: Material parameters used for the thermal analysis.

The set of equations 4.61 to 4.64 simply follow the reverse logic of equations 4.55 to 4.57, which describe heat transfer from the cold side (deep space) to the hot side (spacecraft interior) through the full antenna panel, modeled as a sandwich element composed of honeycomb and MLI. Note that the clock mounting panel size A_{cp} is applied, which has a bigger size than the antenna panel A_{ap}. The function 4.65 and 4.66 actually substitutes equation 4.59. This function simulates the spacecrafts temperature control mode for the timing subsystem and adjusts the temperature of the lumped payload mass in our thermal model to reach the set-point value after a time interval of $t_p = 600s$, if the temperature change exceeds the predefined limit of $T_c \pm 0.5K$. T_c stands for the set-point temperature and t_c is the elapsed time period since the last activation of the control mode. Before the system of differential equations is integrated over the time span of two orbital periods, initial conditions are provided. The temperatures for the first and last nodes are chosen to be $90K$, which is close to the temperature limit of the external MLI according to the technical specifications used in this context [47]. For the other nodes the nominal set-point temperature ($278K$) is applied.
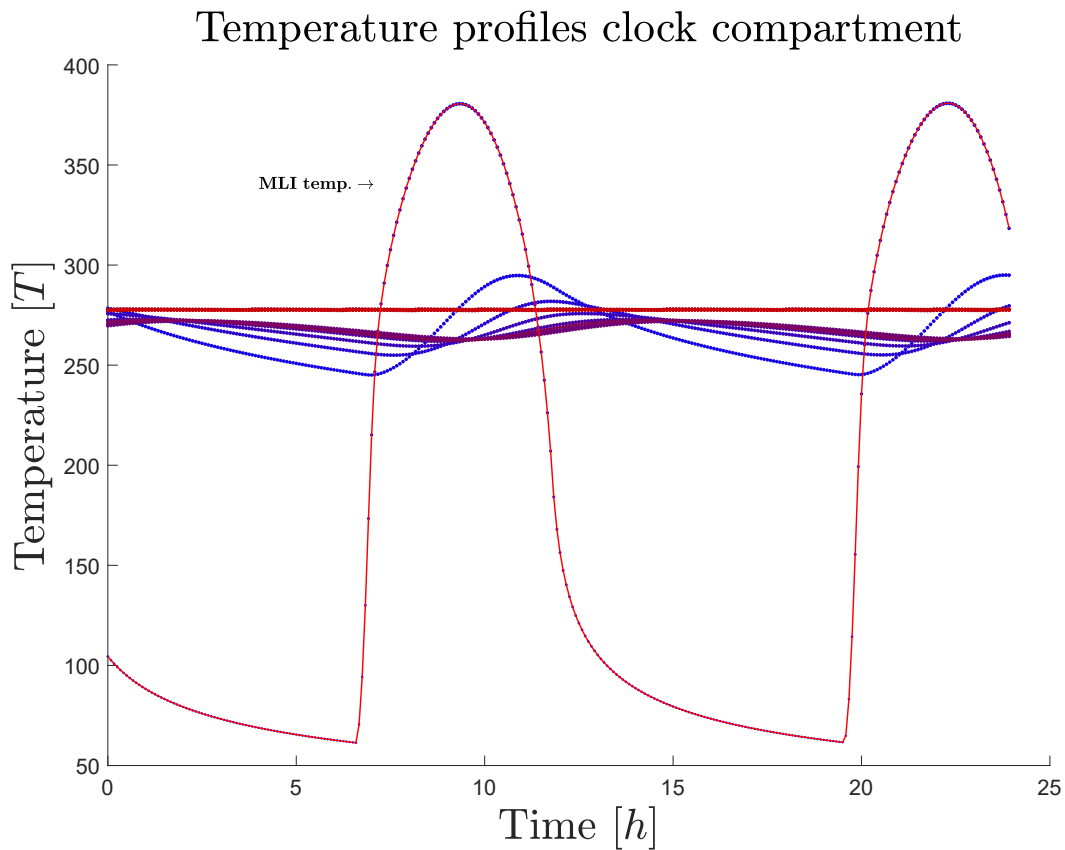
Figure 4.14: Results of the thermal mathematical model. The curve with the largest amplitude renders the MLI surface temperature profile. It nearly reaches its equilibrium temperature after approximately $10h$ and bottoms down to $70K$ before the next Sun illumination cycle starts.

Payload temperature profile

(a)

HC layer temperature profile

(b)
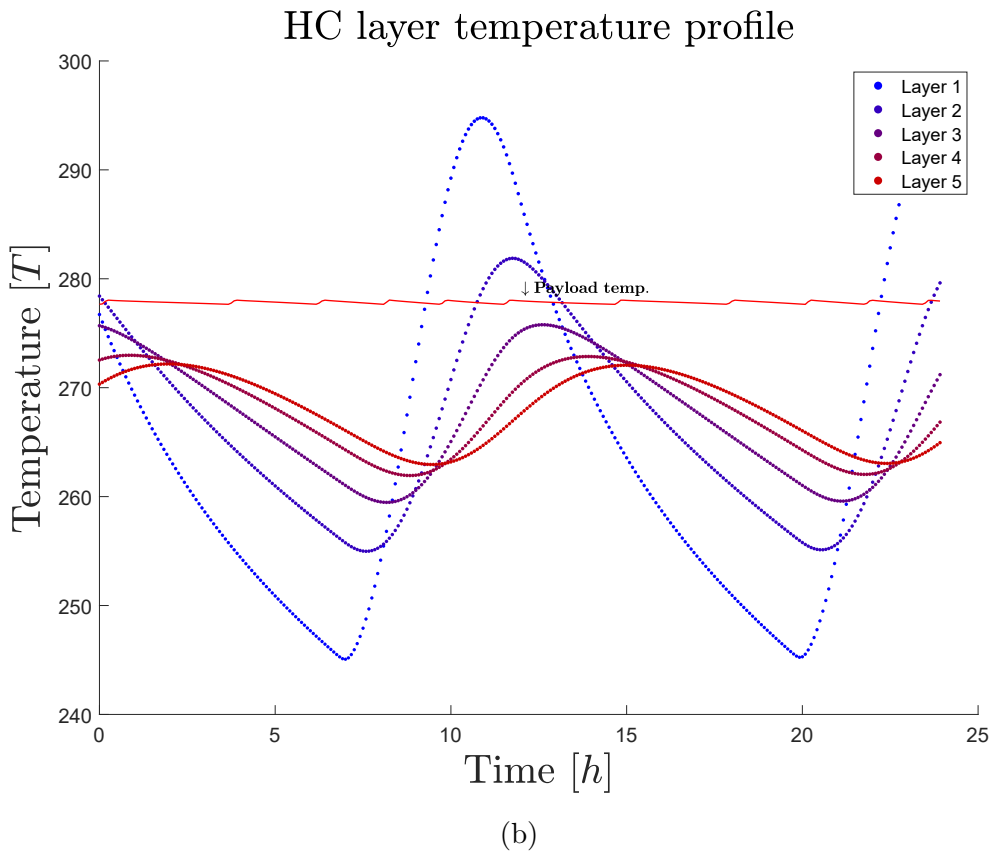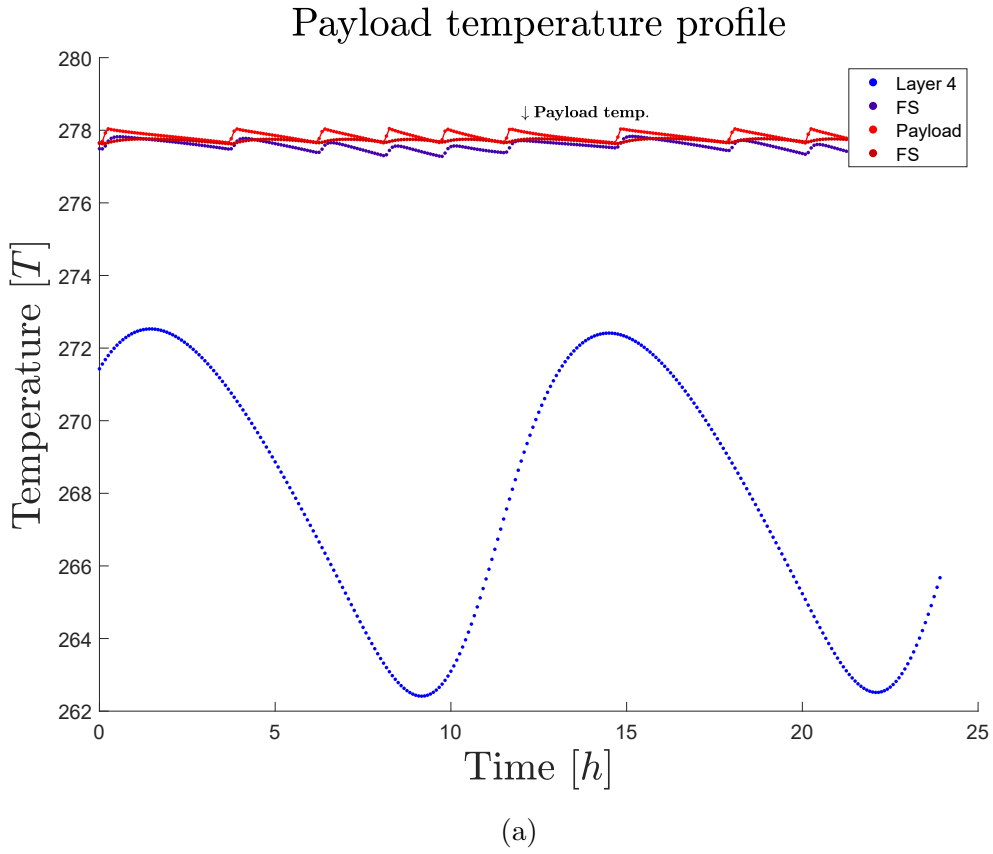
Figure 4.15: Results of the thermal mathematical model. 4.15a shows the temperature profile of the payload and its neighboring nodes, while 4.15b pictures the temperature profiles of the nodes representing the adjacent honeycomb layers.

In equation 4.64, for T_{ext} we use the relation:

$$T_{ext} = \sqrt[4]{\frac{T_i^4}{\frac{\epsilon}{\epsilon_{MLI}^*} + 1}} \tag{4.67}$$

which expresses the external surface temperature of the MLI in dependence of the internal surface temperature, provided that the effective emissivity ϵ_{MLI}^* and the surface emissivity ϵ is given. This formula follows from the consequences of energy conservation by means that all heat transferred through the MLI bulk material must be emitted from the exterior surface into deep space (see [88] for details). The results of this TMM are shown in figures 4.15a and 4.15b. The red line in the former plot shows the nodal temperature profile representing the PHM payload, while the other lines represent the temperature evolution of neighboring nodes. The blue lines describe the nodes for the last honeycomb layer (Layer 4) and its face sheet (FS), where the black line corresponds to the node featuring the face sheet of the mounting panel of the clocks. Figure 4.15b also shows the gradual temperature drop due to the individual honeycomb layers that attenuate the thermal radiation passing through the antenna panel.

We can now determine a correction term $|\Delta\alpha_T|$ for the violation parameter α following the same logic as introduced for the treatment of the magnetic field related systematics. For that purpose, we add the frequency shift term 4.44 to the function $f_{rel,n}$ term in equation 4.17 and compute a new α_T. For the ΔT we plug in the payload temperature profile for the corresponding epoch. For the correction we then obtain $\pm\Delta\alpha_T = \pm 1.9 \times 10^{-5}$. The prior distribution thus denotes $\pi \sim \mathcal{U}\left(-\Delta\alpha_T, +\Delta\alpha_T\right)$.
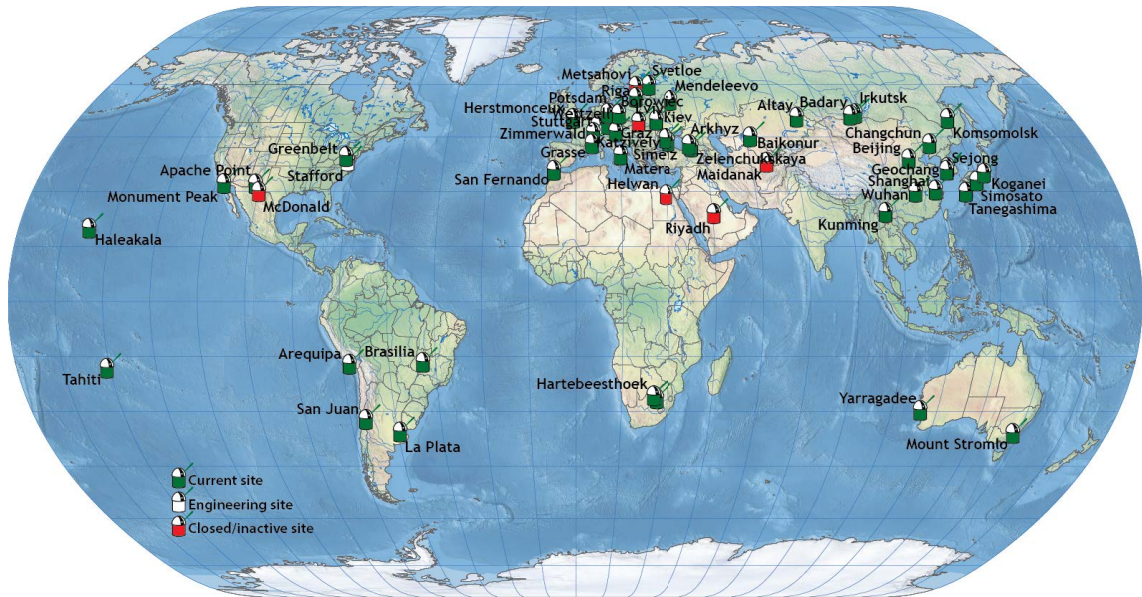
Figure 4.16: Distribution of SLR stations over the globe consolidating the International Laser Ranging Service (ILRS) network[a].

---

[a]`https://ilrs.gsfc.nasa.gov/network/stations/index.html`

4.2.1.3 Prior analysis: SLR statistics

The ILRS coordinates and administrates SLR observations of artificial Earth-bound satellites and Lunar Laser Ranging (LLR) observations generated by SLR and LLR stations distributed all over the globe. SLR data are made accessible by the ILRS via their web page[14]. The ILRS supports a wide range of fields such as geodesy as well as scientific applications which require highly accurate observations for precise positioning purposes. Especially for the gravitational redshift experiment with the GALILEO satellites, a dedicated campaign was launched to intensively track the satellites over a time span of one year starting from May 1st, 2016. Over that time period an increased number of SLR observations were collected over seven days from the beginning of each month. Whenever any of the two satellites were within the measurement range to any SLR station, one or two normal points[15] were generated every 50 minutes for that satellite[16]. These measurements, which are primarily different from pseudo-range observations or other conventional GNSS observations, were used to calibrate the orbit products (precise ephemeris data) and validate their accuracy. SLR data are provided as one-way range residuals representing "observed minus calculated" values, usually expressed in cm. They are constructed from differences of SLR range measurements and corresponding range results that can be obtained from POD solutions. This already hints at their special usefulness: In a similar fashion to clock residuals, they allow for the independent assessment of deficiencies associated with orbit or clock modeling. Larger SLR residuals indicate major systematic errors in the models, while as long as the modeling is perfect, the

---

[14]`https://ilrs.cddis.eosdis.nasa.gov`

[15]`https://ilrs.cddis.eosdis.nasa.gov/data_and_products/data/npt/npt_algorithm.html`

[16]For more information on the trackings statistics: `https://ilrs.cddis.eosdis.nasa.gov/missions/GREAT_exp_stats.html`

	Start Date	End Date	Days included	Number of samples
GSAT0201	05-Dez-2014	16-Dez-2017	1107	10129
GSAT0202	27-Mar-2015	16-Dez-2017	995	7454

Table 4.8: Satellite laser ranging statistics.

residuals should cancel out. To transform SLR residuals into clock residuals, one requires dividing them by c. The equivalence of SLR residuals and clock residuals suggests that they can be leveraged to derive $\Delta\alpha_{SLR}$ corrections for our daily α fits, thus also providing suitable constraints on the statistical parameter space for our Bayesian analysis to derive the marginalized posterior. To compute the corrections, the parameter estimation scheme as explained in chapter 4.1 is used to fit the SLR residuals to our redshift model. Based on the $\Delta\alpha_{SLR}$ statistics thus obtained, we then determine both the sample mean and variance for each clock data set. This eventually can be used to define normally distributed priors for each data set as $\pi \sim \mathcal{N}(\mu_{\Delta\alpha_{SLR}}, \sigma_{\Delta\alpha_{SLR}})$. Since the total amount of SLR data per day is very sparse, so that there are not always enough samples for a day-wise fit, as is the case for the clock residuals, it is not possible to obtain reasonable daily corrections based on our standard Least-Squares approach. Therefore, the $\Delta\alpha_{SLR}$ parameter estimation is done globally. The total number of SLR data points used for parameter estimation includes a total of 17583 measurements. Table 4.8 summarizes the SLR sampling statistics for each of the two satellites. The global Least-Squares fit result can be found in table 4.9.
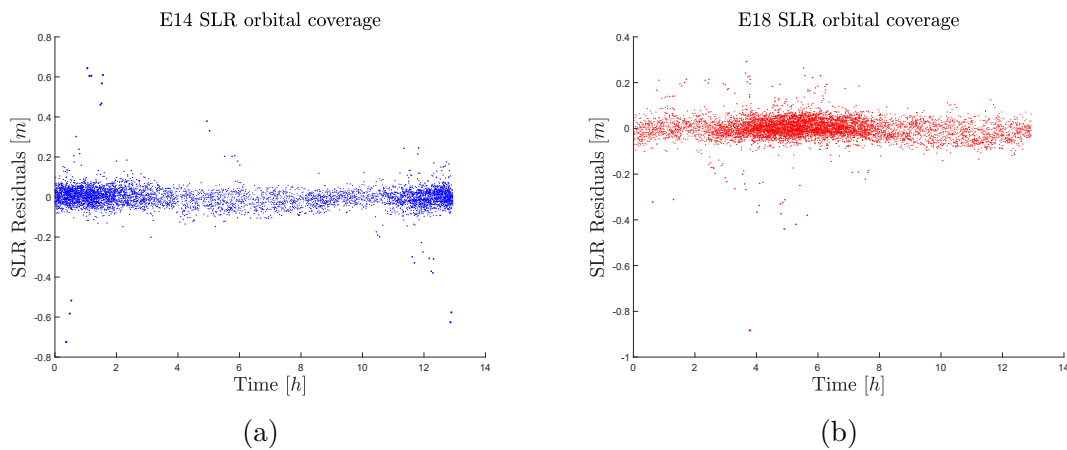
Figure 4.17: The plots show the density of SLR measurements over one GALILEO-specific orbital period. The argument is given in seconds and the vertical axis gives the SLR residual value in meters. The SLR residuals measure the divergence between direct observations and orbit determination results. From the comparison of both plots one recognizes how the SLR measurement coverage is distributed over the specific satellite orbits. Due to the phasing of the satellites, which is approximately 180°, in times where GSAT0202 can be tracked more frequent, less GSAT0201 observations can be performed.

4.3 Results

Table 4.9 and figure 4.19 sum up the preceding considerations regarding the violation parameter estimates giving the potential uncertainty for the combined gravitational and relativistic Doppler redshift effect. In terms of accuracy, we essentially reflect the state of the research published by *Hermann et al.* [53] in 2018[17]. Although the locations of the statistical means differ somewhat from the results in the article, the standard deviations of all posterior distributions per clock data set still agree well with the results. It should be noted that the earlier study presented in the article underestimates the systematic effects owing to the specific frequency sensitivity of atomic clocks to magnetic field perturbations. Based on the recent findings obtained throughout the present study, the potential corrections for the estimated value of the violation factor α constrain a wider interval of $\pm\Delta\alpha_B = \pm1.5 \times 10^{-5}$ instead of $\pm\Delta\alpha_B = \pm0.8 \times 10^{-5}$. The corrected marginalized posterior distributions can be found in figure 4.19. For direct comparison, the marginalized posterior distributions calculated based on the old $\Delta\alpha_B$ value are shown in Figure 4.18. The discussion of the daily α fits presented in 4.7 suggests that the results from the clock 5 data set prove to be the most reliable, largely due to the underlying clock stability and pervasive absence of outliers. This gives reason to focus on the results that emerge from the analysis of this data set. Compared to the final α estimate from the original study given by $\alpha = (2.2 \pm 1.6) \times 10^{-5}$, we present an updated value of $\alpha = (2.01 \pm 1.76) \times 10^{-5}$, which still implies a 4-fold improvement as compared to the final GPA result of 7×10^{-5} given in [120]. If we consider only the gravitational redshift in our violation model, we obtain a result of $5.56 \pm 3.4 \times 10^{-5}$, improving the accuracy by a factor of four relative to the GPA result of 1.4×10^{-4} published in [121].

---

[17]The study was supported by both the ESA project GREAT (General Relativity Experiment with Galileo Satellites 5 and 6) and DLR in the RELAGAL project (RElativistic experiments with GALileo satellites). As part of the GREAT project, a parallel study by *Delva et al.* [31] was published in the same issue, in which an independent statistical analysis was performed based on the same clock data.

$\alpha \pm \Delta\alpha \, (\times 10^{-5})$	Clock 1	Clock 3	Clock 5
Days included	409	153	508
Statistics	-0.33 ± 0.6	8.13 ± 1.5	3.53 ± 0.5
SLR statistics	-2.2 ± 0.5	-8.1 ± 0.9	-1.5 ± 0.9
T statistics	0 ± 1.9	0 ± 1.9	0 ± 1.9
B-field statistics	0 ± 1.5	0 ± 1.5	0 ± 1.5
Posterior statistics	-2.53 ± 1.66	-0.03 ± 2.27	2.03 ± 1.76

Table 4.9: α posterior statistics (statistical sample mean and uncertainties).
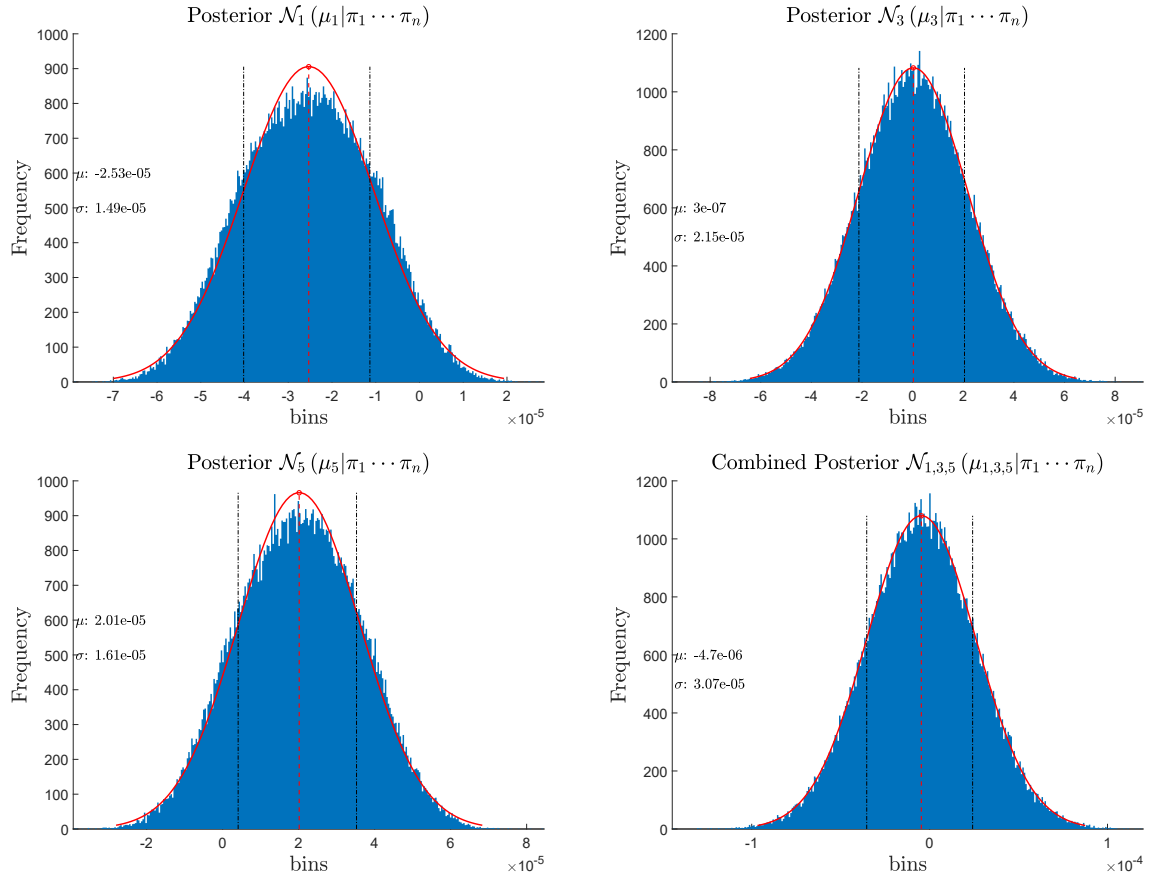
Figure 4.18: Marginalized posterior distributions for all clock data sets including the combined posterior in the lower right corner. The B-field statistic enters with a sampling variance of 0.8×10^{-5}. The uncertainty relates to the highest posterior density interval including 68% of the data and is visualized by the dashed lines in the plots.
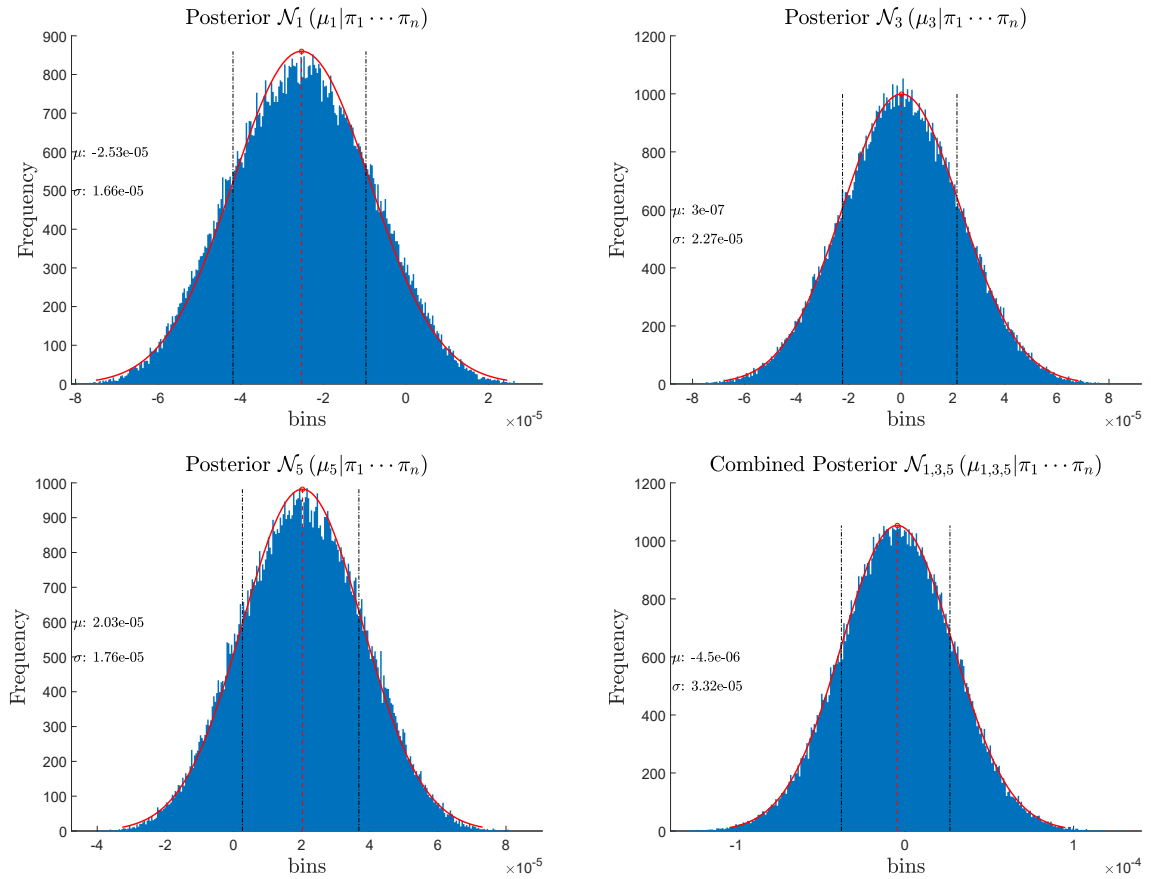
Figure 4.19: Revised marginalized posterior distributions for all clock data sets including the combined posterior in the lower right corner. In contrast to the results in figure 4.18, the B-field statistic enters with a sampling variance of 1.5×10^{-5} instead of 0.8×10^{-5}. The uncertainty relates to the highest posterior density interval including 68% of the data and is visualized by the dashed lines in the plots.

Summary and Outlook

This work deals in essence with the verification of the general relativistic redshift as it can be predicted by the application of special relativity and the equivalence principle of general relativity. Reason for this occasion, at least from a scientific point of view, was the lucky happenstance that the two GALILEO satellites GSAT0202 and GSAT0201 were directed into eccentric orbits owed to a technical malfunction. As a result, the satellites with their high-precision atomic clocks have since been periodically passing through different altitudes in the Earth's gravity field, resulting in a periodic frequency modulation due to time dilation effects that are eventually detected by the atomic clocks. Based on numerous series of satellite observations of GSAT0202 and GSAT0201 covering a total period of about 1000 days, clock solutions were generated, which have been tested for a possible redshift violation on a day-by-day basis under the application of a statistical analysis. As a final result for the combined gravitational and relativistic Doppler redshift effect, we receive $\alpha = (2.01 \pm 1.76) \times 10^{-5}$. If we consider only the gravitational redshift in our violation model, we obtain a result of $5.56 \pm 3.4 \times 10^{-5}$, which exceeds by 4 times the accuracy compared to the GPA result of 1.4×10^{-4} published in [121].

The modeling of systematic effects generating a similar signature or periodicity as that of the redshift is a key component of this study, which we consider in more detail from two different perspectives. First, we attempt to model and constrain the effects of temperature variations and perturbations from the Earth's magnetic field, which are expected to directly affect the accuracy of the atomic clocks. This eventually helps to better understand the resulting measurement limitations of the atomic clocks and to derive combined measurement uncertainties for the α estimation. Second, we address the modeling of orbit perturbations, which are a key factor for the quality of clock solutions, and ultimately predefine the accuracy of the redshift test. Chapter 4 addresses the impact of clock-specific systematics such as temperature and magnetic field effects on the accuracy of the statistical violation parameter estimates, while chapter 3 focuses on modeling SRP perturbations.

Although there has been quite some progress in the field of SRP modeling and

technical information on the physical and technical GALILEO FOC satellite characteristics has been published in favor of pertinent studies, there is still room in the interpretation of the effects of radiation-induced perturbations. To discriminate between the causes of these effects as accurately as possible, we introduce a FE-based SRP model that, unlike conventional a-priori models, also accounts for self-shadowing effects. We show in a simplified orbit determination framework the performance improvement over a FE box-wing model by means of a parameter estimation procedure based on observation data spanning a period of almost one month and recorded from more than 80 MGEX stations worldwide. For the purpose of comparing the two models, we use the ECOM1 as an empirical parameter setup. Thirty-day orbital simulations were also used to show that the application of an empirical ECOM1 model leads to larger deviations than are obtained by means of an additional analytical model, in this case the high-fidelity FE model. Using orbit simulations, it was also demonstrated (see Figure 3.30) that the exclusive use of an empirical ECOM1 model results in a larger difference with respect to precise orbit solutions when compared to using an additional analytical model, in this case the high-fidelity FE model.

It has been been found that the use of an advanced semi a-priori SRP model can significantly enhance the quality of the clock data (see Figure 3.31), assisting precision tests such as those described here. The advantages that may arise from an analytical treatment of SRP also inspire to apply the concept to the analytical modeling of TRP effects, and we would like here to give a brief outlook on the methodological-technical foundations that have been developed in the context of a conceptual design study:

Other than SRP, which emanates from the interaction of radiation from an external source with an objects surface, thermal radiation pressure results from the transfer of momentum due to the radiation emission behavior an object's surface. Hereby, this effect just depends on the surface temperature distribution. The recoil force caused by TRP is given by (see also [88] page 19):

$$\mathbf{F}_{trp} = -\frac{2}{3c} \left(\epsilon \sigma_{sb} A T^4 \right) \mathbf{n} \tag{5.1}$$

The steps required to construct a FE-based TRP model are related to those mentioned in the 3.3.3.2 section. The building process was also carried out in APDL. In a similar manner to the discussed modeling approach used to construct a high-fidelity GMM for modeling SRP, an analogous FE approach can be used to construct a volumetric GMM as a basis for a full thermal transient analysis from which the overall satellite surface temperature distribution can be derived, which is expected to evolve over an orbit. For a given FE solution or resulting temperature distribution, the calculation of the recoil force according to equation 5.1 can then be expanded to an element-wise form analogous to 3.106, where for each nth element the temperature T_n extracted from the distribution must be substituted to obtain the resulting TRP force or acceleration $\mathbf{F}_{trp,n}$. Before one can solve for the heat distribution on the satellite FEM, initial and boundary conditions as well as heat loads must be defined and applied to nodes (with one thermal degree of freedom), surfaces (heat flux etc.) or volume elements (heat generation, thermal flux etc.) of

the corresponding FE mesh. In addition, following the discussion in section 3.3.3.2, it is useful to identify surface elements on the mesh that experience self-shadowing, potentially altering the heat load distribution through the local reduction of heat flux, which in turn depends on the corresponding illumination scenario (as an example 3.20) and the associated satellite-Sun orientation. Ultimately, the resulting TRP-generated force can be calculated based on the thermal distribution results.

The GMM requires a parametric solid model consisting of volume and surface elements 5.1a. This satisfies the requirements for modeling in-plane and through-thickness heat conduction processes, as well as modeling the effects of radiative heat transfer phenomena. Although the external geometry of the satellite is sufficiently known, official information about the inner structure is still largely unknown, as are many of the thermal material parameters necessary to uniquely characterize heat transfer properties, as already noted in section 4.2.1.2. Therefore, the resulting TMM concept is limited by the assumptions made in that section. For demonstration purposes the results of a steady-state thermal simulation using the proposed FE mesh is shown in figure 5.1d. An initial temperature of 293.15 K° was chosen for the interior of the satellite for performance testing purposes (this is near the nominal operating temperature of the atomic clocks), while the temperature of outer space was fixed at 3 K°. In the plot, the space radiators and the underlying structure on the Y-face of the satellite model are hidden, giving a view into the compartment. The red color indicates the compartment's reference temperature set as a boundary condition. Prior to the solution, surface loads were applied to all surface elements which directly face the sun. Depending on the absorptivity α_n of each nth surface element and the orientation of the satellite with respect to the Sun given by the angle θ (see plot 3.12), the expression $q_n = \alpha_n P_\odot \cos\theta$ was used to determine the heat flux imposed as a heat load condition on each of the elements. One can see very well the cooler places, which experience less heat load with given shading. For the illumination scenario a solar irradiance angle of $\theta = 45°$ was chosen.

It is expected that the results of the solid GMM-based TRP calculations, assuming that all necessary technical information about the GALILEO satellites is publicly available, may provide some sound headway towards a complete and closed analysis of radiation pressure induced phenomena. Thus, anomalies such as the Y-bias or the accurate emission characteristics of other satellite surfaces are expected to be sufficiently described.

(a) TMM volumetric model.

(b) Volume and surface mesh.

(c) Outgoing radiant heat flux from the surface.

(d) Satellite temperature distribution.
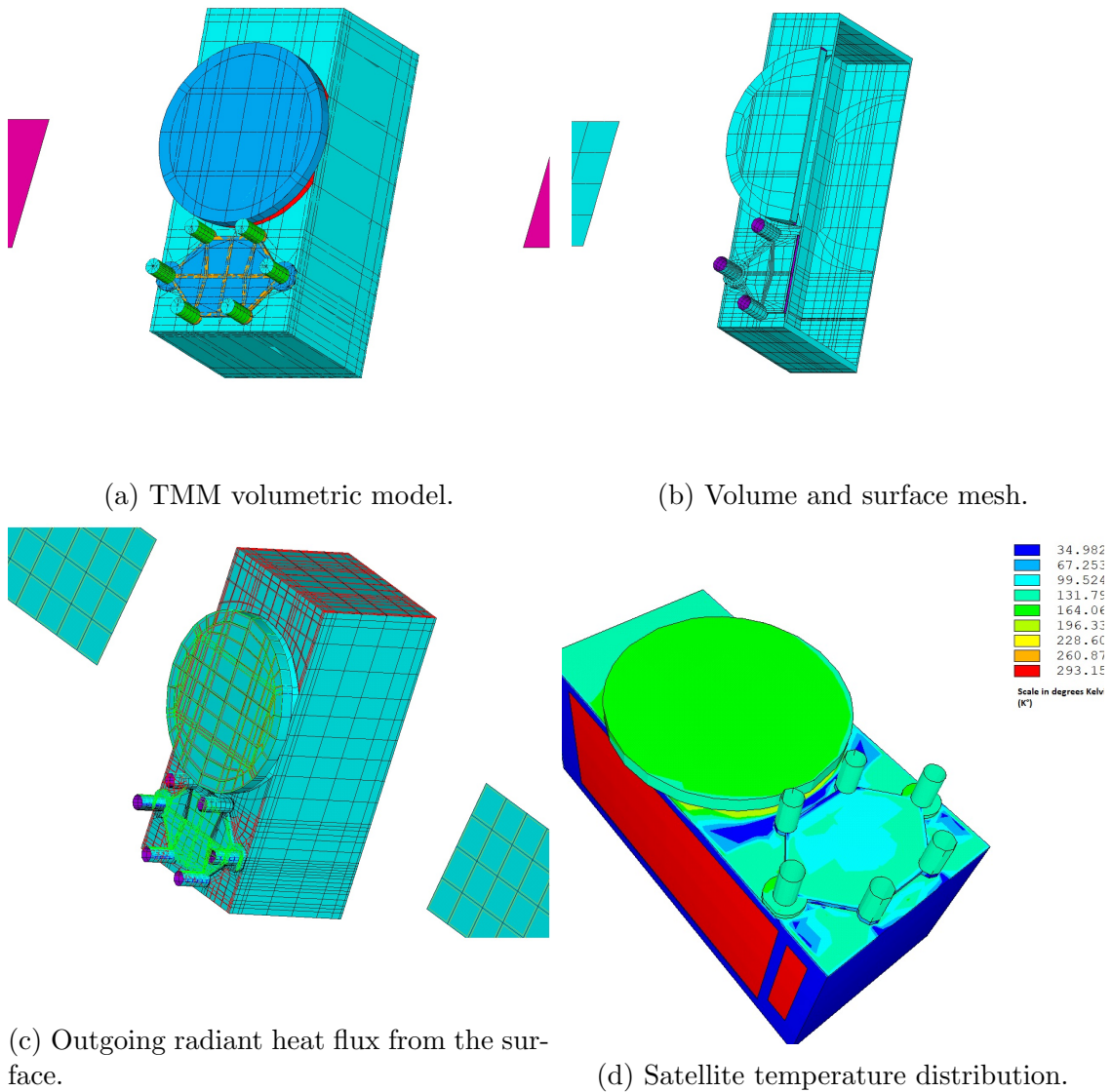
A.1 MCMH Algorithm

Here, we present the Metropolis-Hastings algorithm implementation as shown in 1. The MCMH algorithm belongs to a class of methods drawing random samples from arbitrary probability distributions, which may not be directly tractable. For detailed information, we refer the reader to *Gelman et al.* [43] p. 278 ff. During runtime the algorithm moves through a potential sample space and iteratively traces the true probability distribution. Throughout this process, new sample candidates θ_{n+1} are continuously drawn using a so-called *proposal distribution*, also known as the transition kernel. It determines which jump the stochastic process will perform next. Thereby, the choice of the next candidate θ_{n+1} depends only on the value of the current sample θ_n. Then, after each draw of a new sample candidate θ_{n+1}, a decision is made whether to keep or discard it based on a special acceptance criterion A.3 defined in the following pseudocode. It is precisely this *random walk* property that typically characterizes a Markov chain, in that the future states of the stochastic motion are determined entirely by the current state and do not depend on past states.

1. Initialize sample candidate θ_n randomly

2. Pick a next sample candidate from a proposal distribution $P\left(\theta_{n+1}|\theta_n\right)$

3. Accept or reject the sample θ_{n+1} depending on a uniform random variable $\phi \in [0,1]$:

$$\theta_{n+1} = \begin{cases} \theta_{n+1} & \text{if } \phi \leq a\left(\theta_{n+1}|\theta_n\right) \\ \theta_n & \text{else } \phi > a\left(\theta_{n+1}|\theta_n\right) \end{cases} \qquad \begin{matrix}(\text{A.1}) \\ (\text{A.2})\end{matrix}$$

$$a\left(\theta_{n+1}|\theta_n\right) = min\left\{\frac{f(\theta_{n+1})P\left(\theta_n|\theta_{n+1}\right)}{f(\theta_n)P\left(\theta_{n+1}|\theta_n\right)}, \ 1\right\} \qquad (\text{A.3})$$

4. Increment counter n by 1: $n + 1 \rightarrow (n+1) + 1$

Algorithm 1 MCMH algorithm

Input: Function $f(\theta)$ proportional to the posterior distribution
Output: Accepted θ_{acc} and rejected θ_{rej} samples from posterior sampling chain

Define proposal distribution P: $P\left(\theta_{n+1}|\theta_n\right)$
Initialize states of the Markov Chain $\theta_{old} = \theta_P$
Set total number of samples N

for $n \leftarrow 1, N$ **do**
   $\theta_{n+1} \leftarrow P\left(\theta_{n+1}|\theta_n\right)$
   $a\left(\theta_{n+1}, \theta_n\right) = \frac{f(\theta_{n+1})P(\theta_n|\theta_{n+1})}{f(\theta_n)P(\theta_{n+1}|\theta_n)}$
   if $a\left(\theta_{n+1}, \theta_n\right) > 1$ **then**
      $\theta_n = \theta_{n+1}$
      $\theta_{acc_n} \leftarrow \theta_{n+1}$
      $\theta_{rej_n} \leftarrow$ NaN
   else
      if $a\left(\theta_{n+1}, \theta_n\right) \geq \phi$ **then**
         $\theta_n = \theta_{n+1}$
         $\theta_{acc_n} \leftarrow \theta_{n+1}$
         $\theta_{rej_n} \leftarrow$ NaN
      else
         $\theta_{acc_n} \leftarrow$ NaN
         $\theta_{rej_n} \leftarrow \theta_{n+1}$
      end if
   end if
end for

A.2 MCMH results

The following plots illustrate the posterior statistics of each α data set listed in table 4.9. The computations have been carried out with the software PyMC3 [92], which provides a probabilistic programming framework written in Python.

A.2.0.1 Posterior statistics α Set 1
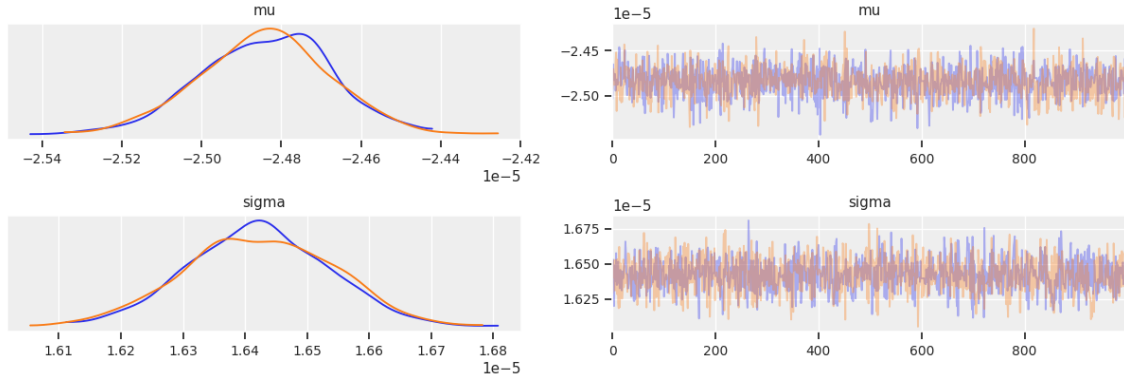
(a) On the left picture, kernel density estimation plots of the sample mean and sample variance distributions are shown. The probability is indicated on vertical axis, while from the horizontal axis the respective value for μ or σ can be read. On the right picture, the associated marginal posterior chains are illustrated.
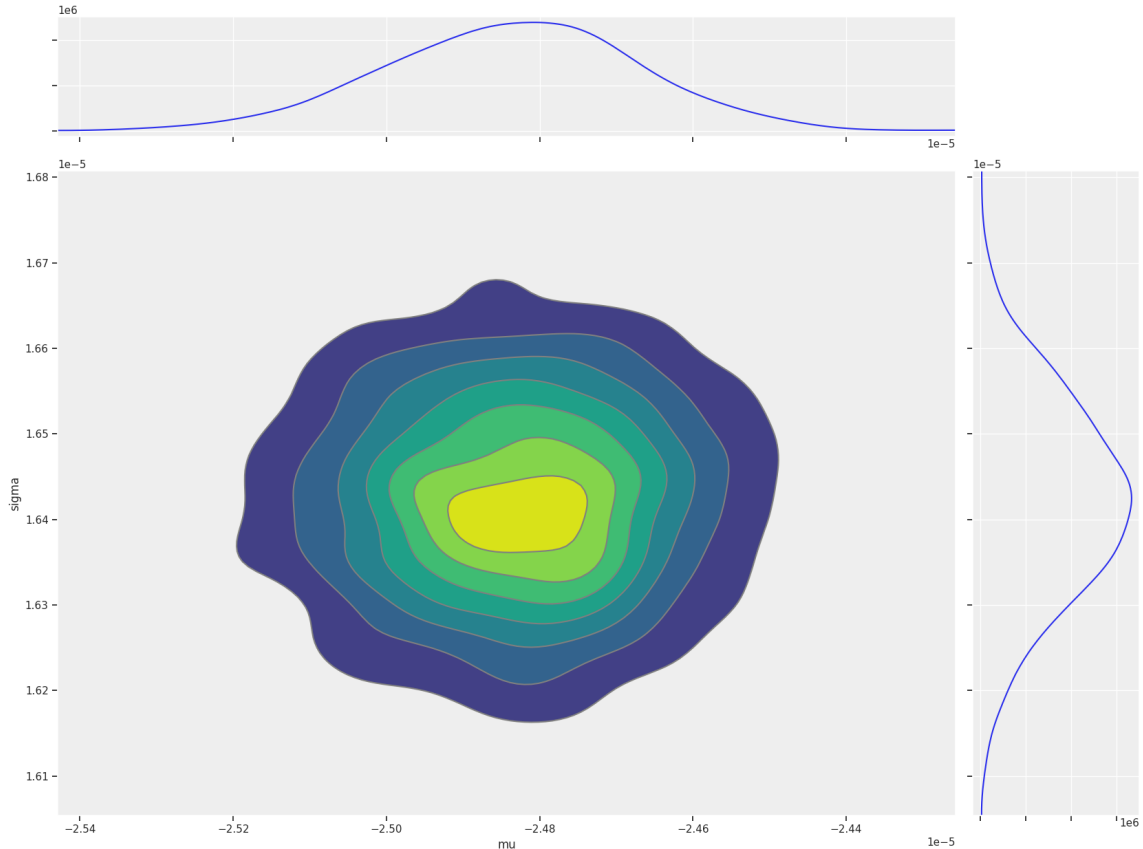
(b) Kernel density estimation of the joint posterior distribution.

Figure A.1: The plots above visualize the Bayesian inference results for the posterior obtained for α data set 1.

A.2.0.2 Posterior statistics α Set 3
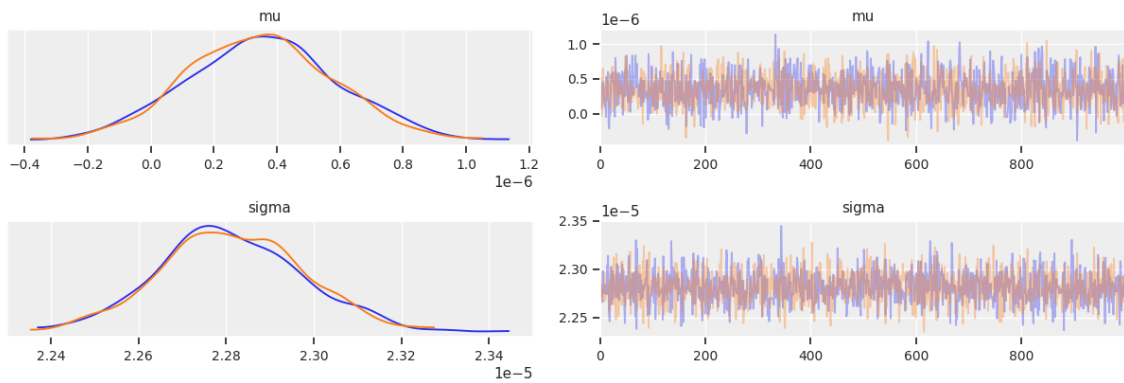
(a) On the left picture, kernel density estimation plots of the sample mean and sample variance distributions are shown. The probability is indicated on vertical axis, while from the horizontal axis the respective value for μ or σ can be read. On the right picture, the associated marginal posterior chains are illustrated.
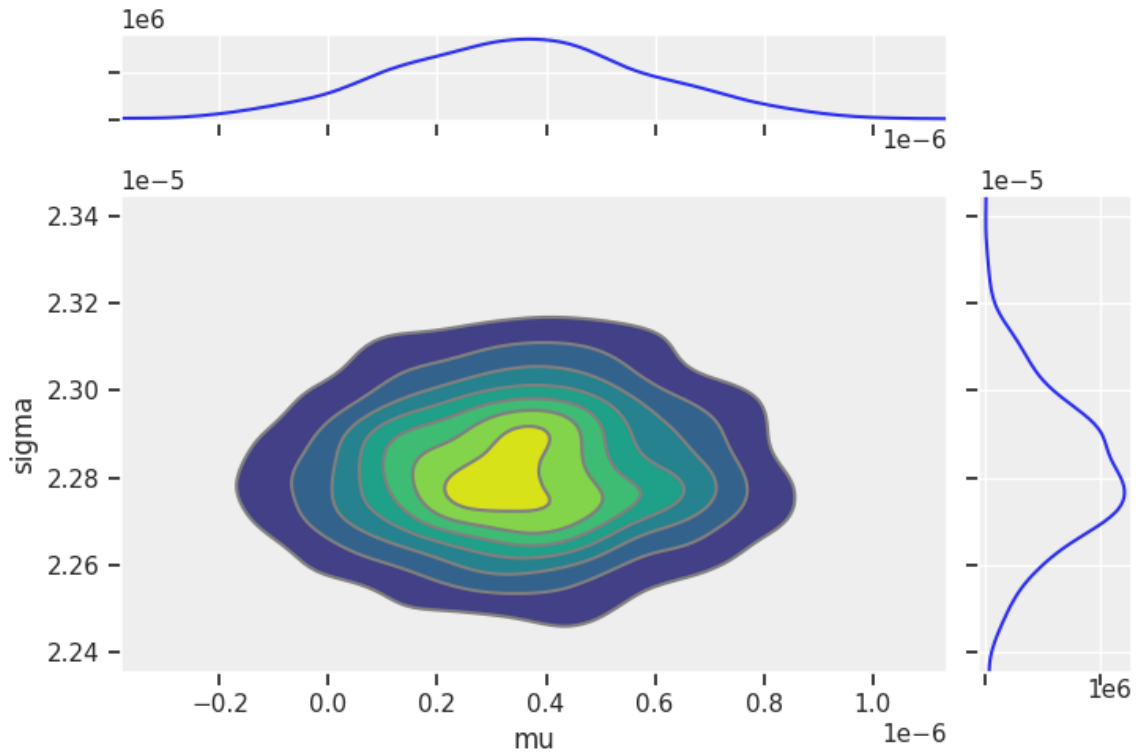
(b) Kernel density estimation of the joint posterior distribution.

Figure A.2: The plots above visualize the Bayesian inference results for the posterior obtained for α data set 3.

A.2.0.3 Posterior statistics α Set 5
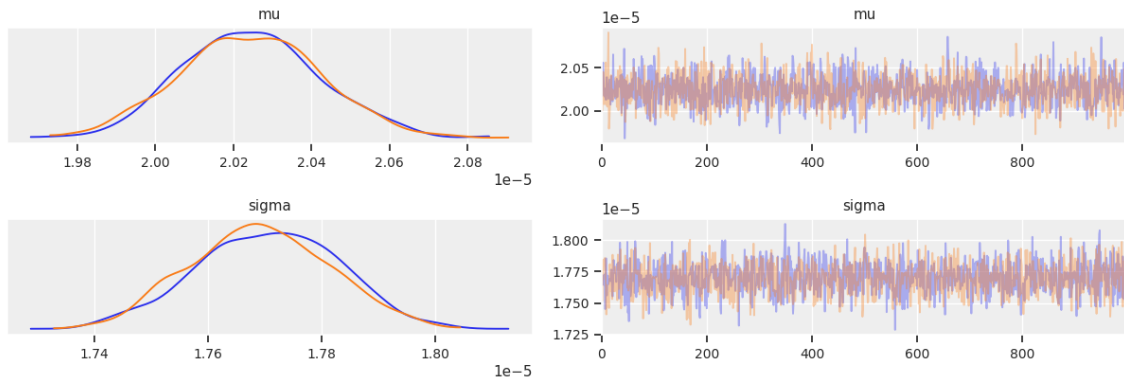
(a) On the left picture, kernel density estimation plots of the sample mean and sample variance distributions are shown. The probability is indicated on vertical axis, while from the horizontal axis the respective value for μ or σ can be read. On the right picture, the associated marginal posterior chains are illustrated.
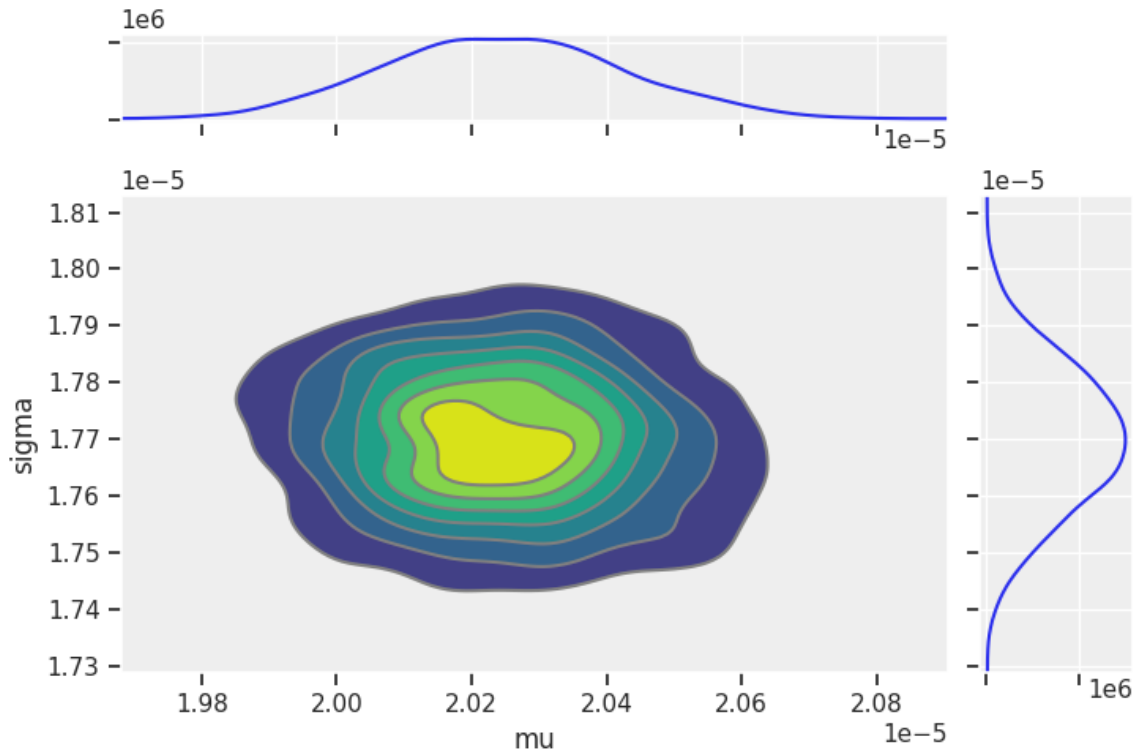
(b) Kernel density estimation of the joint posterior distribution.

Figure A.3: The plots above visualize the Bayesian inference results for the posterior obtained for α data set 5.

Chapter A

List of Algorithms

Chapter A

List of Figures

Chapter A

List of Tables

Chapter A

Bibliography

[1] Benjamin P Abbott, Richard Abbott, TD Abbott, MR Abernathy, Fausto Acernese, Kendall Ackley, Carl Adams, Thomas Adams, Paolo Addesso, RX Adhikari, et al. Observation of gravitational waves from a binary black hole merger. *Physical review letters*, 116(6):061102, 2016.

[2] DN Aguilera, Holger Ahlers, Baptiste Battelier, Ahmad Bawamia, Andrea Bertoldi, R Bondarescu, Kai Bongs, Philippe Bouyer, Claus Braxmaier, Luigi Cacciapuoti, et al. Ste-quest—test of the universality of free fall using cold atom interferometry. *Classical and Quantum Gravity*, 31(11):115010, 2014.

[3] Airbus Defence and Space. *Clock Monitoring and Control Unit - Technical Specification*, 2014.

[4] Kazunori Akiyama, Antxon Alberdi, Walter Alef, Juan Carlos Algaba, Richard Anantua, Keiichi Asada, Rebecca Azulay, Uwe Bach, Anne-Kathrin Baczko, David Ball, et al. First sagittarius a* event horizon telescope results. i. the shadow of the supermassive black hole in the center of the milky way. *The Astrophysical Journal Letters*, 930(2):L12, 2022.

[5] Kazunori Akiyama, Antxon Alberdi, Walter Alef, Keiichi Asada, Rebecca Azulay, Anne-Kathrin Baczko, David Ball, Mislav Baloković, John Barrett, Dan Bintley, et al. First m87 event horizon telescope results. iv. imaging the central supermassive black hole. *The Astrophysical Journal Letters*, 875(1):L4, 2019.

[6] Einstein Albert, W Perrett, and G Jeffery. The foundation of the general theory of relativity. *Ann. Der Phys*, 49:769–822, 1916.

[7] Brett Altschul, Quentin G Bailey, Luc Blanchet, Kai Bongs, Philippe Bouyer, Luigi Cacciapuoti, Salvatore Capozziello, Naceur Gaaloul, Domenico Giulini, Jonas Hartwig, et al. Quantum tests of the einstein equivalence principle with the ste–quest space mission. *Advances in Space Research*, 55(1):501–524, 2015.

[8] Vassilis Angelopoulos. The themis mission. In *The THEMIS mission*, pages 5–34. Springer, 2009.

[9] Daniel Arnold, Michael Meindl, Gerhard Beutler, Rolf Dach, Stefan Schaer, Simon Lutz, Lars Prange, Krzysztof Sośnica, Leos Mervart, and Adrian Jäggi. Code's new solar radiation pressure model for gnss orbit determination. *Journal of geodesy*, 89(8):775–791, 2015.

[10] Neil Ashby. Relativity in the global positioning system. *Living Reviews in relativity*, 6(1):1, 2003.

[11] Neil Ashby, Thomas E Parker, and Bijunath R Patla. A null test of general relativity based on a long-term comparison of atomic transition frequencies. *Nature Physics*, 14(8):822–826, 2018.

[12] Abhay Ashtekar, Beverly K Berger, James Isenberg, and Malcolm MacCallum. *General relativity and gravitation: a centennial perspective*. Cambridge University Press, 2015.

[13] José Ángel Ávila Rodríguez. *On generalized signal waveforms for satellite navigation*. PhD thesis, München, Univ. der Bundeswehr, Diss., 2008, 2008.

[14] D. Barnes, J. Beale, H. Small, and S. Ingalls. Introducing egm2020. In *22nd EGU General Assembly*, page 9884, 2020.

[15] G Beutler, E Brockmann, W Gurtner, U Hugentobler, L Mervart, M Rothacher, and A Verdun. Extended orbit modeling techniques at the code processing center of the international gps service for geodynamics (igs): theory and initial results. *Manuscripta geodaetica*, 19(6):367–386, 1994.

[16] Georg Beyerle. Carrier phase wind-up in gps reflectometry. *GPS solutions*, 13(3):191, 2009.

[17] Alok Bhargava, Luisa Franzini, and Wiji Narendranathan. Serial correlation and the fixed effects model. *The Review of Economic Studies*, 49(4):533–549, 1982.

[18] Matthias Blau. *Lecture notes on general relativity*. Albert Einstein Center for Fundamental Physics Bern, 2011.

[19] Johannes Böhm, Arthur Niell, Paul Tregoning, and Harald Schuh. Global mapping function (gmf): A new empirical mapping function based on numerical weather model data. *Geophysical research letters*, 33(7), 2006.

[20] Grzegorz Bury, Radosław Zajdel, and Krzysztof Sośnica. Accounting for perturbing forces acting on galileo using a box-wing model. *GPS Solutions*, 23(3):1–12, 2019.

[21] Albert J Buschman and Claud M Pittman. *Configuration factors for exchange of radiant energy between axisymmetrical sections of cylinders, cones, and hemispheres and their bases*. National Aeronautics and Space Administration, 1961.

[22] Luigi Cacciapuoti and Ch Salomon. Space clocks and fundamental tests: The aces experiment. *The European Physical Journal Special Topics*, 172(1):57–68, 2009.

[23] Michael F Cohen and Donald P Greenberg. The hemi-cube: A radiosity solution for complex environments. *ACM Siggraph Computer Graphics*, 19(3):31–40, 1985.

[24] Don Colladay and V Alan Kosteleckỳ. Cpt violation and the standard model. *Physical Review D*, 55(11):6760, 1997.

[25] Don Colladay and V Alan Kosteleckỳ. Lorentz-violating extension of the standard model. *Physical Review D*, 58(11):116002, 1998.

[26] Oscar L Colombo. The dynamics of global positioning system orbits and the determination of precise ephemerides. *Journal of Geophysical Research: Solid Earth*, 94(B7):9167–9182, 1989.

[27] Rolf Dach, Stefan Schaer, Daniel Arnold, Etienne Orliac, Lars Prange, Andreja Susnik, Arturo Villiger, and Adrian Jäggi. CODE final product series for the IGS. 2016.

[28] Francesco Darugna, Peter Steigenberger, Oliver Montenbruck, and Stefano Casotto. Ray-tracing solar radiation pressure modeling for qzs-1. *Advances in Space Research*, 62(4):935–943, 2018.

[29] Kenneth Davies. *Ionospheric radio.* Number 31. IET, 1990.

[30] Thierry Dudok De Wit, Laure Lefèvre, and Frédéric Clette. Uncertainties in the sunspot numbers: estimation and implications. *Solar Physics*, 291(9):2709–2731, 2016.

[31] Pacôme Delva, N Puchades, E Schönemann, F Dilssner, Clément Courde, Stefano Bertone, F Gonzalez, A Hees, Ch Le Poncin-Lafitte, F Meynadier, et al. Gravitational redshift test using eccentric galileo satellites. *Physical review letters*, 121(23):231101, 2018.

[32] Arthur Thomas Doodson. The harmonic development of the tide-generating potential. *Proceedings of the Royal Society of London. Series A, Containing Papers of a Mathematical and Physical Character*, 100(704):305–329, 1921.

[33] Thierry Dudok de Wit, Greg Kopp, Claus Fröhlich, and Micha Schöll. Methodology to create a new total solar irradiance record: Making a composite out of multiple data records. *Geophysical Research Letters*, 44(3):1196–1203, 2017.

[34] RJ Eanes. Earth and ocean tide effects on lageos and starlette. In *Proceedings of the Ninth International Symposium on Earth Tides*. E. Sckweizerbart'sche Verlagabuchhandlung, 1983.

[35] Albert Einstein. Über den Einfluß der Schwerkraft auf die Ausbreitung des Lichtes. *Annalen der Physik*, 340(10):898–908, 1911.

[36] Albert Einstein. Die feldgleichungen der gravitation. *Sitzung der physikalische-mathematischen Klasse*, 25:844–847, 1915.

[37] Hans-Juergen Eueler and Clyde C Goad. On optimal filtering of gps dual frequency observations without using orbit information. *Bulletin géodésique*, 65(2):130–143, 1991.

[38] A Feingold. A new look at radiation configuration factors between disks. 1978.

[39] D Felbach, D Heimbuerger, P Herre, and P Rastetter. Galileo payload 10.23 mhz master clock generation with a clock monitoring and control unit (cmcu). In *IEEE International Frequency Control Symposium and PDA Exhibition Jointly with the 17th European Frequency and Time Forum, 2003. Proceedings of the 2003*, pages 583–586. IEEE, 2003.

[40] Henry F Fliegel and Thomas E Gallini. Solar force modeling of block iir global positioning system satellites. *Journal of Spacecraft and Rockets*, 33(6):863–866, 1996.

[41] HF Fliegel, TE Gallini, and ER Swift. Global positioning system radiation force model for geodetic applications. *Journal of Geophysical Research: Solid Earth*, 97(B1):559–568, 1992.

[42] Claus Fröhlich and Judith Lean. Solar radiative output and its variability: evidence and mechanisms. *The Astronomy and Astrophysics Review*, 12(4):273–320, 2004.

[43] Andrew Gelman, John B Carlin, Hal S Stern, and Donald B Rubin. *Bayesian Data Analysis (3rd ed.)*. Chapman and Hall/CRC, 2013.

[44] D.G. Gilmore and M. Donabedian. *Spacecraft Thermal Control Handbook: Fundamental technologies*. Spacecraft Thermal Control Handbook. Aerospace Press, 2002.

[45] Gabriele Giorgi, Martin Lülf, Christoph Günther, Sven Herrmann, Daniela Kunst, Felix Finke, and Claus Lämmerzahl. Testing general relativity using galileo satellite signals. In *2016 24th European Signal Processing Conference (EUSIPCO)*, pages 1058–1062. IEEE, 2016.

[46] Micheal W Glass. Chaparral: A library for solving large enclosure radiation heat transfer problems. Technical report, Sandia National Labs., Albuquerque, NM (United States), 1995.

[47] EADS Astrium GmbH. Environment requirements and test specification. Technical report, EADS Astrium GmbH, 2006.

[48] William H Greene. *Econometrics*. Prentice Hall, 2016.

[49] Frank E Grubbs et al. Sample criteria for testing outlying observations. *Annals of mathematical statistics*, 21(1):27–58, 1950.

[50] Jocelyne Guéna, Michel Abgrall, Daniele Rovera, Peter Rosenbusch, Michael E Tobar, Ph Laurent, André Clairon, and Sébastien Bize. Improved tests of local position invariance using rb 87 and cs 133 fountains. *Physical review letters*, 109(8):080801, 2012.

[51] Manoj Kumar Gupta, Kuldip J Bumtariya, HA Shukla, Pranav Patel, and Ziauddin Khan. Methods for evaluation of radiation view factor: a review. *Materials Today: Proceedings*, 4(2):1236–1243, 2017.

[52] Joachim Hartung, Guido Knapp, and Bimal K Sinha. *Statistical meta-analysis with applications*, volume 738. John Wiley & Sons, 2011.

[53] Sven Herrmann, Felix Finke, Martin Lülf, Olga Kichakova, Dirk Puetzfeld, Daniela Knickmann, Meike List, Benny Rievers, Gabriele Giorgi, Christoph Günther, et al. Test of the gravitational redshift with galileo satellites in an eccentric orbit. *Physical review letters*, 121(23):231102, 2018.

[54] Bernhard Hofmann-Wellenhof, Herbert Lichtenegger, and James Collins. *Global positioning system: theory and practice*. Springer Science & Business Media, 2012.

[55] M Mainul Hoque, Norbert Jakowski, and JA Cahuasquí. Fast ionospheric correction algorithm for galileo single frequency users. In *2020 European Navigation Conference (ENC)*, pages 1–10. IEEE, 2020.

[56] John R Howell, M Pinar Mengüç, Kyle Daun, and Robert Siegel. *Thermal radiation heat transfer*. CRC press, 2020.

[57] Michael Kelly. *The Earth's ionosphere: Plasma physics and electrodynamics*, volume 43. Elsevier, 2012.

[58] WO Kermack, WH McCrea, and ET Whittaker. Iv.—on properties of null geodesics, and their application to the theory of radiation. *Proceedings of the Royal Society of Edinburgh*, 53:31–47, 1934.

[59] John A Klobuchar. Ionospheric time-delay algorithm for single-frequency gps users. *IEEE Transactions on aerospace and electronic systems*, (3):325–331, 1987.

[60] Irving Langmuir. Oscillations in ionized gases. *Proceedings of the National Academy of Sciences of the United States of America*, 14(8):627, 1928.

[61] Alfred Leick, Lev Rapoport, and Dmitry Tatarnikov. *GPS satellite surveying*. John Wiley & Sons, 2015.

[62] H Leuenberger and RA Person. Compilation of radiation shape factors for cylindrical assemblies. Technical report, ELECTRO METALLURGICAL CO NIAGARA FALLS NY, 1954.

[63] Meike List, Stefanie Bremer, Benny Rievers, and Hanns Selig. Modelling of solar radiation pressure effects: Parameter analysis for the microscope mission. *International Journal of Aerospace Engineering*, 2015, 2015.

[64] Andrew D Ludlow, Martin M Boyd, Jun Ye, Ekkehard Peik, and Piet O Schmidt. Optical atomic clocks. *Reviews of Modern Physics*, 87(2):637, 2015.

[65] Paul Melchior. Precession-nutations and tidal potential. In *International Astronomical Union Colloquium*, volume 9, pages 190–212. Cambridge University Press, 1971.

[66] J Mester, R Torii, P Worden, N Lockerbie, S Vitale, and CWF Everitt. The step mission: principles and baseline design. *Classical and Quantum Gravity*, 18(13):2475, 2001.

[67] F Meynadier, P Delva, C le Poncin-Lafitte, C Guerlin, and P Wolf. Atomic clock ensemble in space (aces) data analysis. *Classical and Quantum Gravity*, 35(3):035018, 2018.

[68] Andrea Milani, Anna Maria Nobili, and Paolo Farinella. *Non-gravitational perturbations and satellite geodesy.* 1987.

[69] Charles W Misner, Kip S Thorne, and John Archibald Wheeler. *Gravitation.* Macmillan, 1973.

[70] Oliver Montenbruck, Eberhard Gill, and Fh Lutze. Satellite orbits: models, methods, and applications. *Appl. Mech. Rev.*, 55(2):B27–B28, 2002.

[71] Oliver Montenbruck, Peter Steigenberger, and Urs Hugentobler. Enhanced solar radiation pressure modeling for galileo satellites. *Journal of Geodesy*, 89(3):283–297, 2015.

[72] Frank Negretti. Die Galileo FOC Satelliten von OHB, 4 2015.

[73] Dwight Roy Nicholson and Dwight R Nicholson. *Introduction to plasma theory*, volume 582. Wiley New York, 1983.

[74] Arthur E Niell. Global mapping functions for the atmosphere delay at radio wavelengths. *Journal of Geophysical Research: Solid Earth*, 101(B2):3227–3246, 1996.

[75] The company's webplatform. `https://www.ohb.de/`, 2021.

[76] Chansik Park and PJG Teunissen. A new carrier phase ambiguity estimation for gnss attitude determination systems. In *Proceedings of international GPS/GNSS symposium, Tokyo*, volume 8, 2003.

[77] Steven Peil, Scott Crane, James L Hanssen, Thomas B Swanson, and Christopher R Ekstrom. Tests of local position invariance using continuously running atomic clocks. *Physical Review A*, 87(1):010102, 2013.

[78] Volker Perlick. Characterization of standard clocks by means of light rays and freely falling particles. *General relativity and gravitation*, 19(11):1059–1073, 1987.

[79] Volker Perlick. Allgemeine relativitätstheorie. University Lecture, 2016.

[80] Gérard Petit and Brian Luzum. IERS conventions (2010). Technical report, Bureau International des Poids et mesures sevres (france), 2010.

[81] Dennis Philipp, Eva Hackmann, and Claus Laemmerzahl. Redshift and frequency comparison in schwarzschild spacetime. *arXiv e-prints*, pages arXiv–1711, 2017.

[82] Elena A Plis, Daniel P Engelhart, Russell Cooper, W Robert Johnston, Dale Ferguson, and Ryan Hoffmann. Review of radiation-induced effects in polyimide. *Applied Sciences*, 9(10):1999, 2019.

Chapter A

[83] Eric Poisson and Clifford M Will. *Gravity: Newtonian, post-newtonian, relativistic*. Cambridge University Press, 2014.

[84] Robert V Pound and Glen A Rebka Jr. Apparent weight of photons. *Physical Review Letters*, 4(7):337, 1960.

[85] Robert V Pound and Joseph L Snider. Effect of gravity on gamma radiation. *Physical Review*, 140(3B):B788, 1965.

[86] ChengGang Qin, YuJie Tan, and ChengGang Shao. Test of einstein equivalence principle by frequency comparisons of optical clocks. *Physics Letters B*, 820:136471, 2021.

[87] JF Redor. Introduction to spacecraft thermal control, 1995.

[88] Benny Rievers. *High precision modelling of thermal perturbations with application to Pioneer 10 and Rosetta*. PhD thesis, Staats-und Universitätsbibliothek Bremen, 2012.

[89] Pascal Rochat. Atomic clocks technologies for galileo & related applications. In *Stanford PNT Symposium 2019, Stanford, October*, 10 2019.

[90] Pascal Rochat, Fabien Droz, Qinghua Wang, and Sylvère Froidevaux. Atomic clocks and timing systems in global navigation satellite systems. In *Proceedings of European navigation conference, Gdansk, April*, pages 1–11, 2012.

[91] J Saastamoinen. Atmospheric correction for the troposphere and stratosphere in radio ranging satellites. *The use of artificial satellites for geodesy*, 15:247–251, 1972.

[92] John Salvatier, Thomas V Wiecki, and Christopher Fonnesbeck. Probabilistic programming in python using pymc3. *PeerJ Computer Science*, 2:e55, 2016.

[93] Mark Schenewerk. A brief review of basic gps orbit interpolation strategies. *GPS solutions*, 6(4):265–267, 2003.

[94] Torben Schüler. *On ground-based GPS tropospheric delay estimation*. PhD thesis, Univ. der Bundeswehr München, Fak. für Bauingenieur-und Vermessungswesen . . . , 2001.

[95] Robert Schunk and Andrew Nagy. *Ionospheres: physics, plasma physics, and chemistry*. Cambridge university press, 2009.

[96] Bob Schutz, Byron Tapley, and George H Born. *Statistical orbit determination*. Elsevier, 2004.

[97] René Schwarz, Stefanie Bremer, David Seelbinder, Meike List, Benny Rievers, Takahiro Kato, and Florian Wöske. The hybrid simulation platform for space systems (hps): A modular matlab/simulink-based simulation library for gnc systems development. In *70th International Astronautical Congress (IAC)*, 2019.

[98] Selex ES, Subsidiary of Leonardo S.p.A. *Passive Hydrogen Maser - Technical Specification*, 1 2015. ASD MM07688 02-15.

[99] P Series. Ionospheric propagation data and prediction methods required for the design of satellite services and systems. *Recommendation ITU-R*, pages 531–14, 2019.

[100] European GNSS (Galileo) Open Service. Ionospheric correction algorithm for galileo single frequency users. 2016.

[101] Irwin I Shapiro. Fourth test of general relativity. *Physical Review Letters*, 13(26):789, 1964.

[102] Irwin I Shapiro, Michael E Ash, Richard P Ingalls, William B Smith, Donald B Campbell, Rolf B Dyce, Raymond F Jurgens, and Gordon H Pettengill. Fourth test of general relativity: new radar result. *Physical Review Letters*, 26(18):1132, 1971.

[103] Irwin I Shapiro, Gordon H Pettengill, Michael E Ash, Melvin L Stone, William B Smith, Richard P Ingalls, and Richard A Brockelman. Fourth test of general relativity: preliminary results. *Physical Review Letters*, 20(22):1265, 1968.

[104] Dmitry Sidorov, Rolf Dach, Bernard Polle, Lars Prange, and Adrian Jäggi. Adopting the empirical code orbit model to galileo satellites. *Advances in space research*, 66(12):2799–2811, 2020.

[105] Michael H Soffel. Relativity in astrometry, celestial mechanics and geodesy. In *Relativity in Astrometry, Celestial Mechanics and Geodesy*, pages 1–31. Springer, 1989.

[106] JJ Spilker Jr. Tropospheric effects on gps. *Global Posiotioning System: Theory and Applications*, 1:517–546, 1996.

[107] TA Springer, G Beutler, and M Rothacher. Improving the orbit estimates of gps satellites. *Journal of Geodesy*, 73(3):147–157, 1999.

[108] TA Springer, G Beutler, and M Rothacher. A new solar radiation pressure model for gps satellites. *GPS solutions*, 2(3):50–62, 1999.

[109] Gilbert Strang and Kai Borre. *Linear algebra, geodesy, and GPS*. Siam, 1997.

[110] TJ Sumner. Equivalence principle measurements. *General Relativity and Gravitation*, 36(10):2331–2339, 2004.

[111] Maciej Sznajder. *Degradation of Materials under Space Conditions-Extrapolation of Short Term Laboratory Results on Long Term Space Mission Effects*. PhD thesis, Universität Bremen, 2016.

[112] Byron D Tapley. *Theory of Satellite Geodesy and Gravity Field Determination*. Springer, 1989.

[113] Peter JG Teunissen. Gps carrier phase ambiguity fixing concepts. In *GPS for Geodesy*, pages 263–335. Springer, 1996.

[114] PJ Teunissen, PJ De Jonge, and CCJM Tiberius. Performance of the lambda method for fast gps ambiguity resolution. *NAVIGATION, Journal of the Institute of Navigation*, 44(3):373–400, 1997.

[115] Erwan Thébault, Christopher C Finlay, Patrick Alken, Ciaran D Beggan, Elisabeth Canet, Arnaud Chulliat, Benoit Langlais, Vincent Lesur, Frank J Lowes, Chandrasekharan Manoj, et al. Evaluation of candidate geomagnetic field models for igrf-12. *Earth, Planets and Space*, 67(1):1–23, 2015.

[116] Erwan Thébault, Christopher C Finlay, Ciarán D Beggan, Patrick Alken, Julien Aubert, Olivier Barrois, Francois Bertrand, Tatiana Bondar, Axel Boness, Laura Brocco, et al. International geomagnetic reference field: the 12th generation. *Earth, Planets and Space*, 67(1):79, 2015.

[117] ME Tobar, PL Stanwix, JJ McFerran, J Guéna, M Abgrall, S Bize, A Clairon, Ph Laurent, P Rosenbusch, D Rovera, et al. Testing local position and fundamental constant invariance due to periodic gravitational and boost using long-term comparison of the syrte atomic fountains and h-masers. *Physical Review D*, 87(12):122004, 2013.

[118] Pierre Touboul, Gilles Métris, Manuel Rodrigues, Yves André, Quentin Baghi, Joël Bergé, Damien Boulanger, Stefanie Bremer, Patrice Carle, Ratana Chhun, et al. Microscope mission: first results of a space test of the equivalence principle. *Physical review letters*, 119(23):231101, 2017.

[119] European Union. *European GNSS (Galileo) open service: signal in space interface control document.* Office for Official Publications of the European Communities, 2021.

[120] RFC Vessot and MW Levine. A test of the equivalence principle using a space-borne clock. *General relativity and gravitation*, 10(3):181–204, 1979.

[121] Robert FC Vessot. Clocks and spaceborne tests of relativistic gravitation. *Advances in Space Research*, 9(9):21–28, 1989.

[122] Robert FC Vessot, MW Levine, EM Mattison, EL Blomberg, TE Hoffman, GU Nystrom, BF Farrel, R Decher, PB Eby, CR Baugher, et al. Test of relativistic gravitation with a space-borne hydrogen maser. *Physical Review Letters*, 45(26):2081, 1980.

[123] MR Vujičić, NP Lavery, and SGR Brown. View factor calculation using the monte carlo method and numerical sensitivity. *Communications in numerical methods in Engineering*, 22(3):197–203, 2006.

[124] Todd A Wagner, S Schlamminger, JH Gundlach, and Eric G Adelberger. Torsion-balance tests of the weak equivalence principle. *Classical and Quantum Gravity*, 29(18):184002, 2012.

[125] James R Wertz. *Spacecraft attitude determination and control*, volume 73. Springer Science & Business Media, 2012.

[126] Clifford M Will. The confrontation between general relativity and experiment. *Living reviews in relativity*, 17(1):1–117, 2014.

[127] P Wolf and G Petit. Relativistic theory for clock syntonization and the realization of geocentric coordinate times. *Astronomy and Astrophysics*, 304:653, 1995.

[128] J. Wu, S. Wu, G. Hajj, W. Bertiger, and S. M. Lichten. Effects of antenna orientation on gps carrier phase. 1992.

[129] Philipp Zingerle, Roland Pail, and Thomas Gruber. High-resolution combined global gravity field modelling-the d/o 5,400 xgm2020 model. In *22nd EGU General Assembly*, page 16447, 2020.